PhD PROCEEDINGS

ANNUAL ISSUES OF THE DOCTORAL SCHOOL

FACULTY OF INFORMATION TECHNOLOGY & BIONICS

2015

PhD PROCEEDINGS

ANNUAL ISSUES OF THE DOCTORAL SCHOOL

FACULTY OF INFORMATION TECHNOLOGY & BIONICS
PÁZMÁNY PÉTER CATHOLIC UNIVERSITY

PhD PROCEEDINGS

ANNUAL ISSUES OF THE DOCTORAL SCHOOL

FACULTY OF INFORMATION TECHNOLOGY & BIONICS

2015

PÁZMÁNY UNIVERSITY *e*PRESS
BUDAPEST, 2015

HU ISSN 2064-7271

Kiadja a Pázmány Egyetem eKiadó
Budapest, 2015

Felelős kiadó
Ft. Dr. Szuromi Szabolcs Anzelm O. Praem.
a Pázmány Péter Katolikus Egyetem rektora

Cover image by Zsófia SZTYÉHLIKNÉ BÉRCES, *Two channel fluorescent image of GFP-NE-4C cells on a nanostroctured chip*

Contents

Introduction

It is our pleasure to publish this Annual Proceedings again to demonstrate the genuine interdisciplinary research done at the Jedlik Laboratories by young talents working in the Interdisciplinary Doctoral School of the Faculty of Information Technology at Pázmány Péter Catholic University. The scientific results of our PhD students show the main recent research directions in which our faculty is engaged. Thanks are also due to the supervisors and consultants, as well as to the five collaborating National Research Laboratories of the Hungarian Academy of Sciences, the Semmelweis Medical School and the University of Pannonia. The collaborative work with the partner universities, especially, Katolieke Universiteit Leuven, Politecnico di Torino, Technische Universität München, University of California at Berkeley, University of Notre Dame, Universidad de Sevilla, Universita di Catania is gratefully acknowledged.

As an important development of this special collaboration, we were able to jointly accredit a new undergraduate curriculum on Molecular Bionics with the Semmelweis Medical School, the first of this kind in Europe.

We acknowledge the many sponsors of the research reported here. Namely,

- the Hungarian National Research Fund (OTKA),
- the Hungarian Academy of Sciences (MTA),
- the National Development Agency (NFÜ),
- the Gedeon Richter Co.,
- the Office of Naval Research (ONR) of the US,
- NVIDIA Ltd.,
- Eutecus Inc., Berkeley, CA,
- MorphoLogic Ltd., Budapest,
- Analogic Computers Ltd., Budapest,
- AnaFocus Ltd., Seville,

and some other companies and individuals.

Needless to say, the resources and support of the Pázmány Péter Catholic University is gratefully acknowledged.

Budapest, June 2015.

GÁBOR PRÓSZÉKY

Chairman of the Board of the Doctoral School

PÉTER SZOLGAY

Head of the Doctoral School
Head of the Jedlik Laboratory

Program 1

BIONICS, BIO-INSPIRED WAVE COMPUTERS, NEUROMORPHIC MODELS

Heads: Tamás FREUND, György KARMOS, Zsolt LIPOSITS, Sándor PONGOR

Role of endocannabinoids in the effect of 17β-estradiol (E2) on the synaptic inputs of gonadotropin-releasing hormone (GnRH) neurons

Flóra BÁLINT
(Supervisor: Imre FARKAS, Zsolt LIPOSITS)
Pázmány Péter Catholic University, Faculty of Information Technology and Bionics
50/a Práter street, 1083 Budapest, Hungary
balint.flora@itk.ppke.hu

***Abstract*- Gonadotropin-releasing hormone (GnRH) neurons regulate reproduction centrally. In vivo 17β-estradiol (E2) controls GnRH release in concentration and estrus cycle dependent manner. In vitro patch-clamp electrophysiological data on GnRH neurons of ovariectomized female mice demonstrated that low concentration (10 pM) of E2 decreased spontaneous firing rate which was eliminated by blocking fast synaptic neurotransmission [1]. In the present study, we examined the effect of low concentration of E2 on GABAergic postsynaptic currents (PSCs) in GnRH neurons of acute brain slices obtained from metestrous female mice. It has been demonstrated that activation of the retrograde endocannabinoid machinery inhibits the GABAergic synaptic neurotransmission in GnRH neurons [2], therefore, we analyzed the putative involvement of endocannabinoid signaling mechanisms in the evoked effect of E2. Our results indicate that an interaction exists between estradiol and endocannabinoid signaling, which represents novel regulatory machinery in the execution of the negative estrogen feedback to GnRH neurons.**

***Keywords*- GnRH, endocannabinoid, electrophysiology, estradiol**

I. INTRODUCTION

Gonadotropin-releasing hormone (GnRH) neurons form the final common pathway for the central regulation of reproduction. These neurons are located in a scattered pattern in the preoptic area (POA) of the hypothalamus. The axons of GnRH cells secrete the GnRH into the hypophysial portal circulation at the hypothalamic median eminence (ME). Here, the hormone enters into the bloodstream and regulates the synthesis and secretion of the gonadotropins, such as follicle-stimulating hormone (FSH) and luteinizing hormone (LH). FSH and LH are released into the systemic circulation and act on the gonads to stimulate gonadal steroid secretion. These sexual steroid hormones, such as estrogen, also have an effect on the hypothalamic hormone secretion via classical feedback loops. Both negative and positive feedback mechanisms are controlled by the classical genomic and the non-classical actions of estrogen. Nevertheless, the mechanisms underlying the feedback events are not entirely clear, especially in the case of the negative feedback. Thus our goal was to examine the effects of E2 on GnRH neurons.

17β-estradiol (E2) controls GnRH release in a concentration and estrus cycle dependent manner. *In vitro* patch-clamp electrophysiological studies on GnRH neurons of ovariectomized female mice showed that low concentration (10 pM) of E2 decreased spontaneous firing rate which could be eliminated by blocking fast synaptic neurotransmission [1]. The retrograde endocannabinoid system was suggested to be involved in evoking the effects of E2. Endocannabinoids are synthesized in neurons and control the neurotransmitter release from the presynaptic cells. It was previously shown that GABAergic terminals could also be under the control of the endocannabinoid system as endocannabinoids were shown to be able to decrease the frequency of the GABAergic postsynaptic currents in GnRH neurons [2]. Therefore, our other aim was to investigate the possible interaction between the non-classical effect of the E2 and endocannabinoid signalings.

II. MATERIALS AND METHODS

A. Animals

Adult, gonadally intact female mice were used from local colonies bred at the Medical Gene Technology Unit of the Institute of Experimental Medicine (IEM). They were maintained in 12h light/dark cycle (lights on at 06:00h) and temperature controlled environment (22±2°C), with standard rodent chow and tap water available *ad libitum*. All mice were housed in the same room under same environmental conditions. GnRH-green-fluorescent protein (GnRH-GFP) transgenic mice were used for electrophysiological experiments. In this animal model, a GnRH promoter segment drives selective GFP expression in the majority of GnRH neurons. Phase of the estrous cycle was checked by both evaluating vaginal smear and visual observation of the vaginal opening. All studies were carried out with permissions from the Animal Welfare Committee of the Institute of Experimental Medicine Hungarian Academy of Sciences and in accordance with legal requirements of the European Community.

The present work was supported by grants from the National Science Foundation of Hungary (OTKA K100722), the European Union FP7 funding (FP7/2007-2013) under grant agreement No. 245009.

F. BÁLINT, "Role of endocannabinoids in the effect of 17beta-estradiol (E2) on the synaptic inputs of gonadotropin-releasing hormone (GnRH) neurons" in *PhD Proceedings Annual Issues of the Doctoral School, Faculty of Information Technology and Bionics, Pázmány Péter Catholic University – 2015.* G. Prószéky, P. Szolgay Eds. Budapest: Pázmány University ePress, 2015, pp 13– 15.

B. Brain slice preparation and recording

Mice were deeply anesthetized by Isoflurane inhalation. After decapitation brain was removed rapidly and immersed in ice-cold cutting solution which had been extensively bubbled with a mixture of 95% O2 and 5% CO2. Hypothalamic blocks were dissected, and 250μm-thick coronal slices were prepared from the medial septum/preoptic area (POA) with a VT-1000S vibratome in the ice-cold Na-free oxygenated cutting solution. The slices containing POA were transferred into artificial cerebrospinal fluid (aCSF) saturated with O_2/CO_2 and kept in it for 1 h to equilibrate. Equilibration started at 33°C and was allowed to cool to room temperature.

Electrophysiological recordings were carried out at 33°C, during which the brain slices were oxygenated by bubbling the aCSF with O_2/CO_2. Axopatch 200B patchclamp amplifier, Digidata-1322A data acquisition system, and pCLAMP 10.4 software were used for recording. Cells were visualized with a BX51WI IR-DIC microscope located on an antivibration table. The patch electrodes (OD=1.5 mm, thin wall) were pulled with a Flaming-Brown P-97 puller and polished with an MF-830 microforge. GnRH-GFP neurons were identified by brief illumination at 470 nm using an epifluorescent filter set, based on their green fluorescence, typical fusiform shape, and topographic location in the POA. After control recording (5 min), the slices were treated with various drugs and the recording continued for a subsequent 10 min. Each neuron served as its own control when drug effects were evaluated.

C. Whole-cell patch clamp experiments

The cells were voltage clamped at -70mV holding potential. Pipette offset potential, series resistance (Rs) and capacitance were compensated before recording. Only cells with low holding current (<50 pA) and stable baseline were used. Input resistance (Rin), Rs, and membrane capacity (Cm) were also measured before each recording by using 5-mV hyperpolarizing pulses. To ensure consistent recording qualities, only cells with Rs<20 MΩ, Rin>500MΩ, and Cm >10 pF were accepted. The resistance of the patch electrodes was 2–3 MΩ.

D. Statistical analysis

Each experimental group contained 10–18 recorded cells from six to seven animals. Recordings were stored and analyzed off-line. Event detection was performed using the Clampfit module of the PClamp 10.4 software. Group data were expressed as mean ± SEM. The percentage change in the frequency of the PSCs resulted from the application of various drugs was calculated. Statistical significance was analyzed using ANOVA followed by Newman-Keuls (NK) test and considered at $P < 0.05$.

III. Results

First the effect of the estradiol at low concentration was tested. Measurements were carried out with an initial control recording (5 min), then E2 (10pM) was administered onto the brain slices (n=18) and the recording continued for a subsequent 10 min. The whole-cell patch clamp recordings revealed that E2 significantly diminished frequency of the PSCs (49±7% of the control) (Fig. 1). As this effect occurred within minutes, we can conclude that the inhibition of PSCs was a result of the non-classical effects of the hormone.

In order to investigate the role of the endocannabinoid signaling in this mechanism, the endocannabinoid receptors were blocked by the cannabinoid receptor type-1 (CB1) antagonist, AM251 (1 μM) which was added to the aCSF 10 min before starting the recording. After 5 min control recording, E2 (10pM) was added onto the brain slices (n=12) and the recording continued for a subsequent 10 min. Pretreatment of the brain slices with AM251 significantly attenuated the effect of E2 on the PSCs (86±4%), (Fig. 2). This confirms that the endocannabinoids are involved in execution of gonadal hormone effect.

There are two main types of endocannabinoids in the central nervous system: the anandamide (AEA) and the 2-arachidonoylglycerol (2-AG). We used tetrahydrolipstatin (THL, 10μM) to determine which endocannabinoid takes part in this mechanism and which cell synthesizes it. The diacylglycerol (DAG) lipase is an important component in the synthesis of 2-AG and since THL is a DAG lipase inhibitor, it was added into the intracellular solution in order to block 2-AG synthesis exclusively in the measured GnRH neuron. THL was allowed to enter into the intracellular milieu of the measured cell for 15 min before control recording. After 5 min control recording E2 (10pM) was administered onto the brain slices (n=13) and the recording continued for a subsequent 10 min. This intracellular application of THL into the GnRH neurons eliminated the action of E2 (67±5%) (Fig. 3). These results suggest that the 2-AG is involved in this mechanism and is synthesized by GnRH neurons.

Most of the hormones execute their effects on neuron directly and/or indirectly. The direct effects can be detected by using tetrodotoxin (TTX). TTX inhibits the firing of action potentials in all neurons by binding to the voltage sensitive sodium channels in cell membranes and therefore, the spike-mediated transmitter release is blocked. Thus only miniature postsynaptic currents (mPSCs) can be measured, since the measured cell can no longer receive any action potential related input signal. For mPSC recordings TTX (650 nM) was added to the aCSF 10 minutes before start. After 5 min control recording E2 (10 pM) was administered onto the brain slices (n=12) and the recording continued for a subsequent 10 min. The estradiol significantly decreased the frequency of the mPSCs (50 ± 9%), (Fig. 4) indicating that the effect of the E2 is direct on the GnRH neurons.

The estradiol can take its effects via classical estrogen receptors (ERs). These classical receptors are ERα and ERβ. To examine which receptor type is involved in the non-classical action of the estradiol on the GnRH neurons, subtype selective ER agonists were used in the presence of TTX. After 5 min control recording, the agonists were administered onto the brain slices and the recording continued for a subsequent 10 min. First ERα agonist PPT (10 pM) was administered (n=10), but it had no significant effect on mPSCs (78 ± 6%). Next ERβ

agonist DPN (10 pM) was used (n=10) and we observed a decrease in the frequency of the mPSCs (60±5%) (Fig. 5). These results indicate that ERβ is required for the effect of the estradiol on the GnRH neurons.

Finally the effect of estradiol was tested in the presence of cannabinoid type-1 (CB1) antagonist AM251 (1 μM) and TTX (660 nM) in order to confirm our previous results showing that endocannabinoid signaling is involved in the mediation of the effect of E2 on suppression of fast neurotransmission onto GnRH neurons. After 5 min control recording the E2 was administered onto the brain slices (n=12) and the recording continued for a subsequent 10 min. The CB1 receptor antagonist attenuated the effect of E2 on the mPSCs (86±9%) (Fig. 6), supporting our results.

IV. Conclusions

Endocannabinoid system is involved in the mediation of the effect of E2 on suppression of fast neurotransmission onto GnRH neurons (Fig. 7).In this effect, 2-AG plays a fundamental role. The interaction of estradiol and endocannabinoid signaling mechanisms represents novel regulatory machinery in the execution of the negative estrogen feedback to GnRH neurons.

Acknowledgment

The author wishes to acknowledge Dr. Imre Farkas and Prof. Zsolt Liposits for their excellent supervision.

References

[1] Z. Chu, J. Andrade, M. Shupnik and S Moenter, "Differential regulation of gonadotropin-releasing hormone neuron activity and membrane properties by acutely applied estradiol: dependence on dose and estrogen receptor subtype." J. Neurosci;2 9(17):5616-27. Apr 2009.

[2] I.Farkas, I. Kalló, L. Deli, B. Vida, E. Hrabovszky, C. Fekete, S. Moenter, M. Watanabe, Z. Liposits, "Retrograde endocannabinoid signaling reduces GABAergic synaptic transmission to gonadotropin-releasing hormone neurons." Endocrinology, 151(12):5818-29. Dec 2010

Evoked high frequency oscillations in human hippocampus

Virág BOKODI

(Supervisor: Dániel FABÓ, István ULBERT)
Pázmány Péter Catholic University, Faculty of Information Technology and Bionics
50/a Práter street, 1083 Budapest, Hungary
bokodi.virag@ itk.ppke.hu

***Abstract*—Cortical electrical stimulation (CES) and electrically evoked potentials (EP) are widely used investigational methods to study neural connections and networks both in rodent and human brain. High frequency oscillations (HFO) (ripples and fast ripples) participate in memory consolidation and epileptogenic processes predominantly in and around the hippocampal formation (HcF). We examined the effect of CES under general anaesthesia in the HcF of eight temporal lobe epilepsy (TLE) patients.**

***Keywords*— epilepsy, in vivo, human, hippocampus, cortical electrical stimulation, high frequency oscillations**

I. INTRODUCTION

Epilepsies are the most frequent primary neurological diseases. About 60% of all types of the epilepsies are localization related epilepsies where the seizures rise from a focal alteration of the brain. The largest subgroup of the focal epilepsies is the mesial temporal lobe epilepsy (mTLE), where the hippocampus is often affected and this is the seizure onset zone. Patients with mesial temporal lobe epilepsy may benefit from the surgical removal of the epileptogenic zone.

In these patients, the area responsible for seizure generation is difficult to define precisely. This definition are helped several preoperative techniques, for example interictal and ictal EEG, PET, MRI, CT, these are still time consuming and only partly accurate. [1] Other biomarkers for the epileptogenic zone have been suggested, such as interictal spike and spontaneous high-frequency oscillations.

The most characteristic electrical patterns are the interictal spikes (IIS), which can be measured in epileptic patients. Recent studies resulted that beside the IISs high frequency oscillations (HFO) are also present within the epileptic focus. [2]

The high frequency oscillations are local, oscillatory field potential activities with 80-500 Hz central frequency. [3] Two distinct HFO frequency range was reported in humans, the slow ripples (80-150 Hz), and the fast ripple (150-500 Hz). [4] The cut-off frequency between the two groups has been uncleared yet.

It has been unknown also, that the slow and fast ripples are considered as overlapping or distinct categories. Not only in animal but also in human studies fast ripples (FR) showed higher association to the epileptogenesis. FRs were demonstrated in epileptically transformed rats in several brain regions, where even slow ripples, associated with physiological processes, were also missing. [5] Based on studies using invasive electrodes, FRs were present in the hippocampus and entorhinal cortex of TLE patients ipsilateral to the seizure onset zone. [2] Human epilepsy studies shown, that total removal of HFOs generating area correlates with a good surgical outcome. [6]

Pharmacological and electric stimulation methods have been used to evoke responses both animal and human brain *in vitro* and *in vivo*. In human epilepsy patients, electrical stimulation can evoke cortical, delayed responses with single pulse stimulation, which are similar to EEG spikes, and their locations are related to the seizure onset zone. [7] In *in vivo*, animal model – tetanus toxin injected rats – were found, that single pulse electrical stimulation can also evoke epileptic high-frequency oscillations. [8] Van't Klooster et al. investigated the distribution of frequency of simulation evoked spikes showing slow and fast ripples in human cortex. [1]

The main advantage of the electrical stimulation technique is that it can be scheduled and the monitoring is not necessary for a long time, which has risks of complications and patients discomfort.

Our aim is to characterize the stimulus-evoked high frequency oscillations (evHFO) with small latency in the human hippocampus in temporal lobe epilepsy patients.

II. METHODS

A. Clinical electrodes and recordings

The electrode implantations, recordings and stimulation took place at established epilepsy surgical center in Budapest (National Institute of Clinical Neuroscience). The experiments were performed under general anaesthesia, under surgery, just before the seizure onset zone – in this case it is the hippocampus – was removed. Patients were implanted with subdural strip electrodes in order to stimulation in the temporal-basal area, and laminar multi-electrode in the hippocampus, where the evoked potentials (EPs) have occurred. For the recordings we used one or two laminar electrodes. This 24 contact multi-electrode has been described previously [9, 10].

V. BOKODI, "Evoked high frequency oscillations in human hippocampus" in *PhD Proceedings Annual Issues of the Doctoral School, Faculty of Information Technology and Bionics, Pázmány Péter Catholic University – 2015.* G. Prószéky, P. Szolgay Eds. Budapest: Pázmány University ePress, 2015, pp 17– 20.

B. Cortical electrical stimulation

Systematic bipolar stimulation of each pair of adjacent point of strip electrodes was administered with single pulses of electrical current (5,10,15 mA, 0.5 Hz, 0.1 ms pulse width, 5,10,25 and 50 trials per electrode pair). The sampling rate was 2000 Hz for the HFOs and 20000 Hz for the multi-unit activity (MUA) investigation. The associated evoked responses (EPs) were measured at laminar multi-electrodes. The EPs were analysed in 100 ms interval after the stimulus.

C. Data analysis

Electrophysiological data analyses were performed using NeuroScan 4.5 software, EEGLAB and own developed Matlab scripts.

At first, the movements of electrodes were eliminated to define the border of the involved hippocampus subregions. Hippocampal regions were reconstructed based on histological assessment of the removed HcFs, and subregions were determined as follows: Cornu Ammonis (CA), Dentate Gyrus (DG), Subiculum (Sub, distal, proximal, pro).

The stimulus induced artefacts were cut out and replaced with low-frequency section. The data were band-pass filtered (80-500 Hz for evHFOs, and 500-5000 Hz for MUAs), rectification, baseline correction (-450 ms to -50 ms) and five time smoothing (with 6 ms window) was performed. For the evoked response amplitude, a statistical z-score value, shown in Eq.1., was computed to receive the average EEG amplitude deviation.

$$z = \frac{x - \mu}{\sigma}$$

Eq. 1. Standard z-score, where x is the evoked response amplitude, μ is the mean of the data baseline (-450ms to -50 ms), and σ is the standard deviation of the data baseline

We seek for the biggest z-score value 100ms after stimulation, which we defined the middle point of the evoked HFO.

The frequency of the HFOs was measured after wavelet transformation. The analysis was carried out from the detected HFO's peak ± 25 ms interval, and then the middle 20 ms section was averaged. The peak frequency values were determined, and separated to primary frequencies (with the biggest amplitude), and secondary frequencies (with smaller amplitude).

III. Results

A. The detection

Based on the above described method, the figure shows the result of the HFO detection.

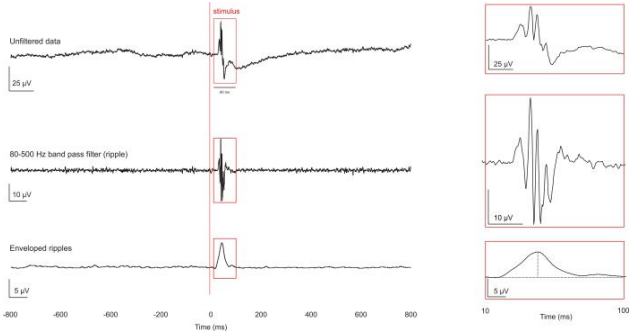

Fig 1. One example of the result of detected evoked HFO. First the unfiltered data; baseline (-450 - -50 ms) and band-pass (80-500 Hz) filtered with ripples; enveloped data (6 ms window, five times). The stimulation was 0 ms, the relevant interval 10-100 ms. The zscore was calculated from the enveloped data, in the 10-100 ms interval beetween the largest peak and baseline (dashed, vertical line).

B. Distribution of HFOs in subregions

Significant HFO activity was evoked in 7 cases (87.5%). Subregion distribution of evHFO is the following (significant HFO / case number): CA2:1/2, CA3: 1/4, DG: 3/6, distal Sub: 5/6, proximal Sub and proSub: 2/2.

	Distribution of evHFOs in hippocampus subregions		
	Case number	***Sum evHFO***	***%evHFO***
CA2	2	1	50%
CA3	4	1	25%
DG	6	3	50%
distal Sub	6	6	100%
proxSub	1	1	100%
proSub	1	1	100%
Sub all	8	8	100%

Table 1. Distributions of evHFO in hippocampus subregions. Case number: the number of patients, where the subregions was occurred. Sum evHFO: cumulative value of evoked high frequency oscillations. Percentage rate of evHFO (%evHFO).

C. Current and location of stimulus

The aim of this examination was to determine the excitability dependences on stimulus strength, stimulus distance and the relationship between them.

We observed that the regional distributions of the evHFO vary with the strength of the stimulation current. Sub had a lower stimulus amplitude threshold (5 mA) than DG (10 mA).

(Fig. 2) The ratio of the evoked activities depended also on the stimulation site. Stimulation closer to temporal pole evoked HFOs with higher probability. (Fig. 3)

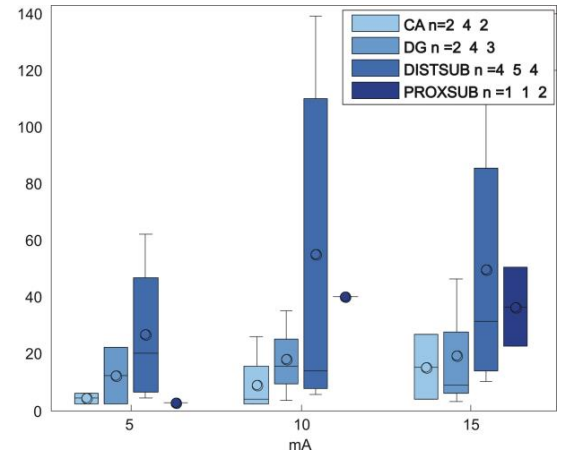

Fig 2. Result of dependeces on stimulus strength. The x axes shows the different stimulus strength (5-15 mA), y axes shows the zscore values. Different colours denote different Hc regions (CA,DG,distSub, proxSUB).

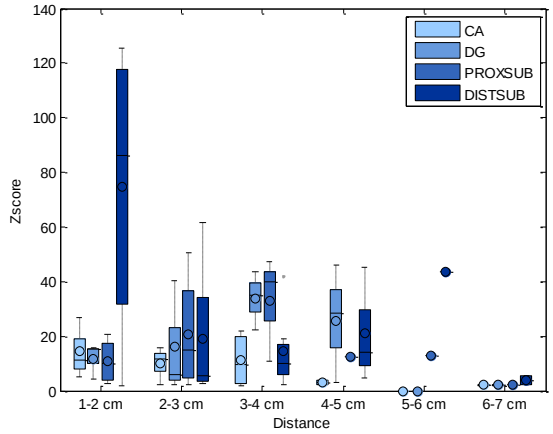

Fig 3. Result of dependeces on stimulus distance. The x axes shows the different distance from temporal pole (1-7 cm), y axes shows the zscore values. Different colours denote different Hc regions (CA,DG,distSub, proxSUB).

D. *Frequency*

We observed that the evoked HFO activities have more frequency components. During an HFO event we found a first order component, which has the biggest power amplitude with average 146.95 ± 63.14 Hz frequency and several secondary components with smaller power amplitude, but higher frequency value, the average is 216.95 ± 89.13 Hz. On average event contains two frequency components.

We found in all hippocampus regions not only HFO with averaged 135-150 Hz, but also fast HFOs with 210-235 Hz central frequency. However, not only in Sub, but in CA and DG regions are observed fast HFOs with 400 Hz.

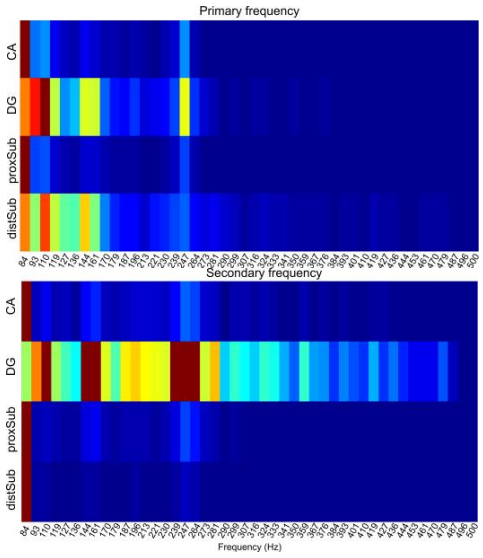

Fig 4. Result of distribution of primary (top figure) and secondary (bottom figure) frequencies in the hippocampal regions. The x axes shows the different frequency values (80-500 Hz), y axes shows the regoins. Values are normalized between 0-1 (blue-red). Note: Outstanding frequencies around 100, 150, 250 Hz which supposed to be artefacts caused by AC harmonics.

E. *Multi unit activity*

As a result we found that in 7 cases (87.5%) there were no overlaps between evoked HFO and evoked multiple unit activities. So, the detected high frequency activities were not comes from cell layers.

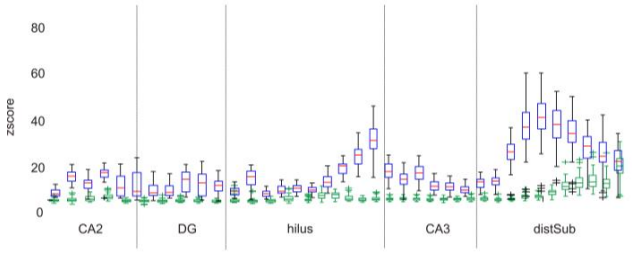

Fig 5. One example of comparison the MUAs and evHFOs zscore. The x axes show the regions, y axes show zscore values. The evHFOs (blue) can be detected in hilus and distSub, by contrast MUAs activity (green), which can be observed just in deeper layer of distSub. The two detected activities are not overlapped.

IV. Conclusion

In most of the cases were detected evoked HFOs with electrical stimulation under general anaesthesia. Based on this, it seems that this method can be able to investigate the epileptic focus not only awake but also in anesthetized state.

The evoked HFOs in DG can sign these oscillation pathological nature.

From the result, that evHFOs were detected in Sub with lower stimulus strength, we can assume that this region has important role of epileptic mechanism evolving.

We could detect evHFOs mainly close to the temporal lobe, which can be the characteristic of epileptic neural network.

FURTHER AIMS

We would like to cluster the detected HFO based on waveform and frequency. Furthermore, we would like to analyze the long latency evoked high frequency oscillations and the spontaneous HFOs also.

REFERENCES

[1] Van't Klooster MA, Zijlmans M, Leijten FS, Ferrier CH, Van Putten MJ, Huiskamp GJ, "Time-frequency analysis of single pulse electrical stimulation to assist delineation of epileptogenic cortex", Brain, 134(Pt 10):2855-66, 2011.

[2] I. Khalilov, M. Le Van Quyen, H. Gozlan, and Y. Ben-Ari, "Epileptogenic actions of GABA and fast oscillations in the developing hippocampus", Neuron, vol. 48, pp. 787-96, 2005.

[3] A. Bragin, J. Engel Jr, R.J.Staba, "High-frequency oscillations in epileptic brain", CurrentOpinion in Neurology, pp. 151-156, 2010.

[4] D. Fabó, "Properties of spontaneous and evoked discharges in the human subiculum", in Clinical NeuroSciences Doctoral School. Budapest, Semmelweis University, 2008.

[5] A. Bragin, C. L. Wilson, J. Almajano, I. Mody, J. Engel JR, "High-frequency oscillations after status epilepticus: epileptogenesis and seizure genesis", Epilepsia, vol. 45, pp. 1017-23, 2004.

[6] Jacobs J, Zijlmans M, Zelmann R, Chatillon CE, Hall J, Olivier A, Dubeau F, Gotman J, "High-frequency electroencephalographic oscillations coorelate with outcome of epilepsy surgery", Ann Neurol, 67(2):209-220, 2010.

[7] A. Valentín, M. Anderson, G. Alarcón, J. J. García Seoane, R. Selway, C. D. Binnie, C. E. Polkey, "Responses to single pulse electrical stimulation identify epileptogenesis in the human brain in vivo", Brain, 125, 1709-1718, 2002.

[8] John D. Rolston, Nealen G. Laxpati, Claire-Anne Gutekunst, Steve M. Potter, Robert E. Gross, "Spontaneous and evoked high frequency oscillations in the tetanus toxin model of epilepsy", Epilepsia, 51(11):2289-2296, 2010.

[9] I. Ulbert, E. Halgren, G. Heit, and G. Karmos, "Multiple microelectrode-recording system for human intracortical applications.", J. Neurosci Methods, vol. 106, (no. 1), pp. 69-79, Mar 2001

[10] I. Ulbert, Z. Magloczky, L. Eross, S. Czirjak, J. Vajda, L. Bognar, S. Toth, Z. Szabo, P. Halasz, D. Fabo, E. Halgren, T. F. Freund, G. Karmo, "In vivo laminar electrophysiology co-registered with histology in the hippocampus of patients with temporal lobe epilepsy," ExpNeurol, vol. 187, pp. 310-8, 2004.

Analysis of the genetic background of type 2 diabetes mellitus using molecular biological methods

Réka DÉNES
(Supervisor: Zoltán GÁSPÁRI, Zsolt RÓNAI)
Pázmány Péter Catholic University, Faculty of Information Technology and Bionics
50/a Práter street, 1083 Budapest, Hungary
denes.reka@itk.ppke.hu

***Abstract*—Type 2 diabetes is a complex disease, caused by complicated interactions between genetic and environmental factors. Our aim in this PhD project is to identify and analyze some of the genetic factors (polymorphisms) of type 2 diabetes. Discovering the risk factors of a disease is of great significance in theoretical as well as practical (clinical) aspects. On one side, it can shed light on the accurate function, role and regulation of given genes and their protein function. On the other hand this knowledge can be used to elaborate more efficient therapeutic approached and can contribute to primary and secondary prevention.**

***Keywords*-WFS1, diabetes mellitus, genetics**

I. Introduction

Diabetes mellitus is one of the most serious health problems world-wide. 382 million people were suggested to suffer from the disease in 2013 [1], whereas this number was only 285 million in 2010 demonstrating the urgent need of efficient prevention and therapy of the illness. 90% of the patients suffer from type 2 diabetes characterized by insulin resistance, whereas type 1 form of the disease is caused by the lack of insulin production.

Polymorphisms are genetic variants similar to mutations. They can affect just one (SNP - single nucleotide polymorphism) or several (VNTR - variable number of tandem repeats) nucleotides. They can be located in the coding and also in the regulatory regions of the genes. Their minor allele frequency is usually higher than 5%, and they cause susceptibility to a certain complex disease or property.

Although the Human Genome Project was completed more than a decade ago, and the sequence of the whole genome is available since [2], identification of the genetic background of complex diseases and traits is still challenging [3]. Two substantially different approaches are available to detect genetic risk factors of polygenic diseases. Genome wide association studies (GWAS) do not require any a priori hypothesis ensuring the analysis of all biologically significant genetic components. However, genome-wide studies always include the investigation of irrelevant targets, and multiple testing requires appropriate correction of the statistical analysis. Consequently, significance threshold is usually defined between 10^{-8} and 10^{-6} [4], which is often too stringent for the identification of biologically relevant genetic variants with statistically small effect.

Candidate gene studies on the other hand focus on the investigation of selected polymorphic loci, providing the possibility of more sensitive analysis of the given polymorphisms. These two complementary techniques possess similar effect sizes, however, being rather different, thus may often provide somewhat contradictory results. According to a recent comprehensive meta-analysis, 7.1% of candidates were confirmed by both methods [5].

Candidate gene study and GWAS share one common aspect: they both require the analysis of large populations necessitating efficient, high throughput genotyping techniques. Genome wide association studies identified several loci associated with diabetes mellitus, which data, however, need verification and may serve as starting point for further genetic and functional analyses [6].

The WFS1 gene is often mentioned as a putative component of type 2 diabetes [7]. The gene is located in the 4th chromosome (Figure 2) and it encodes a transmembrane glycoprotein (wolframin) of the endoplasmic reticulum which is highly expressed in beta cells [8]. On one hand, loss of function mutations in WFS1 can cause insulin-deficient diabetes mellitus as a component of Wolfram syndrome, a rare autosomal recessive disorder [9]. On the other hand, a growing body of evidence indicates that common genetic variations in the same gene can increase the risk for type 2 diabetes [10]. In spite of the large amount of empirical data, the causative relationship between the function of the protein and beta-cell failure remains unknown. As an ER resident protein, it can contribute to the proper folding of insulin, and acts as a regulator of ER stress signaling [11]. These observations clearly suggest that it is crucial to the maintain proper wolframin level in different compartments of the cell. Several different ways of protein regulation have been implicated in disease development in case of WFS1.

II. Methods

Here we present some of the genotyping methods which are employed in the PhD project, such as restriction endonucle-

R. DÉNES, "Analysis of the genetic background of type 2 diabetes mellitus using molecular biological methods" in *PhD Proceedings Annual Issues of the Doctoral School, Faculty of Information Technology and Bionics, Pázmány Péter Catholic University – 2015.* G. Prószéky, P. Szolgay Eds. Budapest: Pázmány University ePress, 2015, pp 21– 23.

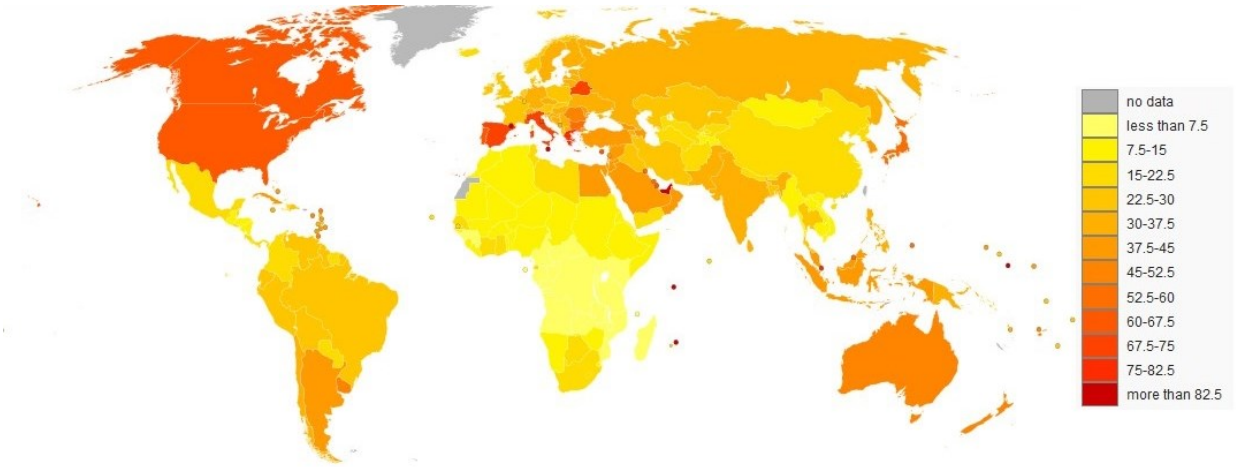

Fig. 1. Prevalence of diabetes mellitus worldwide in 2000 (per 1000 inhabitants) (source: who.int)

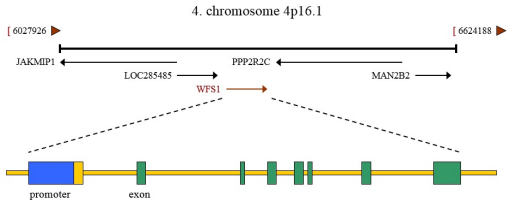

Fig. 2. Location of the WFS1gene

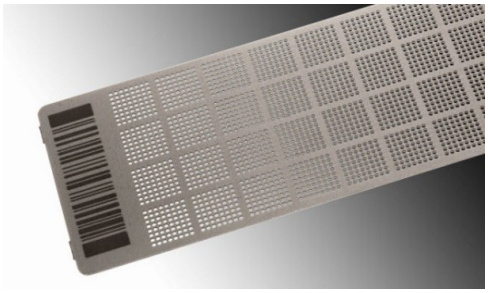

Fig. 3. OpenArray chip

ase based method, allele-specific polymerase chain reaction, TaqMan OpenArray method and melting curve analysis.

All of the presented methods are PCR (polymerase chain reaction)-based methods. PCR is based on using the ability of DNA polymerase enzyme to synthesize new strand of DNA complementary to the offered template strand. Because DNA polymerase can add a nucleotide only onto a preexisting 3'-OH group, it needs a primer to which it can add the first nucleotide. Usually two 8-12 nucleotide-long primers are designed. Since changing the temperature is a crutial criterion during the process the melting point of the two primers required to be equal. This requirement makes it possible to delineate a specific region of template sequence that the researcher wants to amplify. At the end of the PCR reaction, the specific sequence will be accumulated in billions of copies.

Restriction fragment length polymorphism or RFLP can be used to investigate a SNP if the polymorphism is located in the recognition site of a restriction endonuclease. These enzymes are able to recognize a certain nucleotide sequence and cut the DNA. The experiment should be designed in a way that the enzyme would cut in the presence of one allele, but not the other. The next step is to visualize the DNA products.

Gel electrophoresis is the standard lab procedure for separating DNA by size for visualization and purification. Electrophoresis uses an electrical field to move the negatively charged DNA toward a positive electrode through an agarose gel matrix. The gel matrix allows shorter DNA fragments to migrate more quickly than larger ones. Thus, you can accurately determine the length of a DNA segment by running it on an agarose gel alongside a DNA ladder. In that wa, subsequent submarine agarose gel electrophoresis is readily applicable to separate the digested and non-digested fragments thus to determine the genotype of each sample.

Finally, including a control digestion site into the PCR-product increases reliability, because it confirms the efficiency of DNA digestion and proves that lack of digestion is not the consequence of any technical issues.

Allele-specific amplification is an alternative of RFLP, if no restriction endonuclease is available for the analysis of a given locus. Four primers should be designed for the experiment, two of them are outer primers and the other two are allele-specific, which means, that their 3' end is located exactly on the SNP site. Each individual is genotyped in two parallel reactions employing the two outer and one of the allele-specific primers. This latter primers form a PCR-product only if the appropriate allelic variant is present in the investigated sample. We can evaluate the genotype based on the presence or the absence of the allele-specific product using gel electrophoresis.

The TaqMan Openarray technique is a miniaturized real-

time PCR method. As the name suggests, real-time PCR is a technique used to monitor the progress of a PCR reaction in real time. Unlike the traditional methods, which requires gel electrophoresis, it is based on the detection of the fluorescence produced by a reporter molecule which produces increasing signal, as the reaction proceeds. Two allele-specific fluorescent probes labeled with different dyes (e.g. VIC, FAM) are applied to determine the genotype of the samples. The OpenArray technique is a robust method and it employs a low-density array: one OpenArray slide (Figure 3) offers the analysis of 32 SNPs of 96 samples. The primers are designed and fixed on the surface of the slide. It is very fast and sensitive, but also expensive compared to traditional methods.

VNTR-s can usually be investigated by a PCR in combination with a gel electrophoresis. However analysis of short repeats is challenging in this way. Thus, we elaborated a novel melting curve analysis based technique for genotyping a 6 bp insertion / deletion polymorphism. PCR-products with different length possess different melting point, as the longer sequences contain more hydrogen bonds. A fluorescent DNA-intercalator dye (e.g. SybrGreen) can be used for detection, as it can be bound only to double stranded DNA. This offers the possibility of melting point determination: briefly, if fluorescent signal is continuously detected while slowly heating up a DNA fragment, a drop of fluorescence can be detected at the melting point, as DNA is denatured, and amount of dsDNA decreases.

III. Conclusions

Here we presented a few genotyping techniques, which are planned to be use in this PhD project. With these techniques, genotypes of diabetic and control samples can be determined and used for further statistical analysis. Besides genotyping, further plans include protein-modelling, examining putative biological function with luciferase reporter assay and network-based modeling of the selected variants. Our aim at the end of the PhD project is to get closer to the deeper understanding of the genetics of type 2 diabetes mellitus.

Acknowledgment

I would like to thank to my supervisors dr. Zsolt Rónai and dr. Zoltán Gáspári for their help and support.

References

[1] International Diabetes Federation. IDF Diabetes Atlas, 6th edn. Brussels, Belgium:International Diabetes Federation, 2013. http://www.idf.org/diabetesatlas

[2] Venter et al. The sequence of the human genome. Science. 2001 Feb 16;291(5507):1304-51. Erratum in: Science 2001 Jun 5;292(5523):1838. PubMed PMID: 11181995.

[3] Maher, B. Personal genomes: The case of the missing heritability. Nature. 2008 Nov 6;456(7218):18-21. doi: 10.1038/456018a. PubMed PMID: 18987709.

[4] Mansiaux, Y., Carrat, F. Contribution of genome-wide association studies to scientific research: a bibliometric survey of the citation impacts of GWAS and candidate gene studies published during the same period and in the same journals. PLoS One. 2012;7(12):e51408. doi: 10.1371/journal.pone. 0051408. Epub 2012 Dec 11. PubMed PMID: 23240019; PubMed Central PMCID: PMC3519865.

[5] Chang, C. Q., Yesupriya, A., Rowell, J. L., Pimentel, C. B., Clyne, M., Gwinn, M., Khoury, M. J., Wulf, A., Schully, S. D. A systematic review of cancer GWAS and candidate gene meta-analyses reveals limited overlap but similar effect sizes. Eur J Hum Genet. 2014 Mar;22(3):402-8. doi: 10.1038/ejhg.2013.161. Epub 2013 Jul 24. PubMed PMID: 23881057; PubMed Central PMCID: PMC3925284.

[6] Sanghera, D. K., Blackett, P. R., Type 2 Diabetes Genetics: Beyond GWAS. J Diabetes Metab. 2012 Jun 23;3(198). pii: 6948. PubMed PMID: 23243555; PubMed Central PMCID: PMC3521576.

[7] Sandhu MS et al. Common variants in WFS1 confer risk of type 2 diabetes. Nat Genet. 2007 Aug;39(8):951-3. Epub 2007 Jul 1. PubMed PMID:17603484; PubMed Central PMCID: PMC2672152.

[8] Shang L et al. β-cell dysfunction due to increased ER stress in a stem cell model of Wolfram syndrome. Diabetes.2014 Mar;63(3):923-33. doi: 10.2337/db13-0717. Epub 2013 Nov 13. PubMed PMID: 24227685; PubMed Central PMCID: PMC3931392.

[9] Khanim F, Kirk J, Latif F, Barrett TG. WFS1/wolframin mutations, Wolfram syndrome, and associated diseases. Hum Mutat. 2001 May;17(5):357-67. Review. PubMed PMID: 11317350.

[10] Franks PW et al. Replication of the association between variants in WFS1 and risk of type 2 diabetes in European populations. Diabetologia. 2008 Mar;51(3):458-63. Epub 2007 Nov 27. Erratum in: Diabetologia. 2008 Mar;51(3):523. PubMed PMID: 18040659; PubMed Central PMCID: PMC2670195.

[11] Hofmann S, Philbrook C, Gerbitz KD, Bauer MF. Wolfram syndrome: structural and functional analyses of mutant and wild-type wolframin, the WFS1 gene product. Hum Mol Genet. 2003 Aug 15;12(16):2003-12. PubMed PMID: 12913071.

Assessing the compliance of dynamic protein structural ensembles with experimental NMR data

Dániel DUDOLA
(Supervisor: Zoltán GÁSPÁRI)
Pázmány Péter Catholic University, Faculty of Information Technology and Bionics
50/a Práter street, 1083 Budapest, Hungary
dudola.daniel@itk.ppke.hu

***Abstract*—To unfold the functional mechanism of proteins, it is essential to describe their internal dynamics at the atomic level. The analysis of dynamics can be done with theoretical and practical methods, of the latter only NMR spectroscopy provides the required information at multiple time scales. However, the parameters obtained from the measurements reveal only specific aspects of the actual atomic motions and it is necessary to put a physical picture behind them. The approach, which is considered to be the most fruitful is the combination of experiments and calculations, where the parameters derived from the measurements, with proper spatial interpretation, can be used as restraints in molecular dynamics calculations. This approach is highly similar to the traditional structure determination methods, the difference lies in the use of the experimental results.**

In such simulations, experimentally-derived parameters are represented in an ensembles-based manner. Thus, instead of requiring the compliance of each conformer with all of the experimental data, the compliance is interpreted and expected on the ensemble. However, each parameter reflects motions at a given time scale. In order to simulatenously describe protein motions at different time scales, simulations were performed where parameters describing fast motions were applied to subpopulations and those representing slower ones to the full ensemble. After processing the output of the simulations, the applied restraints were compared to corresponding parameters back-calculated from the ensemble. To facilitate the process of back-calculations, the existing CoNSEnsX [1] code base was completely rewritten and restructured, novel functionalities were added.

***Keywords*-protein dynamics; protein ensembles; ubiquitin ensembles**

I. Introduction

Biological macromolecules – like proteins – are typically present as an ensemble of the possible conformations of the given structures. The states and the energy barriers separating these states show great variability among various proteins. These conformations are responsible for the various and specific tasks the protein achieves, which represent the physiological function of the protein. The movements of the structures occur on a timescale of 14 magnitudes and currently there is no experimental method with which these movements could be examined simultaneously. [2] Through the spatial changes of the structure, the molecules show different affinity toward various ligands. Thus, the presence of a specific ligand can cause changes to the systems dynamic equilibrium towards to the conformers with higher affinity for the ligand, even if these conformations are only represent as a small fraction in the absence of the ligand.

For a long time, proteins were represented as single, rigid structures and most of the experimental structure determination methods were not capable to deliver detailed information about the possible movements of the protein. With the advances in NMR technology, the examination of these movements became available even on multiple timescales. NMR spectroscopy is the most suited experimental method for examining these molecular movements on an atomic level, although because of physical limitations of the measurements the movements of different timescales can not be examined simultaneously. The deliberate combination of molecular dynamic simulations and experiments tends to give the the best results for describing atomic level movements of biomolecules.

NMR measurements deliver numerous parameters, which describe dynamical properties of the ensemble in an averaged manner. [3] The usage of these parameters in molecular dynamic simulations requires a suitable and correct underlying physical interpretation. To describe the dynamics of protein ensembles, the following NMR derived parameters are used:

- Nuclear Overhauser Effect (NOE)
- Residual Dipolar Couplings (RDC)
- Lipari-Szabó order parameters ($S^{2^{LS}}$)

Parameters describing internal dynamics are often provided as supplementary information to papers or appended to static structural models. It is important to keep in mind, that models created with the usage of NMR derived parameters, that the experimentally determined parameters describe the whole ensemble, rather that a single structure. In such dynamical ensembles the internal movements can in theory be represented on multiple timescales and they are conducive to deeper understanding the physiological functions of such motions.

Another motivation for representing protein structures in an ensemble-based manner is that in several systems models built upon a single conformer do not represent adequately the actual structure of the given protein. A good example is the group of intrinsically disordered proteins (IDPs), in their case the high flexibility of the structures requires ensemble-based representation. The highly dynamical nature of such proteins has proved to be important and was key in describing numerous biochemical mechanisms, although the atomic level description of such features are often difficult.

D. DUDOLA, "Assessing the compliance of dynamic protein structural ensembles with experimental NMR data" in *PhD Proceedings Annual Issues of the Doctoral School, Faculty of Information Technology and Bionics, Pázmány Péter Catholic University – 2015.* G. Prószéky, P. Szolgay Eds. Budapest: Pázmány University ePress, 2015, pp 25– 28.

To evaluate structural ensembles created with molecular dynamic simulations, it has to be taken into account, which parameters were used during the simulation process and what timescale these parameters represent movements on. At the assessment of these ensembles overfitting should be avoided, because the average of the possible conformations has more degrees of freedom than a single structure, and thus it is easier to find correspondence with the experimental data. It is useful to check the ensemble with cross-validation, for example calculating correspondence with experimental data not used in the MD simulations, calculating the variance from the native structure (if present) or using other validated ensembles.

II. Molecular dynamics simulation

Although the methods of molecular dynamic simulations are under constant development, the models provided by the simulations do not necessarily – and in fact, the often do not – exhibit adequate correspondence with the experimentally derived dynamical parameters. Most simulation programs use an empirical forcefield, in which the molecules are free to move in the presence of water (or implicit solvent, to reduce computational cost). Since the applied forcefield is empirical, adequate correspondence is hard to achieve without other restrictions to the simulation process. One opportunity for decreasing the difference between experimental parameters and the ones back-calculated from the molecular dynamic simulations is to restraining the simulation with the experimental data. With the growing size of the ensemble it becomes more difficult to correctly average the parameters and to avoid under- or overfitting. An alternative approach is to apply stochastic optimization on the conformers created with molecular dynamic simulation and iteratively select conformers, until the newly created sub-ensemble corresponds to the desired parameters. The method is mostly applied on intrinsically disordered proteins, where the conformational space to be considered is large, so the iterative optimization process can be carried out efficiently.

The purpose of the simulations is to generate ensembles that reflect the internal dynamics of the structures: on one hand, the residual dipolar couplings (RDC) derived restraints, which describe movement on the slower timescale would result better correspondence to the whole ensemble; the order parameter (S^2) on the other hand, describes movement on the faster timescale, thus showing better correspondence to the subpopulations of the ensemble. The simulations were carried out involving different setups with reflect to the size of the full ensemble and the subpopulations. A single S^2 parameter set was used to restrain all subpopulations independently of each other and a number of experimentally-derived amide N-H RDC sets were applied on the full ensemble.

III. Motivation

A. The role of dynamical ensembles representing multiple timescales in the process of molecular recognition

Molecular recognition plays an important role in every biological process, in fact, the specific interactions between biological macromolecules are one of the most basic steps in physiological processes. Thus, getting acquainted with molecular recognition is a key for deeper understanding of such processes at a molecular level. One of the current hypotheses state that the molecule undergoes specific conformational changes in the presence of a ligand. This scenario is called induced fit. Newer results suggest that there is an alternative mechanism: the theory of conformational selection states that there are many conformers in the ensemble at the same time and the ligand selects the most suitable conformer to bind to causing a population shift in the direction of the favored conformer. The mechanism of induced fit as well as conformer selection plays a role during the real interaction: after the binding initially binds *via* conformer selection, additional confomational adjustments involving side-chains and backbone segments optimizations happen similar to those predicted by the induced fit mechanism.

B. New models of protein interactions

Prior to the recognition of conformer selection, the lock-and-key model was the accepted theory behind protein-protein and protein-ligand interactions, along with the induced fit model considered as a special case. The lock-and-key model assumes that there is no significant difference in structures regardless of binding state, the ligand (the key) finds the binding site on the protein (lock). Unlike the lock-and-key model, the hypothesis of induced fit suggests that the differences between the bound an unbound states are caused by the interaction with the binding ligands, in which the ligand causes conformational changes to the protein. Both models handles protein structures as a single, stable conformer in the free state, which is a clear oversimplification.

Proteins, however, are dynamic in their nature and exist in numerous conformations at the same time. Beside the native structure – the one with the lowest energy – there are many other conformers which could play a role in the process of conformational selection. The alternative model of conformer selection emphasises the conformational heterogeneity of protein structures and assumes, that the conformers with higher energy state are responsible for the recognition and binding of ligands, causing a population shift in the ensemble in favor of the bound-like conformational state.

IV. Simulation and analysis of own ubiquitin ensembles

The dynamics of biomolecules covers multiple timescales and this behavior can in principle be modeled in molecular dynamics simulations. The changes between energy states occur on the ns timescale, so residual dipolar coupling (RDC) parameters are a good choice to distinguish ensemble subpopulations by conformational state, because RDC parameter sets, if a suitable number of independent experiments can be perormed, carry information about movements on this timescale. The Lipari-Szabó model-free parameters on the other hand deliver dynamical information on the ps-ns timescale. A plausible combination is that there are different subpopulations that

interchange on the slower time scale while the subpopulations themselves can be described by parameters reporting on the faster time-scale.

During the analysis of the ubiquitin ensembles calulated using the subpopulation-based setup, the compliance of experimental data and from the simulation back-calculated dynamical parameters. According to the dynamical information content of the used and back-calculated order parameters, we expected a higher compliance of RDC data sets on the full ensemble and a lower compliance in the subpopulations. Conversely, we expected a lower compliance of order parameters on the full ensemble and a higher in the subpopulations. If our assumption is correct, the calculated compliances should fulfill our expectations: the movements on the slower timescale (RDC) characterize the full population better, while the ones on the faster timescale (order parameters) correspond to the subpopulations.

To verify our hypothesis, I performed a number of molecular dynamical simulations with different setups. We used 25 experimentally delivered N-H RDC sets as restraints on the 6 ns long simulation, from different experimental setups, to ensure a satisfying coverage of motions on the ns timescale. An experimentally measured N-H S^2 parameter set was also included as restraint. In accord with the literature, our experience showed that to keep amide bond planarity (especially to avoid the out-of-plane motions of amide hydrogens), I put additional restraints on all amide bonds to keep them planar.

To simplify and speed up the analysis of such ensembles, the CoNSEnsX software was overhauled and completely rewritten in Python 3. Additionally, some new features were implemented, such as:

- handling RDC sets from different experiments (i.e. adifferent alignments) separately
- option on aligning of the input structures using a user-specified range of residues
- option on selecting Karplus equation parameters used for back-calculation of scalar couplings
- option to directly fetch input structures from pdb.org
- support for accepting NOE distance data in STAR-NMR format (the new standard at rcsb.org)
- redesigned client-side
- vector graphic output of graphs

Other new functions, currently under implementation:

- side-chain S^2 back-calculation
- selection algorithm on ensembles to obtain sub-ensembles with better correspondence to input data
- various server-side enhancements

After the successful simulation, the created ensemble was organized into subpopulations according to the applied restraining scheme. Each RDC set and the order parameter set were back-calculated on the full ensemble and on each subpopulation as well.

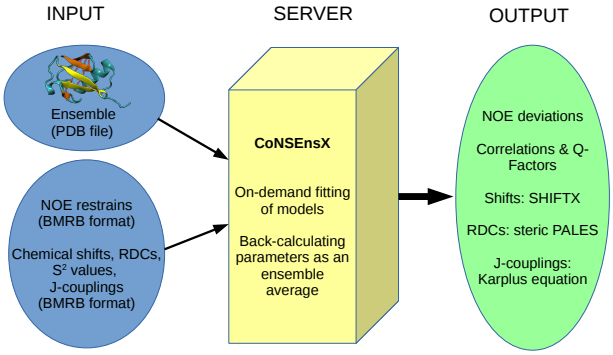

Fig. 1. Schematic on the usage of CoNSEnsX

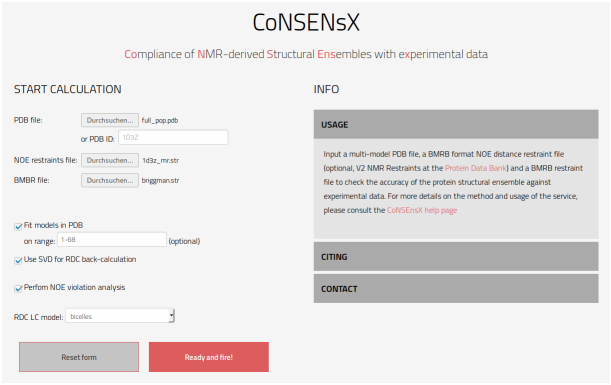

Fig. 2. Redesigned client-side of CoNSEnsX showing off new features

Some calculated results expressed with correlation as a measure of compliance, without attempting to be comprehensive:

CORRELATION	FULL ENSEMBLE	SUBPOPULATION
RDC list 1	0.990	0.894
RDC list 2	0.992	0.927
RDC list 3	0.986	0.909
RDC list 4	0.991	0.951
RDC list 5	0.982	0.942
RDC list 6	0.984	0.946
RDC list 7	0.983	0.943
RDC list 8	0.983	0.943
RDC list 9	0.981	0.942
RDC list 10	0.978	0.944
RDC list 11	0.983	0.941
order parameters	0.695	0.828

From the proportions of the compliance of the experimental and the back-calculated values we can assume that our assumption was right: in the back-calculated RDC correspon-

dences each and every RDC set had a higher correlation value on the whole ensemble and on the other hand, the correspondence of the order parameters was higher on the subpopulation than on the whole population. The other measures of correspondence (Q-value, root mean square deviation) also confirm this relation between the parameters representing movements of different timescales and their correspondence to the (sub)population(s).

Among these measures of correspondence CoNSEnsX also provides three graphs for each back-calculated parameter sets (when all the three graphs make sense):

- correlation of the experimental and the back-calculated values
- experimental and the back-calculated values visualized per residue
- option on selecting Karplus equation parameters used for back-calculate scalar coupling constants
- correlation of the ensemble, average correlation of the models and per model correlation

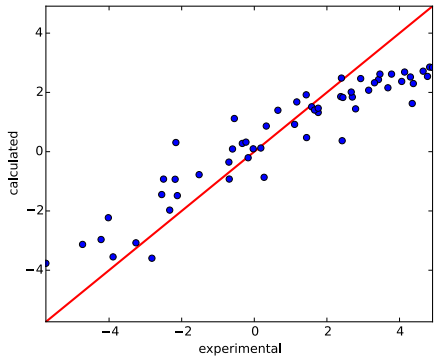

Fig. 3. Example correlation graph (CoNSEnsX output)

All the back-calculated RDC sets yielded a satisfactorily high correlation with the experimental data indicating, that the restraining and the basic configuration of the molecular dynamic simulation was successful. Due to the number of used RDC sets and their different origin, singular value decomposition (SVD) was used by back-calculation of RDC datasets to ensure the best orientation for each molecular structure.

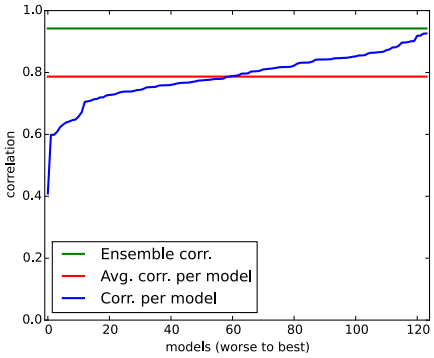

Fig. 4. Example per model correlation graph (CoNSEnsX output)

It must be noted that the models as an ensemble have a much higher compliance with the experimental data than the average of the per model compliances. The correspondence of the ensemble can be even higher that the best available models correspondence, supporting the idea that protein structures should be represented as ensembles of conformers instead of a single/few structure(s).

V. Conclusion

After several attempts, I have managed to create dynamical structural ensembles of ubiquitin where the observed internal dynamics at multiple timescales is satisfactorily represented in a simultaneous manner. Further improvements to the simulation are still possible, with adding additional restraints but without over-restraining the model. I will continue the fine-tuning of the parameters of the simulation but due to the extreme runtime of the simulations at a significant length, rapid experimenting with the physical parameters are not always possible. I have implemented impotant novel features into the rewritten CoNSEnsX software, with other interesting improvements to come, further simplifying the process of back-calculation and basic structure analysis. When the planned improvements and the server-side features are implemented, we expect the rewritten CoNSEnsX software to be ready for publication and available for on-line use.

Acknowledgment

The author would like to thank Dr. Gáspári Zoltán and Bertalan Kovács for their advices on the topic and their kind help at setting up the molecular dynamics simulations.

References

[1] A. F. Ángyán, B. Szappanos, A. Perczel, and Z. Gáspári, "Consensx: an ensemble view of protein structures and nmr-derived experimental data," *BMC Structural Biology*, vol. 10:39, 2010.

[2] Z. Gáspári and A. Perczel, "Protein dynamics as reported by nmr," *Annual Reports on NMR Spectroscopy*, vol. 71, pp. 35–76, 2010.

[3] B. Richter, J. Gsponer, P. Várnai, X. Salvatella, and M. Vendruscolo, "The mumo (minimal under-restraining minimal over-restraining) method for the determination of native state ensembles of proteins," *J Biomol NMR*, vol. 37, p. 117–135, 2007.

Subcellular localization of the components of the nitric oxide system in the hypothalamic paraventricular nucleus of mice

Erzsébet FARKAS
(Supervisor: Csaba FEKETE)
Pázmány Péter Catholic University, Faculty of Information Technology and Bionics
50/a Práter street, 1083 Budapest, Hungary
farkas.erzsebet@koki.mta.hu

***Abstract*—Nitric oxide (NO) is a gaseous transmitter. In the hypothalamic paraventricular nucleus (PVN), it has been implicated in the regulation of energy homeostasis and neuroendocrine control. However, little information is known about the subcellular localization of the components of the NO system in the PVN and whether NO is utilized as an anterograde and/or retrograde messenger by the parvocellular neurons of this nucleus. Neuronal nitric oxide synthase (nNOS) is the enzyme responsible for the NO production of neurons, and the primary mechanism mediating the effects of NO on target neurons is the soluble guanylate cyclase-facilitated production of cGMP. Soluble guanylate cyclase is a heterodimer composed of α (α1 and α2) and β (β1 and β2) subunits, the most prevalent form being the α1/β1 heterodimer. Using antisera against nNOS and the soluble guanylate cyclase α1 and β1 subunits, immuno-electron microscopy was performed to determine the subcellular localization of these proteins in the parvocellular part of the PVN in mice. nNOS was abundantly present in neuronal perikarya and dendrites and also in axon varicosities. In perikarya and dendrites, nNOS-immunoreactivity was widely distributed in the cytoplasm, primarily associated with the endoplasmatic reticulum. nNOS-immunoreacivity was also found to be associated with the perikaryal plasma membrane in close proximity to both symmetric and asymmetric synapses, as well as within axon varicosities forming both symmetric and asymmetric synapses. The soluble guanylate cyclase α1 subunit was found in dendrites and axon varicosities and associated with both the pre- and postsynaptic densities of the synapses. The α1 subunit was associated with both symmetric and asymmetric types of synapses, whereas the β1 subunit was primarily observed in dendrites and frequently associated with the postsynaptic density of synapses. On rare occasions when the β1 subunit was observed in axon varicosities, the immunoreactive varicosities formed symmetric type synapses.**

In summary, these data indicate that nitric oxide may be utilized as both an anterograde and retrograde transmitter in the parvocellular part of the PVN.

Keywords-*nitric oxide; paraventricular nucleus; electron microscopy*

I. INTRODUCTION

Nitric oxide (NO) is a gaseous transmitter that has extremely short half-life in biological systems. It is synthesized by the nitric oxide synthase (NOS) enzymes from the amino acid L-arginine. There are three NOS isoforms: endothelial NOS (eNOS), inducible NOS (iNOS) and neuronal NOS (nNOS). All are present in the nervous system, however, nNOS is the principal isoform that is utilized by neurons. NO primarily exerts its effect through the soluble guanylyl cyclase enzyme (sGC). Soluble GC is a heterodimer molecule. Four sGC subunits, α1, α2, ß1 and ß2, have been identified. The most common form in mammalian tissues is the α1/ß1 heterodimer. The activity of sGC results in an increase of intracellular cyclic GMP (cGMP) levels. This way, NO causes accumulation of cGMP in cells leading to activation of multiple downstream targets, including kinases, ion channels and phosphodiesterases. NO can be utilized as both anterograde and retrograde transmitter.

The hypothalamic paraventricular nucleus (PVN) has been implicated in the regulation of energy homeostasis and the neuroendocrine systems. NO has been shown to play important role in the regulation of these functions including the regulation of food intake, TRH gene expression and CRH release, suggesting that NO may influence the parvocellular neurons of the PVN. However, little information is available about the localization and function of this transmitter system in the PVN.

Therefore, we performed ultrastructural studies to determine the precise localization of the components of the NO transmitter system in the parvocellular part of the PVN and to

E. FARKAS, "Subcellular localization of the components of the nitric oxide system in the hypothalamic paraventricular nucleus of mice" in *PhD Proceedings Annual Issues of the Doctoral School, Faculty of Information Technology and Bionics, Pázmány Péter Catholic University – 2015.* G. Prószéky, P. Szolgay Eds. Budapest: Pázmány University ePress, 2015, pp 29– 32.

understand whether NO can be utilized as an anterograde and/or retrograde transmitter in this nucleus.

II. MATERIAL AND METHODES

The experiments were carried out on ten adult, male, CD1 mice, weighing 30–35 g, housed under standard environmental conditions (light between 06:00 and 18:00 h, temperature 22±1 ^{o}C, mouse chow and water *ad libitum*). All experimental protocols were reviewed and approved by the Animal Welfare Committee at the Institute of Experimental Medicine of the Hungarian Academy of Sciences.

Animals were deeply anesthetized with ketamine/xylazine (ketamine 50 mg/kg, xylazine 10 mg/kg body weight, ip). Five minutes later, the animals were perfused transcardially with 10 ml 0.01 M phosphate-buffered saline (PBS), pH 7.4, followed sequentially by 10 ml of 4% paraformaldehyde in Na-acetate buffer, pH 6.0, and then by 50 ml of 4% paraformaldehyde in Borax buffer, pH 8.5. The brains were rapidly removed and stored in 4% paraformaldehyde in 0.1 M phosphate buffer (PB), pH 7.4, for 24 h at 4 ºC.

Serial, 25µm thick coronal sections were cut on a Leica VT 1000S vibratome (Leica Microsystems, Wetzlar, Germany). The sections were treated with 0.5% H_2O_2 in PBS for 15 min. The sections were cryoprotected in 15% sucrose in PBS for 15 min at room temperature and in 30% sucrose in PBS overnight at 4^{o}C and then, quickly frozen over liquid nitrogen to improve antibody penetration into the tissue. To detect the nNOS-immunoreactivity, pretreated sections were then placed into rabbit anti-nNOS serum (1:200) for 4 days at 4 ^{o}C and after rinsing in PBS and 0.1% cold water fish gelatin/1% bovine serum albumin (BSA) in PBS, incubated in donkey anti-rabbit IgG conjugated with 0.8 nm colloidal gold (Electron Microscopy Sciences, Fort Washington, PA) diluted at 1:100 in PBS containing 0.1% cold water fish gelatin and 1% BSA. After rinsing in 0.2 M sodium citrate, pH 7.5, the gold particles were silver intensified with the Aurion R-Gent SE-LM Kit. (Amersham–Pharmacia Biotech UK, Buckinghamshire, UK). Sections were osmicated, and then treated with 2% uranyl acetate in 70% ethanol for 30 min. Following dehydration in an ascending series of ethanol and propylene oxide, the sections were flat embedded in Durcupan ACM epoxy resin (Fluka) on liquid release agent (Electron Microscopy Sciences)-coated slides, and polymerized at 56 oC for 2 days.

To detect the localization of the sGC subunits, sections were incubated in rabbit antiserum against sGC α1 or ß1 (1:4000) for 4 days at 4 ºC, followed by biotinylated anti-rabbit IgG (1:500) and avidin-biotin-peroxidase complex (ABC Elite 1:1000). Immunoreactivity was detected in 0.05% DAB/0.15%Ni-ammonium-sulfate/0.005% H_2O_2 in 0.05 M Tris buffer, pH 7.6. The immunoreaction product was silver-intensified by using the Gallyas method. After immunostaining, the sections were embedded in Durcupan ACM epoxy resin (Fluka) and then 60–70 nm thick utlrasections were cut with Leica ultracut UCT ultramicrotome (Leica Microsystems, Wetzlar, Germany). The ultrathin sections were mounted onto Formvar-coated single slot grids, contrasted with 2% lead citrate and examined with a Jeol-100 C transmission electron microscope.

Primary antisera	Dilution
rabbit antiserum against nNOS (rabbit polyclonal antibody, Zymed Laboratories, San Francisco, CA)	1:200
rabbit antiserum against soluble guanylyl cyclase α1 (rabbit polyclonal antibody; catalog number G4280, lot number 011K4888; Sigma)	1:4000
rabbit antiserum against soluble guanylyl cyclase ß1 (rabbit polyclonal antibody; catalog number 160897, lot number 134521,Cayman Chemical, Ann Arbor, MI)	1:4000

Specificity of antisera

The specificity of nNOS, sGC α1 and ß1 antisera was reported previously (Szabadits et al., J Neurosci, 2007).

III. RESULTS

Neuronal NOS-immunoreactivity was abundantly present in neuronal perikarya and dendrites and also in axon varicosities in the parvocellular part of the PVN. In perikarya and dendrites, nNOS-immunoreactivity was widely distributed in the cytoplasm, primarily associated with the endoplasmatic reticulum. nNOS-immunoreacivity was also found to be associated with the perikaryal plasma membrane in close proximity to both symmetric and asymmetric synapses, as well as within axon varicosities forming both symmetric and asymmetric synapses. The soluble guanylate cyclase α1 subunit was found in dendrites and also in axon varicosities, and was closely located to both the pre- and postsynaptic sides of synapses in many instances. The α1 subunit was associated with both symmetric and asymmetric types of synapses. The soluble guanylate cyclase α1 subunit was found in dendrites and also in axon varicosities, and was closely located to both the pre- and postsynaptic sides of synapses in many instances. The α1 subunit was associated with both symmetric and asymmetric types of synapses.

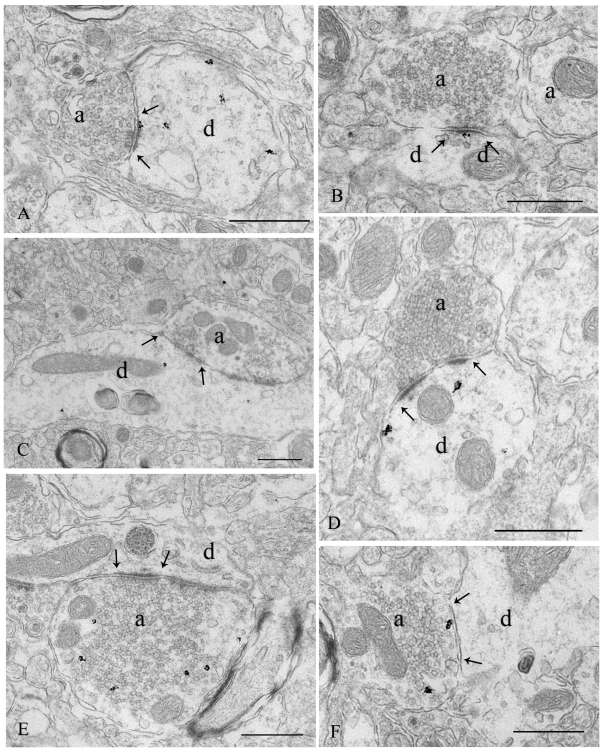

Figure 1. Electron micrographs illustrate the localization of nNOS-immunoreactivity in dendrites (A-D) axons (E, F) and a neuronal perikaryon (G) in the parvocellular part of the paraventricular nucleus in mice. The nNOS-immunoreactivity is labeled with highly electron dense gold–silver granules. nNOS-immunoreactivity can be observed in dendrites in the proximity of the postsynaptic density of both asymmetric (A, B, D) and symmetric (C) synapses. nNOS-immunoreactivity can also be observed in axon varicosities forming asymmetric (E) or symmetric synapses (F). A low-power magnification image shows a nNOS-IR perikaryon (G). In perikarya, nNOS immunoreactivity was widely distributed in the cytoplasm and primarily associated with the endoplasmatic reticulum. Arrows point to synapses. Scale bars=0.5μm in (A-G). a= axon; d= dendrite; Nu= nucleus

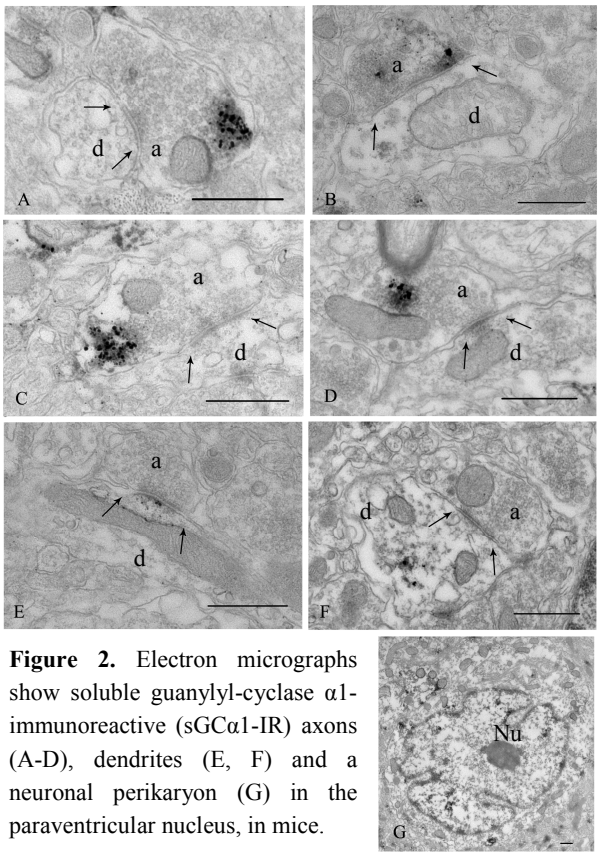

Figure 2. Electron micrographs show soluble guanylyl-cyclase α1-immunoreactive (sGCα1-IR) axons (A-D), dendrites (E, F) and a neuronal perikaryon (G) in the paraventricular nucleus, in mice.

The sGCα1-immunoreactivity is recognized by the presence of the electron dense silver granules. sGCα1-IR axon varicosities form both symmetric (A, D) and asymmetric type synapses (B, E). Similarly both asymmetric (C) and symmetric type synapses (F) are formed on the sGCα1-IR dendrites. Low-power magnification image shows sGCα1-IR perikaryon (G) sGCα1-IR was widely distributed in the cytoplasm. Arrows point to synapses. Scale bars=0,5μm in (A-G). a= axon; d= dendrite; Nu= nucleus

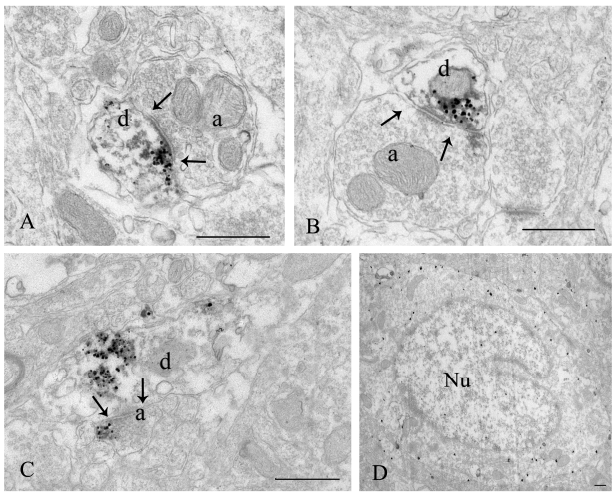

Figure 3. Electron micrographs illustrate (arrows) soluble guanylate-cyclase ß1-immunoreactive (sGCß1-IR) dendrites (A, B, C) axon (C) and neuronal perikaryon (D) in the parvocellular part of the paraventricular nucleus in mice. Soluble sGCß1-IR is recognized by the presence of electron dense silver granules. Asymmetric (A) and symmetric synapses (B, C) are observed on sGCß1-IR dendrites. sGCß1-immunoreactivity is typically associated with the postsynaptic membrane of synapses. A sGCß1-IR axon terminal forms a symmetric synapse with an IR dendrite (C). Low-power magnification image shows a sGCß1-IR perikaryon (G). Arrows indicate the synapses. Scale bars=0.5µm in (A-D). a= axon; d= dendrite; Nu= nucleus

IV. CONCLUSION

1) nNOS-immunoreactivity is present in both the pre- and postsynaptic sites of inhibitory symmetric and excitatory asymmetric synapses as well.

2) Similar to nNOS, soluble guanylyl-cyclase α1 is also present in both the pre- and postsynaptic elements of symmetric and asymmetric synapses.

3) Soluble guanylyl-cyclase ß1 is localized to dendrites and perikarya, and in several instances, present close to the postsynaptic side of both symmetric and asymmetric synapses.

4) Soluble guanylyl-cyclase ß1 subunit was only very rarely seen in axon varicosities.

5) Our data suggest that nitric oxide can be utilized as both an anterograde and retrograde transmitter in the parvocellular part of the PVN in mice.

REFERENCES

[1] 1. Esplugues, J. V. (2002). *NO as a signalling molecule in the nervous system.* British Journal of Pharmacology.

[2] 2. Jin-Dong Ding, A. B. (2004). Distribution of Soluble Guanylyl Cyclase in the Rat Brain. *The journal of comparative neurology* , 437-448.

[3] 3. Kadekaro, M. (2004). Nitric oxide modulation of the hypothalamo-neurohypophyseal system. *Brazilian Journal of Medicinal and Biological Research* , 441-450.

[4] 4. Stojilkovic, Y. J. (2006). Molecular cloning and characterization of alpha1-soluble guanylyl cyclase gene promoter in rat pituitary cells. *Journal of Molecular Endocrinology* , 503-515.

Age-related alterations in the connectivity of resting state functional modules

File BÁLINT
(Supervisors: Dániel FABÓ, István ULBERT)
Pázmány Péter Catholic University, Faculty of Information Technology and Bionics
50/a Práter street, 1083 Budapest, Hungary
balint.file@gmail.com

***Abstract*— The relationship between resting state functional networks and the cognitive decline with advancing age is poorly understood. The current research aimed to test the altered resting state functional networks (RSNs) with respect to aging. The working memory (WM) capacity (forward and backward digit span tests) of young (18-26 years, N= 26) and elderly (60-71 years N=22) subjects were determined and their EEG was recorded by 64 electrodes during eyes open resting condition. The strength of phase synchronization was measured on the reconstructed cortical source signals in different frequency bands. Densely connected regions of these oscillatory networks were identified as functional brain modules. The brain regions were characterized based on their topological role in the network maintenance (within and between-module connections). The brain regions affected by aging were selected to correlate with memory scores. Both in young and elderly, neuronal networks demonstrated significantly nonrandom sub-network characteristics. Our results show a frequency band specific change of the modular organization with ageing. The loss of the governing frontal hub regions in theta and gamma bands were accompanied with a more expressed modular organization in the upper alpha band in the elderly group. Positive correlation was found between the frontal within-module connectivity strength and executive function of WM in the theta and gamma bands. Contrary to this, in the upper alpha band, more extensive frontal hubness statistically predicted lower level WM storage capacity and the characteristic age differences. In summary our results suggest that the less optimal modular pattern in the theta and gamma bands may have compensated by the reorganization of the alpha oscillatory band functional networks with ageing.**

Keywords- resting state, modularity, functional connectivity, EEG, phase synchronization, aging, graph theoretical analysis, working memory

I. INTRODUCTION

The recent challenge of the cognitive neuroscience models of aging is to understand the brain mechanisms that may underlie the cognitive deficits in aging. Considerable age-associated cognitive decline such as learning, long term memory, working memory (short term retention and manipulation of information) were demonstrated in both cross-sectional and longitudinal studies [1]. Recently, it has also hypothesized that the impaired interactions within distributed functional networks seen in resting state, rather than the activity changes of single regions observed under cognitive load. It may play a decisive role in the functional deficits associated with normal and pathological aging. Therefore, the present investigation of functional connectivity between distant brain regions during no task resting condition could provide new insights into the impaired cognition in the aging brain.

Brain oscillations provide such neural mechanisms by establishing sustained coordinated timing of neuronal firing between distant cortical areas which integrates anatomically distributed processing and facilitates neuronal communication [2]. Graph theoretical analyses of complex functional networks, obtained using fMRI and MEG [3], has demonstrated that brain functional networks have a modular (sub-network) structure, where a module is defined as a highly integrated sub-network consisting of regions with much denser connectivity within themselves than between those regions and the rest of the brain. Therefore, studies of brain modules enable to identify groups of brain regions that may serve common functions of neural activity [4]. Alterations of the global functional modular structure and the efficiency and localization of the modular hub regions are observed in clinical states like Alzheimer's disease [5], schizophrenia [6] or epileptic brain networks [7].

The present study was aimed to investigate the modular reorganization of the cortical networks in advanced age and it's relation to working memory functions. EEG data of young and elderly subjects were recorded in eyes-open resting state condition. Our hypothesis was that age dependent changes in connectivity of modules are related to the decline of memory functions. First the age related changes were identified on resting state functional modular characteristics. Finally the assumption was tested by correlation analysis between the individual performance on working memory task and the functional module features of spontaneous cortical activity.

II. METHODS

A. Participants

Healthy young (18-28 years; N = 26; SD= ±2.2 16 women) and elderly (61-71 years; N = 22; SD= ±3.2; 13 women) individuals took part in the study. Prior to the EEG recording the IQ of all participants was tested with the Hungarian

Consultants: Brigitta Tóth PhD, Dr. Márk Molnár, DsC

B. FILE, "Age-related alterations in the connectivity of resting state functional modules" in *PhD Proceedings Annual Issues of the Doctoral School, Faculty of Information Technology and Bionics, Pázmány Péter Catholic University – 2015.* G. Prószéky, P. Szolgay Eds. Budapest: Pázmány University ePress, 2015, pp 33– 36.

standardized version of Wechsler Intelligence Scale (WAIS-R). The IQ and demographic data of the two groups (sex and years of education) were matched. The short term memory was measured outside the EEG chamber by forward (storage capacity) and backward (executive function) digit span tasks.

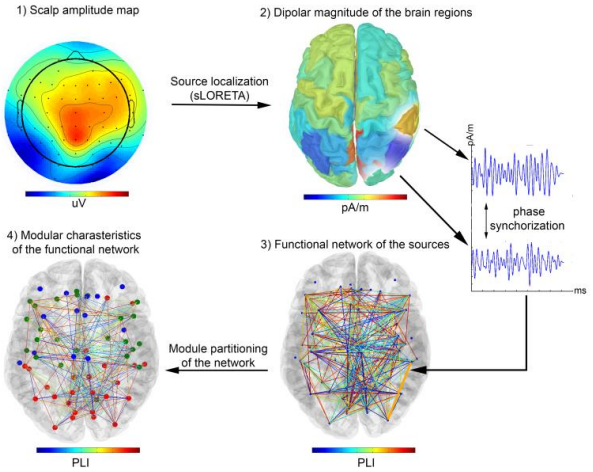

Figure 1. Schematic flowchart of the functional network and module construction of EEG source signals. 1) Preprocessing the scalp EEG 2) Reconstructing the source signals of each brain region 3) Calculation of strength of phase synchronization (functional connectivity) between all pairwise brain regions 4) Partitioning the network to non-overlapping modules and determining the modular parameters of the subgraphs within each analyzed frequency band.

B. EEG recording and preprocessing

The EEG was recorded by 64 Ag/AgCl electrodes placed according to the international 10-20 system using Neuroscan software and amplifiers (Scan 4.3., Nuamps, bandpass: DC-70 Hz, FIR, sampling rate: 1000 Hz). The reference was placed at the tip of the nose and the ground was provided by an electrode placed between Cz and Fz. The 4 min of spontaneous EEG data of subjects were recorded in eyes open resting state condition. The eyes open condition is chosen to match with the general circumstances of the memory tasks. The preprocessing of the EEG data was performed with EEGLab 10.2.5.8b toolbox of Matlab 7.9.1 software. The EEG was filtered (band-bass, Hamming windowed Fast Fourier Transform) in the theta (4-7 Hz) frequency band. The EEG data were segmented into 4096 ms long epochs Artefact detection and removal were performed by Independent Component Analysis function and ADJUST plugin of EEGLab toolbox (optimized to capture blinks, eye movements and generic discontinuities, [8]. Before the source signal reconstruction the EEG recordings were average referenced.

C. Source Signal reconstruction

The time series of the cortical areas were reconstructed by the sLORETA method implemented in the Brainstorm toolbox (http://neuroimage.usc.edu/brainstorm [9]. The forward model was determined on a realistic BEM (boundary element method) head model by the OpenMEEG toolbox [10] using standard brain template (MNI/Colin27, voxel resolution: 1mm3) and standard electrode positions. The inverse model was calculated by the sLORETA algorithm which is a distributed source estimation procedure working with standardized minimum norm source power configuration assuming the high correlation of neighboring sources. The time signals of the dipolar strength corresponding to each voxels were reconstructed with the orientation perpendicular to the cortical surface, and then averaged to 62 cortical regions (areas of interest; AOIs) according to the parcellation scheme introduced by Klein and Tourvilee [11].

D. Functional network of the sources

The time varying dipole strength the AOIs were filtered offline in delta (0.5-4 Hz), theta (4-8 Hz), lower alpha (8-10 Hz), higher alpha (10-13 Hz), beta (13-30 Hz), gamma (30-45 Hz) frequency bands. A Hamming-windowed FFT filter was applied to avoid the phase distortion of the signal. The strength of connectivity was calculated for all pair-wise combinations of AOIs based on the measurement of phase synchronization (phase lag index [PLI]) in five frequency bands obtained for all 4096ms long EEG source time series. PLI is a measure of the asymmetry of distribution of phase differences between two signals by averaging the sign of phase difference [12]:

$$PLI = \left|\left\langle sign\left[\Delta\Phi(t_k)\right]\right\rangle\right|,$$

where $\Delta\Phi$ is the phase difference of two signals at the t_k time point. By eliminating the 0 phase difference PLI isn't affected by the volume conduction. Minimum strength of functional connectivity is expressed by value of PLI around 0 and the most consistent nonzero phase difference is indicated by value of 1.

The resulting functional connectivity network of each epoch provides an abstract mathematical representation of the system, where each AOI represents a node of the network, and the strength of functional connectivity (PLI value) between all pairs of AOIs are defined as edges.

E. Identification of the modular characteristics of the functional networks

In order to investigate the modular organization of RSNs, smaller functional subgraphs or modules were decomposed from the entire RSN [5]. The modularity (Q) of a graph describes the possible formation of communities in the network:

$$Q = \sum_{s=1}^{N}\left[\frac{l_s}{L} - \left(\frac{d_s}{2L}\right)^2\right],$$

where N is the number of modules, L is the total sum of all edge weight in the network, l_s is the sum of all weight in module s, and d_s is the sum of the strength of nodes (the sum of edge weight of a certain node) in module s [4]. The highest Q value of a given network accompanies with the maximal within-module and the fewest between-module connections

The modules of a network are not homogenous groups, but rather weakly linked subgraphs, where each node can be

characterized by its within (Zi) and between module connectivity (participation coefficient; PC) strength [13].

The number of modules, value of modularity and within- and between-module strength of all cortical regions were selected to describe the age related changes of the functional modular organization. These parameters were determined for all epochs, than averaged for each subject respectively.

For providing evidence of the highly modular organization of the RSNs derived from the reconstructed source signal, the maximal modularity value of the biological functional networks were compared to the value of the corresponding random networks. Degree-, weight-, and strength-preserving randomization [14] was applied to generate a null model (random network) for each epoch in every frequency band.

F. Statistical analysis

Statistical analysis was performed with the Statistica software (version 11.0). For the statistical analysis of the level of modularity and average number of modules in each frequency bands repeated measures of ANOVA was performed separately, including random biological network type as a within subject factor and age as between subject factor. The statistical analysis of the within module functional connectivity strength (Zi) within AOIs and between age groups were derived by the mixed mode ANOVA using AOIs (31 cortical regions) as within subject factors, and group (young vs. elderly) as between subject factor. The contralateral AOIs were averaged over the two hemispheres to detect only the bilaterally significant age-related changes in the maintenance of the modular structure. The AOIs showing a significant age-related effect were chosen for the subsequent Pearson correlation analysis with the memory tasks. The correlation analysis was performed for both the forward and backward digit span task, thus the significant level was corrected to $p<0.025$.

III. RESULTS

A. The level of modularity and the average number of modules

The level of modular organization of cortical networks during resting state was significantly higher than the level of modularity of the random networks in all frequency bands [main effect in delta band: $F_{1.46}=10058$, $p<0.001$; main effect in theta band: $F_{1.46}=4853$, $p<0.001$; main effect in lower alpha band: $F_{1.46}=4499$, $p<0.001$; main effect in upper alpha band: $F_{1.46}=1937.7$, p= $p<0.001$; main effect in beta band: $F_{1.46}=3240.3$, $p<0.001$; main effect in gamma band: $F_{1.46}=2768.8$, p $p<0.001$. The post-hoc analysis revealed a significant (p=0.023) increase of the modularity value in the group of young compared to the group of elderly in gamma band.

The numbers of modules of RSNs was found to be significantly lower compared to the random networks in all frequency bands except for the gamma oscillation [main effect in delta band: $F_{1.46}=156.06$, $p<0.001$; theta band $F_{1.46}=89.74$, p= $p<0.001$; main effect in lower alpha band $F_{1.46}=361.43$, $p<0.001$; main effect in upper alpha band: $F_{1.46}=229.44$, $p<0.001$; main effect in beta band: $F_{1.46}=5.47$, p=0.024]. According to the post-hoc comparison the number of modules are found to be lower in the young group compared to the elderly in the alpha1 (p=0.045), alpha2 (p=0.005) and gamma bands (p=0.02).

B. Strength of within and between the module connectivity

The average value of the participation coefficient showed a robust correlation with the number of clusters (>0.8). We decided not to include the participation coefficient in the further analysis, because the numbers of modules determine strongly the value of partition coefficient. The results corresponding to connectivity strength and the intra-modular connectivity strength of each node in each age group is summarized in Figure 1. Significant effects of age-node interaction on the within module connectivity strength of the node were only observed in the theta, upper alpha and gamma bands.

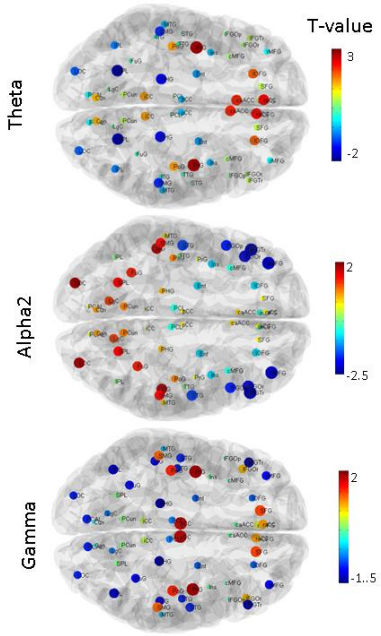

Figure 2. The t-values of the group comparison of each AOIs' within module connectivity in theta, alpha2, gamma bands.

Theta band: In the theta band a significant interaction effect of AOIs and Age group was found [$F_{30.1380}=1.78$, p=0.006; partial eta square= 0.037]. According to the post hoc comparison Zi was found to be lower in the elderly group compared to the young in the precentral gyrus (PrG p=0.002), the superior parietal lobule (SPL p=0.025), the caudal and rostral anterior cingulate cortex (caCC p=0.046, raCC p=0.003). In contrast Zi was found to be higher in the elderly group compared to the young only in the parahippocampal gyrus (PHG p=0.020).

Upper alpha band: In the upper alpha band significant interaction effect of AOIs and Age group was found

[$F_{30.1380}$=1.72, p=0.001; partial eta square= 0.036]. According to the post hoc comparison Zi was higher in the elderly group compared to the young in the Rostral middle frontal gyrus (rMFG; p=0.006), Inferior frontal gyrus – Pars triangularis (IFGTr; p= 0.014), Inferior frontal gyrus – Pars orbitalis (IFGOr; p=0.017). Zi was found to be lower in the elderly group compared to the young only in the Lateral occipital cortex (LOC; p=0.008).

Gamma band: A tendency for interaction effect of AOIs and Age group was found in the gamma band [$F_{30.1380}$=1.32, p=0.117; partial eta square= 0.028]. According to the post hoc comparison Zi was found to be lower in the elderly group compared to the young only in the Superior frontal gyrus (SFG p=0.039), precentral gyrus (PrG p=0.015) and the Posterior Cingulate Cortex (pCC p=0.036).

C. Relationship between the strength of connectivity within the modules and WM capacity

Significant correlations were observed between the individual's within module connectivity strength and memory performance on digit span test (summary of the results presented in Table 1.).

	Frequency band/region Zi	**r(X,Y)**	**p**
Forward digit span	theta band / parahippocampal gyrus	-0.344	0.017
	upper alpha band / rostral middle frontal gyrus	-0.327	0.024
Backward digit span	theta band / precentral gyrus	0.395	0.005
	theta band / caudal anterior cingulate cortex	0.345	0.016
	gamma band / precentral cortex	0.323	0.025

Table 1. Results of the correlation analysis between the functional connectivity strength and the LTM accuracy

IV. CONCLUSION

According to the main findings of the present study, the modular organization of large scale spontaneous neuronal activity was related to working memory functions and was shown to be altered with advancing age. Graph theoretical modularity analysis demonstrated weakening links within functional module of the fronto-parietal regions in the resting state network (precentral, superior frontal and parietal gyri, ACC and PCC) of theta and gamma frequency bands. Additionally these network properties were found to correlate with the executive component of WM capacity. Moreover, a putative lack of inhibitory process mediated by higher alpha oscillation was indicated in the elderly population by the increased within module connectivity strength in the frontal cortical regions (medial and inferior frontal gyrus). Higher level local connectivity strength in the frontal region in the upper alpha band was associated with lower short term memory storage span.

Our results revealed topological changes in the large scale oscillatory connectome in relation to aging. These results have valuable implications since they provide a baseline for evaluating network impairments in age-related neurodegenerative disorders. The present evidence suggests that spontaneous connectivity may have a critical impact on memory performance. The investigation of resting state functional network organization could provide insights into the neural substrates underlying individual variations in memory capacity. Taken together, the analyzed properties of resting state networks could serve as potential biomarker of failing integrity of memory systems. These findings suggest that cognitive decline in normal aging may be causally related to functional disruption of large-scale brain systems that support cognition.

REFERENCES

[1] J. M. Zacks and J. Q. Sargent, *Event Perception : A Theory and Its Application to Clinical Neuroscience*, 1st ed., vol. 53. Elsevier Inc., 2010.

[2] J. Fell and N. Axmacher, "The role of phase synchronization in memory processes.," *Nat. Rev. Neurosci.*, vol. 12, no. 2, pp. 105–18, Feb. 2011.

[3] C. J. Stam and E. C. W. van Straaten, "The organization of physiological brain networks.," *Clin. Neurophysiol.*, vol. 123, no. 6, pp. 1067–87, Jun. 2012.

[4] M. Newman and M. Girvan, "Finding and evaluating community structure in networks," *Phys. Rev. E*, pp. 1–16, 2004.

[5] W. de Haan, W. M. van der Flier, T. Koene, L. L. Smits, P. Scheltens, and C. J. Stam, "Disrupted modular brain dynamics reflect cognitive dysfunction in Alzheimer's disease.," *Neuroimage*, vol. 59, no. 4, pp. 3085–93, Feb. 2012.

[6] A. F. Alexander-Bloch, N. Gogtay, D. Meunier, R. Birn, L. Clasen, F. Lalonde, R. Lenroot, J. Giedd, and E. T. Bullmore, "Disrupted modularity and local connectivity of brain functional networks in childhood-onset schizophrenia.," *Front. Syst. Neurosci.*, vol. 4, no. October, p. 147, 2010.

[7] M. Chavez, M. Valencia, V. Navarro, V. Latora, and J. Martinerie, "Functional Modularity of Background Activities in Normal and Epileptic Brain Networks," *Phys. Rev. Lett.*, vol. 104, no. 11, p. 118701, Mar. 2010.

[8] A. Mognon and M. Buiatti, "An Automatic EEG artifact Detector based on the Joint Use of Spatial and Temporal features," no. May, 2010.

[9] F. Tadel, S. Baillet, J. C. Mosher, D. Pantazis, and R. M. Leahy, "Brainstorm: A user-friendly application for MEG/EEG analysis," *Comput. Intell. Neurosci.*, vol. 2011, 2011.

[10] A. Gramfort, E. Olivi, and M. Clerc, "Forward Field Computation with OpenMEEG," vol. 2011, 2011.

[11] A. Klein and J. Tourville, "101 labeled brain images and a consistent human cortical labeling protocol," vol. 6, no. December, pp. 1–12, 2012.

[12] C. J. Stam, G. Nolte, and A. Daffertshofer, "Phase Lag Index : Assessment of Functional Connectivity From Multi Channel EEG and MEG With Diminished Bias From Common Sources," vol. 1193, pp. 1178–1193, 2007.

[13] R. Guimera and L. Amaral, "Functional cartography of complex metabolic networks," *Nature*, vol. 433, no. February, pp. 895–900, 2005.

[14] M. Rubinov and O. Sporns, "Weight-conserving characterization of complex functional brain networks," *Neuroimage*, vol. 56, no. 4, pp. 2068–2079, 2011.

In vivo and *in vitro* detection of epilepsy with bioinformatic methods

Edit GYŐRI
(Supervisor: István ULBERT, Dániel FABÓ)
Pázmány Péter Catholic University, Faculty of Information Technology and Bionics
50/a Práter street, 1083 Budapest, Hungary
gyori.edit@itk.ppke.hu

***Abstract*—65 million people around the world suffer from epilepsy. This is a chronic condition with complex effects on a psychological function and a person's social situation. Epilepsy can be diagnosed by detecting ictal and interictal epileptiform discharges on patients' electrophysiological recordings. The exact mechanism underlying epilepsy is still unknown. Our research group has set the goal to characterize the local neuronal network mechanisms of epilepsy by comparing this electrical activity in vivo and in vitro by multi-phase electrophysiological approaches.**

***Keywords*—epilepsy, in vivo, in vitro, human tissue, spontaneous population activity, seizure onset**

I. INTRODUCION

Approximately 1 % of the human population suffers from epilepsy [1]. This neurological disorder can affect different areas of the brain, so it can generate different symptoms as well. During an epileptic seizure, the willful control of behavior and consciousness can disappear, automatic series of actions can occur, and memory consolidation processes can be damaged [2]. About one third of people with epilepsy do not respond to antiepileptic drug treatment. In this condition, surgical resection of the brain area generating seizures can be an alternative treatment. This condition is called pharmacoresistant epilepsy. The underlying mechanisms still need to be clearly identified. The complete resection of the seizure-onset zone (SOZ) is mandatory for the positive surgical outcome, which is usually to render the patient seizure free. The resected specimens allow an opportunity to study the in vitro mechanisms of interictal discharges, seizure generation, propagation and pharmacoresistance on viable human central nervous tissue [1]. Before and under the surgery, multimodal neuroimaging and intracranial macro-electrodes (MAE), and intracortical laminar microelectrodes (MIE) are applied to circumscribe the seizure-onset zone [4].

The National Institute of Clinical Neuroscience and the Institute for Cognitive Neurosciences and Psychology of the Hungarian Academy of Science have been running translational epilepsy research for decades, in which the Pázmány Péter Catholic University Faculty of Information Technology and Bionics joined many years ago. Our multiphase collaborative study will assist bridging the gap between conventional diagnostic and investigational approaches of epilepsy, in order to make the clinical methods less invasive and more precise. This cooperation can address questions concerning the basic mechanisms of epilepsy, and may contribute to the development of new treatment methodologies.

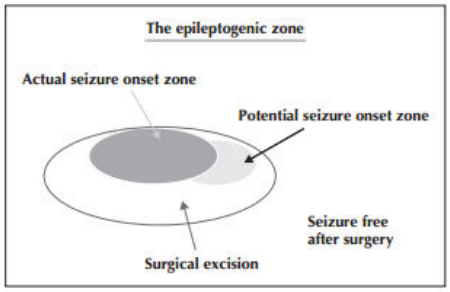

Figure 1. The diagram shows the actual seizure-onset zone, the potential seizure-onset zone, and a surgical resection that includes both seizure-onset zones. Complete resection of both seizure-onset zones should result in seizure-freedom [5].

II. METHODS

In our study we conduct a multi-scale electrophysiological investigational pipeline, with in vivo and vitro phases.

A. In vivo preoperative recording

The involved patients undergo standard preoperative evaluation to locate the SOZ. Beside various non-invasive neuroimaging modalities (PET, MRI, CT), video-EEG is performed, to record spontaneous seizures and interictal spikes (IIS)..

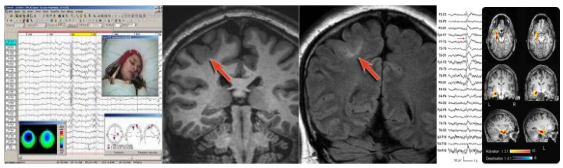

Figure 2 The preoperative Video-EEG, CT and EEG-fMRI brain mapping can help the localization of epileptic focus and achieve the best possible seizure prevalence, and minimize the risks of postoperative neurologic dysfunction.

E. GYŐRI, "In vivo and in vitro detection of epilepsy with bioinformatic methods" in *PhD Proceedings Annual Issues of the Doctoral School, Faculty of Information Technology and Bionics, Pázmány Péter Catholic University – 2015.* G. Prószéky, P. Szolgay Eds. Budapest: Pázmány University ePress, 2015, pp 37– 39.

B. In vivo intraoperative recording

Intraoperative electrocorticography (ECoG) with strip and/or grid electrodes (Figures 3.) has been traditionally used in the surgical management of medically non-treatable epilepsies to identify the location and boundaries of the epileptogenic area, to guide the extent of resection, and to assess its completeness [8]. The spontaneous interictal and ictal discharges, low and high frequency stimulation induced activities are recorded in the areas of cerebral cortex. In some cases, we recorded the spontaneous laminar distribution of intracortical synaptic processes by implanted laminar micro-multi-electrode, which records field potentials (FPs), multiple unit activity (MUA), and action potentials (APs) at the same time from different and well defined cortical depths [6].

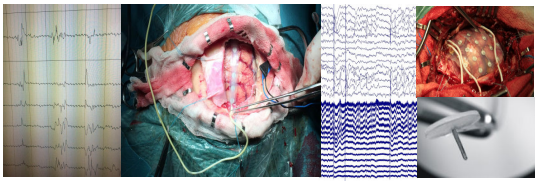

Figure 3. An invasive procedure used to place grid or strip electrodes on the surface of the brain to record electrical activity. The thumbtack is a linear probe for chronic use designed to span cortical layers running parallel to the surface of the brain. It is effective for both field potential and single-unit recordings. The patient is monitored for several days in an epilepsy monitoring unit where ictal and interictal data are collected.

C. In vitro electrophysiology recording

After the resection of the epileptic focus, we are able to do experiments on the human brain slices. First, the blood vessels and meninges are removed to avoid resistance during slicing. The brain tissue block is cut to 500 µm thick slices by low speed (0.18 mm/sec) vibrotome. Subsequently we incubate them in the interface chamber at 33 °C for at least 1 hour in ACSF before starting recordings. Using laminar microelectrodes we record the local field potentials (LFPg) [3]. Parallel to this phase, parts of the resected tissue is transferred to the two-photon microscope. This Ca-imaging technique can gain additional information about the synaptic functions and ion channel mechanisms of the human epileptic network involved in the SPA generation [7].

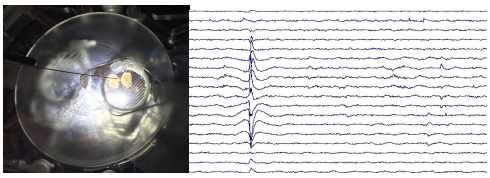

Figure 4. Extracellular recording in human neocortex. We can detect different types of spontaneous population activities with multielectrodes.

III. RESULTS

Spontaneous synchronous population activity (SPA) can be detected by electrophysiological methods in cortical slices of patients with epileptic seizures in vitro. We observed larger and smaller amplitude (Figure 2.) of spontaneous population activities (SPA) in slices of various patients with epileptic episodes in in vitro level. We hypothesize that lower amplitude LFPg is a part of the normal function of the brain, while higher amplitude LFPg belongs to the phenomenon of epilepsy.

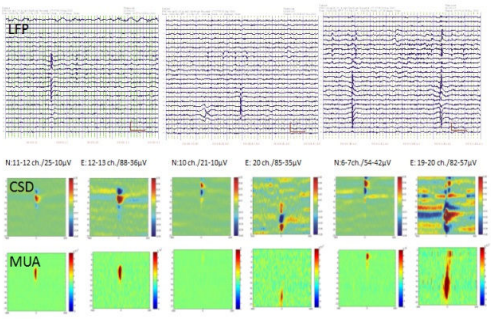

Figure 5. Normal and epileptic SPA from the seizer onset zone of three different patients (drug-resistant status epilepticus). Two types of spontaneous population activities can be found in the same human but their locations and amplitude magnitudes are significantly different.

IV. DISCUSSION

A number of tests are performed to determine whether a person has epilepsy and, if so, what kind of seizures the patient has. The collaboration of three institutes (MTA, OKITI, PPKE-ITK) can help to follow the epileptic forms from in vivo level to in vivo with a multi-scale electrophysiological investigational pipeline. The cooperation of the fields of epileptology, neurosurgery, molecular interventions and bioinformatic can facilitate the clarification of the basic mechanisms underlying epilepsy.

V. FURTHER AIMS

We would like to compare the SPAs in different areas of epileptic brain tissue after the resection (Figure 6.).

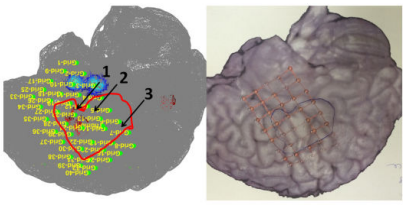

Figure 6. The areas of sampling for in vitro electrophysiology

REFERENCES

[1] Dossi E , Blauwblomme T , Nabbout R, Huberfeld G, Rouach N, Multi-electrode array recordings of human epileptic postoperative cortical tissue

[2] Galer S, Urbain C, De Tiège X , Emeriau M, Leproult R, Deliens G, Nonclerq A , Peigneux P, Van Bogaert P, Impaired sleep-related consolidation of declarative memories in idiopathic focal epilepsies of childhood

[3] Köhling R, Avoli M., Methodological approaches to exploring epileptic disorders in the human brain in vitro

[4] Jing Zhang, Weifang Liu, Hui Chen, Hong Xia, Zhen Zhou, Shanshan Mei, Qingzhu Liu, Yunlin Li, Multimodal neuroimaging in presurgical evaluation of drug-resistant epilepsy

[5] Lüders HO, Najm I, Nair D, Widdess-Walsh P, Bingman W., The epileptogenic zone: general principles

[6] Ulbert I, Halgren E, Heit G, Karmos G., Multiple microelectrode-recording system for human intracortical applications

[7] Bálint Péter Kerekes; Kinga Toth; Attila Kaszás; Balázs Chiovini; Zoltán Szadai; Gergely Szalay; Denes Palfi; Attila Bagó; Klaudia Spitzer; Balázs Rózsa; István Ulbert; Lucia Wittner, Combined two-photon imaging, electrophysiological, and anatomical investigation of the human neocortex

[8] Kuruvilla A, Flink R., Intraoperative electrocorticography in epilepsy surgery: useful or not?

Implementation of a loop-mediated isothermal amplification into degas-driven microfluidic system

Márton HARTDÉGEN
(Supervisor: Kristóf IVÁN)
Pázmány Péter Catholic University, Faculty of Information Technology and Bionics
50/a Práter street, 1083 Budapest, Hungary
hartdegen.marton@itk.ppke.hu

***Abstract*—Nowadays, Laboratory-on-a-Chip (LoC) devices are widespread in medical diagnosis, and different regions of industry. In food safety LoC is a possible solution to make a rapid, cheap and disposable scientific quality checking device for food products. We present a special LoC that performs isothermal DNA amplification with degas-driven flow to detect *Listeria monocytogenes*. Simulations in Comsol Multiphysics were calculated to describe the modification of air-concentration in PDMS bulk, then a system-level simulation model was used in Matlab to predict the spreading of fluid in microfluidic channels. Finally, microfluidic devices were fabricated, and loop-mediated isothermal amplification (LAMP) was tested. The results of LAMP were evaluated with gel electrophoresis and PCR then validated with the traditional method. We demonstrated a new and easy-to-use LAMP method and device in microfluidic environment and a 25g/ml concentration DNA sample was amplificated to 200-250g/ml concentration. The successful tests projected further development possibilities. Thus, we would like to construct an automated sample preparation system, and an optical system to be able to detect turbidity on chip.**

***Index Terms*—microfluidics; Lab-on-a-Chip; food safety; Loop-mediated isothermal amplification; *Listeria monocytogenes*;**

I. Introduction

Food safety receives an increasingly important role in the world. In the USA alone, there are 76 million cases of food-borne illness leading to 325.000 hospitalizations and 5.000 deaths [1]. One of the most widely known illnesses of these is *listeriosis*, which is a bacterial infection caused by *Listeria monocytogenes*. The infection of food with the *Listeria* bacterium could be detected by traditional microbiological methods [2, 3], but these methods require very long analysis times (>24h) and adequate sample preparation methods. LoC (Lab-on-a-Chip) systems are new opportunities to decrease the sampling and examination time in clinical applications: the smaller size, the lower number of samples and the more exact detection leading to lower costs per measurement [4, 5]. To design LoC microfluidic devices, predefined flow characteristic and geometry are needed. Hongjun et al. [6] described one special simulation method that determines the liquid filling in microfluidic channels. Furthermore, this method is relatively exact and the simulation time is a few seconds. This system was implemented in Matlab, and the channel geometry was designed in CorelDraw. In general, most of the microfluidic devices require external power sources for fluid transportation [7]. We report here a power-free pumping method for polydimethylsiloxane (PDMS). According to Henry's law, the equilibrium concentration of gas dissolved in PDMS is proportional to the partial pressure of the gas around the PDMS [8]. By placing the PDMS bulk in vacuum then bringing it back to the atmosphere, the PDMS bulk begins to absorb air toward the new equilibrium [6]. This phenomenon was simulated in Comsol Multiphysics. The PCR (polymerase chain reaction) technique was used to amplify the DNA of bacteria in the sample [9]. Although PCR is the most widely known and used DNA amplification method, it has a big disadvantage for miniaturization namely, the temperature cycling and the long running time. Armes et al.[10] developed the recombinase polymerase amplification (RPA) method that is an isothermal nucleic acid amplification test. This PCR needs thermostable polymerases, and it is performed in a short time, because the thermostable polymerases have a rapidly declining activity at PCR temperatures. Another isothermal method for amplifying nucleic acids is the loop-mediated isothermal amplification. This method was described by Notomi et al. in 2000 [11]. This method relies on an auto-cycling strand displacement DNA synthesis that is performed by a DNA polymerase with high displacement activity and a set of two inner and two outer primers [12]. We report here a degas-driven microfluidic system to detect *Listeria monocytogenes* with loop-mediated isothermal amplification (LAMP). We use a novel, system-level simulation method to determine the flow characteristic of the device. Furthermore, we take advantage of gas solubility of PDMS therefore our device does not require any external support equipment and to top it all the detection of turbidity is perceptible for the naked eye.

II. Methods

A. Simulation in Comsol Multiphysics 5.0

The following equation was implemented in Comsol Multiphysics to describe the air and pressure change in PDMS bulk

$$\frac{\phi(r,t)}{\partial t} = \nabla \left[D(\phi, r) \nabla \phi(r,t) \right] \tag{1}$$

where $\phi(r,t)$ is the density of the diffusing material at time t and location r, the ∇ is the vector differential operator

M. HARTDÉGEN, "Implementation of a loop-mediated isothermal amplification into degas-driven microfluidic system" in *PhD Proceedings Annual Issues of the Doctoral School, Faculty of Information Technology and Bionics, Pázmány Péter Catholic University – 2015.* G. Prószéky, P. Szolgay Eds. Budapest: Pázmány University ePress, 2015, pp 41– 44.

and $D(\phi, r)$ is the collective diffusion coefficient for density ϕ [13]. In this equation the temperature change and the chemical properties of PDMS were neglected.

B. Simulation in Matlab

In 2011 Hongjun et al. [6] published a new model and simulation methodology to simulate the transient liquid filling process in microfluidic devices. In this system-level simulation the microfluidic device is composed of a network of connected components. The components are equivalent to the microchannels and are connected via junctions. The junctions have two states: void or filled. In the first case, the inlet and the outlet pressure is equal. Therefore, the pressure in the junction remains the same as the ambient pressure. In the second case, when the junction is filled, we can calculate the flow rates with the following equation

$$\sum_{m=1}^{M} Q_m^j - \sum_{n=1}^{N} Q_n^j = 0 \tag{2}$$

where N is the total number of junctions and M is the total number of microchannels. The states of microchannels can be classified into three categories: void, fully filled and partially filled. In the first case the inlet and the outlet pressure is equal:

$$P_{in} - P_{out} = 0 \tag{3}$$

In fully filled case the flow within the channel is governed by

$$\frac{12\beta L\mu Q}{W^4\gamma} - (P_{in} - P_{out}) = 0 \tag{4}$$

where $Q = \int_0^H \int_0^W u \; dydz$ is the flow rate, $\beta = \frac{W}{H}$ is the aspect ratio of the channel. In the third case, based on Newton's second law, the momentum change is balanced by surface tension force, pressure difference and viscous force. When we assume, that the system is in quasisteady state, the momentum change is negligible. Thus, the force balance equation is the following

$$2\sigma\cos\theta(1+\beta) + (P_{in} - P_{out})W - \frac{12\mu l}{W\gamma}\frac{dl}{dt} = 0 \tag{5}$$

where $U = \frac{dl}{dt}$, σ is the surface tension coefficient, θ is the contact angle and l is the filling length within the channel.

C. Fabrication of microfluidic devices

After the successfull simulations, we implemented the calculated structure and flow characteristic in PDMS based microfluidic chip. Based on the available resources, fabrication could be made either by 3D printing or by a laser cutter. Our experiments showed higher spatial resolution can be achieved by a laser cutter, so the Epilog Zing Laser Cutter (30W) was used. At first we laid the microfluidic chip out in CorelDraw then we cut the frame of PDMS out. We used the following parameter settings in the laser cutter: 90% speed, 100% energy and 1000Hz. Then different cutting parameters were used to etch the channels into the PDMS bulk (90% speed, 20% energy and 1000Hz). At last the different layers were sealed with two-sided adhesive (3M 96042).

D. PCR and LAMP

In our experiment both traditional PCR and LAMP were planned. The PCR served as a control measurement. Four different DNA samples were prepared: *Listeria monocytogenes* (ATCC 19177 [CCM 4699] and ATCC 19111 [CCM 5576]) as positive samples, *Listeria Iianovi* (ATCC 19119 [CCM 5884^T] and *Listeria seeligeri* (ATCC 35957[CCM3970^T]) as negative control. The samples were coded and referred to as $C1$, $C2$, $C7$ and $C9$ respectively.[14] The samples were stored under oil agar slant at -20 C°, then they were put on Tryptone Soya Agar (TSA) in a Petri dish for 24 hours at 37 C°. Then the samples were placed on a new Petri dish for another 24 hours at the same temperature. When finished, the cell culture was grown properly for further preparation. The protocols MasterPure^{TM} Complete DNA and RNA Purification Kit were used. After the preparation of DNA samples preparation, the concentrations of the samples were measured, shown in Table 1. Two experimental setups were designed. The first one was a standard PCR procedure, while the second one was a LAMP on the microfluidic device. The aim of the traditional PCR was to confirm the results of the LAMP.

TABLE I
The concentrations of DNA in different samples, where $C1$ and $C2$ are *Listeria monocytogenes*, $C7$ is *Listeria Iianovi* and $C9$ is *Listeria seeligeri*. **A**: The measurement results of Gergely Huszka[14] **B**: The repeated measurement results

	C1	**C2**	**C7**	**C9**
A	$29,8ng/\mu l$	$134,6ng/\mu l$	$27,1ng/\mu l$	$92,5ng/\mu l$
B	$28,1ng/\mu l$	$133,9ng/\mu l$	$27,4ng/\mu l$	$91,9ng/\mu l$

E. Gel electrophoresis

To confirm the results the LAMP samples were investigated with gel electrophoresis. 0.4-0.5g agarose gel, 1ml 50x TAE buffer ($2,0M$ Tris acetate, $0,05M$ EDTA, pH $8,0$) and 49ml distilled water were mixed then it was microwaved for 2min to melt completely. As the gel cooled down samples were put in the gel boxes and $130V$ electrical field were applied for 20-25 minutes.

III. Results

A. Flow characterization

The aim of the simulations was to minimize the thickness of PDMS and the required vacuuming time, and to optimize the desired flow characteristic in microchannels. First air concentration and pressure change was simulated in Comsol. In 2D models very fine and in 3D models moderate mesh was used. The simulation times of the change of air concentration in 2D case was 2-5 minutes, but in 3D case it could be more hours. We must note here that the 3D model was inaccurate due to the applied boundary conditions and the rare mesh. Despite the inaccuracies of this model we determined the ideal thickness of PDMS (Fig.1). To perform a LAMP reaction in microfluidic channel, a continuous and laminar flow is

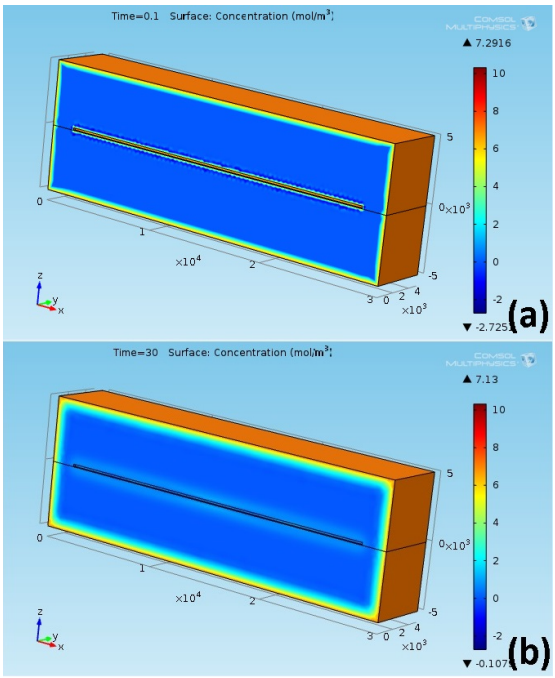

Fig. 1. The change of air concentration in Comsol 3D model on extremely fine mesh. The PDMS bulk is $3\times0.5\times0.5$ mm and the vacuumchannel is $2600\times20\times20$ μm. (**a**) The boundary transition can be observed at $t = 0.1$ (**b**) The growth of concentration in the vacuumchannel at $t = 50$.

needed. Furthermore, the ideal flow volume in $100\mu m$ cross-sectional microchannel is 100-150μl/min. To achieve this different channel structures with different parameter settings was simulated in Matlab then the necessary parameters of channels were determined.

B. LAMP

After the sample preparation the microfluidic chip were vacuumed for 50min then LAMP reaction mixtures and the sample was pipetted in the two inlets. Hereupon the chip was placed on the heater system at at 65 C° for 40 minutes then at 80 C° for 10 minutes to stop the LAMP reaction. The increased amount of DNA was detected by turbidity, therefore after the process the result of the LAMP test was observable by naked eye Fig.2 [14].

C. Validation

To validate the experiments traditional gel electrophoresis was executed Fig.3. The order of the samples in the wells is the following: first the negative control was placed, then the tribe $C1$ finally the tribe $C2$. The strains $C1$ and $C2$ of *Listeria monocytogenes* and the negative control were shown by the test. Be well worth seeing that the LAMP reaction gives a stripe (the traditional PCR gives separating marks), because the formation of DNA is continuous therefore the DNA strands are in different size.

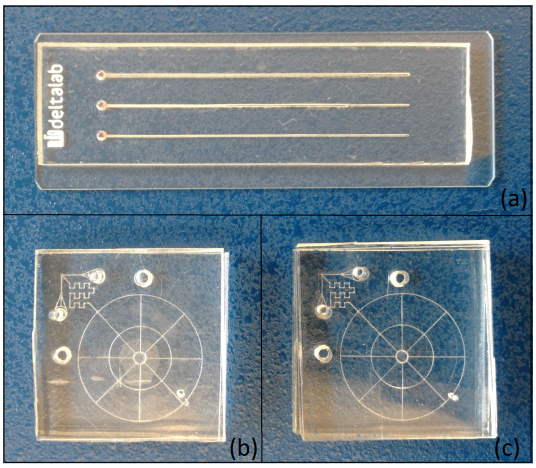

Fig. 2. The designed microfluidic chips (**a**) Microfluidic chip to measure flow characteristic of 200μm$\times$6cm microchannel (**b**) Sealed version of the LAMP microfluidic chip (**c**) Unsealed version of the LAMP microfluidic chip

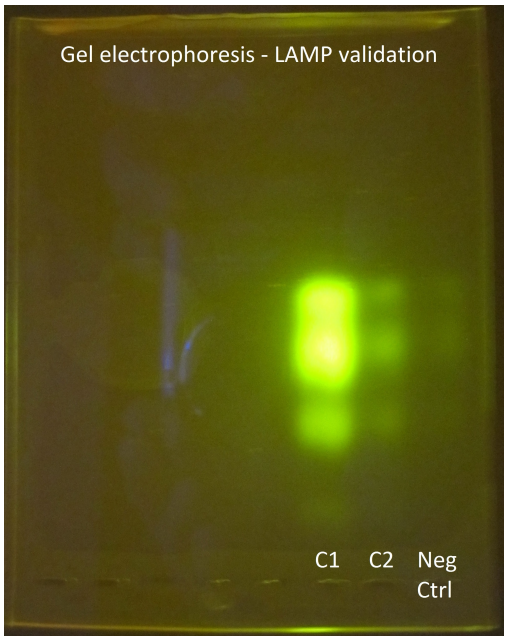

Fig. 3. The validation of LAMP with gel electrophoresis. The DNA of the $C1$ and $C2$ tribes are present. Unfortunately the negative control is present to due to the contamination

IV. Conclusion

In summary, we have demonstrated a degas-driven microfluidic chip that uses loop-mediated isothermal amplification to amplify DNA of *Listeria monocytogenes* from food samples. This easy-to-use LoC device could be manufactured at low cost (based on PDMS), and the time of measurement is quicker than the traditional methods. An additional advantage is the easy reproducibility and with the integration of LAMP and

the turbidity based detection method, the sample handling and labeling mistakes can be minimized.

ACKNOWLEDGMENT

I would like to thank to my supervisor dr. Kristóf Iván for his continuous help and support. I also want to thank the help and guidance to Sándor Földi. Thanks are also due to Prof. Barnabás Garay for his continuous help in mathematics and in computational dynamics.

REFERENCES

[1] National Institute of Allergy and Infectious Disease Health Matters Foodborne Diseases fact sheet. http://www.niaid.nih.gov/factsheets/foodbornedis.htm. Accessed 13. September 2003.

[2] Ágnes Belák, Gabriella Kiskó, Mónika Kovács, Anna Maráz, *Gyors és molekuláris biológiai módszerek alkalmazása élelmiszerek mikrobiológiai vizsgálatára* Nemzeti Tankönyvkiadó, 2011.

[3] Ágnes Belák, *Élelmiszer-biztonsági szempontból jelentös baktériumok kimutatása, PCR-alapú molekuláris azonosítasa és tipizálása* Doktori értekezés, 2009.

[4] Whitesides, George M. "The origins and the future of microfluidics." Nature 442.7101 (2006): 368-373.

[5] Dimov, Ivan K., et al. *Stand-alone self-powered integrated microfluidic blood analysis system (SIMBAS).* Lab on a Chip 11.5 (2011): 845-850.

[6] Song, Hongjun, Yi Wang, and Kapil Pant. "System-level simulation of liquid filling in microfluidic chips." Biomicrofluidics 5.2 (2011): 024107.

[7] Hosokawa, Kazuo, et al. "Power-free poly (dimethylsiloxane) microfluidic devices for gold nanoparticle-based DNA analysis." Lab on a Chip 4.3 (2004): 181-185.

[8] Sander, R. "Compilation of Henry's law constants, version 3.99." Atmospheric Chemistry and Physics Discussions 14.21 (2014): 29615-30521.

[9] Bartlett, John MS, and David Stirling. "A short history of the polymerase chain reaction." PCR protocols. Humana Press, 2003. 3-6.

[10] Armes, Niall A., and Derek L. Stemple. "Using recombinase-polymerase amplification to propagate target DNA without the use of thermocycling or thermophilic enzymes." U.S. Patent No. 7,270,981. 18 Sep. 2007.

[11] Notomi, Tsugunori, et al. "Loop-mediated isothermal amplification of DNA." Nucleic acids research 28.12 (2000): e63-e63.

[12] Tang, Meng-Jun, et al. "Rapid and sensitive detection of Listeria monocytogenes by loop-mediated isothermal amplification." Current microbiology 63.6 (2011): 511-516.

[13] Thambynayagam, Michael. "The Diffusion Handbook: Applied Solutions for Engineers by RK." (2011).

[14] Gergely Huszka, *Nukleinsav erösítési folyamat megvalósítása mikrofluidikai környezetben* Diplomaterv, 2014.

Heterogeneous neuronal behaviour during human neocortical population activity

Katharina HOFER
(Supervisor: István ULBERT)
Pázmány Péter Catholic University, Faculty of Information Technology and Bionics
50/a Práter street, 1083 Budapest, Hungary
hofer.katharina@hallgato.ppke.hu

***Abstract*— Epilepsy is a neurological disorder associated with neuronal hyperactivity. When pharmacological treatment proves to be ineffective, surgical tissue removal is considered as an alternative. Cortical brain tissue obtained this way or from brain tumour surgery shows spontaneous population activity (SPA), which has previously been attributed to epileptic processes exclusively. A detailed investigation of the involvement of different neuron types (as has been done for other population activities in other brain regions) would help to clear up the origin of this population activity, which is still unknown.**

This study investigates the roles different types of neurons play in the generation of the spontaneous population activity found in the neocortex in vitro.

The local field potential gradient was recorded from brain tissue slices obtained from epileptic and non-epileptic patients using a laminar multielectrode. Both SPA and single neuron activity were detected and analysed using crosscorrelations. In addition to the tissue origin, the neuronal cell type and the neuronal location within the cortical layers were also taken into consideration.

While some neurons increase, some decrease and some do not change their firing during SPAs, the extent to which neurons change their firing and the ratios of the neurons behaving in different ways significantly differ between epileptic tissue and non-epileptic tissue. Moreover, principal cells and interneurons also show significant differences in their cell firing. The involvement of a neuron also depends on its location relative to the site of the SPA.

Thus, even though slices from both epileptic and non-epileptic tissue generate spontaneous population activity, the involvement of different groups of neurons differs significantly.

***Keywords*- human; neocortex; electrophysiology; multielectrode; synchronous population activity; cell firing properties; PETH; crosscorrelation; neocortical layers**

I. INTRODUCTION

Epilepsy is one of the most common neurological disorders in humans. Even though epileptic seizures are thought to be related to hyperactivity of neuronal circuits, it is still unclear which changes within a neuronal network render it epileptic.

Various animal models have been employed to study the underlying mechanisms of this disorder (for a review see: Sarkisian, 2001), but validation from human tissue analyses is also important. This can be achieved by studying living human brain tissue in vitro. This kind of tissue can be obtained during surgeries (similar to brain tumour surgeries) in which resection of the epileptic focus is employed as a treatment alternative for approximately one third of the patients, who are pharmacoresistant (Löscher, 2002).

During electrophysiological recordings from human neocortical slices obtained from epilepsy patients as described above, spontaneous synchronous population activity (SPA) is known to appear (Kohling et al. 1998; Roopun et al. 2009). This population activity has been compared to interictal activity recorded during electroencephalography (EEG) from the scalp of epileptic patients (in vivo). However, although SPA has been observed in human neocortical tissue slices obtained during tumour surgery (Pallud et al. 2014), the observed SPA has been associated with epileptic processes, as brain tumours are often associated with epilepsy (van Breemen et al. 2007). Here, SPA are described in tissue slices from non-epileptic brain tumour patients, in which no interictal activity could be detected as well as in tissue from epileptic patients.

This shows that SPA is not the in vitro correlate of the in vivo interictal spikes, raising the question of the origin of this neocortical population activity. Nonetheless, it opens the possibility of studying SPA and comparing it between epileptic and non-epileptic networks. In this study, the firing properties of neurons during SPA are investigated in order to shed light on the differences between epileptic and non-epileptic neuronal networks.

II. MATERIALS & METHODS

A. Tissue preparation

Neocortical tissue was obtained from epileptic patients (*EPI*) or from tumour patients without epilepsy (*TU*). Note that the *TU* tissue did not include tissue from the actual tumour. After surgical resection, the tissue was immediately stored in ice cold sucrose solution (248 mM sucrose, 26 mM NaHCO3, 1 mM KCl, 10 mM MgCl2, 1 mM CaCl2, and 10 mM glucose, equilibrated with 5% CO2 - 95% O2). Keeping the slices in the same ice cold solution, the pia mater as well as large blood vessels were removed and the tissue was cut into 500 μm thick slices perpendicular to the neocortical layers. The slices were then transferred to an interface chamber and perfused with artificial cerebrospinal fluid (ACSF; 124 mM NaCl, 26 mM

Supported by OKTA K81354, OKTA PD77864, ANR-TÉT Neurogen, ANR-TÉT Multisca, TÁMOP-4.2.1.B-11/2/KMR-2011-0002, Bolyai Research Fellowship (to Lucia Wittner), PhD student grant by the Hungarian government (to KH)

K. HOFER, "Heterogeneous neuronal behaviour during human neocortical population activity" in *PhD Proceedings Annual Issues of the Doctoral School, Faculty of Information Technology and Bionics, Pázmány Péter Catholic University – 2015.* G. Prószéky, P. Szolgay Eds. Budapest: Pázmány University ePress, 2015, pp 45– 48.

NaHCO3, 4 mM KCl, 2 mM MgCl2, 2 mM CaCl2, and 10 mM glucose, equilibrated with 5% CO2 - 95% O2). They were incubated for at least one hour before recording in the same chamber.

B. *Electrophysiological recordings*

The local field potential gradient (LFPg) was recorded at 20 kHz sampling rate using a 24 contact laminar multielectrode (Ulbert et al. 2001; 150 mm intercontact distance). The laminar multielectrode array was placed on the surface of the slice, perpendicularly to the neocortical cell layers. Because of this, the spatial information (over the different neocortical layers) was preserved.

C. *Data analysis*

Data were analysed using the Neuroscan Edit 4.5 program (Compumedics Neuroscan, Charlotte, NC) and custom written code for Matlab (The MathWorks, Natick, MA).

SPA was detected using an amplitude threshold of three times the standard deviation after applying Hamming window spatial smoothing two times and bandpass filtering between 1 Hz and 30 Hz. Using agglomerative hierarchical clustering (Ward method using Euclidean distances), SPAs were clustered into a supragranular/granular *(supra-gran)* and an infragranular *(infra)* group. The parameter used for clustering was the location of the largest current source density (CSD) sink or source. The CSD was calculated from the LFPg using standard techniques (Ulbert et al. 2004).

Cell activity was clustered from the extracellularly recorded LFPg after applying 500 Hz high pass filtering (zero phase shift, 48 dB/octave) using custom code written in Matlab. After the detection, the averaged action potentials as well as the autocorrelograms were used to sort the cells into principal cells *(PCs)*, interneurons *(INs)* or undeterminable cells *(uc)* manually. In addition, using the number of the channel with the largest action potential amplitude of each cell as spatial information, the cells were grouped into supragranular *(supra)*, granular *(gran)* and infragranular *(infra)* cells.

For all event related calculations the peak times of SPA and action potentials were used.

For each cell, firing parameters such as average firing frequency, interspike interval and a measure for the amount of cell bursting (burstiness, after Viskontas et al. 2007) were calculated.

For the recordings in which both cell activity and SPA were observed, the timing of cellular activity before, during and after the SPA was analysed (crosscorrelation). For this purpose, peri-event time histograms (PETHs) were generated for the time window from -300 ms to +300 ms around the SPA with a bin size of 5 ms. Comparing each clustered cell to each SPA that occurs in the same recording resulted in 840 SPA–cell comparisons and thus 840 PETHs. For visualisation, each PETH was standardised for the product of the square roots of the total number of cell spikes and the SPA events. Note that this merely served the purpose of visualising the data in heat map graphs. This standardisation did not influence the statistical tests performed. The firing change was calculated as the number of cell spikes per bin occurring from -30 ms to +30 ms around the SPA divided by 440 ms of baseline firing (from -300 ms to -85 ms and from 85 ms to 300 ms). Thus, the calculated firing change reflects the ratio by which a given cell changed its firing during the SPA. Values above one indicate an increase in cell firing, values below one indicate firing decrease. The non-parametric Krustal Wallis test was used to check for significant differences in firing change between the groups.

III. Results & Discussion

A. *Occurrence of single cell and population activity*

Synchronous population activity (SPA) was detected in 32 percent of slices originating from tumour patients (n=179 slices from 29 patients) and 48 percent of slices from epilepsy patients (n=196 slices from 35 patients). In the same slices, neuronal cell firing could be detected in 80 percent of *TU* slices and 79 percent of *EPI* slices. This occurrence of SPA in tissue obtained from epileptic as well as non-epileptic tumour patients shows that SPA observed in vitro cannot directly be compared to interictal activity observed during EEG in epilepsy patients.

For the purpose of investigating the involvement of single neurons in the population activity, cell clustering was performed in addition to the detection of SPA in 23 slices from 6 tumour patients and 54 slices from 14 epilepsy patients. 29 SPAs and 182 cells were isolated from *TU* tissue, 66 SPAs and 479 clustered cells were isolated from *EPI* tissue.

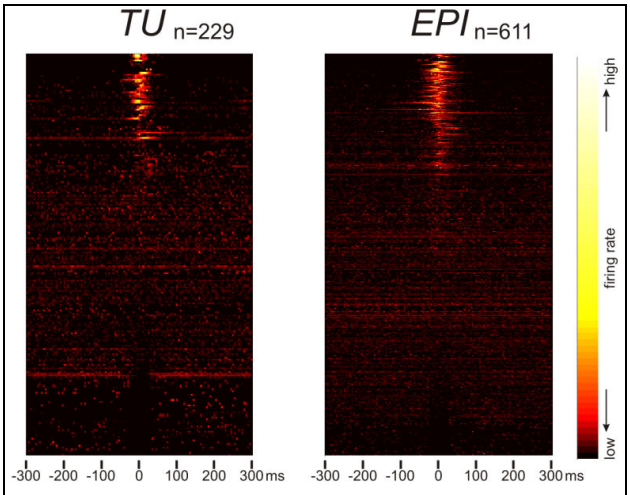

Figure 1. SPA–cell relations for cells according to origin of tissue. SPA–cell relations for recordings obtained from tumour (*TU*, left panel) and epileptic (*EPI*, right panel) patients. Each row shows one PETH standardised as described in the Methods section. The x-axis represents time, with the SPA occurring at time 0. The cellular firing rate is colour coded, yellow and white indicate high, while red and black indicate low firing rates. Note the non-linear colour coding as visualised by the colour bar. The PETHs were sorted by firing change in a descending manner, showing cells that increase their firing at the top, while cells that decrease their firing are represented at the bottom of the graph. The increase in the firing of cells during SPA was significantly higher in *EPI* cells than in *TU* cells ($p<0.05$).

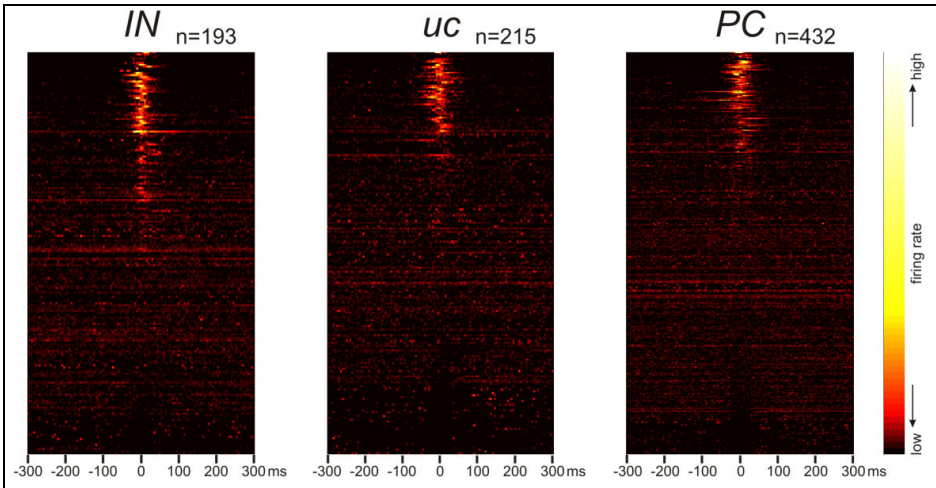

Figure 2. SPA–cell relations for different cell types. Firing behaviour of cells during SPA, according to their cell type. PETHs are represented as described in Figure 1. Interneurons (*IN*, left panel) showed significantly higher firing increases during SPA than unclassifiable cells (*uc*, middle panel) and principal cells (*PC*, right panel) ($p<0.05$).

B. *Differences in firing behaviour between TU cells and EPI cells*

Both the average firing frequency (medians: *TU*: 0.1878 Hz; *EPI*: 0.3552 Hz) and the interspike interval (medians: *TU*: 0.1239 s; *EPI*: 0.2927 s) were significantly larger for *EPI* cells compared to *TU* cells ($p<1E-4$ and $p<0.001$, respectively). While this may seem like a contradiction, it can be explained by a more regular firing pattern of *EPI* cells and a more irregular firing rate in *TU* cells. In fact, the coefficient of variation of the interspike intervals was significantly higher for *TU* cells in comparison to *EPI* cells (medians: 19.51 and 10.16, respectively, $p<0.05$). Moreover, cells from *TU* tissue showed significantly higher burstiness than cells from epileptic tissue ($p<1E-6$), which may also contribute to the differences in firing regularity.

When comparing the firing change of cells during SPAs, *EPI* cells showed a significantly higher firing increase compared to *TU* cells ($p<0.05$; Figure 1). This shows that *EPI* cells are more synchronised than *TU* cells, as they increase their firing in response to the population activity to a greater extent. However, in spite of these differences in firing increase, both the *TU* and the *EPI* group comprise cells with very heterogeneous firing patterns. As can be seen in Figure 1, the individual firing patterns of the cells during SPAs are quite diverse. Some cells gradually increase their firing and stop abruptly after the SPA, while others start firing at a high rate during the SPA and successively fade out afterwards. Other cells seem to be tightly locked to a specific phase of the SPA and only fire at a high rate for 20 ms or less.

Thus, the differences between *TU* and *EPI* cells are subtler than one might have expected, as epilepsy is characterised by reoccurring seizures, which are "abnormal excessive or synchronous neuronal activity in the brain" (Fisher et al. 2005: 471). Interestingly, when comparing neuronal cell activity to interictal discharges in epilepsy patients in vivo, Keller et al. (2010) also found some cells that modify their firing while others do not, where the modified group featured various different patterns of firing increase and decrease.

C. *Differences between different cell types*

Principal cells *(PC)* exhibited both a significantly smaller interspike interval and a significantly higher burstiness than unclassifiable cells *(uc)* and interneurons *(IN)* ($p<1E-7$ and $p<0.01$, respectively). In addition, unclassifiable cells showed a smaller average firing frequency compared to principal cells and interneurons ($p<0.001$). This can be explained as cells with few spikes (and thus a low average firing rate) have noisier averages, which makes it more difficult to categorize them.

In terms of firing behaviour during SPA, interneurons displayed a significantly larger firing increase than both unclassifiable cells and principal neurons ($p<0.05$; Figure 2). This is especially interesting as principal cells and interneurons play different roles during neuronal synchrony (for a review see: Buzsáki, 2006).

D. *The effect of cell location on firing behaviour*

Cells located in the supragranular layers *(supra)* had a significantly larger interspike interval than cells located in the granular *(gran)* or infragranular *(infra)* layers ($p<0.001$). However, there were no significant differences in average firing frequency. *Infra* cells burst significantly less than *supra* or *gran* cells ($p<1E-4$). When considering the different firing patterns of cells in different locations, one has to take into account that the SPAs do not occur over all layers equally.

The involvement of a cell during an SPA depended on the location of the SPA which it was compared to (Figure 3). When the SPA occurred in the same cell layer in which the cell was located, it was considered local. If there was no SPA in the cell layer of the cell it was considered not local.

Striking differences were found when comparing the firing of local and non-local cells. Local cells increase their firing more than non-local cells ($p<1E-8$). As can be seen in Figure 3, only few non-local cells change their firing. This suggests that SPA is a very local event, as most of the cellular contribution stemmed from cells from the same spatial range.

IV. Conclusion

Spontaneously occurring synchronous population activity (SPA) was observed in neocortical brain slices obtained from epilepsy patients or non-epileptic tumour patients, challenging the view of SPA as the in vitro correlate of interictal spikes observed during EEG in epileptic patients.

Some, but not all, cells clustered from these extracellular laminar recordings changed their firing during the occurrence of SPA. Cells in epileptic tissue fire more regularly and show a higher involvement during the population activity than cells from non-epileptic tissue, as evident by their larger increase in cell firing during the SPA. Nonetheless, the firing patterns of cells during SPA in both groups were very heterogeneous and depended on multiple factors. For example, the cell type influences a cell's contribution to the SPA, while the spatial relation of the cell to the population activity also has a strong impact on its firing properties, making the SPA seem to be a very local event.

Compellingly, neither the cell type nor the cell location were sufficient to describe the role of any given cell in the population activity. The firing activities of the various cells are very heterogeneous, but show significant differences between the epileptic and the non-epileptic group. Thus, small but crucial changes in the neuronal network seem to make the difference between an epileptic and a non-epileptic neuronal network.

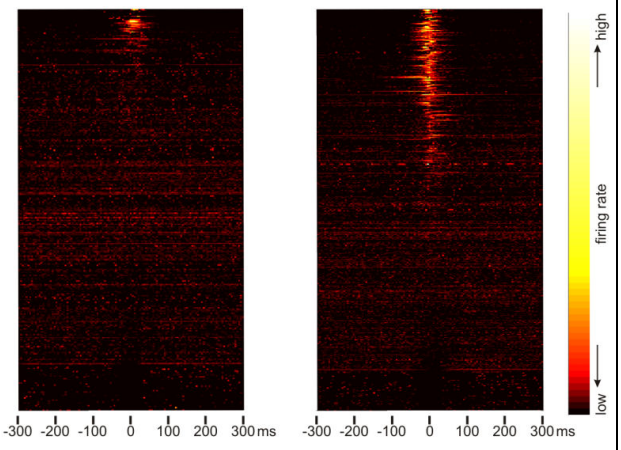

Figure 3. SPA–cell relations for differently located SPAs and cells. Firing behaviour of cells during SPA, differentiating SPAs and cells occurring in the same cell layer (local) or in different cell layers (not local). PETHs are represented as described in Figure 1. There was a significant difference in firing change between local and not local cells ($p<1E-8$).

Acknowledgment

The author would like to thank Kinga Tóth, Ágnes Kandrács and Csilla Szábó for participating in the experiments and the data analysis, the surgeons Attila Bagó, Loránd Erőss and László Entz for the collaboration and Richárd Csercsa and Andor Magony for the Matlab routine WaveSolution used for spike detection. In addition, the author is especially grateful to István Ulbert and Lucia Wittner for their excellent supervision and support. Last but not least, the author would like to thank the patients participating in the study.

References

[1] G. Buzsáki, Rhythms of the Brain, cycle 6: Synchronization by Oscillation, Oxford University Press, New York, 464 pages, ISBN: 978-0-19-530106-9. (2006)

[2] R.S. Fisher, W. Van Emde Boas, W. Blume, C. Elger, P. Genton, P. Lee, and J. Jr. Engel, Epileptic Seizures and Epilepsy: Definitions Proposed by the International League Against Epilepsy (ILAE) and the International Bureau for Epilepsy (IBE). Epilepsia 46: 470–472. (2005)

[3] C.J. Keller, W. Truccolo, J.T. Gale, E. Eskandar, T. Thesen, C. Carlson, O. Devinsky, R. Kuzniecky, W.K. Doyle, J.R. Madsen, D.L. Schomer, A.D. Mehta, E.N. Brown, L.R. Hochberg, I. Ulbert, E. Halgren and S.S. Cash, Heterogeneous neuronal firing patterns during interictal epileptiform discharges in the human cortex. Brain: 133; 1668–1681 (2010)

[4] R. Kohling, A. Lucke, H. Straub, E.J. Speckman, I. Tuxhorn, P. Wolf et al., Spontaneous sharp waves in human neocortical slices excised from epileptic patients. Brain; 121 (Pt 6): 1073–87 (1998).

[5] W. Löscher, Current status and future directions in the pharmacotherapy of epilepsy. Trends Pharmacol. Sci. (2002)

[6] J. Pallud, M. Le Van Quyen, F. Bielle, C. Pellegrino, P. Varlet, M. Labussiere, N. Cresto, M.-J. Dieme, M. Baulac, C. Duyckaerts, N. Kourdougli, G. Chazal, B. Devaux, C. Rivera, R. Miles, L. Capelle, G. Huberfeld, Cortical GABAergic excitation contributes to epileptic activities around human glioma. Sci. Transl. Med. 6, 244ra89 (2014).

[7] A.K. Roopun, J.D. Simonotto, M.L. Pierce, A. Jenkins, C. Nicholson, I.S. Schofield, R.G. Whittaker, M. Kaiser, M.A. Whittington, R.D. Traub, and M.O. Cunningham, A nonsynaptic mechanism underlying interictal discharges in human epileptic neocortex. PNAS vol.107 no.1 pp338–343 (2009)

[8] M.R. Sarkisian, Overview of the Current Animal Models for Human Seizure and Epileptic Disorders. Epilepsy Behav. Jun; 2(3): 201–216. (2001)

[9] I. Ulbert, E. Halgren, G. Heit, G. Karmos, Multiple microelectrode-recording system for human intracortical applications. J Neurosci Methods 106: 69–79. (2001)

[10] I. Ulbert, G. Heit, J. Madsen, G. Karmos, E. Halgren. Laminar analysis of human neocortical interictal spike generation and propagation: Current source density and multiunit analysis in vivo. Epilepsia 45 (Suppl 4): 48–56. (2004)

[11] M.S. van Breemen, E. B. Wilms, C. J. Vecht, Epilepsy in patients with brain tumours: Epidemiology, mechanisms, and management. Lancet Neurol; 6, 421–430 (2007).

[12] I.V. Viskontas, A.D. Ekstrom, C.L. Wilson and I. Fried, Characterizing Interneuron and Pyramidal Cells in the Human Medial Temporal Lobe In Vivo Using Extracellular Recordings. Hippocampus 17: 49–57 (2007)

Changes of environmental requirements during differentiation of neural cells

Attila JÁDY
(Supervisor: Emília MADARÁSZ)
Pázmány Péter Catholic University, Faculty of Information Technology and Bionics
50/a Práter street, 1083 Budapest, Hungary
jady.attila@hallgato.ppke.hu

***Abstract*— Depending on developmental stages, the differentiating neural cells display importantly different responses to environmental stimuli. According to previous results the basic metabolic needs shift with the advancement of neural differentiation: the metabolic profile reflects the origin and stage of differentiation of neural cells. In the recent period, motility changes in response to cation influx were compared between neural stem cells and differentiating neuronal precursors. Data obtained on optogenetically modified stem and neuronal precursor cells demonstrated that opening of light-activated cation channels reduces the motility of developing neural cells while does not influence the move of neural stem cells.**

***Keywords*: neural stem cell, neuronal differentiation, oxygen consumption, metabolism, cell motility, optogenetic stimulation**

I. INTRODUCTION

Besides the needs for growth factors, adhesive surfaces and cell activation patterns, the changes in metabolism play important roles in decision on integration or decay of young neural cells in the course of development, regeneration and physiological neuron-replacement [1]. Previous data on NE-4C [2] neural stem cells and on their differentiating progenies showed that neural cells in different stages of cell differentiation require significantly different environment for survival [3].

In order to explore biochemical processes behind the differentiation-dependent changes of cell metabolism, the O_2-consumption of embryonic NE-4C (Fig. 1.) and adult-derived hippocampal (HC_A) [4] (Fig. 2.) neural stem cells were compared to the O_2-uptake by primary neurons (Fig. 3/A.) and astrocytes (Fig. 3/B.).

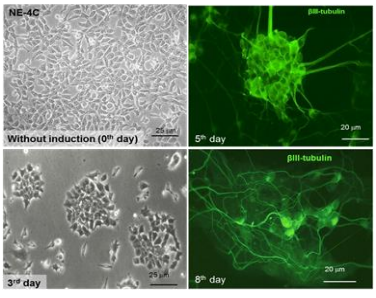

Figure 1. NE-4C cells, derived from the anterior brain vesicles of p53-deficient mouse embryo (E9), proliferate as non-differentiated epithel-like cells in maintaining cultures (RA 0), but give rise to neurons (5th and 8th days) if induced by all-trans retinoic acid (RA).

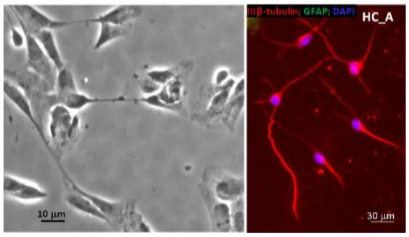

Figure 2. HC_A cells, derived from the adult mouse hippocampus, proliferate as non-differentiated epithel-like cells in maintaining cultures, but give rise to neurons if induced by EGF withdrawal.

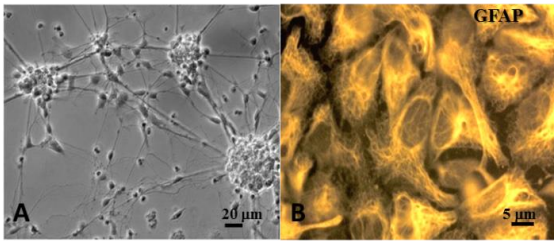

Figure 3. **A**: Phase-contrast picture of a primary neuron-enriched culture on the 7th day after plating. **B**: Primary astrocyte culture. were stained with antibodies to glial fibrillary acidic proteins (GFAP)

Besides the metabolic needs, differences in cell motility were found when responses to cation channel opening were compared between radial glia-like neural stem cells (RGl^{ChR2+}) and their differentiated progenies, both obtained from channelrhodopsin - expressing transgenic mice [5]. RGl-type cell populations were isolated from $CAG^{loxp}Stop^{loxp}$Chr2(H134)-EYFP transgenic mouse embryos and transfected with Cre-recombinase coding constructs (RGl^{Chr2+}) or were used as ChR2-non-expressing (RGl^{Chr2-}) controls [5].

II. EXPERIMENTAL SETUP

A. Cell cultures

The cells were maintained in the appropriate media in water-saturated air atmosphere containing 5% CO_2, at 37 °C. The culture media were changed on every 2nd or 3rd day. NE-4C, HC_A, RGl^{ChR2+} and RGl^{ChR2-} cells were serially split using 0,05 (w/v) % tripsin with 1mM EDTA.

Richter Centenary Foundation Grant

A. JÁDY, "Changes of environmental requirements during differentiation of neural cells" in *PhD Proceedings Annual Issues of the Doctoral School, Faculty of Information Technology and Bionics, Pázmány Péter Catholic University – 2015.* G. Prószéky, P. Szolgay Eds. Budapest: Pázmány University ePress, 2015, pp 49– 51.

Non-induced NE-4C cells, primary neurons and astrocytes were maintained in 5% or 10% FCS MEM media (MEM – minimum essential medium, 5% or 10% heat-inactivated FCS – foetal calf serum, 0.4 mM L-glutamin, 0.04 mg/ml gentamicin, 2,5 ug/ml amphotericin), in plastic dishes covered with poly-L-lysine.

Non-induced HC_A, RGl^{ChR2+} and RGl^{ChR2-} cells were grown in AK(c-RGD) coated dishes [6] in serum free conditions (50% DMEM – Dulbecco's modified Eagle medium, 50% F12-HAM, 2% B27 (with retinal), 2 mM L-glutamine, 0.02 mg/ml gentamicin, 1.25 ug/ml amphotericin and optionally 40 ng/ml EGF - epidermal growth factor). For induction of neuronal development, EGF was withdrawn from the medium. RGl^{ChR2+} cells were protected from light during all culture procedures.

B. Instrumental studies on O_2-consumption

Cells were seeded into 96-well Seahorse plates (1-3 x 10^4 cells/well) coated with appropriate adhesive peptides and were maintained as non-differentiated stem cells or were induced with appropriate treatment for neural differentiation. Before the assays, the media were changed to artificial cerebrospinal fluid (ACSF) containing 45 mM NaCl, 3 mM KCl, 2 mM $CaCl_2$, 1 mM $MgCl_2$, 10 mM HEPES; pH = 7.2. For metabolic assays, the ACSF were supplemented with one of the following metabolites: 5 mM D-glucose (glc), 5 mM Na-lactate (lac), 5 mM D,L-β-hydroxi-butyrate (BOHB), 2.5 mM glutamine (gln) or 5 mM pyruvate (pyr). The O_2-consumption and extracellular acidifaction was determined with Seahorse XF96 Extracellular Flux Analyzer (Seahorse Bioscience, USA) (Fig. 4.). The data were plotted as OCR (oxygen consumption rate: pmole O_2 consumption/min) and ECAR (extracellular acidification rate mpH/min) as a function of time. For comparing the reactions to different added material, OCR and ECAR values were related to those in non-treated control cultures and plotted as relative OCR and ECAR values.

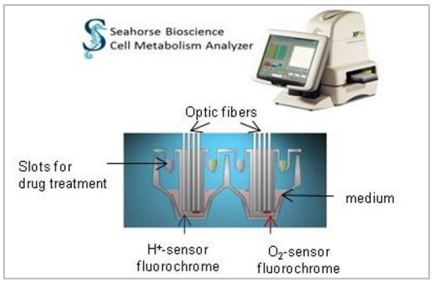

Figure 4. The cell metabolism analyzing devices

C. Studies on cell motility

RGl^{ChR2+} and RGl^{ChR2-} cells were plated onto AK-c(RGDfC)-coated optically optimized 35 mm culture dishes (Ibidi; Germany) and were maintained as non-differentiated stem cells or were forced to differentiate to neurons by withdrawal of EGF from the medium.

Non-induced RGl^{ChR2+} and RGl^{ChR2-} cultures or those on the 1st and 5th day of induction were placed on the stage of the Zeiss Axiovert 200M inverted fluorescence microscope equipped with an Axiovision 4.6 software. The cells were illuminated with 488 nm light (0.13 mW/mm^2) for 300 ms in every 5 min and pictures were taken during a 24 hours period. The pictures were analyzed with Cell track program and then analyzed with MATLAB.

III. Brief Results and Conclusions

The Seahorse XF96 cell metabolism analyzer (Seahorse Bioscience) was employed to determine the impact of various metabolic fuel substances on the bioenergetic processes of NE-4C, HC_A cells, primary neurons and astrocytes. Fluorimetric sensors enabled sensitive in situ measurement of O_2 consumption rate (OCR) and the rate of the extracellular pH drift (ECAR) in a 2.28 µl fluid volume above the cells. The oxygen content in the cell-covering fluid decreases with time in parallel with the O_2-consumption of cells. Acidification (pH) of the extracellular medium was measured in parallel with oxygen content in each well. The oxygen consumption rate (OCR) indicates the respiration activity, because the electron transport chain consumes oxygen. The extracellular acidification rate (ECAR) demonstrates mainly the intensity of glycolytic activity, because its lactate production acidifies the environment. The metabolic state of cells was tested at the end of metabolic assays by monitoring mitochondrial responses to respiration blocking drugs.

The unexpected finding of the study was that in response to glucose addition, all types of cells in ACSF decreased the O_2-uptake (Fig. 5).

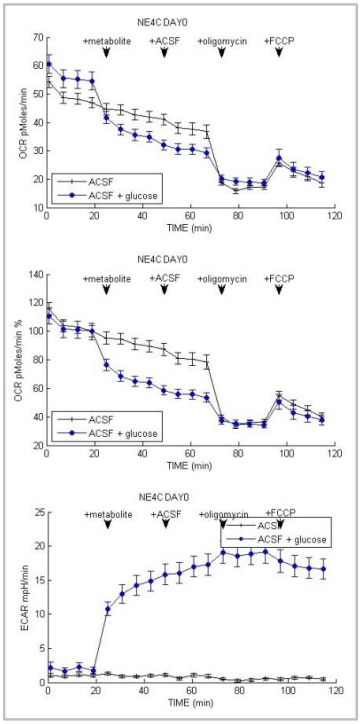

Fig. 5. Metabolic response of NE-4C cells to addition of glucose

It could be explained by starvation effect of cells kept in fuel-free ACSF for several hours. Starving cells might produce a burst of ATP by rapid glycolysis, which in turn might block the mitochondrial ATP productions, e.g. O_2-uptake. When experiments were repeated with fuel-supplemented ACSF, the O_2-consumption was still reduced in response to glucose addition, but in a smaller extent. The biochemical explanation of the phenomenon needs further experiments.

During differentiation, however, the oxygen consumption and metabolite requirements of developing neural cells changed. Results obtained on viability, O_2-consumption and extracellular acidification of distinct neural stem cell lines demonstrated that different neural stem/progenitor populations and also their differentiating progenies display specific, cell-type and developmental stage-dependent demands for survival.

Cell motility studies also indicated important shifts in responses to cation channel opening with differentiation. For this studies channelrhodopsin expressing (RGl^{ChR+}) and non-expressing (RGl^{ChR-}) sister-cells were used, both capable for neuron-production (Fig. 6.).

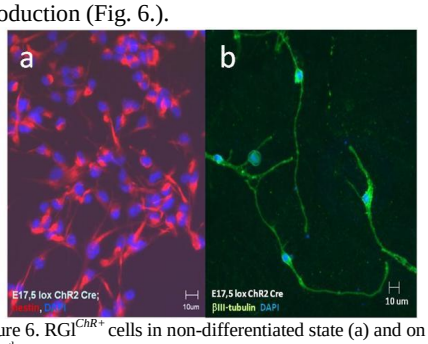

Figure 6. RGl^{ChR+} cells in non-differentiated state (a) and on the 7th day of neuronal differentiation (picture was taken by Tímea Kőhídi)

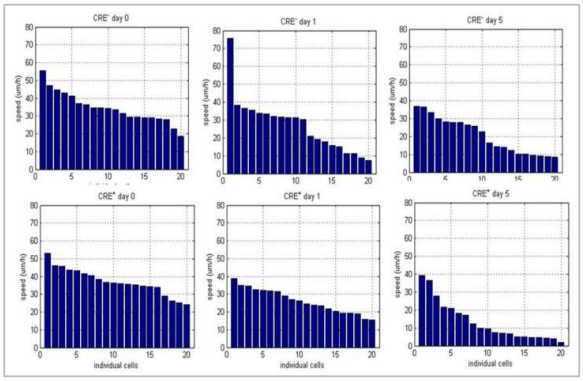

Figure 7. The average speed of translocation of cell-centers in cultures of RGl^{ChR-} (upper pictures) and RGl^{ChR+} (lower pictures) cells on the zero, 1st and 5th day of neuronal differentiation.

Analyses of cell motility demonstrated that opening of light-gated cation channels did not affect the motility of non-induced cells, while reduced significantly the move of differentiating neurons (Fig. 7.).

There was no significant difference between the motility of non-induced (day 0) RGl^{ChR-} and RGl^{ChR+} cells, both showing a migratory phenotype (moving in average about 100μm a day). There was still no difference in the motility between the two groups after one day of EGF-withdrawal: cells with shorter migratory routes (50-100 mm or even less) appeared in both populations. After five days of EGF-withdrawal, however, the proportion of non-motile cells increased and the lengths of migratory routes decreased significantly in the RGl^{ChR+} cells compared to the RGl^{ChR-} group.

ACKNOWLEDGMENTS

I want to thank the support and guidance to my supervisior, Prof. Emília Madarász.

I would like to thank Prof. László Tretter for providing assay opportunities, theoretical and technical help in metabolic assays. I thank Tímea Kőhídi for her basic help and work with RGl cells and cell motility studies. I thank Katalin Gaál for her excellent technical help.

REFERENCES

[1] Anita Zádori, Viktor Antal Ágoston, Kornél Demeter, Nóra Hádinger, Linda Várady, Tímea Kőhídi, Anna Göbl, Zoltán Nagy, Emília Madarász, "Survival and differentiation of neuroectodermal cells with stem cell properties at different oxygen levels"; Experimental Neurology, vol. 227, pp. 136–148, 2011

[2] Katalin Schlett and Emília Madarász, "Retinoic Acid Induced Neural Differentiation in a Neuroectodermal Cell Line Immortalized by p53 Deficiency"; Journal of Neuroscience Research, vol. 47, pp. 405–415, 1997

[3] Attila Jády, Tünde Kovács, Renáta Bencsik, Szilamér Ferenczi, László Tretter, Emília Madarász: Diverse Fuel Requirements Of Different Neural Stem/Progenitor Populations: Changing Metabolic Routes With Neural Differentiation; 9th FENS Forum of Neuroscience (Federation of European Neuroscience Societies) 05-09.07.2014, Milan, Italy (poster)

[4] Károly Markó, Tímea Kőhídi, Nóra Hádinger,Márta Jelitai, Gábor Mező, Emília Madarász, "Isolation of radial glia-like neural stem cells from fetal and adult mouse forebrain via selective adhesion to a novel adhesive peptide-conjugate"; PLoS One (6) e28538, 2011

[5] Tímea Kőhidi, Attila Jády, Noémi Papp, Károly Markó, Zsuzsanna Környei, Tibor Andrási, Emília Madarász; Effects of optogenetic stimulation on motility of differentiating neural stem cells; 15th Biannual Conference of the Hungarian Neuroscience Society 22-23.01.2015; Budapest (poster)

[6] K. Markó, M. Ligeti, G. Mező, N. Mihala, E. Kutnyánszky, É. Kiss, F. Hudecz, and E. Madarász, A Novel Synthetic Peptide Polymer with Cyclic RGD Motifs Supports Serum-Free Attachment of Anchorage-Dependent Cells, Bioconjugate Chemistry, vol. 19, no. 9, pp. 1757–1766, Sep. 2008.

Modelling horizontal gene transfer in bacterial communities

János JUHÁSZ
(Supervisor: Sándor PONGOR)
Pázmány Péter Catholic University, Faculty of Information Technology and Bionics
50/a Práter street, 1083 Budapest, Hungary
janos.juhasz@itk.ppke.hu

***Abstract*- Multispecies bacterial communities for example the microbiota of the gastrointestinal tract can be remarkably stable and resilient even though they consist of cells and species that compete for resources and produce a large number of antimicrobial agents. Computational modelling suggests that horizontal transfer of resistance genes may greatly contribute to the formation of stable and diverse communities. These communities are capable of protecting themselves with antimicrobial agents while preserving a varied metabolic repertoire of the constituent species. In other words, horizontal gene transfer of resistance genes makes a community compatible in terms of exoproducts and capable to maintain a diverse metagenome. The same property may allow microbiota to protect its host organism, or if used as a microbial therapy, to purge pathogens and restore a protective environment.**

***Keywords*- horizontal gene transfer; antibiotic resistance; agent-based model; microbiome formation; self defence; microbial therapy**

I. INTRODUCTION

Multispecies microbial communities are a major form of life that can coexist with many other organisms. It is well known that the human body carries 10 times more microbial cells than human cells. One of the many properties of microbial communities is that they can protect their host organism against infections or colonisation of pathogens [1][2]. Little is known about the mechanism of such territorial defence. One of our goals is to understand if horizontal gene transfer can contribute to the emergence of protective properties in microbial communities like the human gut microbiota.

Horizontal gene transfer (HGT) is the process by which bacteria acquire genetic material from neighbouring cells [3]. Nowadays it is considered the key to many important processes such as the spreading of antibiotic resistance genes [4][5][6]. Dense microbial communities for example the gut microbiota are now considered a hot spot for HGT [7]. Microbial evolution is believed to be the major factor of forming the community structure of microbial consortia [8][9]. The spreading of resistance genes is interesting, because members of microbial communities have to be resistant or tolerant to many exoproducts of other species in the community. One of the mechanisms that can explain their shield against antimicrobial factors is their natural tolerance toward various chemicals, but the spread of specific resistance genes is also a plausible mechanism that could explain the formation of mutual resistance in multispecies communities. We hypothesize that the mutual resistance toward the antimicrobial factors of the consortia is a key factor for forming a stable and divers community. One of our goals is to follow the build-up of this property via computer simulations of HGT between coexisting bacterial species.

Competition between bacteria can lead to collapse of the community or to stable coexistence [10][11]. This competition can be realized by antimicrobial factors that the bacterial cells produce against other species [12]. We are interested in how species coexisting in populated niches and become accustomed to each other and forming a community that is resistant against newcomers.

The model below shows that simple computational agents can take over resistance genes from their neighbours, and can form diverse communities that both produce and resistant to a large number of antimicrobial factors. The community is capable of keeping invader species away with this complex antimicrobial profile. On the other hand complex microbial consortia are also capable of populating and environment dominated by a single highly resistant species, which phenomenon is used in microbial transplantation [13].

II. THE MODEL

The formation of multispecies microbial communities was simulated with computational agents that represented the cells. In the model the agents move and take up genes randomly from the agents within a certain distance. The cells have randomly generated genomes with two types of genes. The type encodes antimicrobial factors (AM) that can kill susceptible bacteria. The other type of genes encodes specific resistance against one specific AM. The rest of the genome is not represented. The agents are also naturally tolerant to a predefined number of AMs, this number is called the survival threshold. The agents move randomly on a circular 2D surface (representing a Petri dish) and take up resistance genes from their immediate neighbours via horizontal gene transfer (HGT). We assumed that the transfer of genes responsible for the AM production takes longer time than our simulations, so only the resistance genes are exchanged. As a result the pool of resistance genes became homogenous, so all species contains the same resistance genes while they produce a different set AMs.

For community evolution experiments, a given number of "naive" or starting agents were created first. The naive agents carried an equal number of randomly chosen AM production genes and their matching resistance genes. As a result, these agents represented different species with their different genomes. The cells were placed randomly on the surface and

J. JUHÁSZ, "Modelling horizontal gene transfer in bacterial communities" in *PhD Proceedings Annual Issues of the Doctoral School, Faculty of Information Technology and Bionics, Pázmány Péter Catholic University – 2015.* G. Prószéky, P. Szolgay Eds. Budapest: Pázmány University ePress, 2015, pp 53– 56.

started their life circle which contained random movement, horizontal gene transfer, division and/or extinction. Simulation was left to proceed until no more HGT occurred in the community.

III. RESULTS

A. *Community genotypes*

During the simulations we monitored the number of species, the number of AM and the number of resistances produced. It became apparent that the formation of a diverse community was primarily determined by the following parameters: the speed of HGT, the level of non specific and the number of contacts made by the agents which is determined by the density of population and/or the speed of random movement. I mapped the parameter space in a grid-like fashion. This experiment required a large number of simulations, each of the resulting in a final distribution of species and genomes. I carried out preliminary experiments in order to identify the simulation outcomes. Two main outcomes were observed (Figure 1):

Diverse community (A in Figure 1). In this case the agents form a homogenous, mixed population typically consisting about 20 species that produce about 100 AMs. Every species produce only a few AM, but resistant to all AMs appearing within the community. This outcome is analogous with the formation of a healthy and stable microbial community, relatively large number of AM are produced in the community and each species contains large number of resistance genes.

No diversity (B in Figure 1). This outcome is close to monoclonal community; as only one of the species survives the others die out. This scenario is observed when the initial conditions do not allow HGT to take place, so only the starting genome of the sole surviving species remains.

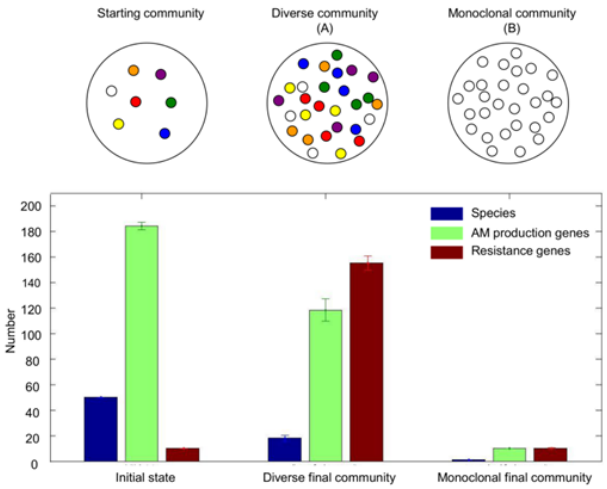

Fig. 1. Composition of the model communities. If horizontal gen transfer is possible, the starting community (left) can evolve to a diverse community (A), in which a substantial part of the starting clones are preserved. If horizontal gene transfer is not effective, a non-diverse, "monoclonal" community will form (B), with essentially one clone. The numbers in the diagram represent the average; the error bars the standard deviation, respectively, calculated from 100 simulations.

B. *Factors governing community evolution*

In order to identify the conditions those are needed for the formation of diverse and strong communities producing large number of antimicrobials, a large number of simulations were carried out with systematically varied parameters which were the rate of HGT, the natural tolerance threshold, and the strength of each species (number of produced AMs). In Figure 2, the blue areas represent the parameter combinations where HGT is not effective or the species produce more AM than they can tolerate (this results the diagonal division). Diverse communities cannot form there; descendants of one species can be found (monoclonal community). On the other hand, the results in Figure 2 show that diverse communities can form under a large variety of parameter combinations. Community strength (expressed number of AM producing and resistance genes) depends on the rate of HGT i.e. strong communities that produce many AMs form if HGT is intensive during the maturation process. This can be seen on B in Figure 2 as an increase of the red area toward higher HGT values. Strong species form less diverse communities, even though the community perform large number of AMs. Weak species form diverse community easily but they do not produce many AMs. In this model the metabolic properties of the species are not represented explicitly, so metabolic capability of the community is measured through the diversity of species. As a result an optimal bacterial community with wide metabolic capability and multiple AM production appears at intermediate strength values, so superbugs are not team players in this model.

C. *Territorial defence*

Invasion was modelled with naive and mature communities. To a community of 50 agents 25 "invader" agent were added from one species in which the species strength (the number of AM and resistance genes) changed from experiment to experiment (Table 1). I found that a naive community could be easily taken over by the invader

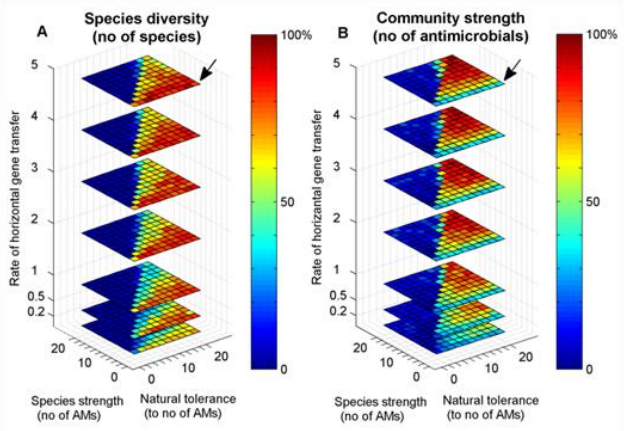

Fig. 2. Strength and diversity of the community depends on the rate of HGT and the properties of individual species: number of AM produced and the natural tolerance to AMs. HGT promotes community strength (top vs. bottom planes). Species carrying few AM genes can form diverse, but weaker community (black arrows).

TABLE 1.

TERRITORIAL DEFENCE: VULNERABILITY OF NAIVE AND MATURE COMMUNITIES TO AN INVADING SPECIES PRODUCING VARYING NUMBER OF ANTIMICROBIAL FACTORS.

	Community 1 (invader)[3]				**Community 2: naive (resident)[1,3]**	**Community 2: mature (resident)[2,3]**
	#cells	*#species*	*#AFs*	*#resistances*	*% of survivors[3]:*	*% of survivors[3]:*
1	25	1	10	10	25	100
2	25	1	20	20	0	100
3	25	1	50	50	0	100
4	25	1	75	75	0	90
5	25	1	100	100	0	53
6	25	1	125	125	0	17
7	25	1	150	150	0	3

[1.] Naive community: 50 cells, corresponding to 50 species harbouring a total of 181 AM production genes, and the same number of resistance genes.
[2.] Mature community: 50 cells, corresponding to 15 species harbouring a total of 109 AM genes and180 resistance genes on the average.
[3.] All numbers indicate the average of 100 experiments.

TABLE 2.

MICROBIAL THERAPY: PURGING A PATHOGEN WITH A TRANSPLANT OF A MATURE MICROBIAL COMMUNITY

	Community 1 (transplant)[1]				**Community 2: single pathogen species (resident)[1,2]**			
	#cells	*#species*	*#AFs*	*#resistances*	*#cells*	*#AFs*	*#resistances*	*% survivors*
1	25	10	81	180	25	20	20	0
2	25	10	81	180	25	20	50	0
3	25	10	81	180	25	20	75	0
4	25	10	81	180	25	20	100	0
5	25	10	81	180	25	20	125	2
6	25	10	81	180	25	20	150	27

[1.] Mature community.
[2.] All numbers indicate the average of 100 experiments.

population, while the mature community eliminated the invaders. Only highly resistant "superbugs" (rows 4-7-in Table 1) could grow in this case. The results show that a mature community is likely to be more resistant to external attacks than a naive community in which the species are not acclimatized to the AMs of each other.

D. Microbial therapy

An opposite scenario is where a highly resistant population of a single species populates an environmental niche, and a multi-species invader consortium appears in the niche. This is a biologically relevant scenario and a suitable model for the infections caused by an antibiotic resistant opportunistic pathogen such as *Clostridium difficile*. Cleaning multi-resistant pathogens from host organism is a serious problem. Antibiotics used in infections or following surgery usually do not harm them while they can wipe out the healthy microbiota weakened by the antibiotic treatment. This is because many of the opportunistic pathogens are spore-formers. The spores survive the antibiotic treatment after which the microbiota will have to grow back in the presence of a relatively higher *C. difficile* level. The result is a disordered, unbalanced community which cannot fulfil its biological roles. Our model predicts that once a community forms, its composition will not change by itself, so a disordered community will not necessarily revert to its original, healthy state after antibiotic treatment [14]. Microbiome transplantation i.e. treating a dysbiotic microbiota with a healthy microbial community seems to be a promising avenue according to our model and may be relevant treatment of recurring *C. difficile* infections [13].

In order to simulate this situation a series of resident virtual pathogens were constructed, that contained varying number of AM production genes and their resistance genes. They represented the strong, multi-resistant monoclonal dysbiotic population and they were treated with a mature community of cell agents, which contained fewer genes individually than the pathogen, but where the overall community produced a large number of AMs. The results in table 2 show that the pathogen could be purged out under certain conditions, unless it contained an unusually high number of resistance genes (rows 5-6 in Table 2).

E. Limitations of the model

According to our models, superbugs (agents with large number of AM and resistance genes) can always invade mature communities. However the model does not show how resistant a superbug needs to be to achieve it. Second, the model parameters are symbolic values and the results should be interpreted only as a general indication of superbugs being dangerous, and not saying about anything the existence of such superbugs in natural communities. Producing AMs and materials of AM resistance could require large amount of energy from the cells, which would decrease their overall fitness in the community. Currently the model does not contain a metabolic component or competition on resources, only deals with AMs and resistances, consequently the metabolic burden of antibiotic resistance is not included.

IV. DISCUSSION

In this work a contact-based computational model of HGT were introduced in which random moving computational agents can acquire resistance genes from their neighbours. The simulations suggest that HGT can facilitate the formation of resistant communities that protect themselves by antimicrobial factors. Such mature communities are difficult to invade by pathogens from outside environment. Their collective territorial defence protects them and their host organism. An implant of such microbiota may be capable of purging a monoclonal pathogen from an environmental niche. In other words, the presence of a large number of antimicrobial agents may be crucial for the collective defence and stability of natural microbial communities by keeping invaders away. Another implicit suggestion of the model is that HGT helps a community preserve its diverse metabolic repertoire via the presence of multiple species. Based on these findings, HGT can be suggested as a viable target to study experimentally with respect to the stability of multi-species microbial

consortia and their resistance profile. Such investigations can be highly relevant in developing treatments for intractable infections that are resistant to multiple anti-microbial therapies.

Parts of this work was published in [15].

ACKNOWLEDGEMENT

This project was developed in the Faculty of Information Technology and Bionics, Pázmány Péter Catholic University, Budapest. Thanks are due to my supervisor, Prof. Sándor Pongor and to Attila Kertész-Farkas (ICGEB, Trieste), who was the first developer of the agent-based simulation program.

REFERENCES

[1] B. Stecher and W.-D. Hardt, "The role of microbiota in infectious disease.," *Trends Microbiol.*, vol. 16, no. 3, pp. 107–14, Mar. 2008.

[2] B. P. Willing, S. L. Russell, and B. B. Finlay, "Shifting the balance: antibiotic effects on host-microbiota mutualism.," *Nat. Rev. Microbiol.*, vol. 9, no. 4, pp. 233–43, Apr. 2011.

[3] M. P. Francino, *Horizontal Gene Transfer in Microorganisms.* Norfolk, UK: Caister Academic Press, 2012, p. 202.

[4] T. Akiba, K. Koyama, Y. Ishiki, S. Kimura, and T. Fukushima, "On the mechanism of the development of multiple-drug-resistant clones of Shigella.," *Jpn J Microniol*, vol. 4, pp. 219–227, 1960.

[5] E. V Koonin, K. S. Makarova, and L. Aravind, "Horizontal gene transfer in prokaryotes: quantification and classification.," *Annu Rev Microbiol*, vol. 55, pp. 709–742, 2001.

[6] E. V Koonin and Y. I. Wolf, "Evolution of microbes and viruses: a paradigm shift in evolutionary biology?," *Front. Cell. Infect. Microbiol.*, vol. 2, no. September, p. 119, Jan. 2012.

[7] L. Liu, X. Chen, G. Skogerbo, P. Zhang, and R. Chen, "The human microbiome: a hot spot of microbial horizontal gene transfer.," *Genomics*, vol. 100, pp. 265–270, 2012.

[8] T. W. Schoener, "The newest synthesis: understanding the interplay of evolutionary and ecological dynamics.," *Science*, vol. 331, pp. 426–429, Jan. 2011.

[9] J. N. Thompson, "The coevolving web of life.," *Am. Nat.*, vol. 173, pp. 125–140, 2009.

[10] V. Venturi, A. Kerenyi, B. Reiz, D. Bihary, and S. Pongor, "Locality versus globality in bacterial signalling: can local communication stabilize bacterial communities?," *Biol. Direct*, vol. 5, p. 30, 2010.

[11] Á. Kerényi, D. Bihary, V. Venturi, and S. Pongor, "Stability of Multispecies Bacterial Communities: Signaling Networks May Stabilize Microbiomes," *PLoS One*, vol. 8, no. 3, p. e57947, Mar. 2013.

[12] A. Bryskier, Ed., *Antimicrobial Agents: Antibacterials and Antifungals.* Washington DC: American Society of Microbiology Press., 2005.

[13] A. Vrieze, P. F. de Groot, R. S. Kootte, M. Knaapen, E. van Nood, and M. Nieuwdorp, "Fecal transplant: a safe and sustainable clinical therapy for restoring intestinal microbial balance in human disease?," *Best Pract. Res. Clin. Gastroenterol.*, vol. 27, no. 1, pp. 127–37, Feb. 2013.

[14] V. Bucci, S. Bradde, G. Biroli, and J. B. Xavier, "Social interaction, noise and antibiotic-mediated switches in the intestinal microbiota.," *PLoS Comput. Biol.*, vol. 8, no. 4, p. e1002497, Jan. 2012.

[15] J. Juhász, A. Kertész-Farkas, D. Szabó, and S. Pongor, "Emergence of collective territorial defense in bacterial communities: horizontal gene transfer can stabilize microbiomes.," *PLoS One*, vol. 9, no. 4, p. e95511, Jan. 2014.

Investigation of the role of GABAergic inhibition in epileptic human neocortex

Ágnes KANDRÁCS
(Supervisor: István ULBERT)
Pázmány Péter Catholic University, Faculty of Information Technology and Bionics
50/a Práter street, 1083 Budapest, Hungary
agnes.kandracs@gmail.com

***Abstract*—Bicuculline is a competitive antagonist of the gamma-aminobutyric acid A receptor. By using this agent we have investigated the effect of the blockade of GABAergic inhibition in human neocortical tissue resected from patients with focal epilepsy or patients with tumour but without epilepsy. Local field potential gradient (LFPg) recordings were obtained from postoperative tissues by 24 channel laminar multielectrodes. Current source density (CSD) and multiple unit activity (MUA) were calculated, furthermore time-frequency analysis was performed in order to observe high-frequency oscillations (HFO).**

We have detected bicuculline events in 67% of slices from epileptic and in 42% of slices from tumour patients where the frequency of occurrence was 0,12±0,15 Hz and 0,09±0,11 Hz, respectively. These events can be characterized by a high-amplitude LFPg peak (128,01±86,14 μV in epileptic and 110,07±77,61 μV in non-epileptic tissue) with a duration of 348±73,28 ms in epileptic and 326±95,55 ms in tumour patients. MUA and HFO, included both ripples and fast-ripples, have been observed during this activity in all cases.

Our results show that there are similarities in the features of bicuculline events in epileptic and non-epileptic patients, although further investigation is needed to clarify the role of GABAerg inhibition in epileptic processes.

***Keywords*-human, electrophysiology; epilepsy; inhibtion; bicuculline; population activity; local field potential**

I. Introduction

65 million people worldwide currently live with epilepsy [7]. In the case of the failure of medical treatment in patients with focal epilepsy, the resection of the epileptogenic zone can provide a solution [1].

Postoperative neocortical tissue is able to generate spontaneous synchronous population activity (SPA) in vitro. The SPA consists of a fast, high-amplitude local field potential gradient (LFPg) transient followed by a slower, long lasting wave. During this event increased multiple unit activity (MUA) and high frequency oscillation have been observed. This phenomenon is considered to be the result of excitatory and inhibitory network mechanisms [2][3][4]. Our preliminary data show that not only epileptic neocortical tissue is capable of generating SPAs. Postoperative neocortical tissue from patient with tumour but without epilepsy has been used as control.

The gamma-aminobutyric acid A ($GABA_A$) receptor antagonist Bicuculline is largely used to induce epileptiform (interictal-like) activity in animal cortical tissue [5][6]. By using this agent we investigated the effect of the blockade of GABAergic inhibition in human neocortical tissue resected from patients with focal epilepsy or with tumour but without epilepsy. A special attention was paid to the changes in the population activity during the whole process.

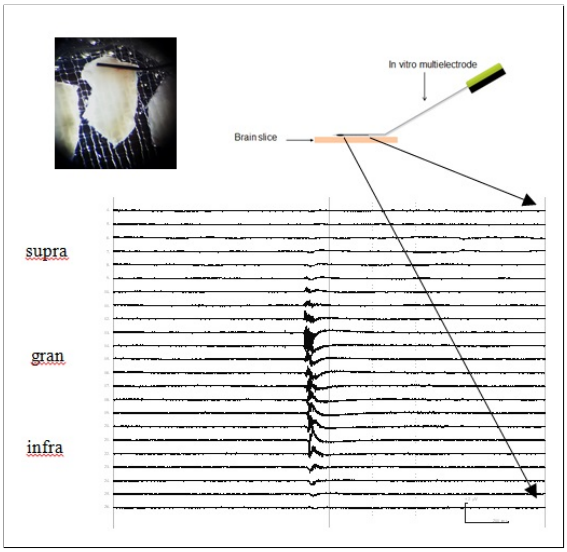

Fig. 1. Positioning of 24 channel laminar multielectrode on neocortical slices.

II. Methods

Postoperative neocortical tissue resected from epileptic (n = 10) and tumour (n = 6) patients have been investigated. Slices of 500 μm thickness were cut in cold sucrose solution with a vibratome. LFPg recordings have been performed in an interface chamber while slices were being perfused with oxygenated artificial cerebrospinal fluid (ACSF) on body temperature (35-37 °C). 24 channel laminar multielectrode has been placed on the tissue perpendicularly to the brain surface. So that, ch. 1-9 covered the supragranular layer, ch. 10-12 covered the granular layer and ch. 13-23 covered the infragranular layer of the neocortex (figure 1). On active slices (epileptic: n = 15, tumour: n = 12) 20 μM Bicuculline bath was applied.

Á. KANDRÁCS, "Investigation of the role of GABAergic inhibition in epileptic human neocortex" in *PhD Proceedings Annual Issues of the Doctoral School, Faculty of Information Technology and Bionics, Pázmány Péter Catholic University – 2015.* G. Prószéky, P. Szolgay Eds. Budapest: Pázmány University ePress, 2015, pp 57– 60.

Population activity detection and high frequency oscillation examination were performed by home written routines for Matlab, then LFPg, MUA and power-source density (CSD) were analyzed by using Neuroscan Edit 4.5. In case of tumour patients, the absence of epilepsy has been testified by scalp EEG recordings. Tumour patients with epileptic seizure(s) were excluded from this study.

III. Results

A. Characterization of Bicuculline induced interictal-like activity

We examined 15 slices from 10 epileptic patients and 12 slices from 6 tumour patients. Patients with tumour and at least one epileptic seizure have been excluded from this study. 10 epileptic slices generated at least one Bicuculline induced interictal-like activity, 3 slices shown only simple cell activity and 2 of them were non-active. From tumour patients 5 slices could generate interictal-like activity, 6 slices shown simple cell activity and 1 of them seemed dead. As a result the $GABA_A$ receptor antagonist Bicuculline could induce interictal-like activity in 77% of active slices in epileptic patients and in 45% of active slices in tumour patients.

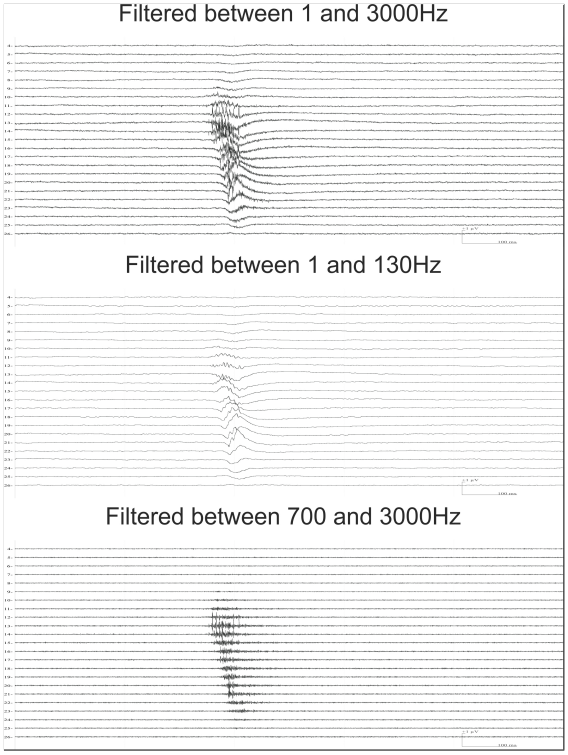

Fig. 2. Characterization of Bicuculline induced interictal-like activity: a slow transient with high amplitude and the superimposed multiple unit activity.

The obtained LFPg had similar properties to SPAs in epileptic and in tumour slices. That is, recordings filtered between 1 and 130 Hz showed a long lasting slow wave with high amplitude, while using band-pass filter between 700 and 3000 Hz revealed superimposed MUA in both cases (figure 2). CSD analyses showed that Bicuculline induced events are results of local currents.

The properties of Bicuculline induced interictal-like activities in slices from epileptic and tumour patients showed slight differences.

- Average recurrence frequencies of Bicuculline induced events in epileptic and tumour patients were 0,12±0,15 Hz and 0,09±0,11 Hz, respectively.
- Average amplitudes of LFPg peaks were 128,01±86,14 μV in epileptic slices and 110,07±77,61 μV in tumour slices.
- Average MUA amplitude of 11,49±8,94 μV have been observed during Bicuculline induced events in epileptic slices, while the average MUA amplitude was 20,15±9,05 μV in tumour slices.
- Average durations of Bicuculline induced events were 348±73,28 ms in epileptic and 326±95,55 ms in tumour patients.

B. Different types of Bicuculline induced interictal-like activity

Bicuculline induced events have been classified by different properties. On the basis of location in neocortex, 5 types of events have been observed in epileptic tissue: in entire neocortex (n=5), in supragranular-granular layer (n=2), in granular-infragranular layer (n=1), in supragranular layer (n=1) and in infragranular layer (n=2). In tumour tissue 2 types of events have been observed: in entire neocortex (n=5) and in supragranular layer (n=1). On the basis of recurrence, 2 types of events have been revealed: recurrent (n=9 in epileptic and n=5 in tumour slices) and single event during 1-1,5 hour phase (n=2 in epileptic and n=1 in tumour slices). Single events only occurred once during the whole experiment while recurrent events returned periodically. We have observed complex (n=5) and simple (n=6) events in epileptic tissue. Only simple events have appeared in tumour tissue (n=6). Simple event means SPA-like activity with one clear peak while during complex events multiple waves appeared sometimes in different layers of the neocortex. Cells showed distinct behavior in some cases: during 6 epileptic events and during 2 tumour events they had a long lasting (seizure-like) burst phase. In 5 epileptic and 4 tumour slices there was no change in cellular activity.

C. Comparison between spontaneous population activity and Bicuculline-induced interictal-like activity

Applying 20 μM bath on active slices with SPA we have investigated the effect of GABAergic inhibition in epileptic and tumour tissue. As a result SPA disappeared and in some cases (n=8) interical-like activity turned up (figure 3). SPAs had more than $\sim$40 times higher (SPA/Bic=42,92) average recurrence frequency than Bicuculline induced events on the

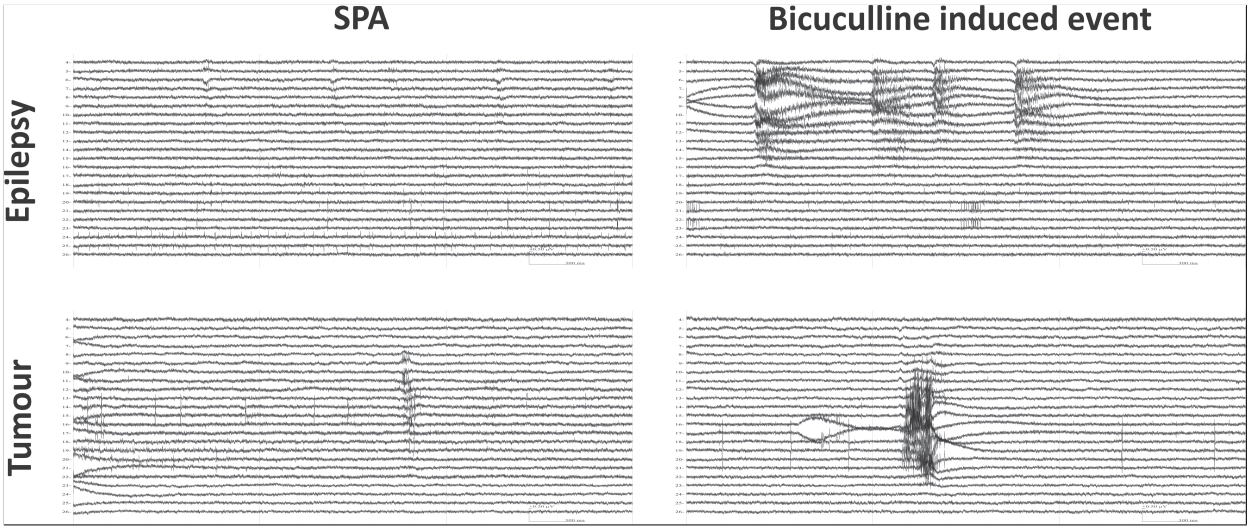

Fig. 3. Spontaneous population activity versus Bicuculline induced event in epileptic and tumour patients.

same epileptic spot while SPAs had more than ∼100 times higher (SPA/Bic=108,86) average recurrence frequency than interictal-like activity on the same spot in tumour slice. In the same time Bicuculline induced events had ∼8 times higher average LFPg amplitude (Bic/SPA=8,14) in epileptic and ∼4 times higher average LFPg amplitude (Bic/SPA=3,86) in tumour patients than SPAs on the same spot. Finally the average MUA amplitude in the peak of interictal-like activity was ∼15 times higher than in the peak of SPA (Bic/SPA=15) in epileptic tissue, while the same value was ∼2 (Bic/SPA=1,91) in tumour tissue.

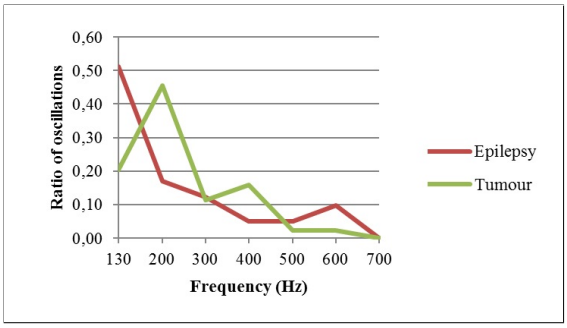

Fig. 4. Typical frequency ranges of high frequency oscillations during Bicuculline induced interictal-like activity in epileptic and tumour tissue.

D. Time-frequency analysis

We have performed time-frequency analysis of Bicuculline induced interictal-like activity in both epileptic and tumour cases. The typical frequency range of high frequency oscillations during Bicuculline induced interictal-like activtiy can be seen in Figure 4. There is a global maxima at 130 Hz (more than half of cases) as well as we can see a local maximum around 600 Hz. The typical frequency range in tumour tissue is around 200 Hz (almost the half of cases) furthermore a local maximum is visible around 400 Hz.

IV. Conclusions

The blockade of GABAergic inhibition by applying Bicuculline results interictal-like activity in vitro in human neocortical tissue resected from patients with epilepsy (77%) or patients with tumour but without epilepsy (45%). Bicuculline induced events can be characterized by a long lasting slow wave with superimposed multiple unit activity and high frequency oscillation.

Applying Bicuculline on slices with spontaneous population activity blocks SPA and can induce interictal-like events with lower recurrence frequencies but with higher local field potential gradient and multiple unit activity amplitudes.

Bicuculline induced interictal-like activities are similar in epileptic and non-epileptic tissue, but the average recurrence frequency, the average amplitude of local field potential gradient and the average duration is higher in epileptic slices, while the average amplitude of multiple unit activity is higher in tumour slices. Lower MUA intensity in tissue from patient with epilepsy can be the result of epileptic cell death, while higher LFPg and duration can show the effect of network reorganization.

Typical frequency ranges of high frequency oscillations in epileptic tissue are around 130 Hz and around 600 Hz while these values are around 200 Hz and around 400 Hz in tumour tissue. High frequency oscillations in the fast ripple frequency range can be characteristic feature of epilepsy.

In summary, our results show that the network properties of interitctal-like events induced by Bicuculline show slight differences in epileptic and non-epileptic patients, although further investigation is needed to clarify the role of GABAergic inhibition in epileptic processes.

ACKNOWLEDGEMENT

The author would like to thank Lucia Wittner and István Ulbert for supervision as well as Kinga Tóth and Katharina Hofer for collaboration and advice.

REFERENCES

[1] J. Janszky and A. Szűcs, "Az epilepsziás rohamok diagnózisa és kezelése, " *Hippocrate: Neurológia*, pp.104-109, March-April, 2002.

[2] R. Köhling, A. Lücke, H. Straub, E. J. Speckmann, I. Tuxhorn, P. Wolf, H. Pannek, and F. Oppel, "Spontaneous sharp waves in human neocortical slices excised from epileptic patients," *Brain*, vol. 121, pp. 1073-1087, 1998.

[3] Á. Kandrács, "Humán agyi elektromos tevékenység vizsgálata in vitro körülmények között, " B. S. thesis, Pázmány Péter Catholic University Faculty of Information Technology and Bionics, Budapest, Hungary, 2012

[4] Á. Kandrács, "Az operáció során eltávolított humán epilepsziás neocortex elektrofiziolgiai jeleinek szoftveres analízise, " M. S. thesis, Pázmány Péter Catholic University Faculty of Information Technology and Bionics, Budapest, Hungary, 2014

[5] A. Bragin, I. Mody, C. L. Wilson and J. Engel Jr., "Local Generation of Fast Ripples in Epileptic Brain, " *The Journal of Neuroscience*, vol. 22, no. 5, pp. 2012-2021, March 2002

[6] G. A. R. Johnston, "Review: Advantages of an antagonist: bicuculline and other GABA antagonists," *British Journal of Pharmacology*, vol. 169, pp. 328-336, 2013

[7] A. T. B. David J. Thurman, Ettore Beghi, Charles E. Begley, W. A. H. Jeffrey R. Buchhalter, Ding Ding, Dale C. Hesdorffer, K. L. Lewis Kazis, Rosemarie Kobau, Barbara Kroner, David Labiner, K. P. Giancarlo Logroscino, Marco T. Medina, Charles R. Newton, A. S. Angelia Paschal, Pierre-Marie Preux, Josemir W. Sander, T. T. William Theodore, and S. Wiebe, "Standards for epidemiologic studies and surveillance of epilepsy," *Epilepsia*, vol. 52, pp. 226, 2011

Intrinsic disorder in proteins of the central nervous system

Annamária KISS-TÓTH
Supervisor: Zoltán GÁSPÁRI
Pázmány Péter Catholic University, Faculty of Information Technology and Bionics
50/a Práter street, 1083 Budapest, Hungary
gaspari.zoltan@itk.ppke.hu

***Abstract*—Protein structure and function prediction is a great challenge in proteomics. Analyzing a protein's structural preferences, such as secondary structure and intrinsic disorder tendency is an important step towards determining its function.**

The aim of this study is to take a closer look at the secondary and tertiary structures of a set of proteins located in the central nervous system. These proteins were obtained from two sources: a previously published journal article pertaining *de novo* genes and their encoded *de novo* proteins and the Synaptome Database. An exhaustive bioinformatical analysis is performed to determine intrinsic disorder tendency, search for coiled-coil structures and transmembrane regions, and predict three-dimensional structures. Preliminary results show that the majority of the analyzed sequences contain only short disorder regions and coiled-coil structures, if any at all. Only a small part of the proteins is predicted to be mostly disordered. After further examination, a subset of these proteins will be selected in the future for more in-depth analysis.

***Keywords*-de novo protein, synaptic protein, structure prediction**

I. Introduction

Proteins in the central nervous system have a wide range of functions. They can serve as messengers, structural building blocks or take part in ion conduction. Some of these proteins are believed to have *de novo* origins. These so-called *de novo* proteins are a product of previously non-coding DNA sequences [1]. Finding *de novo* proteins is not easy. Recent research shows that approximately 75 percent of the human genome is transcribed in some stage of the cell cycle. The resulting non-coding RNAs become *de novo* genes and are suitable for protein coding if they are willing to change. These genes can be identified with comparative genome analysis. Gene prediction methods can identify all regions in a genome which are responsible for protein coding. If a coding region is identified in a genome which has no corresponding coding regions in evolutionary relatives, we can speak of a potential *de novo* protein.

What is the practical significance of these proteins? They are only present in small quantities in the body since the conversion of non-coding regions to coding is not an easy task. However, some non-coding regions become coding through gene mutation and part of the resulting proteins even manage to survive long term instead of destroying or being destroyed by the cells. These *de novo* proteins serve a purpose. Some of them have been linked to terminal diseases such as Alzheimers disease and cancer and thus identifying their structure and function is crucial [2].

Many of the central nervous system proteins reside and function in synapses. The synapse is essential to the function of the brain and may be an important source of dysfunction underlying many neuropsychiatric disorders. Consequently, it is an excellent candidate for large-scale genomic and proteomic study. Determining the secondary and tertiary structures of these proteins is the first step towards determining their function in the human body.

SynaptomeDB is a database which contains genes encoding the components of the synapse including neurotransmitters and their receptors, adhesion/cytoskeletal proteins, scaffold proteins, and transporters [3]. The contents of this database are constantly expanded manually, it currently holds almost 2000 sequences.

II. Methods

A. De novo proteins

24 *de novo* genes (previously described in literature) and the proteins encoded by them were obtained from the NCBI and Ensemble databases [4]. An extensive computational analysis was executed to obtain clues about the molecular function of at least some of them.

First, the *de novo* status of the described protein-coding genes was carefully re-checked. I performed a similarity search with BLAST algorithm on the de novo genes, the corresponding messenger RNAs, and the encoded proteins to find out if similar sequences occur in other species.

Second, various computational tools were applied for sequence analysis, structure- and function prediction. Intrinsic disorder tendency was examined with IUPred webserver [5]. Transmembrane regions and coiled-coil structures were identified in the sequences with the help of Phobius and Coils, respectively [6, 7]. Tertiary structure prediction was performed with I-TASSER (**Figure 1.**) [8]. I-TASSER is based on three-dimensional similarity search, and besides providing possible three-dimensional models, identifies a protein's closest known structural analogs as well. These analogs are not necessarily evolutionary relatives but their function might give a clue to the protein's function. The likelihood of acquiring valid structures for *de novo* proteins is slim.

A. KISS-TÓTH, "Intrinsic disorder in proteins of the central nervous system" in *PhD Proceedings Annual Issues of the Doctoral School, Faculty of Information Technology and Bionics, Pázmány Péter Catholic University – 2015.* G. Prószéky, P. Szolgay Eds. Budapest: Pázmány University ePress, 2015, pp 61– 63.

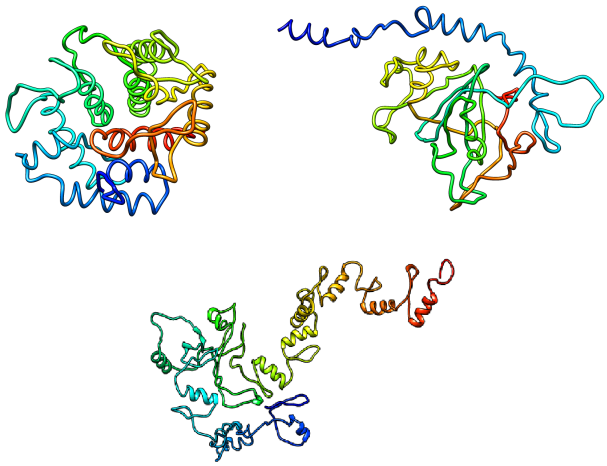

Fig. 1. Results of three-dimensional structure prediction with I-TASSER for 3 *de novo* proteins viewed in Chimera: *Myeloma-overexpressed gene protein* (Q96EZ4, top left), *Uncharacterized protein FLJ46757* (Q6ZR03, top right) and *epstein-barr virus-induced zinc finger protein* (AAD43569.1, bottom).

B. SynaptomeDB proteins

The gene IDs of the genes were obtained from the database and the Uniprot IDs of the corresponding proteins. This way a list of 1873 synaptic proteins was created. The entire content of Uniprot was downloaded and the FASTA sequences of these proteins were extracted with the help of a program written in Perl. Then, once again various sequence analysis tools were applied.

First, intrinsic disorder tendency was analyzed with 2 different disorder predictors, IUPred and RONN (**Figure 2.**) [9]. Applying the online servers would be too time-consuming for this many proteins, the predictor's outputs were processed with Perl. The minimum sequence length was set to 30, shorter disordered regions were discarded. The consensus of the prediction results was also calculated.

Second, coiled-coil structures were identified in the sequences with 2 different predictors, Coils and Paircoil, using Perl (**Figure 3.**) [10]. The consensus of the prediction results was also calculated.

III. Results

A. De novo proteins

Re-checking the *de novo* status of these genes brought unexpected results. I was unable to reproduce 1 of the 24 genes and its encoded protein. Furthermore, the I-TASSER prediction results and BLAST search for 1 *de novo* protein (*Epstein-barr virus-induced zinc finger protein*) indicate that it has homologs in such distant relatives as *Physeter catodon* (sperm whale). This effectively casts doubt on the genes de novo origin.

The coiled-coil search yields no results, none of the proteins possesses such structures. The transmembrane region search is somewhat more successful, in 3 individual cases a single transmembrane region was found.

With regards to the intrinsic disorder prediction and tertiary structure prediction, preliminary results show that many of these proteins possess a long intrinsically disordered segment and that in many cases even for the folded parts the predicted three-dimensional structures acquired with I-TASSER cannot be regarded as valid.

A few of the remaining sequences might be worth a closer look. Therefore, this subset of proteins has been selected for more in-depth analysis whose results will be detailed.

B. SynaptomeDB proteins

The computational analysis of the synaptic proteins proved to be more successful. Both the disorder prediction and coiled-coil search yielded more reliable results.

The results of the disorder prediction show that approximately 50 percent of these proteins showed no intrinsic disorder tendencies at all, meaning they have a fixed three-dimensional structure even without the binding of a ligand. The majority of the remaining sequences contain shorter disordered regions between 30 and 100 amino acid residues. The likelihood of finding at least one disordered section increases in longer proteins.

The numerical results of the coiled-coil search were similar. In more than 50 percent of these proteins, no such structures were found, and most of the remaining sequences only contain short coiled-coils less than 100 residues long. In some cases, a more significant portion of the protein takes up this form. Such an example is the *Coiled-coil domain-containing protein 22 (O60826)* with approximately 25 percent. In one case, the entire protein consists of only coiled-coils, this is *Tropomyosine beta chain (P07951)*.

At first glance, there is no obvious connection between a protein's disorder tendency and willingness to form coiled-coil structures. In many cases, a completely ordered protein contains several coiled-coils, or a partially disordered one has

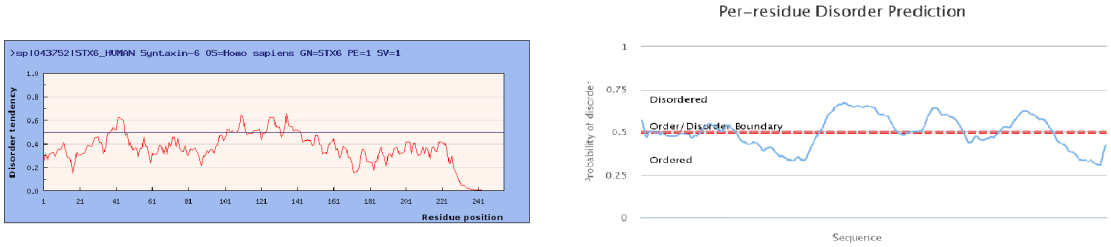

Fig. 2. Results of disorder prediction for *Syntaxin-6* protein (O43752) with IUPred (left) and RONN (right). The regions above the 0.5 line are considered disordered.

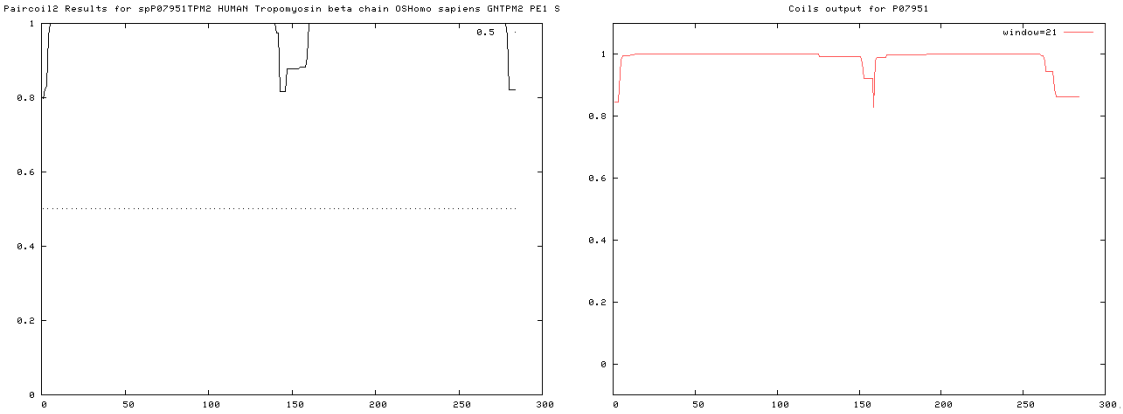

Fig. 3. Results of coiled-coil prediction for *Tropomyosine beta chain* (P09751) with Paircoil2 (left) and Coils (right). The regions above the 0.5 line are considered part of a coiled-coil form.

no coiled-coils at all. A possible correlation between the two requires further research.

IV. Conclusion and future plans

In case of the *de novo* proteins, ultimately very few reliable results were obtained. The similarity search-based bioinformatics tools often fell short in analyzing evolutionary unrelated proteins.

In case of the synaptic proteins, the relationship between the disorder prediction results and the coiled-coil prediction results will be further examined. A connection between the location of the ordered/disordered regions and coiled-coil regions might be possible.

Many proteins contained in SynaptomeDB are not only located in synapses. To extract the ones which specifically participate in synaptic processes, GO term filtering will be performed.

The synaptic protein sequences will also be explored with the use of several more bioinformatics tools such as HMMER to search for homolog protein sequences and sequence alignments.

Acknowledgment

The kind help of Zoltán Gáspári and my fellow PhD researchers is acknowledged for their expertise and helpful insights into my research and the creation of this manuscript.

References

[1] Diethard Tautz and Tomislav Domazet-Loso. The evolutionary origin of orphan genes. Nature Reviews Genetics (2011).
[2] Chuan-Yun Li et al. A human-specific de novo protein-coding gene associated with human brain functions. Computational biology (2011).
[3] Chen Xie, Yong E. Zhang Jia-Yu Chen, Chu-Jun Liu,3 Wei-Zhen Zhou,1 Ying Li,3 Mao Zhang,3 Rongli Zhang,Liping Wei, and Chuan-Yun Li. Hominoid-specific de novo protein-coding genes originating from long non-coding RNAs. PLoS Genet. 8(9): e1002942 (2012).
[4] Pirooznia M, Wang T, Avramopoulos D, Valle D, Thomas G, Huganir RL, Goes FS, Potash JB, Zandi PP. SynaptomeDB: an ontology-based knowledgebase for synaptic genes.Bioinformatics (2012).
[5] Zsuzsanna Dosztnyi, Veronika Csizmk, Pter Tompa and Istvn Simon. IUPred: web server for the prediction of intrinsically unstructured regions of proteins based on estimated energy content. Bioinformatics (2005) 21, 3433-3434.
[6] Lupas, A., Van Dyke, M., and Stock, J. Predicting Coiled-coils from protein sequences, Science 252:1162-1164 (1991).
[7] Lukas Kll, Anders Krogh and Erik L. L. Sonnhammer. A combined transmembrane topology and signal peptide prediction method. Journal of Molecular Biology, 338(5):1027-1036 (2004).
[8] Y Zhang. I-TASSER server for protein 3D structure prediction. BMC Bioinformatics, 9: 40 (2008).
[9] Yang, ZR, Thomson, R, McNeil, P, and Esnouf. RONN: the bio-basis function neural network technique applied to the detection of natively disordered regions in proteins. RM (2005).
[10] Bonnie Berger, David B. Wilson, Ethan Wolf, Theodore Tonchev, Mari Milla, and Peter S. Kim. Predicting coiled-coils by use of pairwise residue correlations, Proceedings of the National Academy of Science USA, vol 92, pp. 8259-8263 (1995).

Effects of body temperature on the occurrence and parameters of sleep spindles

Kinga KOCSIS
(Supervisor: István ULBERT)
Pázmány Péter Catholic University, Faculty of Information Technology and Bionics
50/a Práter street, 1083 Budapest, Hungary
kocsis.kinga@itk.ppke.hu

***Abstract*—It is important to understand the temperature dependence of cerebral electrical activity. This relation needs to be considered both as an experimental factor as well as a possible diagnostic and therapeutic tool. My present aim was to examine whether parameters of sleep spindle oscillations (7-15 Hz) are affected by different core body temperatures under urethane anesthesia in mice. Spindle frequency change is highly correlated with body temperature modification. At 39 °C, few or no sleep spindle was present, that is a putative consequence of an intense desynchronization and the shortening of synchronized periods of urethane anesthesia. These results are yet to be implemented in further experiments in order to exclude body temperature effect on the occurrence and variability of sleep spindle parameters.**

Keywords—sleep spindle oscillations; body temperature modification

I. INTRODUCTION

Physiological and pathological temperature changes of the brain can be derived from modified local metabolism, blood perfusion, function as well as from tissue damage [5]. Frequency distribution of the electroencephalogram (EEG) can be highly affected by even slight temperature changes, like those of the circadian rhythm or the menstrual cycle. Elevating body temperature is known to provoke higher frequencies in brain waves [4].

The relation between EEG frequencies and cortical temperature is similar to the temperature dependence of the Na/K channel [3]. Thus, a possibility arises that this latter is a limiting factor in determining EEG frequency. It is a well known fact that temperature has an effect on the velocity of biological processes [1, 15]. In case Q_{10} is 2.5, 1 °C change in cortical temperature is sufficient to shift EEG frequencies above 10 Hz with 1 Hz [3], so as the frequency of sleep spindle oscillations.

Our current knowledge on sleep spindles has been mainly acquired in human EEG studies. These oscillations are transient, 7-15 Hz, 1-3 sec long transient oscillations arising during slow-wave sleep stage II. and in superficial anesthesia. They have a putative role in memory consolidation [7], changes in their parameters and dynamics can be related to pathological brain states.

In humans, the proportion of EEG frequencies between 11.25 and 12.0 Hz was elevated, while the participance of the ones between 12.25 and 14.0 Hz was reduced by lowering brain temperature by 0.2 °C Hz [6]. During menstrual cycle, the biggest variance was measured in the sleep spindle frequency range. The proportion of higher spindle frequencies (14-15 Hz) was elevated by proximal (trunk and upper limb) heating in young adults and aged people without sleep disorders. In contrast, it was suppressed in aged people suffering from sleep disorders [10]. By lowering rectal temperature of children undergoing hypothermic bypass surgery, sleep spindle frequency of the patients was gradually reduced (0.54 ± 0.31 Hz/°C), while spindle length was elevated (0.69 ± 0.39 sec/°C). No correlation was found between the amplitude of spindles and temperature change. Although these results support previous data, age depandence and characteristics of modified spindle oscillations are yet to be established [11].

The praeoptic area (POA), the principal thermoregulatory region of the mammalian brain, is the putative brain region where sleep regulation is connected with thermoregulation. The firing rate of its thermosensitive neuron subpopulations is elevated at sleep induction. Although sleep can be induced by experimental heating of the POA, at the maximum daily brain temperature level sleep propensity is low. Thus, the key determining factor behind circadian sleep regulation is not the brain temperature. Sleep can be the most easily induced and sustained at minimal core temperature. However, circadian body temperature changes can be desynchronized from the sleep-wake cycle. According to [13], skin temperature may serve as a potential circadian rhythmic input signal to POA neurons as it shows inverse tendency to brain temperature values [14].

Thermoregulation can be highly inhibited during sleep [8]. In non-REM sleep, the proportion of cortical slow oscillations can be elevated by skin heating [10]. However, appropriate intensity, surface area, duration and timing of brain temperature elevation are crucial in order to provide better sleep quality. Sleep quality could be largely improved by a surface feedback control applied in resting place, especially in elderly people whose behavioural responses given to unfavorable temperature changes are reduced [10].

II. MATERIALS AND METHODS

A. Animal preparation

Acute extracellular electrophysiological recordings were performed in C57/BL6 mice (3♂ 1♀, 18-25 g). The animals were seduced with isoflurane, then urethane was administered intraperitoneally (1.5 g/kg). Craniotomy was made above the ventral posteromedial nucleus (VPM) of the thalamus [9]. Core body temperature was constantly monitored with a rectal

This work has been supported by the National Brain Research Program NAP-B (KTIA_NAP_13-2-2014-0016).

K. KOCSIS, "Effects of body temperature on the occurrence and parameters of sleep spindles" in *PhD Proceedings Annual Issues of the Doctoral School, Faculty of Information Technology and Bionics, Pázmány Péter Catholic University – 2015.* G. Prószéky, P. Szolgay Eds. Budapest: Pázmány University ePress, 2015, pp 65– 68.

thermometer and regulated with a heating pad. It was sustained at 37 °C during the stereotaxic surgery, and modified by 1 °C between each recording session. Electrophysiological signals were recorded in a maximum temperature shift of ±0.2-0.3 °C. Body temperature was modified in two directions in the physiological range (between 34 and 39 °C) in order to exclude the effect of changes in alertness.

B. Electrophysiological recordings

Reference electrode was inserted in neck muscles. Recordings were made with a 16-channel linear electrode with contacts 100 µm apart (NeuroNexus, Ann Arbor, MI, USA, Fig. 1.). Intan RHD2000 (Intan Technologies Llc., Los Angeles, CA) recording system was used (gain 1000, resolution 16 bit, sampling frequency 20 kS/sec).

By stimulating the receptive field (the whiskers of the mice), VPM was identified on the base of intense multi-unit activity (MUA). MUA measurements and audiomonitoring were done in parallel with the recording of the local field potential (LFP). The duration of each recording session was 20-30 minutes at a particular target body temperature.

C. Data analysis

MUA filtering (>500 Hz) and sleep spindle detection were performed on two channels with a custom-written Matlab program (Barthó, P.). The latter was achieved by smoothing, filtering (<15 Hz) the MUA signal and establishing a threshold. Automatic threshold detection was followed by manual refinement of spindle sorting. Spindle length, frequency, cycle number as well as the fast Fourier transformation based [2] Welch's power spectrum density distribution [16] and the spectrogram of each recording were calculated by custom-written Matlab programs. Spectral density was calculated from segments smoothened with a Hamming window to reduce noise ratio [12]. Spectrograms were given by calculating short-time Fourier-transforms, what provides high-resolution information about the changes of the frequency composition in time.

III. RESULTS

Mean spindle length and cycle number are shown to correlate with temperature change only in certain cases, strong negative effect on spindle length can only be seen in recording 3 (third panel in Fig. 3./A and 3./B).

Mean sleep spindle oscillation changes robustly along with core body temperature (Fig. 2., Fig. 3./C). There is a considerable difference between the frequency variance of spindles detected at the same temperature even in the same animal. For this reason, I summarized the frequency changes induced by ±1 °C temperature change for all measurements and animals. The positive effect of relative body temperature is shown to be significant (forth panel in Fig. 3./D, two-sample t-test, $p<0.05$).

Manually detected spindles with a frequency above 15 Hz need to be reconsidered (Fig. 2.). Although their shape and distribution are highly comparable to sleep spindles of the characteristic frequency range, it is necessary to reexamine their origin.

Frequency change of the 'slow oscillation' range (0-20 Hz) induced by temperature elevation is indicated by the rightward shift of the peaks in the frequency density spectrum (Fig. 4./A).

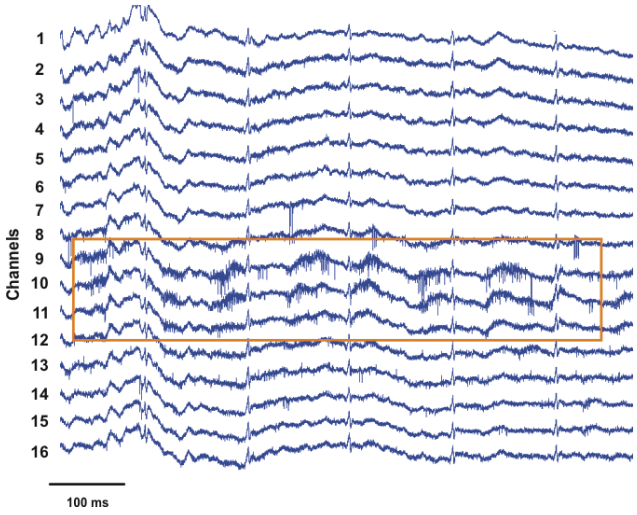

Fig. 1. Wideband multichannel extracellular recording from the ventral posteriomedial nucleus. A single sleep spindle oscillation is highlighted (frame).

In most cases, at the highest temperature level (39 °C, red line), no characteristic frequency distribution is present and sleep spindle frequency range is not accentuated. It can be seen in the example spectrogram as well (recording 2, Fig. 4./B), that, at 39 °C, few or no sleep spindle frequency could be extracted. Furthermore, the duration of synchronized periods possessing characteristic slow frequency distribution gets shorter, their occurrence becomes rare by body heating.

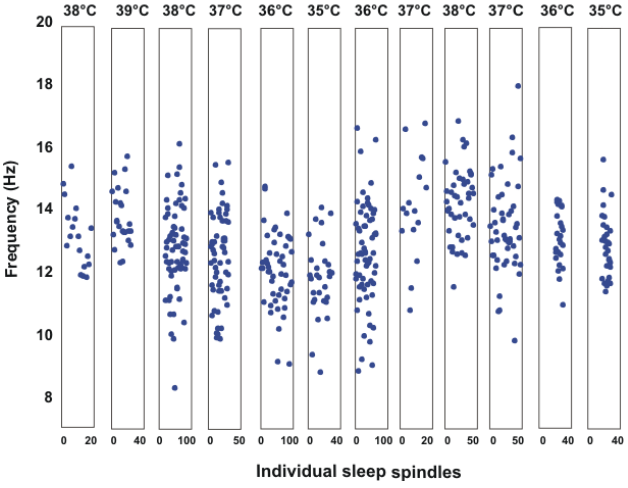

Fig. 2. Individual sleep spindle frequencies (averaged across cycles) at bidirectionally changing body temperature values in recording 3.

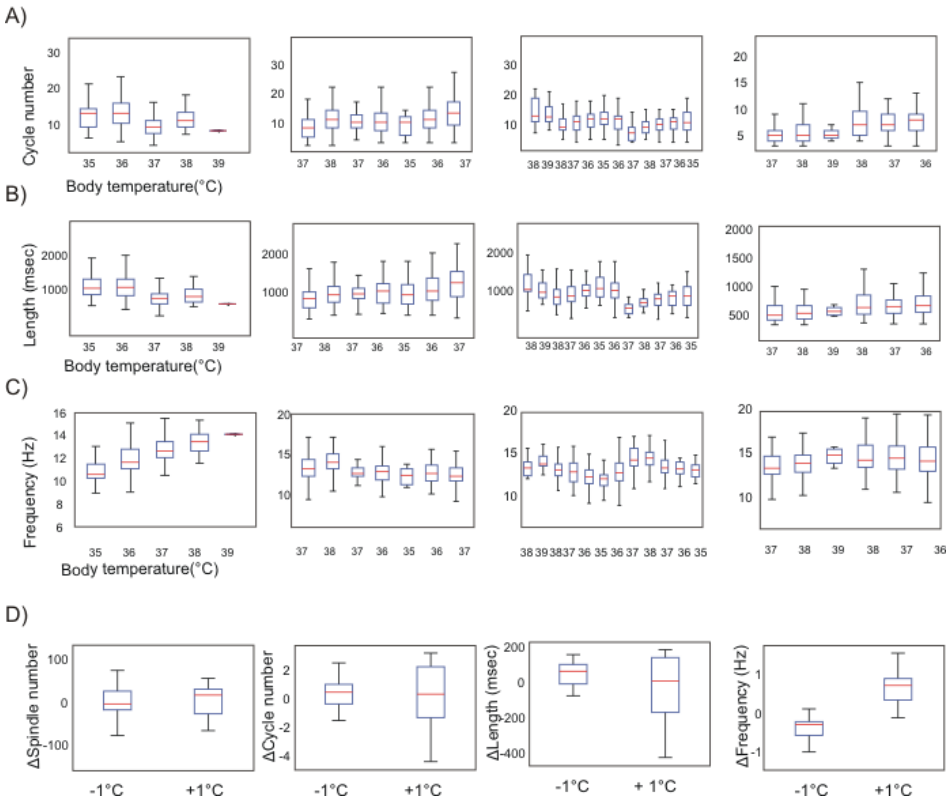

Fig. 3. Changes of sleep spindle parameters at different body temperatures in each animal. A-C). Median values (with the 25th and 75th percentiles) of cycle number, length and frequency, respectively at different body temperatures in the four animals (first to forth panel). D) Effect of body temperature modification (±1°C) on sleep spindle number per recording, cycle number per spindle, spindle length and frequency, respectively. Median values with the 25th and 75th percentiles are provided for all measurement and animals.

IV. Discussion

I have shown that body temperature changes may have an important role in defining the occurrence of synchronous activity and the proportion of different EEG frequencies under urethane anesthesia in mice. Sleep spindle parameters are also modified by its effect. Spindle frequency is shown to be in strong positive, while spindle length has a weaker negative relationship with body temperature change. All these results are in accordance with previous data acquired in humans [11]. Frequency distribution of the recordings shows as well a robust connection between the change of the spindle frequency range and body temperature. Spectral analysis also indicates that the highly reduced proportion of sleep spindles at 39 °C could be caused by the intense desynchronization and the shortening of synchronized periods of urethane anesthesia.

The question arises whether firing rate and firing pattern of particular neurons change at different temperature values. The relative firing times and current-source density distribution (CSD) of a certain unit during sleep spindles at different temperatures are also yet to be considered.

One of my future aims is to investigate whether other types of anesthetics have similar effect on the occurrence and parameters of sleep spindles as urethane. Also, it is left to measure and modify directly brain temperature in order to understand the relation between brain temperature, core body temperature and sleep spindle parameters.

It is very important to understand the temperature dependence of the brain's electrical activity and blood perfusion as well as their relation, either as an experimental factor, or even a possible tool applied in sleep disorders, neurological and psychiatrical diseases.

Changes of the relative frequency spectrum are not strictly due to a given experimental intervention, e.g. pharmacological treatment, but to the shift of the peaks in the absolute frequency spectrum. It is also crucial to consider that larger temperature changes can lead to the loss of integrity in functions and mechanisms associated with different frequencies, because oscillations can shift so much from their original ('euthermic') frequency range [4].

All this needs to be taken into consideration for data analysis, but already for selecting our animal subject regarding its sex, age and physiological status. All of these can have an influence on circadian body temperature changes and the general thermoregulational capacities. It is especially important in experiments led on freely moving animals where external thermoregulation is difficult to achieve.

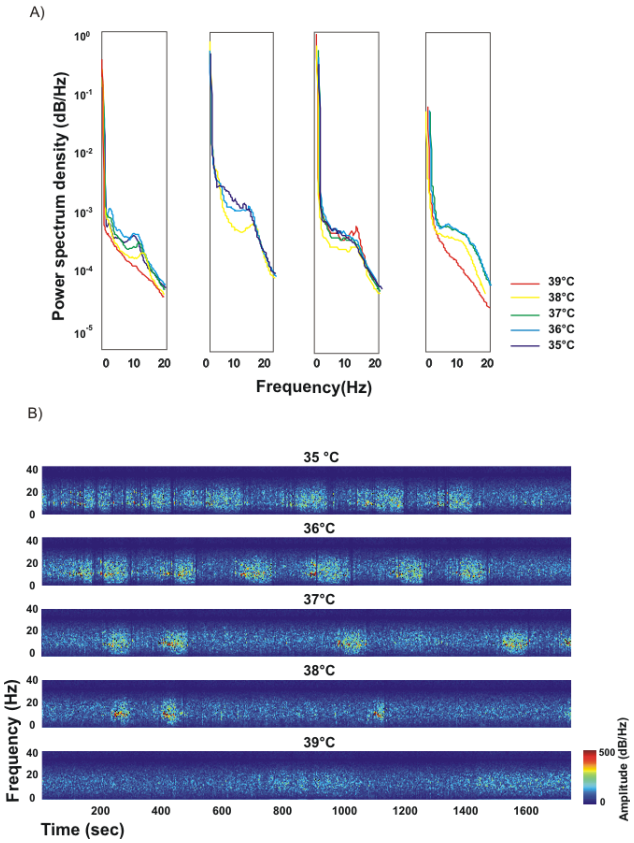

Fig. 4. Results of the spectral analysis. A) Welch's power spectrum density distribution of brain signals recorded at different body temperatures in each animal. B) Spectrogram of recording 1 showing the frequency distribution of the full-length recording in time in the frequency range of 0-40 Hz at different body temperatures. Amplitude of the spectral density is represented by a color scale.

ACKNOWLEDGMENT

I thank Péter Barthó and Márton Csernai for their help in data analysis.

REFERENCES

[1] Arrhenius, S. (1889): Über die Reaktionsgeschwindigkeit bei der Inversion von Rohrzucker durch Säuren. *Zeitschrift für Physikalische Chemie*, 1889, 4: pp. 226–248.

[2] Cooley, J.W., Tukey, J.W. (1965): An Algorithm for the Machine Calculation of Complex Fourier Series. *Mathematics of Computation*, 19(90), pp. 297-301.

[3] Deboer T., Tobler I. (1995): Temperature dependence of EEG frequencies during natural hypothermia. *Brain Research*, 670(1): pp. 153-156.

[4] Deboer, T. (1998): Brain temperature dependent changes in the electroencephalogram power spectrum of humans and animals. *Journal of Sleep Research*, 7: pp. 254–262.

[5] Demirhan, A., Kaymaz, M., Ahiska, R., Güler, I. (2010): A survey on appliation of quantitative methods on analysis of brain parameters changing with temperature. *Journal of Medical Systems*, 34(6): pp. 1059-1071.

[6] Driver, S., Dijk, D. J., Werth, E., Biedermann, K. and Borbély, A. A. (1996): Sleep and the sleep electroencephalogram across the menstrual cycle in young healthy women. *Journal of Clinical Endocrinology and Metabolism.*, 81: pp. 728-735.

[7] Fogel, S.M., Smith, C.T., and Cote, K.A. (2007). Dissociable learning-dependent changes in REM and non-REM sleep in declarative and procedural memory systems. *Behavioural Brain Research*, 180: pp. 48–61.

[8] Krauchi, K., Deboer, T. (2010): The interrelationship between sleep regulation and thermoregulation. *Frontiers in Bioscience*, 15, pp. 604-625.

[9] Paxinos G., Watson C. (1998) The rat brain in stereotaxic coordinates, 4th Edition. San Diego, California, USA: Academic Press.

[10] Raymann, R.J.E.M., Swaab, D.F., Van Someren, E.J.W.(2008): Skin deep: enhanced sleep depth by cutaneous temperature manipulation. *Brain*, 131(2): pp. 500-513.

[11] Schmitt, B., Jenni, O.G., Bauersfeld, U., Schüpbach, R., Schmid E.,R. (2002): Spindle activity in children during cardiac surgery and hypothermic cardiopulmonary bypass. *Journal of Clinical Neurophysiology*, 19(6): pp. 547-552.

[12] Smith, S.W.(1997-98): The Scientist and Engineer's Guide to Digital Signal Processing. California Technical Publishing, San Diego, CA. pp. 141-232.

[13] Van Someren, E.J.W. (2000): More than a marker: interaction between the circadian regulation of temperature and sleep, age-related changes, and treatment possibilities. *Chronobiology International,17*: pp. 313-54.

[14] Van Someren, E.J.W. (2004): Sleep propensity is modulated by circadian and behavior-induced changes in cutaneous temperature. *Journal of Thermal Biology*, 29: pp. 437-44.

[15] Van't Hoff, J. H. (1884): Etudes De Dynamique Chimique. Muller, Amsterdam.

[16] Welch P.D. (1967): The use of fast Fourier transform for the estimation of power spectra: A method based on time averaging over short, modified periodograms. *IEEE Transactions on Audio and Electroacoustics*, 15(2): pp. 17-20.

The dance of proteins: dynamic structural ensembles of the PDZ1-PDZ2 tandem in the PSD-95 protein

Bertalan KOVÁCS
(Supervisor: Zoltán GÁSPÁRI)
Pázmány Péter Catholic University, Faculty of Information Technology and Bionics
50/a Práter street, 1083 Budapest, Hungary
kovacs.bertalan@itk.ppke.hu

***Abstract*—Protein dynamics has often a key role in protein function like ligand binding, its fine-tuning and regulation. However, correct and detailed description of internal dynamics is a challenging task. NMR spectroscopy is one of the most useful tools to obtain information about protein dynamics at the atomic level. By combining NMR-derived mobility parameters with molecular dynamics calculations, a realistic insight into protein dynamics can be achieved. Here we present the generation of dynamic structural ensembles of the first two PDZ domains of the PSD-95 protein called PDZ tandem by restrained ensemble-based molecular dynamics. This PDZ tandem is a structurally independent unit and plays an important role in the signal-mediated biological response of PSD-95. We were able to capture several important aspects of the internal mobility of the PDZ tandem, in particular, the largely independent reorientation of the two PDZ domains.**

***Keywords*-Protein dynamics, molecular dynamics, NMR spectroscopy**

I. Introduction

Proteins are not rigid bodies, instead, they can adopt a number of continuously interconverting conformer state. This fact challenges the very basis of our understanding of protein function. The discovery of intrinsically disordered proteins (IDPs), which often have biological function dispite their lack of fixed three dimensional structure, showed that the old "key-lock" paradigm is no more sustainable, since it relies on the assumption that protein function always necessitates a well-defined rigid structure [1], [2].

NMR spectroscopy is the far most powerful technique to investigate dynamic molecules. It has the advantage of allowing for experiments in solution state, where proteins can maintain their dynamic behavior. The resulting data are, however, often ambiguous and difficult to interpret. Parameters gained by NMR measurements do not usually reflect all the possible conformers of a molecule, rather a hypothetical, time-averaged structure which may not even be present [3].

Protein structure representation also needs to be reconciled with the concept of molecular motion, because the traditional, rigid model does not imply a realistic view of the dynamic nature of molecules. Therefore it has to be replaced by an ensemble-based representation that reflects internal dynamics by including more than only one conformer in the molecular model. However, generating a reliable ensemble of conformers remains a difficulty to overcome. Generally, distance or mobility parameters provided by NMR measurements are applied as restraints to the entire molecule, which is subsequently submitted to computer-simulated structure refinement in order to make it fulfill all the external restraints. This approach can be improved by applying the restraints not to each conformer, but to the average structure [3].

The post synaptic density protein 95 (PSD-95, also known as SAP90) is a protein reportedly showing internal dynamics [4]–[6]. It consists of 5 domains, the first two of which (PDZ1-PDZ2) form a structurally independent subunit called PDZ tandem (Figure 1). The PDZ domain is a frequently occurring, well-studied protein binding unit; it recognizes short sequence motifs at the C-terminus of polypeptides. It usually plays a key role in lingad binding, regulates ion channeling and different signal transduction processes of PSD-95, however exact atomic-level mechanism of target protein binding is unknown [6]. Furthermore, several studies indicate that the two domains have to be in close proximity in PDZ tandems in order to fold and function properly [6]. Also, a recent paper showed that the first two PDZ domains of the PSD-95 have a rigid structure, while ligand binding induces considerable interdomain mobility which, with the help of a 5 amino acid residue long linker, allows the two PDZ domains to reorient independently [7].

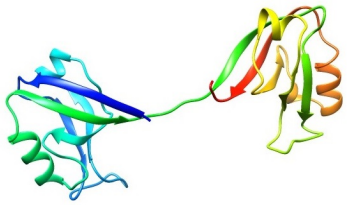

Fig. 1: The PDZ1-PDZ2 tandem of PSD-95.

This work aims at describing the internal dynamic properties of the PDZ tandem, and generating a dynamic structural ensemble of conformers by carrying out externally restrained molecular dynamics simulations.

II. Methods

For creating dynamic structural ensembles, Molecular Dynamics (MD) simulations were carried out, using open-

B. KOVÁCS, "The dance of proteins: dynamic structural ensembles of the PDZ1-PDZ2 tandem in the PSD-95 protein" in *PhD Proceedings Annual Issues of the Doctoral School, Faculty of Information Technology and Bionics, Pázmány Péter Catholic University – 2015.* G. Prószéky, P. Szolgay Eds. Budapest: Pázmány University ePress, 2015, pp 69– 72.

source program GROMACS 4.5.5. [8]. In molecular dynamics modeling, molecules are considered solid spheres that interact through covalent bonds and electrostatic potentials. The magnitude of these interactions is determined by molecular mechanics force fields. In the simulation, all the forces are calculated from the potential and summed up to each atom (Equations 1 and 2). Afterwards, Newton's equation of motion is solved numerically (Equation 3), accelerations are calculated and the atoms are displaced according to their velocities and the applied time step (Equation 4). For the first step, random velocities are generated.

$$\boldsymbol{F_i} = -\frac{\partial V}{\partial \boldsymbol{r_i}} \tag{1}$$

$$\boldsymbol{F_i} = \sum_j \boldsymbol{F_{ij}} \tag{2}$$

$$\frac{\mathrm{d}^2 \boldsymbol{r_i}}{\mathrm{d}t^2} = \frac{\boldsymbol{F_i}}{m_i} \tag{3}$$

$$\frac{\mathrm{d}\boldsymbol{r_i}}{\mathrm{d}t} = \boldsymbol{v_i}; \quad \frac{\mathrm{d}\boldsymbol{v_i}}{\mathrm{d}t} = \frac{\boldsymbol{F_i}}{m_i} \tag{4}$$

In Equations 1 to 4 $\boldsymbol{F_i}$, $\boldsymbol{r_i}$, m_i and $\boldsymbol{v_i}$ indicate the force on the atom number i, the position, the mass and the velocity of the same atom, respectively. V indicates the potential energy and t the time.

Experimental parameters are usually included in the simulation as external restraints. The modeled system is forced to comply with the these restraints by the following algorithm: deviation of the simulated parameters from their experimental values is calculated and transformed in an energy penalty term. Force derived from this penalty is added afterwards to the sum of the forces effecting the individual atoms, as seen in Equations 1 and 2.

Instead of simulating a single molecule, ensemble-based representations were created that consisted of several (4-32) replicas. In order to apply external restraints to the entire ensemble instead of each single molecule, in-house extension of GROMACS software was used. In the present simulations, NOE parameters and the Lipari-Szabó model free

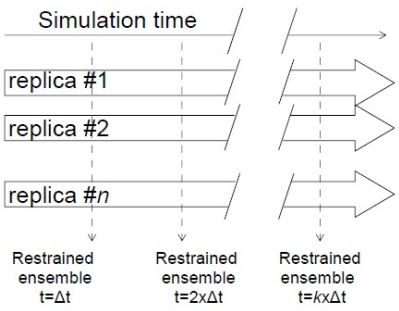

Fig. 2: Generating structural ensembles from the molecular dynamics simulation.

parameters (S^2) were applied as external restraints, measured and published by Wang *el al* in 2009 [7]. NOEs are used as distance restraints, which keep atom pairs from moving away from each other further than a certain distance. Such distance restraints can be applied to the whole ensemble by averaging the sixth power of the atom-atom distances (r^{-6}). S^2 parameters, on the other hand, describe the mobility of each N-H bond vector in the protein: a value close to 1 indicates a structurally rigid amino acid residue, whereas values near to 0 belong to mobile residues. Deviation from the experimental S^2 parameters is calculated in each step of the simulation after rotating each replica in a common molecular frame according to the algorithm described by Vendruscolo *el al.* in 2004 [9]. Also, a profitable feature of the in-house extension module of GROMACS is that it allows for local fitting of external restraints to shorter protein range, for example a single domain. This is useful when one or more domains are presumed to move independently. This way, also the penalty energy terms and the derived forces will be calculated separately for the different domains.

Structural ensembles were created by taking a sample of the trajectory of each replica (Figure 2). Evaluation of the generated ensembles was carried out by the CoNSEnsX server[1] [10]. This algorithm plots the calculated S^2 parameters against the experimental ones and calculates their correlation. It also determines the violated NOE restraints, when the calculated values – averaged over the entire ensemble – exceed the experimental ones.

Analysis of secondary structure was carried out with the DSSP algorithm[2] [11]. For each replica of the ensembles, secondary structure assignment was done, and the structural motifs were compared to each other. To illustrate the variability of the secondary structural elements, which indicates a certain mobility of the residues, Shannon entropy was calculated, according to Equation 5,

$$H_i = -\sum_j p_{ij} \log p_{ij} \tag{5}$$

where p_{ij} indicates the probability of the secondary structural motif number j of residue number i.

III. Results and Discussion

A. Analysis of calculated order parameters

600 ps long simulations were carried out on ensembles of 8 replica of the PDZ1-PDZ2 tandem of PSD-95. 149 S^2 and 10681 NOE parameters were used as external restraints. The effect of the external restraining was investigated by running several different simulations, each with different restraint set. As it can be seen on Figure 3, the correlation between calculated end experimental S^2 improves as local fitting of restraints is applied to the distinct domains, as well as when NOE restraints are added to model. The fact that the calculated S^2 values are close to zero for the opposite domain to which

[1] http://consensx.chem.elte.hu/
[2] http://swift.cmbi.ru.nl/gv/dssp/

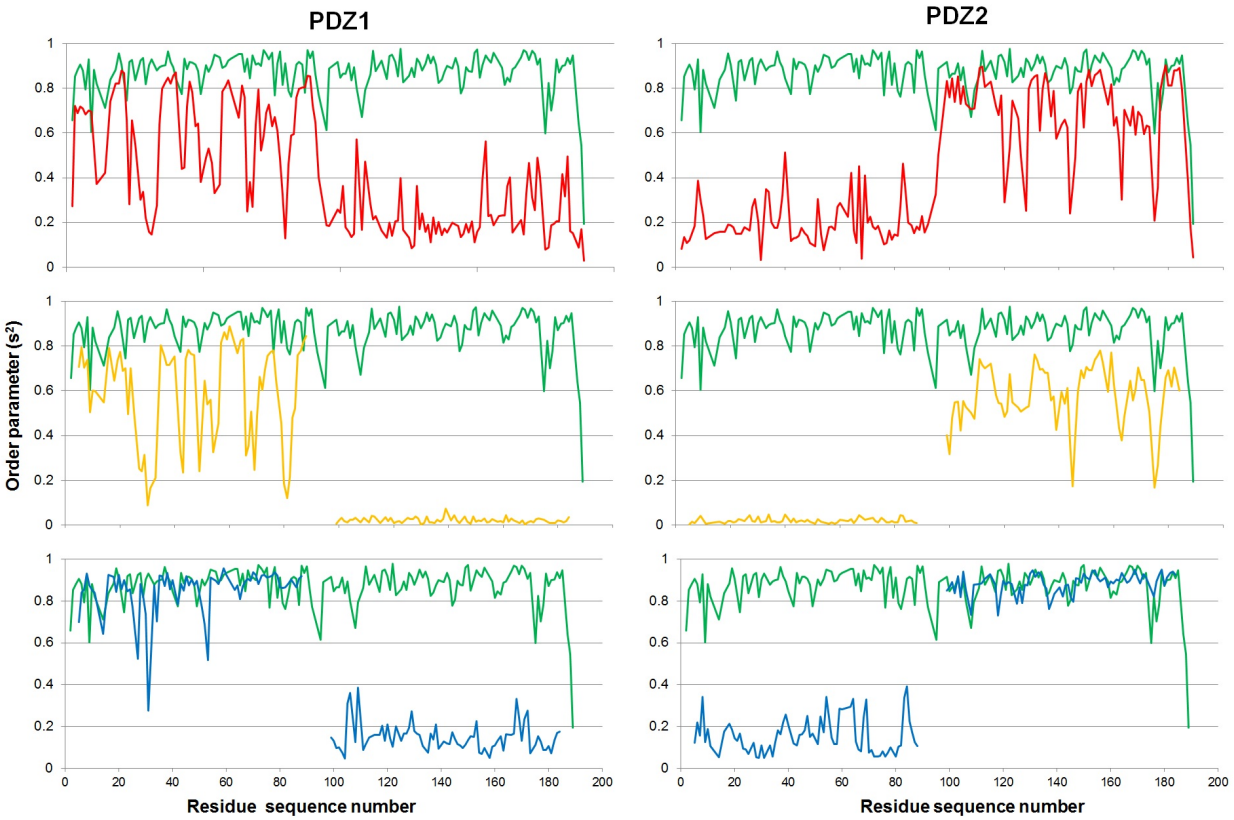

Fig. 3: Experimental and calculated S^2 parameters of structural ensembles fitted locally to PDZ1 (left) and PDZ2 (right) domains. Colors indicate: —— experimental S^2 values, and calculated S^2 values in the following order: —— no local fitting of S^2 restraints, —— local fitting of S^2 restraints and —— local fitting of S^2 and additional NOE restraints.

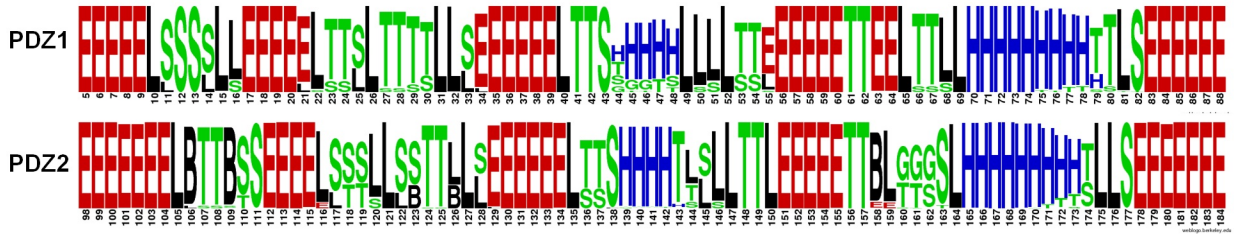

Fig. 4: Variability of secondary structural elements at each amino acid residue position on PDZ1 and PDZ2 domains of PSD-95. Secondary structure assignment was done for 496 conformer of a dynamic structural ensemble.

ensemble fitting was done (see Figure 3, yellow lines) cannot be explained otherwise but assuming that when the atoms of one domain stick together, the atoms of the other one get dispersed. Even though the addition of NOE parameters to the model results in somewhat higher S^2 in the same, non-fitted regions, it is probably due to the fact that the two domains become more compact and organized. The same effect is indicated by the root-mean-square deviation (RMSD) between calculated and experimental S^2: 0.35, 0.37 and 0.13 for PDZ1, and 0.25, 0.33 and 0.07 for PDZ2 domain; for simulation without local fit, with local fit and with additional NOE, respectively. It is interesting to note that among 10681 NOE values there are no interdomain restraints, which also fortifies the conclusion that the two PDZ domains move independently.

B. Analysis of secondary structure variability

In order to gain reliable insight into the secondary structure variability, a longer simulation was done, at the end of which an ensemble with 496 conformer could be obtained. Secondary structure assignment of each member of the ensemble and

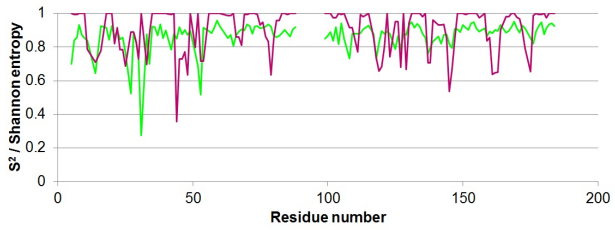

Fig. 5: Normalized Shannon entropy (——) and S^2 parameters (——) plotted together. Shannon entropy is calculated from secondary structural assignment based on an about 500 sized dynamics structural ensemble.

comparison of their DSSP assignment to each other by plotting them on a weblogo[3] reveals some key information about the nature of PDZ domains (Figure 4). Firstly, it can be seen that the structurally most conserved regions are the very motifs that define PDZ domain: three β-sheets, an α-helix, a β-sheet, an α-helix and a β-sheet, respectively. Secondly, the less conserved regions are those with the more structural flexibility, such as residues 10-15 in PDZ1 or 160-165 in PDZ2.

Variability of secondary structural motif in each residue is reflected by the Shannon entropy (Equation 5). Normalized Shannon entropy subtracted from 1 $(1 - H)$ can be compared with the S^2 parameters, since they both vary between 1 and 0. Such a plot can be seen on Figure 5. The chart shows that the two parameters, despite a generally bad correlation, move together in some regions (around 15-20, 22-25, 110-120 or 130-135). It can be deduced that these two values measure the same characteristics, i.e. the internal mobility of the protein. However, secondary structure analysis can be carried out by less computation, thus providing an alternative way of investigation of protein dynamics when molecular dynamics is too expensive.

IV. Conclusion

Internal dynamics often plays a key role in protein-ligand interactions or regulation processes, however, it is a challenging task to find a method that provides a reliable insight into molecular motion. NMR spectroscopy is a powerful tool for obtaining such data on protein structure that also incorporate dynamic information. Combined with computer simulations, a realistic, ensemble-based representation of protein dynamics can be achieved.

The first two PDZ domains of PSD-95 form a structurally independent subunit called PDZ tandem. By means of molecular dynamic simulation, in which Lipari-Szabó order parameters (S^2) and NOE parameters were included as external restraints, we succeeded in creating a realistic dynamic ensemble that reflects internal mobility. The results showed that the two domains perform considerable interdomain mobility in the PDZ tandem, which is possible due to a short linker between the domains. Also, it has bee proved that secondary structure variability, which can be effectively expressed with the Shannon entropy, is comparable to order parameters.

[3]http://weblogo.berkeley.edu/

Acknowledgment

Guidance and generous support of my supervisor, Zoltán Gáspári is herein gracefully acknowledged, as well as the help of many of my colleges and co-students, like Annamária Kis-Tóth, Domokos Meszéna, Gergely Csány and Dániel Dudola. I would also like to thank Nóra Epresi for implementing S^2 restraining with local fit. This research project was funded by KAP-1.1-14/022.

References

[1] P. E. Wright and H. Dyson, "Intrinsically unstructured proteins: re-assessing the protein structure-function paradigm," *Journal of Molecular Biology*, vol. 293, no. 2, pp. 321 – 331, 1999.

[2] A. K. Dunker, C. J. Brown, J. D. Lawson, L. M. Iakoucheva, and Z. Obradovi, "Intrinsic disorder and protein function," *Biochemistry*, vol. 41, no. 21, pp. 6573–6582, 2002.

[3] A. F. Ángyán and Z. Gáspári, "Ensemble-based interpretations of NMR structural data to describe protein internal dynamics.," *Molecules (Basel, Switzerland)*, vol. 18, pp. 10548–67, Jan. 2013.

[4] D. G. Stathakis, K. B. Hoover, Z. You, and P. J. Bryant, "Human postsynaptic density-95 (PSD95): location of the gene (DLG4) and possible function in nonneural as well as in neural tissues.," *Genomics*, vol. 44, no. 1, pp. 71–82, 1997.

[5] C. M. Petit, J. Zhang, P. J. Sapienza, E. J. Fuentes, and A. L. Lee, "Hidden dynamic allostery in a PDZ domain.," *Proceedings of the National Academy of Sciences of the United States of America*, vol. 106, no. 43, pp. 18249–18254, 2009.

[6] H.-J. Lee and J. J. Zheng, "PDZ domains and their binding partners: structure, specificity, and modification.," *Cell communication and signaling : CCS*, vol. 8, p. 8, 2010.

[7] W. Wang, J. Weng, X. Zhang, M. Liu, and M. Zhang, "Creating conformational entropy by increasing interdomain mobility in ligand binding regulation: a revisit to N-terminal tandem PDZ domains of PSD-95.," *Journal of the American Chemical Society*, vol. 131, pp. 787–96, Jan. 2009.

[8] B. Hess, C. Kutzner, D. van der Spoel, and E. Lindahl, "Gromacs 4: algorithms for highly efficient, load-balanced, and scalable molecular simulation," *Journal of Chemical Theory and Computation*, vol. 4, no. 3, pp. 435–447, 2008.

[9] R. B. Best and M. Vendruscolo, "Determination of protein structures consistent with nmr order parameters," *Journal of the American Chemical Society*, vol. 126, no. 26, pp. 8090–8091, 2004.

[10] A. Angyan, B. Szappanos, A. Perczel, and Z. Gaspari, "Consensx: an ensemble view of protein structures and nmr-derived experimental data," *BMC Structural Biology*, vol. 10, no. 1, p. 39, 2010.

[11] W. G. Touw, C. Baakman, J. Black, T. a. H. te Beek, E. Krieger, R. P. Joosten, and G. Vriend, "A series of PDB-related databanks for everyday needs," *Nucleic Acids Research*, vol. 43, no. D1, pp. D364–D368, 2014.

Study of plasma separation performance in cascade microfluidic structures

Eszter LEELŐSSYNÉ TÓTH
(Supervisor: Kristóf IVÁN, Péter FÜRJES)
Pázmány Péter Catholic University, Faculty of Information Technology and Bionics
50/a Práter street, 1083 Budapest, Hungary
toth.eszter@itk.ppke.hu

***Abstract*—Several diagnostic applications require high sensitive detection of cells (cancer or bacteria) and molecules (proteins, DNAs or viruses) from low volume human blood. These Lab-on-a-Chip systems need high performance blood plasma separation substructures. Zweifach-Fung type plasma separation systems establish a cell-free layer near the channel wall in low Reynolds regime and promote plasma separation through high resistance daughter channels. Single Zweifach-Fung type separation structures are capable of achieving high plasma purity, however, the separated plasma yield is limited. The plasma yield can be increased by the application of cascade separation systems, however, the purity is deteriorated subsequently from branch to branch due to the thinning of the cell-depleted layer. Our goal is to improve the plasma purity by the recovery of the cell-free layer after each bifurcation by applying inertial forces evolving in different geometrical singularities.**

***Index Terms*—microfluidics; Lab-On-a-Chip; plasma separation**

I. Introduction

The precisely controlled manipulation of fluids in micro-analytical systems or microchemical reactors is a key issue in terms of the final applicability of these devices. Besides fluidic transport, integrated functional microfluidic elements (pumps, mixers, separators, etc.) are also essential building blocks of the sample preparation systems. Diagnostic applications require reliable detection of cells and molecules from low volume sample. Considering deterioration of the detection limit by cell lysis, Lab-on-a-Chip systems need high performance blood plasma separation substructures. Although single Zweifach-Fung type separation structures are capable of achieving high plasma purity [1], the separated plasma yield is limited, thus series of bifurcations are applied to improve performance. Zweifach-Fung type plasma separation systems can establish a cell-free layer near the channel wall due to viscous lift forces and shear forces and promote plasma separation through high resistance daughter channels. Altough plasma yield can be increased by the application of cascade separation systems, the purity of the plasma may be deteriorated subsequently from branch to branch due to the thinning of the cell-depleted layer. The plasma purity can be improved by the recovery of the cell-free layer after each bifurcation by applying inertial forces evolving in multiple contractions and expansions of the channel. Geometrical singularities were designed and integrated in the main stream channels in order to enhance the inertial effects in the laminar flow system to recover the cell-free layer near the channel walls. The effects of these perturbations were characterised by Finite Element Modelling considering different flow rates and viscosities affected by preliminary dilution of whole blood. Test structures were fabricated by soft lithography technique in polydimethylsiloxane (PDMS) and the performance of the different geometries was characterised by applying adequate particle models for the cell size distribution and concentration of human blood.

II. Materials and methods

A. Geometry of singularities

Six different geometric perturbations were designed to aid the development and recovery of cell free layer before each cascade side branches. These perturbations were 250-1000 μm long and 335-600 μm wide. The main channels were 100 μm and the side branches were 10μm wide each.

B. Microfabrication

The microfluidic channels were realized in Polydimethilsiloxane (PDMS) with rapid prototyping. SU-8 negative photoresist [2] was patterned by spin-coating (Brewer Science Cee 200CBX spin-coater [3]), litographic exposure (Süss MicroTech MA6 mask aligner [4]) and a final development step, as illustrated in Figure 1. PDMS prepolymer was poured onto the developed replica and polymerized in two days in room conditions. At the final step of the fabrication process, PDMS was sealed to glass by low temperature bonding after oxygen plasma treatment applying 200 W plasma power, 100 kPa chamber pressure and 1400–1900 sccm oxygen flow (Terra Universal Plasma Preen Cleaner/Etcher [5]).

C. Dark field microscopy

The measurement of particle trajectories is a challenging task. To model the red blood cells in a possible blood analyte we have used yeast cells as their size characteristic and distribution is similiar to the red blood cells [6]. Yeast solution was diluted to be able to see individual trajectories. Dark field mode of the Zeiss AxioVert A1 [7] inverted microscope was used. This imaging method facilitates the recording of the light scattered from the cells crossing the light beam, local

E. LEELŐSSYNÉ TÓTH, "Study of plasma separation performance in cascade microfluidic structures" in *PhD Proceedings Annual Issues of the Doctoral School, Faculty of Information Technology and Bionics, Pázmány Péter Catholic University – 2015.* G. Prószéky, P. Szolgay Eds. Budapest: Pázmány University ePress, 2015, pp 73– 75.

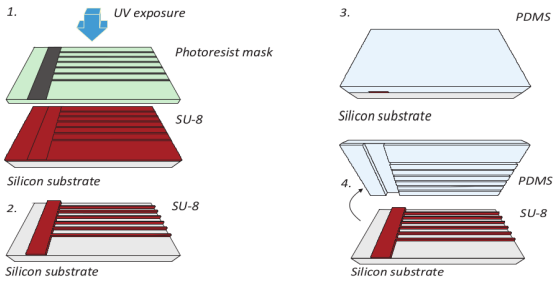

Fig. 1. Schematic view of PDMS rapid prototyping. UV light passes the photoresist mask exponing the SU-8. The developed photoresist then serves as a moulding replica for PDMS moulding.

Boundary	Model	Boundary condition	Value
Inlet	CFD	Laminar inflow with average flow velocity	0.01-5 $\mu L/s$
Inlet	Trajectory	Particle inlet	100 particles with uniform density
Channel wall	CFD	No slip	-
Channel wall	Trajectory	Bounce	-
Outlet	CFD	Pressure	0 Pa
Outlet	Trajectory	Freeze	-

TABLE I
SUMMARY OF BOUNDARY CONDITIONS FOR THE NUMERICAL MODEL

cell concentration from the lateral distribution of the scattered light intensities, i.e. from the local brightness levels of the image were estimated.

D. Numerical modeling

COMSOL Multiphysics was used to calculate a laminar and stationary velocity field by solving the Navier-Stokes equation [8]. The pre-calculated velocity field then was used for the calculation of particl trajectories. The particle tracing based model calculates, follows and depicts the individual particle trajectories according to the hydrodynamic drag force described by Stokes' law. The lift force was not considered due to the low Reynolds number and the small difference between the particle and water density. Laminar inflow boundary condition was applied on the inlet with different average velocities and zero pressure was set at the outlet. On the channel walls, no slip boundary conditions were defined for the laminar flow model and bounce boundary was used for the trajectory model as summarized in Table I. The properties of room temperature water (density: 1000 kg/m^3, kinematic viscosity: 10^{-6} m^2/s) were applied as material parameters. Properties of the model particles were set to be in correspondence with the principal properties of red blood cells (density: 1100 kg/m^3, particle diameter: 6 μm [9] [10]). Spherical particle geometry was used as an approximation of the cell geometry and this approach was in accordance with the experimental methods, as well.

III. RESULTS

A. Flow rate dependency of the velocity field

The modeled and measured velocity fields were recorded in the case of 4th geometry (Figure 4). At small flow rates the velocity field is stable (Figure 4 A-B). An order of magnitude increase in the flow rate however results in recirculations and vortices in the channel (Figure 4 C-E) which could be reproduced experimentally. These recirculations need to be avoided as they can compromise the purity of the separated plasma.

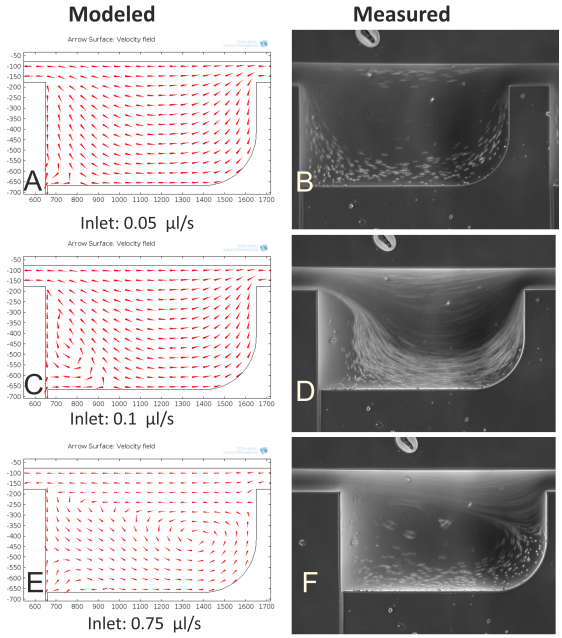

Fig. 2. Effect of flow rate on the velocity field. The modeled and measured velocity fields were recorded in the case of 4th geometry. At small flow rates the velocity field is stable (A-B). An order of magnitude increase in the flow rate however results in recirculations and vortices in the channel (C-E) which could be reproduced experimentally. These recirculations need to be avoided as they can compromise the purity of the separated plasma.

B. Particle trajectory modell

Particle trajectories modeled in COMSOL Multiphysics were in a good agreement with the experiments (Figure 3). the developing of the cell free layer were also well visible.

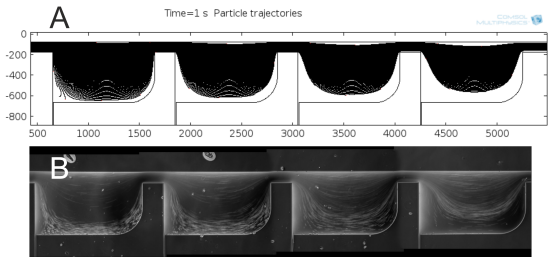

Fig. 3. Modeled (A) and measured (B) particle trajectories were in a good agreement. The development of the cell free layer is visible at the widenings of the channel.

Inlet Flow rate [$\mu L/s$]	Plasma out flow rate [$\mu L/s$]	Efficiency
0.01	0.000229	2.29%
0.05	0.001147	2.29%
0.10	0.002299	2.30%
0.50	0.011744	2.35%
1.00	0.023855	2.39%
5.00	0.126858	2.54%

TABLE II
EFFECT OF FLOW RATE ON PLASMA SEPARATION EFFICIENCY. IN THE CASE OF THE MOST EFFICIENT GEOMETRY (SMALL CIRCLE, 6^{TH} GEOMETRY) PLASMA SEPARATION EFFICIECIES WERE RECORDED. TWO ORDER OF MAGNITUDE ENCREASE IN THE FLOW RATE RESULTED IN ONLY 0.25% INCREASE IN THE EFFICIENCY.

C. *Efficiency of plasma separation*

The efficiencies of the microchanels were modeled and calculated as the ratio of the sum of the plasma flow rate at the outlets and the inlet flow rate (Figure 4). Although the efficiencies seem similar in the case of geometries 2-5 the first and the last one are outliers. Smaller singularities tend to have better outlet efficiencies. In the case of the best structure (6^{th} geometry) the efficiency was further studied. Table II shows the efficiency values at six different flow rates. We can conclude that the efficiency can not be increased significantly with the increase of the inlet flow rate. Two order of magnitude encrease in the flow rate resulted in only 0.25% increase in the efficiency.

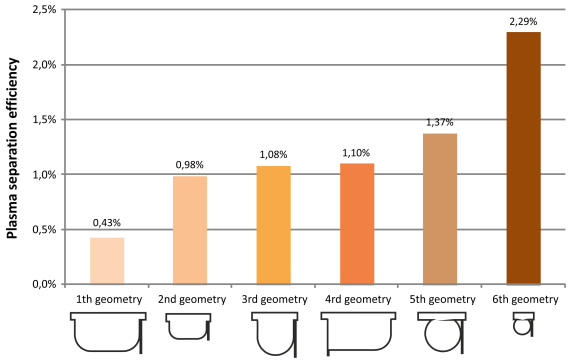

Fig. 4. Modeled plasma separation efficiency at the six different geometric singularities. Smaller singularities have better efficiency. Altough the efficiencies seem to be similar in the case of geometries 2-5, the 1 and the 6 deviate more from the average. The most efficient geometry is the 6^{th} geometry.

D. *Cell-free layer recovery*

The development and recovery of the cell free layer near the channel walls was well captured in the intensity analysis of the recorded microscopic images (Figure 5). The cell free layer at the outlet of the channel is clearly visible.

IV. CONCLUSION

Flow behaviour and particle distribution affected by geometric perturbations were characterised by Computational Fluid Dynamics (CFD) module of COMSOL Multiphysics (solving pressure and velocity field) and Particle Tracing Module (calculating particle trajectories). Test structures were fabricated

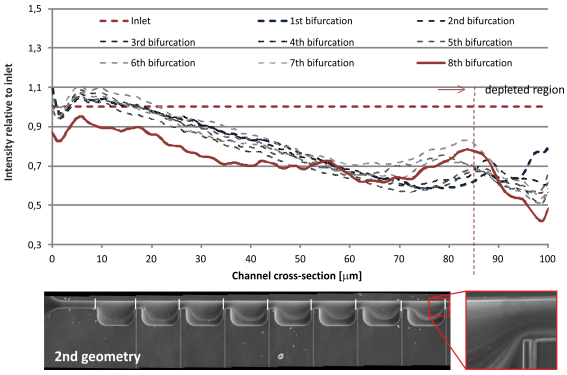

Fig. 5. The relative light intensity distributions across the channel narrowings were recorded after each geometric perturbation. The development and recovery of the cell free layer is well demonstrated both on the diagram and the microscopic image.

in polydimethylsiloxane (PDMS) and the performance of the different geometries was characterised experimentally recording particle trajectories by dark field microscopy applying different flow rates. Inertial forces in geometrical singularities led to the recovery of the cell-free layer after the bifurcations. This process was shown both in measurements and model results and its applicability in enhanced cascade type plasma separation systems was proposed.

V. ACKNOWLEDGEMENT

The author is grateful to supervisors dr. Péter Fürjes and dr. Kristóf Iván for their help and support. The professional assistance of Eszter Holczer, Anna Borbála Tóth and the technical staff of MTA EK MFA is highly appreciated. The research was funded by KAP grant of the Pázmány Péter University.

REFERENCES

[1] Z. Fekete, P. Nagy, G. Huszka, F. Tolner, A. Pongrácz, P. Fürjes, Performance characterization of micromachined particle separation system based on Zweifach-Fung effect, *Sensors and Actuators B* 162 (2012) 89-94
[2] MicroChem Corp. Available online: http://www.microchem.com (accessed on 14 May 2015).
[3] Brewer Science Inc. Available online: http://www.brewerscience.com (accessed on 14 May 2015).
[4] 22. SÜSS MicroTec AG. Available online: http://www.suss.com (accessed on 14 May 2015)
[5] Terra Universal Inc. Available online: http://www.terrauniversal.com
[6] Tóth, E. L., Holczer, E. G., Iván, K., Fürjes, P. (2014). Optimized Simulation and Validation of Particle Advection in Asymmetric Staggered Herringbone Type Micromixers. *Micromachines*, 6(1), 136–150. http://doi.org/10.3390/mi6010136
[7] ZEISS International. Available online: http://www.zeiss.com (accessed on 14 May 2015).
[8] Fürjes, P., Holczer, E. G., Tóth, E., Iván, K., Fekete, Z., Bernier, D., … Giannone, D. (2014). PDMS microfluidics developed for polymer based photonic biosensors. *Microsystem Technologies*. http://doi.org/10.1007/s00542-014-2130-y
[9] Density of Blood. Available online: http://hypertextbook.com/facts/2004/MichaelShmukler.shtml (accessed on 14 May 2015).
[10] Kutz, M. *Standard Handbook of Biomedical Engineering and Design*; McGraw-Hill: New York, NY, USA, 2003.

Development of an *in silico* tumor ratio calculating method

Zselyke MAGYARI
(Supervisor: Istvn PETÁK, Andrs HORVÁTH)
Pázmány Péter Catholic University, Faculty of Information Technology and Bionics
50/a Práter street, 1083 Budapest, Hungary
magzs@digitus.itk.ppke.hu

***Abstract*—In 2013 the concept of driver genes were introduced by Vogelstein *et al*. Forty five approved drugs targeting driver genes are already available in the market and hundreds are currently in clinical trials or under research. Precise evaluation of the molecular diagnostic results is needed to identify driver genes and then to find the most effective targeted therapy. Before starting diagnostic tests the tumor ratio on the sample plate has to be determined. In practice pathologists assess the tissue or cytological died sample to give tumor percentage, which is further used for molecular profilng. An *in silico* tumor-ratio calculating method is urgently needed to standardize the calculation of the tumor- normal tissue distribution. Methods presented here were based on k-means clustering and brightness enhancement. It became clear at the beginning that the reliability of the automatically calculated value reflecting tumor cells' percentage depends on the complexity of the died sample's image. First of all, color of immune cells is the same like color of tumor cells on the images, they mostly differ in size and they usually do not form a continuous cell mass, meaning they can be usually found as single small dots on an image. Excluding immune cells was the biggest challenge during the development. The presented tumor ratio calculating methods were acceptable in most cases, although they have their own weaknesses. These methods were good starting points for further development as the results highlighted the bottleneck of these calculators.**

***Index Terms*—driver gene; targeted therapy; tumor ratio; *in silico* calculation**

I. Introduction

The Human Genome Project produced the first complete sequences of individual human genomes (HGP 1990-2006), in contrast to the expectations merely 15 –20 thousand genes were identified. In 2013 the concept of driver genes ($\sim$ 140) were introduced by Vogelstein *et al.*, and proved to be responsible for cancer development. Most human cancers are caused by two to eight sequential alterations that develop over the course of 20 to 30 years. Proteins encoded by the so called driver genes are building blocks of approximately 12 signal transduction pathways [1]. Forty five approved targeted drugs are already available in the market (FDA and/or EMA approval) and hundreds are currently in clinical trials, or under research. Selectively targeting driver gene abberations could slow or stop local tumor progression, or could withdraw cells' ability to give metastasis. Approximately 3.5 million cancer patients were registered in 2012 in Europe, from that 1.75 ended with death [2][3]. Targeted therapy alone, or together with standard therapy before/after or without surgery could face up to the disease. Precise evaluation of the molecular diagnostic results is needed to identify driver gene or genes and then to find the most effective targeted drug. Image processing decision supporting systems in medical practice are extremely important nowadays. Scientists make an effort in several fields to improve methods: ex. analysing CT scans, or helping early breast cancer detection based on mammographic images [4][5]. An *in silico* tumor ratio calculating method is also urgently needed to standardize the calculation of tumor- normal tissue distribution, and in some cases to ease the decision for pathologists, as in practice pathologists assess the tissue or cytological died sample (Hematoxylin and eosin stain) and determine the ratio, which is further used to determine the exact molecular profile, based on his or her professional experience. This way of detection is time-consuming and circumstantial as the available tools for marking tumor region are reasonably rudimentary.

II. Materials and methods

Scripts were created using python language. Several packages were used for image processing (ex. OpenCV, Image, Matplotlib, Scipy, etc.). Original images: 8 images of tissue or cytological hematoxylin + eosin died samples.

1. Delete background: K-means clustering of all pixels according to the HSV color codes were performed. The one, where the dark pixels enrichment was the lowest were selected. Those pixels, which were enrolled to the selected cluster, were changed to white. Finally only cells containig area (ex. tissue) remained, which were considered as 100 percent for the ratio calculating method.
2. Find the most likely tumor area:

First method: Brightness enhancement of the original image, which process kept only specifically stained area, where most probably the tumor cells' seeds can be found.

The second method: Separation of that cluster where the dark pixels enrichment is the highest. After adaptive thresholding the resulted image (in all two cases) was used to find contours. All detected contours had specific descriptors: center, size and angle, which were used to fit an ellipse to the original image. Selected ellipses' area (only a raw selection to skip very small

Zs. MAGYARI, "Development of an in silico tumor ratio calculating method" in *PhD Proceedings Annual Issues of the Doctoral School, Faculty of Information Technology and Bionics, Pázmány Péter Catholic University – 2015.* G. Prószéky, P. Szolgay Eds. Budapest: Pázmány University ePress, 2015, pp 77– 79.

(noise) ellipses, and huge ones which were caused by the sharp edge between the background and the cells containing area) were considered as tumor region (those pixels color was changed to red to help ratio calculation).
3. Ratio calculation:
After deleting background hunderd percent became all the remaining, not white pixels. Tumor area: red pixels. All other pixels refer in this calculator to healthy/non tumor cells, tissue.

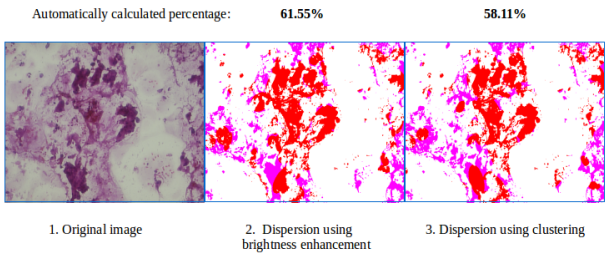

Fig. 1: White: background, Red: tumor area, Pink: normal tissue area according to the calculation. Mostly tumor regions were found, altough several smaller tumor areas were omitted (ex. bottom left image section).

Basics

The k-means clustering algorithm:

Input: number of clusters, k, and a set of observation vectors to cluster (image as a matrix of HSV color codes).
It returns a set of centroids, one for each of the k clusters.
A vector v belongs to cluster i if it is closer to centroid i then any other centroids. If v belongs to i, we say centroid i is the dominating centroid of v. The k-means algorithm tries to minimize distortion, which is defined as the sum of the squared distances between each observation vector and its dominating centroid. Each step of the k-means algorithm refines the choices of centroids to reduce distortion. The change in distortion is used as a stopping criterion: when the change is lower then a threshold, the k-means algorithm terminates (*scipy.org*). The presented method does not use a maximum number of iterations.

$$\arg\min_{\mathbf{S}} \sum_{i=1}^{k} \sum_{\mathbf{x} \in S_i} \|\mathbf{x} - \boldsymbol{\mu}_i\|^2$$

K-means clustering formula.

Thresholding:

Thresholding is used to segment an image by setting all pixels whose intensity values are above a threshold to a foreground value and all the remaining pixels to a background value. We used adaptive thresholding.
Input: grayscale or color image.
Output: binary image representing the segmentation.
Used threshold type: $BINARY$.
Used adaptive method: $MEAN\ C$. The threshold value $T(x, y)$ is a mean of the n x n neighborhood of (x, y) minus c (*OpenCV documentation*).

$$\mathtt{dst}(\mathtt{x},\mathtt{y}) = \begin{cases} \mathtt{maxValue} & \text{if } \mathtt{src}(\mathtt{x},\mathtt{y}) > \mathtt{T}(\mathtt{x},\mathtt{y}) \\ \mathtt{0} & \text{otherwise} \end{cases}$$

Binary thresholding formula.

Detecting contours:

The contour is a boundary of object, a population of points (pixels).
Used mode: retrieving all of the contours without establishing any hierarchical relationships.
Used method: $CHAINAPPROX\ NONE$ stores absolutely all the contour points. That is, any 2 subsequent points $(x1, y1)$ and $(x2, y2)$ of the contour will be either horizontal, vertical or diagonal neighbors (*OpenCV documentation*).

III. Results

K-means pixel clustering method for selecting and deleting the background pixels were successful in all cases. The reliability of the automatically calculated value reflecting the percentage of tumor cells in a sample depended on the complexity of the died image. First of all immune cells' color is usually the same like tumor cells' color on the sample image, they differ in size mostly, and they usually do not form a continuous cell mass, meaning they can be usually found as single small dots on an image. Immune cells should not increase the tumor ratio, so they had to be classified as normal tissue area in all cases. Excluding immune cells was the biggest challenge during the development.
Analysis of the results given by the clustering method: Mainly the tumor ratio given by this method is acceptable. As this method was completely based on the color of pixels it was not able to differ immune cells from tumor cells. Idea to fix this method's weakness: small dots in the likely tumor area cluster (darkest pixels containing cluster) in clustered image likely immune cells smaller area refers to smaller contour size using contour's center the created ellipse area should be smaller start deleting the drawn ellipses, to exclude the area under these ellipses, from the smallest to biggest until a given threshold. Main problem: because of the tumor cells' type (ex. cells from several types of tissue), cells can have their own contour, in which case the method gives them individual ellipses, small enogh to be deleted when the program starts to

delete immune cells.
Analysis of the results given by the method based on brightness enhancement: Tumor ratio given by this method is acceptable too, mainly does not differ from the clustering method. It is observable that enhancing the brightness highlight the seeds of tumor cells, but also keeps cytoplasmic region, and unfortunately immune cells too. Turned out that tumor cells' seeds stain the same like immune cells' seeds too. The developed fixing workflow was applied also for this method and was not producing the expected improvement, despite the fitted ellipses' area were generally smaller, because the counturs were maily based on seeds, not cells.

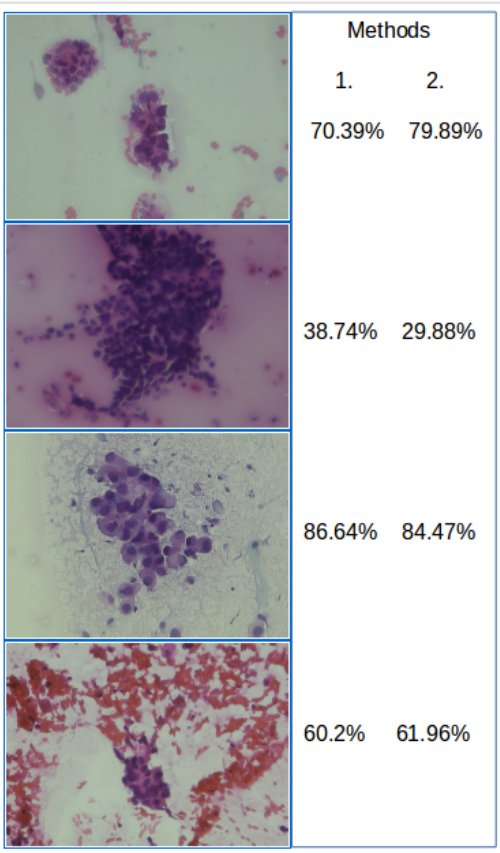

Fig. 2: Tumor ratio calculated using the detailed two method in four cases. Tumor percentage for the first and third image is acceptable. Second image: having huge tumor mass with individually fitted ellipses to the cells's contours' center do not cover the hole tumor area, tumor percentage is greately underrated with both metods. For the last image the calculated ratio is much bigger then it sould be because the hue of the normal tissue is similar to tumor region, so the method detect some healthy cells as tumor cells incorrectly, increasing the ratio.

IV. Conclusion

The presented tumor ratio calculating methods have their own weaknesses but they are good starting points for further development as the results highlighted the bottleneck of these calculators. Ellipses fitted to the center of the contours roughly took out tumor area, but they are not precise enough. Making difference between immune cells and tumor cells is the biggest challenge, but it has to be done very accurately for all types of samples (for all tumor hystology types).

V. Further plans

Using ellipses to cut out tumor area has to be rejected, a method should be developed which is able to draw round the real edges of tumor cells containing area tightly. After the likely tumor area will be tightly cut (closed lines along the edges, area calculated for all shapes) testing the method with thousands of sample images the immune cell specific size of shape will turn out, then usig the limits the immune cells could be exclude precisely.

VI. References

References

[1] B. Vogelstein, N. Papadopoulos, V. E. Velculescu, S. Zhou, L. A. Diaz, and K. W. Kinzler, "Cancer genome landscapes," *Science*, vol. 339, pp. 1546–1558, Mar 2013.
[2] M. M. Center, A. Jemal, J. Lortet-Tieulent, E. Ward, J. Ferlay, O. Brawley, and F. Bray, "International variation in prostate cancer incidence and mortality rates," *Eur. Urol.*, vol. 61, pp. 1079–1092, Jun 2012.
[3] J. Ferlay, E. Steliarova-Foucher, J. Lortet-Tieulent, S. Rosso, J. W. Coebergh, H. Comber, D. Forman, and F. Bray, "Cancer incidence and mortality patterns in Europe: estimates for 40 countries in 2012," *Eur. J. Cancer*, vol. 49, pp. 1374–1403, Apr 2013.
[4] A. P. Dhawan, G. Buelloni, and R. Gordon, "Enhancement of mammographic features by optimal adaptive neighborhood image processing," *IEEE Trans Med Imaging*, vol. 5, no. 1, pp. 8–15, 1986.
[5] Y. Tan, L. H. Schwartz, and B. Zhao, "Segmentation of lung lesions on CT scans using watershed, active contours, and Markov random field," *Med Phys*, vol. 40, p. 043502, Apr 2013.

Using two-photon imaging combined with simultaneous recordings to validate CSD analysis

Domokos MESZÉNA
(Supervisor: István ULBERT)
Pázmány Péter Catholic University, Faculty of Information Technology and Bionics
50/a Práter street, 1083 Budapest, Hungary
meszena.domokos@itk.ppke.hu

***Abstract*—This study aims to investigate several questions related to extracellularly recorded potentials of the underlying neural activity. We design an experimental method for analysing extracellular data focusing particularly on the patterns of transmembrane currents (CSD - Current Source Densities). The extracellular potential pattern can be easily re-calculated From the CSD distribution, but the inverse problem is not solvable (structurally non-identifiable). In other words, there are an infinite number of equally correct membrane current solutions for the given extracellular potential pattern. Our task is to assemble a new measurement tool to generate more reliable experimental data (practical identification process) and thus to improve the CSD analysis and the model fitting in single cell level. This complex set-up has been already tested on pre-experiments. We are able to record intra- and extracellular single cell activity (Patch-Clamp technique) and population activity (LFP) at the same time by using a multi-channel laminar microelectrode in vitro on rat or mice hippocampal slices. We integrate the electrophysiological measurements with a two-photon (2P) microscopy for imaging the cellular structure and for determining the exact electrode placements by optical investigation. The experimental method we describe here can determine crucial unknown parameters for CSD analysis such as the exact electrode-cell distance. Using the 2P microscope imaging technique during the recordings has a widespread impact, because we can uniquely specify the solution space of the CSD calculations. This complex experiment can be an important additional information for the further investigations of single cell dynamics.**

***Keywords*-Extracellular Recordings; LFP; Current sources and sinks; Physical models; Poisson equation; CSD analysis; Multi-Compartmental Models**

I. Introduction

The cortex of the brain consists of billions of neurons interconnected in complex neural networks. These neurons communicate with action potentials, which are standardized pulse-like alterations of the membrane potential (both positive and negative directions are allowed). In single-unit recordings, electrodes are positioned close to the neural cell body, and the firing rate is measured by counting *spikes*, which are the so called extracellular *signatures* of the action potentials.

However, complications may arise when more than one neuron are involved in the generation of extracellular potential pattern. For example, if two firing neurons have the same electrode-cell distance, it can be very difficult to differentiate the occurring spikes without knowing any further information about the neural structures [1]. Recently, multi-electrode arrays were developed (from 16 up to 512 channels) and automatic spike sorting algorithms were implemented to record hundreds of neurons simultaneously in one experiment [2]. Despite the technological advances, several aspects of extracellular potential generation remain poorly understood. The main, currently unsolved questions are the following:

- What is the origin of the great amplitude variability among extracellular potential patterns, while intracellular action potentials are so conserved? Can we calculate back the original governing currents from its produced potentials?
- Which are the most important parameters of the neural signal integration and output formation? Can we define an exact input-output function for the recorded neurons?
- How likely is that different neurons produce similar spike amplitude and thus they produce clustering problems and biased source localizations?

II. Background and Methods

A. Current source density analysis

The electrostatic background of the extracellular potentials has been quite well understood for decades. [8], [9] Due to the laws of electromagnetism, extracellular potentials are generated as result of ionic currents through the cell membrane. The equation (which describes how potentials are generated by electrical charges) is known as the Poisson equation in electrostatics (with the conductivity σ replaced by the dielectric constant ϵ).

In discrete case, the calculation of the averaged current source density (as the second spatial derivative of the potential) is the following:

$$\sigma \frac{d^2\Phi(x,t)}{dz^2} = -C(x,t) \tag{1}$$

$$C(x_j) = -\sigma \frac{\Phi(x_j+h) - 2\Phi(x_j) - \Phi(x_j-h)}{d_x^2} \tag{2}$$

Where the potential is neglected along the direction of the ortogonal z-y plane. (Smaller dendritic branches are neglected as well, we consider the neuron as a line source.) We note the current source density with C. The crucial and very non-linear distance parameter is denoted by d_x. The conductance is σ and Φ is the extracellular potential.

D. MESZÉNA, "Using two-photon imaging combined with simultaneous recordings to validate CSD analysis" in *PhD Proceedings Annual Issues of the Doctoral School, Faculty of Information Technology and Bionics, Pázmány Péter Catholic University – 2015.* G. Prószéky, P. Szolgay Eds. Budapest: Pázmány University ePress, 2015, pp 81– 84.

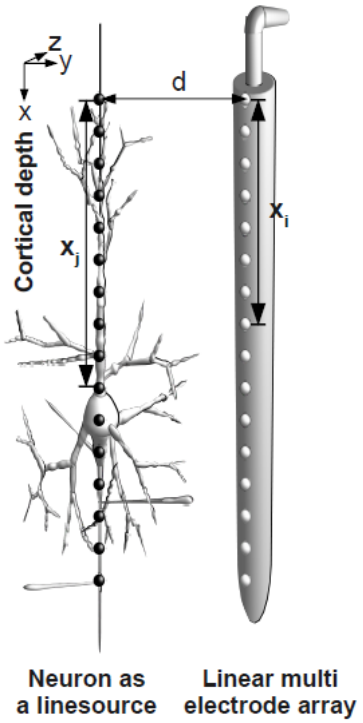

Fig. 1. The parallel position of the neuron and the electrode in optimal case. Along the array, white dots indicate the electrode contacts. On the neural axis, black dots denote the point sources. [6], [7]

To narrow down the possible solution space, we have to introduce more assumptions. The position of the neuron to the electrode has to be parallel, as it would be in the optimal case. On Fig. 1, white dots indicate the electrode contacts along the multi-electrode array. On the neural axis, black dots denote the negative and positive point sources (See Fig. 1). In general, the model has a main active current *sink* (meaning depolarization or positive ion influx from the point of view of the neuron), and a set of smaller *sources* (meaning hiperpolarizations, or positive ion outflow across the membrane). And there are still more assumptions regarding the isotropy of the extracellular field, the ohmic medium, frequency independent conductivities, etc. More details are described in Pettersen's works: [10].

B. Two-photon microscopy

Two-photon Ca^{2+} microscopy is a fluorescence imaging technique that allows for imaging of living tissue under specific conditions (both *in vivo* and *in vitro* methods are possible). In rat and mice experiments, such imaging studies have been restricted mostly to Ca^{2+} measurements from neurons that were individually dye-loaded through a Patch-pipette (glass microelectrode). The advantage of Ca^{2+} imaging is that it allows for real-time analysis of individual cells and even subcellular compartments.

The concept of two-photon excitation is based on the idea that two photons of lower energy than needed for one photon excitation can also excite a fluorophore in one quantum event [5]. The excitation results in the emission of a fluorescence photon, typically at a higher energy than either of the two excitatory photons. Therefore a high flux of excitation photons is required, which is usually generated by a *femtosecond laser* [4]. We use the Femto2D-uncage system (Femtonics, Budapest, Hungary) in our experiments.

The imaging laser wavelength is set to 900 nm (infrared range). The excitation is delivered to the sample, and the fluorescent signal is collected using lenses and separated using dichroic mirrors. For more technical details about the two-photon imaging system, see the works of G. Katona or B. Kerekes [3], [4]. It is worth to note, that two-photon excitation can be a superior alternative to confocal microscopy due to its deeper tissue penetration, efficient light detection, and reduced phototoxicity.

C. Simultaneous electrophysiology recordings

Patch-clamp recordings are made with glass microelectrodes (5-9 $M\Omega$) filled with special intracellular solution. The measurement set-up consists a MultiClamp 700B Amplifier and a data acquisition software, pClamp8 as well (both were provided by the Axon Instruments Company, Foster City, California). Cells are held at $-65mV$ in current clamp recordings.

Extracellular gradient recordings are recorded with a linear 24 channel multi-electrode array (Neuronelektród Kft.,

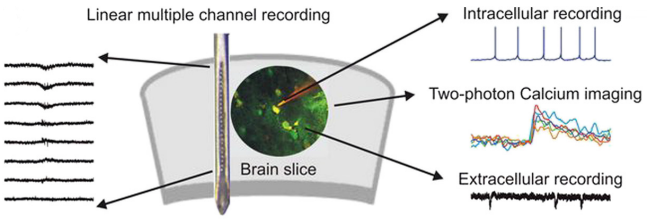

Fig. 2. Schematic flow chart of the complete recording process (with the courtesy of B. Kerekes from our research group) [3].

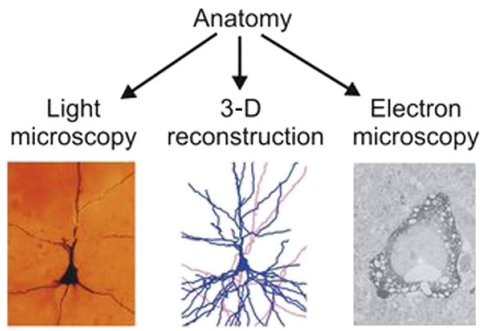

Fig. 3. Off-line anatomical investigation possibilities after the recordings (with the courtesy of B. Kerekes from our research group) [3].

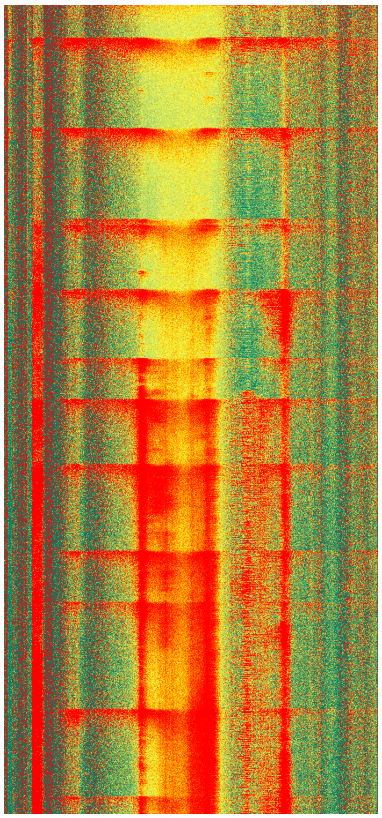

Fig. 4. "Line scan" mode Ca^{2+} activity measurements. This heatmap shows the activity of the same choosen CA3 layer neuron, which can be seen on the Fig. 5. It is strange at first sight, but the time is on the y-axis (from the top to the bottom) and spatial distribution is represented along the x-axis. *(Our group's unpublished picture)*

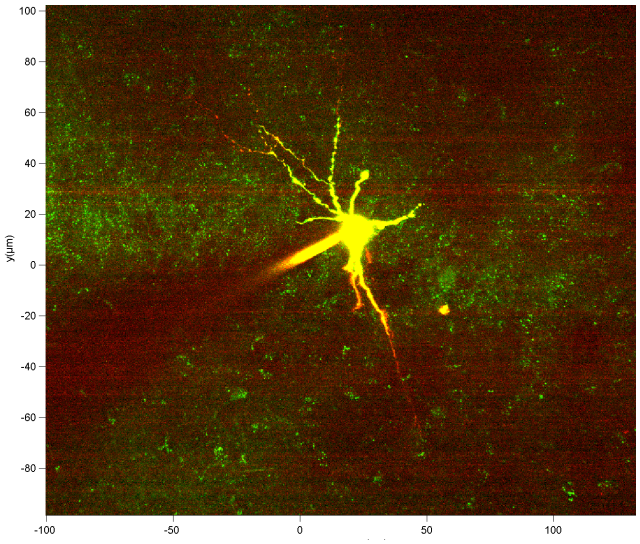

Fig. 5. Hippocampal CA3 layer neuron, fulfilled with fluorescent dye. Note the glass micropipette track and the illuminating color of the mixed dies. *(Our group's unpublished picture)*

Budapest, Hungary). Filtered and digitized signals can be analysed using LabView programs (written in our lab). The linear multi-electrode is placed on the surface of the brain slice. This way, the whole extent of the examined sample is covered and we are able to record simultaneously from different regions of interest.

In conclusion, the use of electrophysiology combined with two-photon imaging is very promising especially to achieve good temporal and spatial resolutions, respectively. And it has new application possibilities, such as cell-fullfilment and 3D reconstruction or local glutamatergic excitation. During the off-line processing, slices could be investigated using light or electron microscopy or with other histological techniques (Please see Fig. 2, Fig. 3 and for more details: [3]).

III. Results

Fig. 4 and Fig. 5 are the results from one of our experiments. On the first figure we can see a line scan process. This heatmap shows the activity of the same choosen CA3 layer neuron, which can be seen on the Fig.5. Please note, that Patch-Clamp method is capable of filling the neuron with tracer dye, thus reconstructing the complete cell morphology, which improves the CSD accuracy even further. On Fig. 5 we show a fulfilled neuron by using OGB-1 (green) and Alexa594 (red) fluorescent dies.

Recently, our group have successfully performed separated parts of the complete set-up. We already have acceptable Patch-Clamp, multi-electrode, and 2P Ca^{2+} signals. However, until now, we are still unable to integrate all of the parts at the same time. But the preliminary results are very promising, we plan to finish experimental design and execute the first complete measurements during the late summer. We also plan to present our achievements at some international conferences in the beginning of the next academic semester.

IV. Conclusion

This paper works on several questions related to extracellularly recorded potentials of the underlying neural activity. We design a new experimental method for validating extracellular data focusing particularly on the patterns of transmembrane currents (CSD - Current Source Densities). Our investigations are currently in the testing phase. We have described earlier the complex methodology, which has been already tested on pre-experiments. This method can determine the inter-electrode distance using the two-photon imaging technique and as a consequence, it can uniquely specify the solution space of the CSD calculations.

Finally, we can conclude, that these investigations can help us to understand neural communication dynamics better, thus in the future, they would be applicable even for the therapy of neural diseases.

ACKNOWLEDGMENT

The author would express deep gratitude to his supervisor, István Ulbert, D.Sc. for the promotion of the doctoral research work. In addition, the author wish to express thanks to Zoltán Somogyvari, ”Soma”, for his excellent advices, and to Bálint Kerekes and Ildikó Pál, for their technical assistances and their encouragements. This research has been funded by the KAP-1.1-14/032 Project.

REFERENCES

[1] Pettersen, K. H., Lindén, H., Dale, A. M., and Einevoll, G. T. (2012). Extracellular spikes and CSD. Handbook of Neural Activity Measurement, 92-135.

[2] Gold, C., Henze, D. A., Koch, C., and Buzsáki, G. (2006). On the origin of the extracellular action potential waveform: a modeling study. Journal of neurophysiology, 95(5), 3113-3128.

[3] Kerekes, B. P., Tóth, K., Kaszás, A., Chiovini, B., Szadai, Z., Szalay, G., ... and Wittner, L. (2014). Combined two-photon imaging, electrophysiological, and anatomical investigation of the human neocortex in vitro. Neurophotonics, 1(1), 011013-011013.

[4] Katona, G., Szalay, G., Mak, P., Kaszs, A., Veress, M., Hillier, D., ... and Rzsa, B. (2012). Fast two-photon in vivo imaging with three-dimensional random-access scanning in large tissue volumes. Nature methods, 9(2), 201-208.

[5] Denk, W., Strickler, J. H., and Webb, W. W. (1990). Two-photon laser scanning fluorescence microscopy. Science, 248(4951), 73-76.

[6] Somogyvári, Z., Zalányi, L., Ulbert, I., and Érdi, P. (2005). Model-based source localization of extracellular action potentials. Journal of neuroscience methods, 147(2), 126-137.

[7] Somogyvári, Z., Cserpán, D., Ulbert, I., and Érdi, P. (2012). Localization of singlecell current sources based on extracellular potential patterns: the spike CSD method. European Journal of Neuroscience, 36(10), 3299-3313.

[8] Nicholson, C., and Freeman, J. A. (1975). Theory of current source-density analysis and determination of conductivity tensor for anuran cerebellum. Journal of Neurophysiology, 38(2), 356-368.

[9] Mitzdorf, U. (1985). Current source-density method and application in cat cerebral cortex: investigation of evoked potentials and EEG phenomena. Physiological reviews, 65(1), 37-100.

[10] Pettersen, K. H., Devor, A., Ulbert, I., Dale, A. M., and Einevoll, G. T. (2006). Current-source density estimation based on inversion of electrostatic forward solution: effects of finite extent of neuronal activity and conductivity discontinuities. Journal of neuroscience methods, 154(1), 116-133.

Investigation of the subcellular distribution of CB_1 cannabinoid receptors with correlated confocal and superresolution STORM microscopy

Vivien MICZÁN
(Supervisor: István KATONA, András HORVÁTH)
Pázmány Péter Catholic University, Faculty of Information Technology and Bionics
50/a Práter street, 1083 Budapest, Hungary
miczan.vivien@itk.ppke.hu

***Abstract*—The operational principles and plasticity of chemical synapses in the brain cannot be understood without a better knowledge on the distribution and quantity of synaptic proteins. The endocannabinoid signalling system plays a key role in the regulation of neurotransmitter release in various different synapse types of the central nervous system. Nonetheless little is known about the regulation of the amount and subcellular distribution of the CB_1 cannabinoid receptor which is situated in axon terminals and mediates retrograde synaptic transmission. We choose STochastic Optical Reconstruction Microscopy (STORM) to study the nanoscale distribution of the CB_1 receptors, which offers a spatial resolution at an order of magnitude better than achievable with conventional light microscopy. We combined the STORM method with confocal microscopy to obtain superresolution data with cell- and compartment-specific context regarding the molecular distribution of the selected protein. We performed double anti-CB_1 and anti-neuroligin-2 fluorescent immunostaining on perfused mouse hippocampal slices and used correlated confocal and STORM imaging. We determined the location of the synapses with the help of the confocal image of the postsynaptic active zone marker neuroligin-2. We showed that CB_1 receptor number correlates with bouton size, and surprisingly, CB_1 receptor density was similar in the intrasynaptic and the extrasynaptic zone [14].**

***Keywords*-CB_1 cannabinoid receptor; STORM; confocal microscopy;**

I. Introduction

There are billions of neurons in the mammalian brain forming a myriad of synapses. Thousands of different proteins could play a role in maintaining these synapses, and the quality and quantity differ in specific diseases even in a cell or cell-type specific manner. Investigating the organization of these synapses is the main goal of molecular neuroanatomy, and quantitative examination of the synaptic signalling pathways can bring us closer to understanding the physiological and pathophysiological functions of the brain and could help designing new drugs to prevent and treat neurological diseases [20]. An example of this approach was the unvailing of the function of molecular constituents of the endocannabinoid system: the CB_1 cannabinoid receptor [11], the DGL-α (diacylglycerol-lipase-α) [10] and the MGL (monoacylglycerol-lipase) [7] enzymes. The endocannabinoid system is one of the most powerful regulator of synaptic transmission in the central nervous system and it acts in a retrograde manner as a synaptic circuit breaker preventing neurons from excessive synaptic activity [9]. This mechanism has pathophysiological role for example in stress-induced analgesia [16] and epilepsy [13]. In order to understand the various physiological and disease-related functions of the system in detail further examination is needed. CB_1 cannabinoid receptor is a key element in the system and is expressed in various regions of the central nervous system being the most frequent G-protein coupled receptor in the brain [12]. Its role in retrograde signalling and epileptic hyperactivity was first described in the hippocampus [18] [26] which is a cortical region, part of the limbic system and important in memory formation and spatial navigation [19]. The receptor is most abundant in the axon terminals of GABA-ergic axon terminals of the hippocampus [11] [23] but its role in modulating synaptic transmission is proven in both excitatory and inhibitory synapses [18] [26]. Its endogenous ligands are 2-AG (2-arachydonoylglycerol) and anandamide and an exogenous ligand is THC (Δ-9-tetrahidrocannabinol), the psychoactive component of Cannabis sativa [21]. Its abundance shows strong cell-type specificity and its amount changes in a different way in pathophysiological conditions: in epilepsy it is reduced in excitatory [13] and rises in inhibitory synapses [3]. The subcellular distribution of the receptor is an interesting question, since the distance of the receptors from their downstream effectors (voltage-gated calcium channels, which are situated in the active zone [27]) can play an important role in the signalling pathway. It was shown previously using electron microscopic imaging with immunogold staining that a domain-specific increase can be seen in the receptor number near synapses of hippocampal interneurons [17], however free diffusion of the receptors in the axon terminals were shown in neural culture by tracking quantum dots attached to the proteins [15]. So far no powerful method existed for studying the nanoscale domain-specific distribution of CB_1 receptors and their regulation, however it could help us understand physiological and pathophysiological processes in synaptic transmission. Our aim was to investigate the intracellular

V. MICZÁN, "Investigation of the subcellular distribution of CB1 cannabinoid receptors with correlated confocal and superresolution STORM microscopy" in *PhD Proceedings Annual Issues of the Doctoral School, Faculty of Information Technology and Bionics, Pázmány Péter Catholic University – 2015.* G. Prószéky, P. Szolgay Eds. Budapest: Pázmány University ePress, 2015, pp 85– 88.

compartment specific distribution of the CB_1 protein. In order to achieve this goal we combined two microscopy techniques: we used STORM superresolution microscopy [22] to individually register the 3 dimensional coordinates of the CB_1 localization points (LPs) and confocal microscopy to image the postsynaptic marker neuroligin-2 near the CB_1-positive terminals in order to put our STORM images into a subcellular context and compare synaptic and extrasynaptic areas based on distance and density measurements on the CB_1 LPs.

II. MATERIALS AND METHODS

A. Perfusion and preparation of tissue sections

All animal experiments were approved by the Hungarian Committee of the Scientific Ethics of Animal Research, and were performed according to the Hungarian Act of Animal Care and Experimentation. Minimal number of mice were sacrificed and all efforts were made to minimise pain.

Adult wild type C57BL/6 mice (n=3) were deeply anesthetised by intraperitoneal avertin injection and were transcardially perfused with 0.9% saline and 4% paraformaldehyde (PFA) solution (dissolved in 0.1 M Phosphate buffer, PB, pH 7.4). After perfusion brains were removed from the skull and postfixed in 4% PFA solution for 2 hours. 500 μm coronal sections were made using a Leica (Nussloch, Germany) VT-1000S vibratome, then the samples were embedded in 2% agarose and resliced in PB to achieve ideal section thickness (20 μm) for STORM imaging.

B. Immunostaining

Immunostaining was performed in 24-well plates in a free-floating manner. After washing in TBS buffer, nonspecific binding of antibodies was prevented by using 1% albumin from human serum (Sigma) dissolved in TBS. In order to help antibody penetration into cells, slices were treated with 0.3% Triton in TBS.

The following primary antibodies were used in TBS for overnight incubation on orbital shaker: guinea pig anti-CB_1 [6] 1:1000, rabbit anti-neuroligin-2 1:1000 (Synaptic Systems, catalog no. 129203). After several washing steps in TBS, slices were exposed to secondary antibodies for 2 hours in the following concentrations in TBS: anti-guinea pig Alexa-488-conjugated secondary antibody (Jackson) 1:400, anti-rabbit Alexa-647-conjugated secondary antibody (Jackson) 1:400. After washing in TBS and PB, slices were mounted and dried on #1.5 borosilicate coverslips which were previously cleaned with acetone. Coverslips with the samples were stored at $4\,^{\circ}\mathrm{C}$ until imaging. Right before STORM imaging slices were covered in imaging buffer optimized for STORM microscopy [4] and were placed on glass slides. The freshly prepared imaging medium contained the following ingredients: 5% glucose, 0.1 M mercaptoethylamine, 1 mg/ml glucose oxidase and catalase (2.5 μl/ml water-based solution from Sigma) dissolved in Dulbeccos PBS (Sigma). Coverslips were sealed with nail polish and imaged not more than 3 hours per sample.

C. Correlated confocal and STORM imaging

The following equipment was used for STORM and confocal imaging: CFI Apo TIRF 100x objective (NA: 1.49) and Nikon Ti-E inverted microscope equipped with Nikon N-STORM system, C2 confocal scanner and Andor iXon Ultra 897 EMCCD camera. 3D STORM experiment was possible by using a cylindrical lense [8]. Imaging was controlled with Nikon NIS-Elements AR software equipped with N-STORM module. A 300 mW laser (VFL-P-300-647, MPB Communications, Montreal, Canada) was used for STORM imaging. Region of interests were selected based on an image acquired by 488 nm illumination. 488 nm and 647 nm illumination was used for the confocal z-stack imaging (512x512x15 pixels, 78x78x150 nm resolution). DUAL filter cube (Nikon) and an EMCCD were used for STORM image acquisition. Low-intensity 405 nm activator (in order to achieve sparse activation of fluorophores) and high intensity 647 nm reporter illumination were used in 4000 cycles. A TIRF illuminator was utilized to prevent out-of-focus background. A Perfect Focus System was used to stabilise the focal plane. In order to minimise errors due to differences in antibody penetration, samples were collected from similar depths and only those localization points were counted that fell into a -300 to +300 nm range from the center plane to prevent errors caused by light scattering.

D. Correlated confocal and STORM analysis

Confocal stacks were deconvolved by using a classical maximum likelihood estimator algorithm with 40 iterations and theoretical point spread function with the Huygens software (SVI, Netherlands). STORM images were analysed with the STORM module of the NIS-Elements software to determine the coordinates of the localization points. Finding localization points and overlapping peaks was improved by a 3D-DAOSTORM algorithm [1]. Each image was analysed with the same parameters with the help of Python and AutoHotkey scripts.

E. Intrasynaptic/extrasynaptic density analysis

Intrasynaptic/extrasynaptic density analysis was performed by a custom-made script. Confocal image from the z-stack corresponding to the STORM data was selected. Axon terminals were chosen on the confocal image based on the following criteria: a neuroligin-2 cluster is placed on the postsynaptic side, and the synapse is not above or below the bouton. Manual registration of STORM and confocal images were performed which was made possible by the similar staining pattern in the CB_1 channel with both imaging modalities. A freehand selection of CB_1 localization points was performed to save coordinates for further analysis. Then a convex hull was placed on the outermost CB_1 LPs. Boundaries of the synapses were marked on the convex hull based on the neuroligin-2 confocal channel and the hull parts were assigned as synaptic or extrasynaptic. Distance of each CB_1 LPs from synaptic and extrasynaptic hull parts were measured and CB_1 receptors were assigned into synaptic and extrasynaptic sets based on

the distances (Fig. 1.). Density of LPs was defined by the ratio of the number of LPs in the set and the length of the corresponding convex hull part. Axon terminals belonging to the pyramidal layer of the hippocampal CA1 region (n=41) were taken into consideration and these boutons were selected from 3 animals.

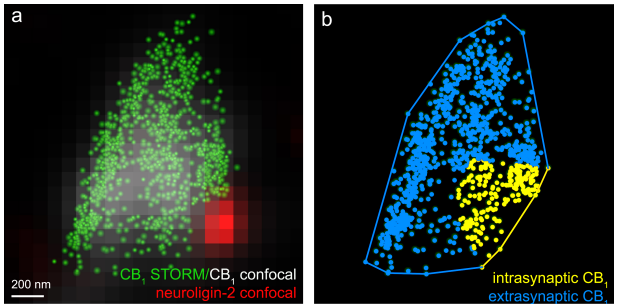

Fig. 1. Assigning CB_1 receptors into synaptic and extrasynaptic subsets based on the confocal image of the neuroligin-2 staining a) Correlated STORM anti-CB_1-staining (green) , and confocal image of anti-CB_1 (white) and anti-NLG2 (red) staining of the same bouton in hippocampal CA1 region. Position of the NLG2 signal marks the synapse. b) CB_1 localizations assigned as synaptic (yellow) or extrasynaptic (cyan) receptors on the same bouton based on their distance from the synaptic and extrasynaptic hull parts

F. Statistical analysis

Statistical analysis were performed using STATISTICA 12 software (StatSoft, Tulsa, OK). Normality analysis of data was performed by Kolmogorov–Smirnov test. Since the samples did not show normal distribution nonparametric tests were used. Pooling of individual animals were done after not significant Kruskal–Wallis test (bouton perimeter: p=0.7402, bouton CB_1 number: p=0.3732, intrasynaptic density: p=0.6334, extrasynaptic density p=0.068). Spearman rank correlation was used to compare bouton perimeter and CB_1 NLP. Sign test were used to compare intrasynaptic and extrasynaptic densities.

III. Results

CB_1 receptor regulates neurotransmitter release through the activity of voltage gated calcium channels which happens in the synaptic active zone. Therefore our goal was to investigate whether there is an increase in receptor density in the synaptic zone. To achieve this we performed STORM imaging of fluorescent-dye-tagged CB_1 receptors. On the single-channel STORM images active zone is not visible so a synaptic marker is essential. In order to avoid errors due to the crosstalk subtraction of dual-channel STORM images [2] and the crossreaction of antibodies we used single-channel STORM imaging combined with confocal imaging of the postsynaptic marker neuroligin-2 which visualizes inhibitory synapses [25][24].

A. CB_1 receptor number correlates with bouton size

First we wanted to know whether CB_1 number depends on the bouton size. A convex hull was fitted on the outermost CB_1 data and its length was measured. We found linear correlation between CB_1 localization point number and the approximated bouton perimeter (Fig. 2.). This lead us to the conclusion that CB_1 number per membrane length will be a good measure of receptor density.

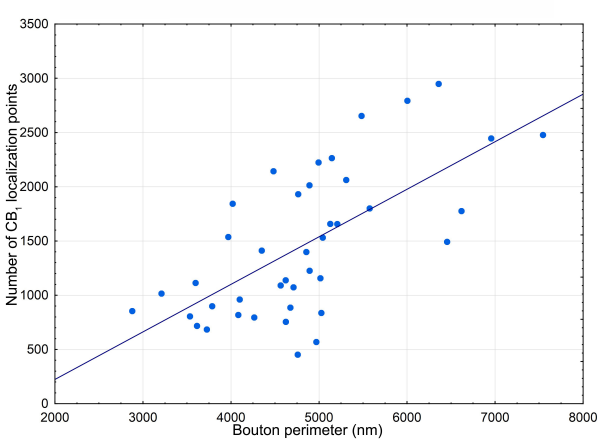

Fig. 2. Correlation of CB_1 receptor number and estimated bouton perimeter (n=41 boutons, n=3 animals, Spearman rank correlation, R=0.6463, $p<0.01$

B. CB_1 receptor density is similar in the intrasynaptic and extrasynaptic compartments in the axon terminals of hippocampal CA1 interneurons

CB_1 STORM coordinates and confocal images of anti-neuroligin-2 and anti-CB_1 immunostaining were overlaid using the CB_1 confocal channel. With the help of the neuroligin-2 signal the position of synapses could be determined and each CB_1 localization point was classified into a synaptic or extrasynaptic pool based on the distance from the synaptic and extrasynaptic hull parts. Then we measured both hull lengths and receptor numbers to calculate receptor densities.

We found that CB_1 density is similar in the synaptic and in the extrasynaptic zone.

IV. Discussion

Linear correlation between CB_1 LPs and bouton perimeter is in accordance with previous results of our research group [5]. usSince bigger boutons have more CB_1 recepors in a homogenous distribution we used the LP/perimeter ratio as a descriptor of receptor density. We found similar receptor densities in the two compartments which is a surprising regarding that CB_1 controls synaptic vesicle release which happens in the synaptic zone [27].However these data can fit well to the findings of Mikasova et al. where no specific anchoring mechanism of CB_1 receptors was shown near the active zone of axon terminals [15]. A possible explanation of the contradiction of these data with the previously reported elevation of perisynaptic CB_1 density [17]could be that electron microscopic measurements require dehydration of tissues which can cause anisotropic shrinkage of the samples so distance measurements can be distorted. This effect can be surpassed by STORM imaging which does not require dehydration of samples. This result raises both methodical and biologial questions, for example

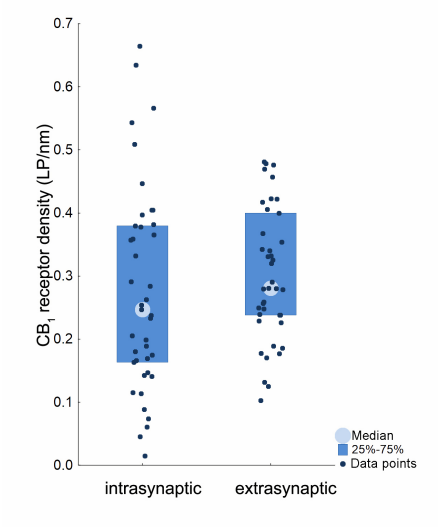

Fig. 3. CB_1 receptor density is similar in the synaptic and extrasynaptic zone. n=41 boutons, n=3 animals, Sign Test, p=0.1183

why CB_1 receptors are expressed in such a high number and why they are homogeneously distributed? What is the role of the CB_1 receptors which are in far away from the effector molecules? Superresolution microscopy can prove extremely useful in pursuing these quesstions.

Acknowledgment

I would like to thank my supervisors Dr. István Katona and Dr. András Horváth and Barna Dudok, László Barna, Balázs Pintér and Erika Tischler and all members of the Laboratory of Molecular Neurobiology of the IEM-HAS for help and support. Anti-CB_1 antibody was a gift from Masahiko Watanabe (University of Hokkaido, Sapporo, Japan).

References

[1] H. Babcock, Y. M. Sigal, and X. Zhuang, "A high-density 3d localization algorithm for stochastic optical reconstruction microscopy," *Opt Nanoscopy*, vol. 1, no. 6, 2012.

[2] M. Bates, B. Huang, G. T. Dempsey, and X. Zhuang, "Multicolor super-resolution imaging with photo-switchable fluorescent probes," *Science*, vol. 317, no. 5845, pp. 1749–53, 2007.

[3] K. Chen, A. Ratzliff, L. Hilgenberg, A. Gulyas, T. F. Freund, M. Smith, T. P. Dinh, D. Piomelli, K. Mackie, and I. Soltesz, "Long-term plasticity of endocannabinoid signaling induced by developmental febrile seizures," *Neuron*, vol. 39, no. 4, pp. 599–611, 2003.

[4] A. Dani, B. Huang, J. Bergan, C. Dulac, and X. Zhuang, "Superresolution imaging of chemical synapses in the brain," *Neuron*, vol. 68, no. 5, pp. 843–56, 2010.

[5] B. Dudok, L. Barna, M. Ledri, S. I. Szabo, E. Szabadits, B. Pinter, S. G. Woodhams, C. M. Henstridge, G. Y. Balla, R. Nyilas, C. Varga, S. H. Lee, M. Matolcsi, J. Cervenak, I. Kacskovics, M. Watanabe, C. Sagheddu, M. Melis, M. Pistis, I. Soltesz, and I. Katona, "Cell-specific storm super-resolution imaging reveals nanoscale organization of cannabinoid signaling," *Nat Neurosci*, vol. 18, no. 1, pp. 75–86, 2015.

[6] Y. Fukudome, T. Ohno-Shosaku, M. Matsui, Y. Omori, M. Fukaya, H. Tsubokawa, M. M. Taketo, M. Watanabe, T. Manabe, and M. Kano, "Two distinct classes of muscarinic action on hippocampal inhibitory synapses: m2-mediated direct suppression and m1/m3-mediated indirect suppression through endocannabinoid signalling," *Eur J Neurosci*, vol. 19, no. 10, pp. 2682–92, 2004.

[7] A. I. Gulyas, B. F. Cravatt, M. H. Bracey, T. P. Dinh, D. Piomelli, F. Boscia, and T. F. Freund, "Segregation of two endocannabinoid-hydrolyzing enzymes into pre- and postsynaptic compartments in the rat hippocampus, cerebellum and amygdala," *Eur J Neurosci*, vol. 20, no. 2, pp. 441–58, 2004.

[8] B. Huang, W. Wang, M. Bates, and X. Zhuang, "Three-dimensional super-resolution imaging by stochastic optical reconstruction microscopy," *Science*, vol. 319, no. 5864, pp. 810–3, 2008.

[9] I. Katona and T. F. Freund, "Endocannabinoid signaling as a synaptic circuit breaker in neurological disease," *Nat Med*, vol. 14, no. 9, pp. 923–30, 2008.

[10] I. Katona, G. M. Urban, M. Wallace, C. Ledent, K. M. Jung, D. Piomelli, K. Mackie, and T. F. Freund, "Molecular composition of the endocannabinoid system at glutamatergic synapses," *J Neurosci*, vol. 26, no. 21, pp. 5628–37, 2006.

[11] I. Katona, B. Sperlagh, A. Sik, A. Kafalvi, E. S. Vizi, K. Mackie, and T. F. Freund, "Presynaptically located cb1 cannabinoid receptors regulate gaba release from axon terminals of specific hippocampal interneurons," *J Neurosci*, vol. 19, no. 11, pp. 4544–58, 1999.

[12] D. M. Lovinger, "Presynaptic modulation by endocannabinoids," *Handb Exp Pharmacol*, vol. 184, no. 184, pp. 435–77, 2008.

[13] A. Ludanyi, L. Eross, S. Czirjak, J. Vajda, P. Halasz, M. Watanabe, M. Palkovits, Z. Magloczky, T. F. Freund, and I. Katona, "Downregulation of the cb1 cannabinoid receptor and related molecular elements of the endocannabinoid system in epileptic human hippocampus," *J Neurosci*, vol. 28, no. 12, pp. 2976–90, 2008.

[14] V. Miczan, "A szuperrezolucios storm kepalkotas felhasznalasa az idegtudomanyban," Masters's thesis, 2014.

[15] L. Mikasova, L. Groc, D. Choquet, and O. J. Manzoni, "Altered surface trafficking of presynaptic cannabinoid type 1 receptor in and out synaptic terminals parallels receptor desensitization," *Proc Natl Acad Sci U S A*, vol. 105, no. 47, pp. 18 596–601, 2008.

[16] R. Nyilas, L. C. Gregg, K. Mackie, M. Watanabe, A. Zimmer, A. G. Hohmann, and I. Katona, "Molecular architecture of endocannabinoid signaling at nociceptive synapses mediating analgesia," *Eur J Neurosci*, vol. 29, no. 10, pp. 1964–78, 2009.

[17] G. Nyiri, C. Cserep, E. Szabadits, K. Mackie, and T. F. Freund, "Cb1 cannabinoid receptors are enriched in the perisynaptic annulus and on preterminal segments of hippocampal gabaergic axons," *Neuroscience*, vol. 136, no. 3, pp. 811–22, 2005.

[18] T. Ohno-Shosaku, T. Maejima, and M. Kano, "Endogenous cannabinoids mediate retrograde signals from depolarized postsynaptic neurons to presynaptic terminals," *Neuron*, vol. 29, no. 3, pp. 729–38, 2001.

[19] J. O'Keefe and J. Dostrovsky, "The hippocampus as a spatial map. preliminary evidence from unit activity in the freely-moving rat," *Brain Research*, vol. 34, no. 1, pp. 171–175, 1971.

[20] P. Pacher, S. Batkai, and G. Kunos, "The endocannabinoid system as an emerging target of pharmacotherapy," *Pharmacol Rev*, vol. 58, no. 3, pp. 389–462, 2006.

[21] D. Piomelli, M. Beltramo, A. Giuffrida, and N. Stella, "Endogenous cannabinoid signaling," *Neurobiol Dis*, vol. 5, no. 6 Pt B, pp. 462–73, 1998.

[22] M. J. Rust, M. Bates, and X. Zhuang, "Sub-diffraction-limit imaging by stochastic optical reconstruction microscopy (storm)," *Nat Methods*, vol. 3, no. 10, pp. 793–5, 2006.

[23] P. Somogyi and T. Klausberger, "Defined types of cortical interneurone structure space and spike timing in the hippocampus," *J Physiol*, vol. 562, no. Pt 1, pp. 9–26, 2005.

[24] V. T. Takacs, T. F. Freund, and G. Nyiri, "Neuroligin 2 is expressed in synapses established by cholinergic cells in the mouse brain," *PLoS One*, vol. 8, no. 9, e72450, 2013.

[25] F. Varoqueaux, S. Jamain, and N. Brose, "Neuroligin 2 is exclusively localized to inhibitory synapses," *Eur J Cell Biol*, vol. 83, no. 9, pp. 449–56, 2004.

[26] R. I. Wilson and R. A. Nicoll, "Endogenous cannabinoids mediate retrograde signalling at hippocampal synapses," *Nature*, vol. 410, no. 6828, pp. 588–92, 2001.

[27] R. I. Wilson, G. Kunos, and R. A. Nicoll, "Presynaptic specificity of endocannabinoid signaling in the hippocampus," *Neuron*, vol. 31, no. 3, pp. 453–62, 2001.

Role of macrophages in energy homeostasis

Ágnes POLYÁK
(Supervisor: Krisztina J. KOVÁCS)
Pázmány Péter Catholic University, Faculty of Information Technology and Bionics
50/a Práter street, 1083 Budapest, Hungary
polyak.agnes@itk.ppke.hu

***Abstract*—Obesity is characterized by chronic low grade inflammation and an imbalance between energy intake and expenditure. Macrophages accumulate into adipose tissues but their role in energy homeostasis has not been elucidated yet.**

Impaired macrophage trafficking affects the development of obesity, mice with Cx3CR1 deficiency do not become obese after 10 weeks of fat enriched diet (FatED). We used this model to evaluate the role of macrophages in fat storage and fat usage.

White adipose tissue (WAT) is responsible for energy storage, while brown adipose tissue (BAT) expends energy. Macrophages accumulate into both tissues in response to FatED, express inflammatory cytokines and NPY. NPY promotes lipogenesis and adipogenesis and inhibits lipolysis, shifting the metabolic balance towards fat accumulation.

***Keywords*-brown adipose tissue, white adipose tissue, macrophage, NPY, energy homeostasis**

I. Introduction

Obesity is associated with chronic low grade inflammation and macrophage infiltration into adipose tissues [1][2][3]. However, little is known about the role of macrophages in the development of obesity. Numerous neurotransmitters, hormones, and factors have been implicated in coordinated control of energy homeostasis, centrally and peripherally [4]. Neuropeptide Y and its Y receptors are important players in the regulation of energy homeostasis. While their role in feeding regulation is well recognized, functions in other critical aspects of energy homeostasis are largely unknown [5]. In addition to expression and release in the central nervous system, NPY coexists and is co-released with norepinephrine (NE) from postganglionic sympathetic nerves [6], and can be expressed locally in peripheral tissues including adipose tissue [7][8][9]. The cellular source of NPY in adipose tissue is controversial. Kos et al. found NPY expression in human abdominal subcutaneous adipose tissue derived adipocytes, but not in preadipocytes [9]. On the contrary, Singer et al. showed that Npy gene expression in fat is primarily derived from adipose tissue macrophages (ATMs) in obese animals. They found elevated Npy expression in response to 16 weeks of HFD in EWAT, but not in inguinal subcutaneous, dorsal subcutaneous and brown adipose tissue [8]. NPY expression in BAT has not been proven yet.

Our aim was to investigate the NPY expression in BAT and to reveal the cellular source of NPY expression.

II. Materials and Methods

A. Animals and diet

Experiments were performed in male Cx3CR1 +/gfp, and Cx3CR1 gfp/gfp mice In these mice, the cx3cr1 gene was replaced by a gfp reporter gene such that heterozygote Cx3CR1+/gfp mice express GFP in cells that retain receptor function, whereas cells in homozygote Cx3CR1gfp/gfp (Cx3CR1/, knockout (KO)) mice are labeled with GFP and also lack functional Cx3CR1. [10].

Animals were housed in groups of 4-5/cage at the minimal disease (MD) level of the Medical Gene Technology Unit of the Institute, had free access to food and water and were maintained under controlled conditions: temperature, 21 °C $\pm$ 1 °C; humidity, 65%; light-dark cycle, 12-h light/12-h dark cycle, lights on at 07:00. At 35 days of age both Cx3CR1 +/gfp (n=8) and Cx3CR1 gfp/gfp (n=10) mice were randomly distributed into two equal groups. The first group, normal diet (ND), received standard chow [VRF1 (P), Special Diets Services (SDS), Witham, Essex, UK calorie content: 14,24 KJ/g]. The second group received fat-enriched diet (FatED), by providing a 2:1 mixture of standard chow and lard (Spar Budget, Budapest, Hungary). The calorie content of this mixture is 22,02 KJ/g). All procedures were conducted in accordance with the guidelines set by the European Communities Council Directive (86/609 EEC) and approved by the Institutional Animal Care and Use Committee of the Institute of Experimental Medicine (permit numbers: PEI/001/35-4/2013 and PEI/ 001/29-4/2013).

B. Experimental design

Mice were fed with ND or FatED. After 10 weeks mice were decapitated, epididymal white adipose tissue (EWAT) and interscapular brown adipose tissue were collected, sampled and stored at -70°C for RT-PCR, or fixed in 4% buffered paraformaldehyde for histology.

C. NPY immunohistochemistry

Tissues were fixed by immersion in 4% paraformaldehyde in 0.1 M phosphate buffer, pH 7.4 (PB) for 3 days. Subsequently, they were stored in 1% paraformaldehyde in 0.1 M PB at 4°C. Tissues were paraffin-embedded, sectioned and mounted on glass slides. NPY staining was performed by the standard immunohistochemical method. The slides were deparaffinized in xylene (3 x 5 min) and hydrated in 100% ethanol (2 x 5 min) and 96, 70, 50% ethanol for 5 min each. Following KPBS washes (2 x 5 min) endogenous peroxidase was blocked by

Á. POLYÁK, "Role of macrophages in energy homeostasis" in *PhD Proceedings Annual Issues of the Doctoral School, Faculty of Information Technology and Bionics, Pázmány Péter Catholic University – 2015.* G. Prószéky, P. Szolgay Eds. Budapest: Pázmány University ePress, 2015, pp 89– 92.

incubation for 10min with 0.3% H2O2. After KPBS washes (4 x 5 min) antigen retrieval was performed with 10mM citrate buffer (pH 6.0) in a pressure cooker for 2 x 20min. After washes in KPBS, nonspecific binding was blocked by 2% normal goat serum (diluted in dilution solution (DS)(0.3% Triton X-100 + 0.02% sodium azide in KPBS)) for 60min. The sections were incubated with rabbit anti-mouse NPY (4RG2 kindly provided by R. Corder, Geneva, Switzerland) antibody diluted 1:1000 in DS for overnight at 4°C. Following KPBS washes (4 x 5 min), slides were incubated for 60min using biotinylated goat anti-rabbit (1:1000 in DS, Vector Laboratories, Burlingame, CA). After rinsing in KPBS, avidin biotin amplification was performed with a Vectastain Elite ABC kit (Vector Laboratories). Washes in KPBS (4 x 5 min) and 0.1M sodium acetate were performed and immunoreactivity was visualized with nickel-enhanced diaminobenzidine (DAB-Ni) substrate: 20 mg 3,3-Diaminobenzidine tetrahydrochloride hydrate (DAB; Sigma-Aldrich, St. Louis, MO) + 10 ml distillated water + 10 ml 3% nickel-ammonium sulfate in 0.2 M sodium acetate buffer + 300 μl 0.3% H2O2 for 5 min.

D. Cell culture

Raw 264.7 murine macrophage cells were purchased from the American Type Culture Collection (ATCC) and cultured in Dulbeccos Modified Eagles Medium (DMEM, high glucose) with 10% fetal bovine serum, 100 units/mL penicillin and 100 ng/mL streptomycin (Invitrogen) at 37°C with 5% CO2 in humidified air. Cells were treated with LPS (055:B5 serotype, 0.1 μg/ml), insulin (1 μM), leptin (20 nM) and harvested after 24 h.

E. Gene expression analysis by quantitative real-time PCR

For total RNA isolation, adipose tissue blocks and RAW cells were homogenized in TRI Reagent (Ambion). Total RNA was isolated using Total RNA Mini Kit (Geneaid) according to the manufacturer's instructions. To eliminate genomic DNA contamination, DNase I treatment was introduced (1 U/reaction, reaction volume: 50 μl RNase-free DNase I, Fermentas). Sample quality control and the quantitative analysis were carried out by NanoDrop (Thermo Scientific). cDNA synthesis was performed with the High Capacity cDNA Reverse Transcription Kit (Life Technologies) according to the manufacturer's instructions.

The chosen primer sequences used for the comparative CT experiments were verified with the Primer Express 3.0 program. The primers (Microsynth) were used in real-time PCR reaction with Fast EvaGreen qPCR Master Mix (Biotium, USA, CA) on an ABI StepOnePlus instrument. The gene expression was analyzed using the ABI StepOne 2.1 program. The amplicons were tested by Melt Curve Analysis on ABI StepOnePlus instrument. Experiments were normalized to gapdh expression.

F. Primer design

Primers used for the comparative CT (threshold cycle) experiments were designed by the Primer Express 3.0 program. Primer sequences were the following:

GAPDH:f: TGA CGT GCC GCC TGG AGA AA r: AGT GTA GCC CAA GAT GCC CTT CAG

GFP: f: GGA CGA CGG CAA CTA CAA GA r: AAG TCG ATG CCC TTC AGC TC

NPY: f: CAGATACTACTCCGCTCTGCGACACTACAT r: TTCCTTCATTAAGAGGTCTGAAATCAGTGT

Y1R: f: TGATCTCCACCTGCGTCAAC r: ATGGCTATG-GTCTCGTAGTCAT

Y2R: f: ATCATCTTGCTAGGGGTAGTTGG r: CGGACC-CATTTTCCACTCTCC

Y5R f: GTGAACTTTCTCATAGGCAACCT r: GCAT-GATATGGCACATGGCTTT

G. Statistical analysis

The results are shown as means $\pm$ SEM. Statistical analysis was performed by factorial ANOVA with NewmanKeuls post-hoc test in Statistica 11 (StatSoft Inc.). In all cases $p < 0.05$ was considered significant.

III. RESULTS

In response to FatED NPY expression was elevated both in BAT and EWAT in +/gfp mice (BAT: 6.3 fold, treatment effect: $F(1,10) = 34.06$, $p < 0.01$; genotype effect: $F(1,10) = 20.48$, $p < 0.001$; treatment * genotype: $F(1,10) = 21.98$, $p < 0.001$; EWAT: 68 fold, treatment effect: $F(1,14) = 31.57$, $p < 0.001$; genotype effect: $F(1,14) = 22.72$, $p < 0.001$; treatment * genotype: $F(1,14) = 24.44$, $p < 0.001$). We found differences in expression of NPY receptors only in BAT. Y1 receptor mRNA elevated only in +/gfp Cx3CR1 FatED mice (treatment effect: $F(1,11) = 17.61$, $p < 0.01$; treatment * genotype: $F(1,11) = 7.58$, $p < 0.05$), while Y2 receptor mRNA elevated in both FatED groups (treatment effect: $F(1,11) = 17.74$, $p < 0.05$) (Fig.1A-B))

To reveal the cellular source of NPY in adipose tissues, we performed an NPY immunohistochemistry. In obese WAT, macrophages surround dead or dying adipocytes, and form crown like structures (CLS). We found NPY positive cells forming CLS in +/gfp FatED EWAT (Fig.1D). As expected, based on the qPCR results, we also found NPY positive cells present in groups in the BAT of +/gfp FatED mice (Fig.1C).

As NPY mRNA expression seemed to change similarly as inflammatory cytokines measured previously, we made a correlation analysis between NPY and inflammatory cytokines in BAT and WAT. NPY positively correlated with GFP (previously we used GFP expression to evaluate the amount of macrophages in the tissue) and inflammatory cytokines in both tissues (Table 1.), suggesting that NPY is an inflammatory marker.

To support our findings, as macrophages express NPY, we treated macrophage cell cultures with LPS, insulin and leptin to induce NPY expression. NPY expression was elevated in response to all treatments, but LPS had the greatest effect (Fig.2A). LPS also induced inflammatory cytokine (TNFa, MCP-1, FKN) expression in RAW cells (Fig.2B).

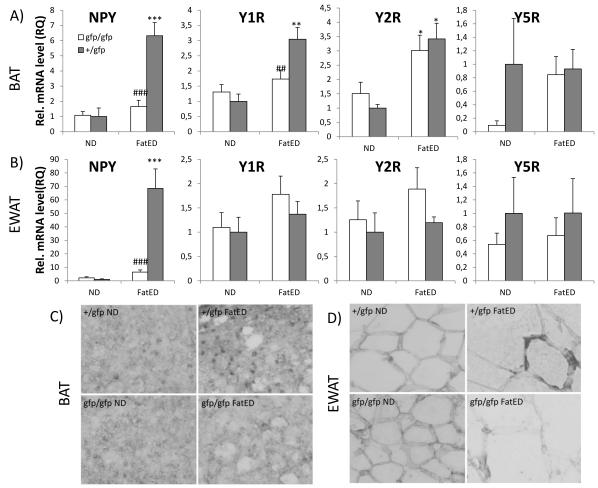

Fig. 1. Relative mRNA expression of NPY and its receptors in BAT and WAT. NPY immunohistochemistry in BAT and WAT.

BAT						
NPY vs.	GFP	FKN	MCP-1	IL1a	IL1b	TNFa
r	0.6117	0.8234	0.6646	0.7035	0.7074	0.6745
p	0.020	0.000	0.010	0.005	0.005	0.008
EWAT						
NPY vs.	GFP	FKN	MCP-1	IL1a	IL1b	TNFa
r	0.8031	0.6038	0.9193	0.5837	0.7570	0.8319
p	0.001	0.029	0.000	0.036	0.003	0.000

TABLE I
CORRELATIONS BETWEEN NPY AND GFP, AND NPY AND INFLAMMATORY MARKERS IN BAT AND WAT.

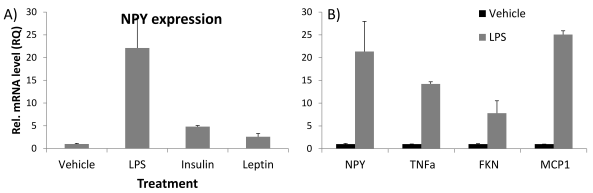

Fig. 2. Relative mRNA expression of NPY in vehicle, LPS, insulin and leptin treated RAw264.7 macrophage cell culture. Expression of NPY and inflammatory markers in LPS treated cell culture

IV. DISCUSSION

We described for the first time that NPY expression is upregulated in response to FatED in the BAT. We provide evidence that adipose tissue macrophages are the source of local NPY expression in BAT and WAT and NPY can be regarded as an inflammatory marker.

We showed previously that in response to FatED macrophages infiltrate into WAT and BAT of control mice and express inflammatory cytokines, while the development of obesity is attenuated in fractalkine receptor deficient mice. These mice are prone to obesity, macrophages do not infiltrate into the tissues, and the levels of inflammatory cytokines are lower [11][12]. As fractalkine plays a significant role in macrophage trafficking, and we did not found infiltrated macrophages in fractalkine deficient FatED fed mice [12], we used this model to reveal the role of macrophages in energy homeostasis.

Elevated NPY expression was detected in the BAT and WAT of FatED fed control mice, while in gfp/gfp Cx3CR1 mice lack of macrophage infiltration is associated with low level of NPY. Our results are in accord with the results of others who found attenuated high-fat diet induced weight gain, fat accumulation, decreased expression of inflammatory cytokines and genes involved in lipogenesis and gluconeogenesis, lack of CLS in WAT-macrophage depleted mice [13], suggesting that macrophages participate in the regulation of lipogenesis and the development of obesity. Regulation of adipogenesis/lipogenesis and lipolysis is also affected by NPY. In NPY knockout mice WAT mass was reduced, expression of genes involved in adipogenesis/lipogenesis was found to be decreased, whereas proteins involved in lipolysis increased in gonadal WAT. In 3T3-L1 cells, administration of NPY inhibits lipolysis through the Y1 receptor, and stimulates lipogenesis following a reduction in cAMP response element-binding protein (CREB) and SIRT1 protein expression [14].

Unlike WAT, NPY expression in BAT has not been reported yet. We found elevated Y1R and Y2R in control FatED mice, but in gfp/gfp Cx3CR1 mice only Y2R was upregulated, suggesting that in our model the effect of Y1R dominates. NPY acting on Y1 receptors has an anti-lipolytic effect in adipose tissue [5][15], activation of Y2R stimulates fat angiogenesis, macrophage infiltration, and the proliferation and differentiation of new adipocytes, resulting in abdominal obesity and a metabolic syndrome-like condition [16]. Y1R in macrophages transmit anti-inflammatory effect inhibiting MCP-1 and TNF release [17].

Positive correlation between NPY and inflammatory cytokine expression in both BAT and WAT suggest that the sources of local NPY expression are the macrophages. Using RAW 264.7 macrophage cell culture we proved that significant NPY expression can be induced by proinflammatory stimuli like LPS, in macrophages.

In conclusion our results suggest that in response to FatED macrophages accumulate into BAT and WAT of control mice, they express NPY, which acts on Y1R to inhibit lipolysis, and on Y2R to promote lipogenesis, adipogenesis and angiogenesis, leading to fat accumulation and obesity (Fig.3). While in gfp/gfp Cx3CR1 mice, where macrophage infiltration is impaired, lack of excess NPY results in the maintenance of lipolysis/lipogenesis balance, and normal body weight.

REFERENCES

[1] G. Ghigliotti, C. Barisione, S. Garibaldi, P. Fabbi, C. Brunelli, P. Spallarossa, P. Altieri, G. Rosa, G. Spinella, D. Palombo, R. Arsenescu, and V. Arsenescu, "Adipose tissue immune response: novel triggers and consequences for chronic inflammatory conditions," *Inflammation*, vol. 37, no. 4, pp. 1337–53, 2014.

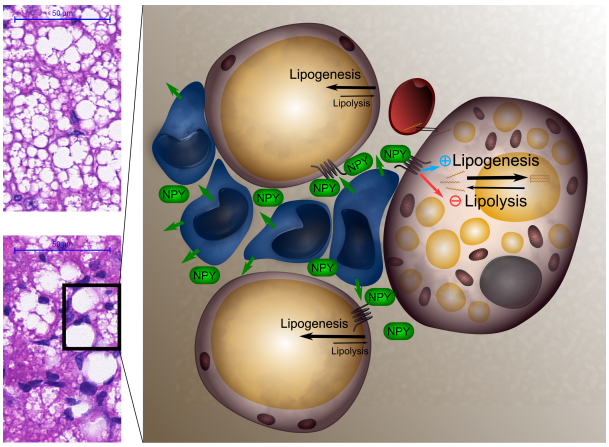

Fig. 3. During obesity macrophages accumulate into the adipose tissues, white and brown adipocytes, and lipid droplets enlarge. Macrophages express NPY, which acting on NPY receptors shifts the lipolysis/lipogenesis balance towards fat accumulation.

[2] N. Esser, S. Legrand-Poels, J. Piette, A. J. Scheen, and N. Paquot, "Inflammation as a link between obesity, metabolic syndrome and type 2 diabetes," *Diabetes Research and Clinical Practice*, vol. 105, no. 2, pp. 141–150, 2014.

[3] N. Lanthier and I. A. Leclercq, "Adipose tissues as endocrine target organs," *Best Practice & Research in Clinical Gastroenterology*, vol. 28, no. 4, pp. 545–558, 2014.

[4] K. Loh, H. Herzog, and Y. C. Shi, "Regulation of energy homeostasis by the npy system," *Trends Endocrinol Metab*, vol. 26, no. 3, pp. 125–35, 2015.

[5] L. Zhang, L. Macia, N. Turner, R. F. Enriquez, S. J. Riepler, A. D. Nguyen, S. Lin, N. J. Lee, Y. C. Shi, E. Yulyaningsih, K. Slack, P. A. Baldock, H. Herzog, and A. Sainsbury, "Peripheral neuropeptide y y1 receptors regulate lipid oxidation and fat accretion," *International Journal of Obesity*, vol. 34, no. 2, pp. 357–373, 2010.

[6] M. P. Owen, "Similarities and differences in the postjunctional role for neuropeptide-y in sympathetic vasomotor control of large vs small arteries of rabbit renal and ear vasculature," *Journal of Pharmacology and Experimental Therapeutics*, vol. 265, no. 2, pp. 887–895, 1993.

[7] K. P. Yang, H. Y. Guan, E. Arany, D. J. Hill, and X. A. Cao, "Neuropeptide y is produced in visceral adipose tissue and promotes proliferation of adipocyte precursor cells via the y1 receptor," *Faseb Journal*, vol. 22, no. 7, pp. 2452–2464, 2008.

[8] K. Singer, D. L. Morris, K. E. Oatmen, T. Wang, J. DelProposto, T. Mergian, K. W. Cho, and C. N. Lumeng, "Neuropeptide y is produced by adipose tissue macrophages and regulates obesity-induced inflammation," *PLoS One*, vol. 8, no. 3, p. e57929, 2013.

[9] K. Kos, A. L. Harte, S. James, D. R. Snead, J. P. O'Hare, P. G. McTernan, and S. Kumar, "Secretion of neuropeptide y in human adipose tissue and its role in maintenance of adipose tissue mass," *American Journal of Physiology-Endocrinology and Metabolism*, vol. 293, no. 5, pp. E1335–E1340, 2007.

[10] S. Jung, J. Aliberti, P. Graemmel, M. J. Sunshine, G. W. Kreutzberg, A. Sher, and D. R. Littman, "Analysis of fractalkine receptor cx(3)cr1 function by targeted deletion and green fluorescent protein reporter gene insertion," *Molecular and Cellular Biology*, vol. 20, no. 11, pp. 4106–4114, 2000.

[11] A. Polyak, S. Ferenczi, A. Denes, Z. Winkler, R. Kriszt, B. Pinter-Kubler, and K. J. Kovacs, "The fractalkine/cx3cr1 system is implicated in the development of metabolic visceral adipose tissue inflammation in obesity," *Brain Behav Immun*, vol. 38, pp. 25–35, 2014.

[12] A. Polyak, "Fractalkine/cx3cr1 signaling in brown adipose tissue and diet induced obesity," FACULTY OF INFORMATION TECHNOLOGY & BIONICS, PZMNY PTER CATHOLIC UNIVERSITY, Tech. Rep., 2014.

[13] L. Bu, M. M. Gao, S. Qu, and D. X. Liu, "Intraperitoneal injection of clodronate liposomes eliminates visceral adipose macrophages and blocks high-fat diet-induced weight gain and development of insulin resistance," *Aaps Journal*, vol. 15, no. 4, pp. 1001–1011, 2013.

[14] S. Park, C. Fujishita, T. Komatsu, S. E. Kim, T. Chiba, R. Mori, and I. Shimokawa, "Npy antagonism reduces adiposity and attenuates age-related imbalance of adipose tissue metabolism," *Faseb Journal*, vol. 28, no. 12, pp. 5337–5348, 2014.

[15] M. Labelle, Y. Boulanger, A. Fournier, S. St Pierre, and R. Savard, "Tissue-specific regulation of fat cell lipolysis by npy in 6-ohda-treated rats," *Peptides*, vol. 18, no. 6, pp. 801–8, 1997.

[16] L. E. Kuo, J. B. Kitlinska, J. U. Tilan, L. Li, S. B. Baker, M. D. Johnson, E. W. Lee, M. S. Burnett, S. T. Fricke, R. Kvetnansky, H. Herzog, and Z. Zukowska, "Neuropeptide y acts directly in the periphery on fat tissue and mediates stress-induced obesity and metabolic syndrome," *Nat Med*, vol. 13, no. 7, pp. 803–11, 2007.

[17] L. Macia, E. Yulyaningsih, L. Pangon, A. D. Nguyen, S. Lin, Y. C. Shi, L. Zhang, M. Bijker, S. Grey, F. Mackay, H. Herzog, and A. Sainsbury, "Neuropeptide y1 receptor in immune cells regulates inflammation and insulin resistance associated with diet-induced obesity," *Diabetes*, vol. 61, no. 12, pp. 3228–3238, 2012.

Investigation of neural stem cells' response to nanostructured biosensor surfaces

Zsófia BÉRCES
(Supervisor: Anita PONGRÁCZ, Kristóf IVÁN)
Pázmány Péter Catholic University, Faculty of Information Technology and Bionics
50/a Práter street, 1083 Budapest, Hungary
berces.zsofia@itk.ppke.hu

***Abstract*—Surface quality of implantable biosensors for recording electrical signals in the central nervous system is of great importance with respect to long-term use in chronic animal experiments. In our work the interaction of cell cultures and nanotextured surfaces was investigated as a model of implanted device surface and living tissue interaction. We have developed a robust, maskless nanostructuring method, which can be integrated into our neural biosensor fabrication process. Morphology of the fabricated nanograss has been characterised using scanning electron microscopy. The nanopillars are between 520-800 nm in height and their density is 18-70/μm^2. The specific surface area is 30 times larger compared to the reference. GFP-NE-4C cells are cultured on the nanostructured and platinized surfaces and are investigated by fluorescent microscopic imaging.**

***Index Terms*—neural implant; nanostructuring; biocompatibility**

I. Introduction

Cells in their natural environment interact with nanoscale structures like the extracellular matrix and its proteins. In case of fibroblasts and osteoblasts it is already demonstrated that surfaces with specific surface roughness parameters show better cell adhesive properties [1]. On the other hand, there are only a few results in the case of neural and glial cells. In 1997, Turner et al. showed lower astrocyte adhesion on nanostructured samples compared to smooth ones using immortalized cell line. In the same article, the authors presented that primer neural and glial cells react the other way around [2]. Later on many groups investigated neural cell adhesion on nanostructured biosurfaces. Most of them used porous silicon [3]–[5] or etched Si surfaces with nanometer scale structures [6]–[10]. In other cases, they used different materials, such as GaP [11] or polymers [12]. These experiments aimed to enhance neural implant efficiency and make the implants capable of conducting chronic in vivo experiments. Other groups have concluded that surface nanostructuring can be used to examine self-developing neural circuits [8] and it is also capable of neurite guiding [4], [8]. As a result, this substrate preparation approach is suitable for modelling neural circuits.

By modulating the specific surface area, wetting properties and nano-pattern regularity of the nanostructured samples, several groups published better neural cell adhesion and viability on nanostructured surfaces compared to the smooth references in the past few years [7], [10], [11], [13]. In 5-day long experiments, neural cells showed surface preference. They were observed to migrated to nanostructured parts of the sample [9]. In the case of neuroprosthesis in living tissue, the reaction of the surrounding glial cells is as important as the adhesion of the neurons. The astrocytes and microglias are key factors in neuron metabolism and function. They play an emphatic role as the protectors of the central nervous system against diseases and injuries. In case of physical injury such as the microelectrode implantation they generate an aggressive neuroprotective reaction called gliosis [14]. As a result, the so-called glial scar remains around the injury and the foreign body which hinders electrical recordings. As a consequence in neural implant surface development it is also important to investigate the neuroprotective reaction of the glial cells to the proposed surface. Since these cells work in a close cooperation with neurons and also with each other, it is also important to examine them in tissue-like co-cultures. It was also shown that after brain injury specific cells acquire stem cell properties and take a very important role in the wound healing process [15], [16].

My work aims to develop bioimplant surfaces with nanoscale patterns using novel combination of micro- and nanomachining techniques. The proposed maskless nanopatterning method can easily be integrated into the fabrication process of neural microelectrodes. The expected results are envisioned to minimize the immune response of the neural tissue to the surface of the implanted microelectrodes and thus enable efficient functionality in long-term experiments. As a model for the tissue-implant interface a cell line with neural stem cell like properties is investigated on the designed implant surface samples. Adhesion and differentiation of the stem cells on the surfaces can be a forecast for the behavior of the stem cells in-vivo upon the injury caused by the implant insertion.

II. Materials and Methods

A. Sample design and fabrication

My investigations are based on fluorescent microscopic measurements of cell adhesion. To measure the preferential behaviour of cells on nanostructured and smooth reference surfaces, micropatterned chips are designed. Patterns are in the range of the contact site of a microelectrode array usually used for neural recording. Figure 1 A) shows the micro pattern of the Si wafer. Different type of chips are marked with arrows.

Z. SZTYÉHLIKNÉ BÉRCES, "Investigation of neural stem cells' response to nanostructured biosensor surfaces" in *PhD Proceedings Annual Issues of the Doctoral School, Faculty of Information Technology and Bionics, Pázmány Péter Catholic University – 2015.* G. Prószéky, P. Szolgay Eds. Budapest: Pázmány University ePress, 2015, pp 93– 96.

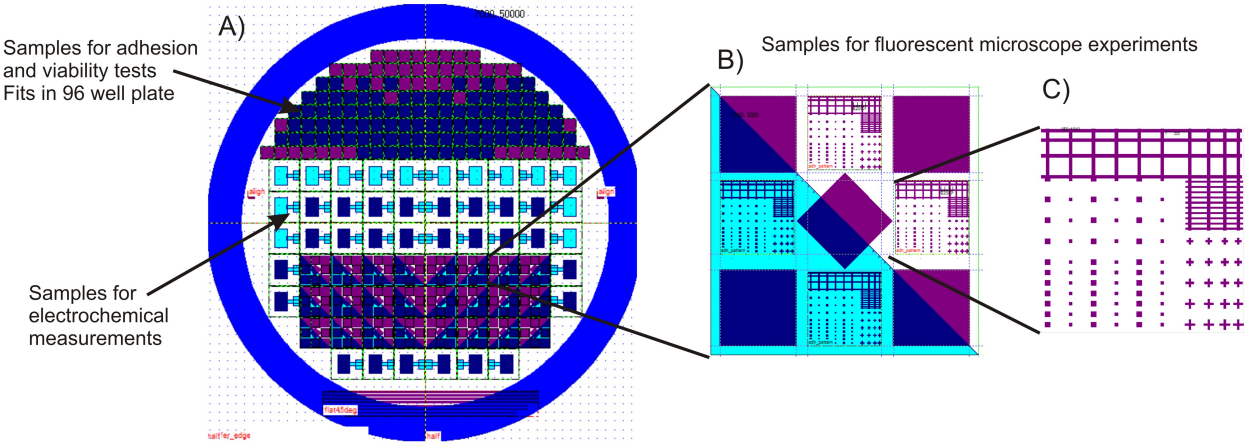

Fig. 1. A) Layout of the pattern to be transferred on the Si wafer. Light blue shows platinum, purple represents black silicon covered areas without platinum coating and dark blue areas represent platinum coated black silicon. The samples for different experiments can be seen. B) Sample for fluorescent measurements. C) Part of the sample shown on B). Different microstructures are designed based on literature or inspired by our microelectrode (contact site sizes and spacing).

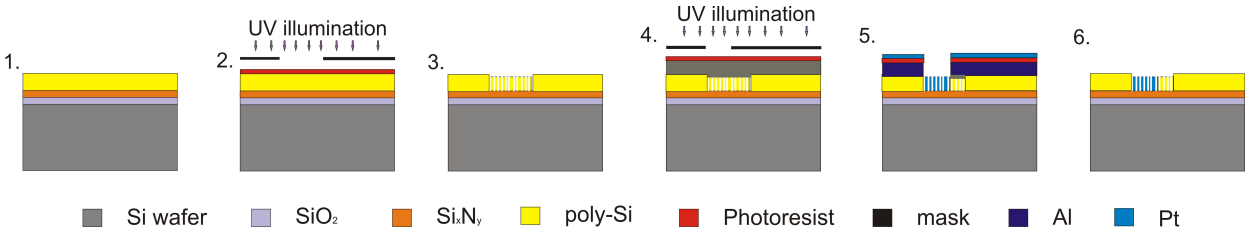

Fig. 2. Schematic process flow of the fabrication method.

Figure 1 B and C show the map of a chip for fluorescent microscopy measurements. During the fabrication process first, 500 nm thick thermal oxide is grown on a 4" (100) oriented Si wafer. Then 1000 nm poly-Si is deposited in a Tempress LPCVD equipment. The micropatterning of the black-Si is performed by photolitography and microstructured in poly-etchant. Nanopattern formation is carried out by deep reactive ion etching (DRIE) at cryogenic temperature. After black-Si formation platinum deposition is performed and followed by a second patterning step using lift-off process. Figure 2 shows the schematic process flow of the fabrication method. Chips with no nanostructures but with the same ecthed micropatterns as the nanostructured ones were also fabricated to investigate the effect of edges to the cellular behavior. Advantages of the process are that the nanostructuring is maskless and it can fully be integrated into an implantable Si microelectrode fabrication process.

B. Surface characterisation

The effect of the different etching parameters and platinum layer thicknesses is investigated using SEM. From the images the pillar height and density parameters of the fabricated samples are also extracted.

C. Cell culturing

1) Sample preparation: The fabricated silicon wafers were diced to fit in the 24 well plates. Chip size is $7,3x7,3$ mm. Samples were soaked in 70% etanol for 20 mins in order to be sterilised. Samples shown on 1 B were placed into 24 well plates and one of each type were coated with poly-L-lysine (PLL) to enhance adhesion. Arrangement is shown on Figure 3. For the PLL coating samples were immersed into PLL solution of 0,5 μg PLL in 100ml PBS. After 20 minutes of incubation solution was removed and the samples were dried.

2) Cell line: The GFP-NE-4C cell line is a neuroectodermal cell line derived from embrionic forebrain vesicles of p53 deficient mices [18]. Cells express green fluorescent protein (GFP) in the cell plasm. GFP emits green light upon illumination of approx. 480 nm blue light therefore is capable of flurescent imaging.

3) Culturing and fixation method: 10^5 GFP-NE-4C cells were seeded in each well. Cultures were grown in minimum essential medium (Sigma, M2279), with 10% fetal calf serum, 2% glutamine and 0,1% gentamicine. The cultures were incubated in 37°C at 5% CO_2 for 24 hours.

After the incubation the cultures were fixed on the Si samples. First they were rinsed with PBS than incubated in

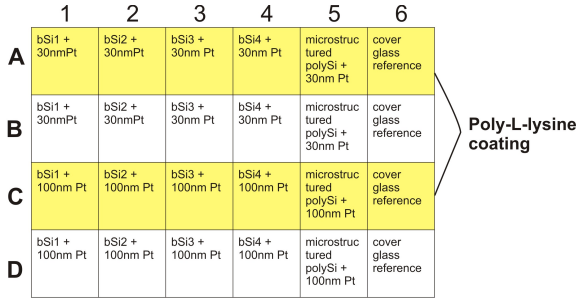

Fig. 3. 24 well plate setup for cell culturing. GFP-NE4C (mice neural stem cells) were cultured in 24 well dishes for 24h on the different micro- and nanostructured samples and on glass reference samples with and without adhesive poly-L-lysine (PLL) coating.

4% parafolmadehyde for 20 minutes. After 2 subsequent PBS rinsing steps samples were stored in PBS with 1% Azide till they were be preapred for study. Samples were then placed onto microscope slides coated with Mowiol ®cotaining DAPI (4',6-diamidino-2-phenylindole) stain and covered with a microscope cover glass. DAPI binds to specific regions of DNA and upon illumination with approx. 350nm wavelength light emits blue light. Therefore nuclei of the cells can be visualised.

D. Fluorescent microscopy imaging

Fluorescent images were taken using a Zeiss Axio Vert.A1 microscope both with GFP and DAPI channels. For aquisition, multichannel imaging and basic image enhancement Zeiss Zen Blue edition software was used. A two channel image of the cells on a patterned sample is shown on Figure 4. Images taken on the DAPI channel were used to determine the cell counts on the different surfaces.

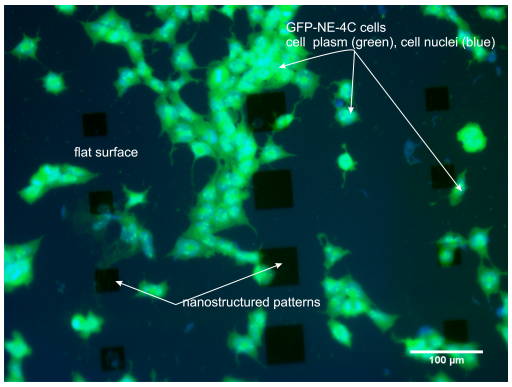

Fig. 4. Fluorescent image of GFP-NE-4C cells on the fabricated samples after 24h adhesion assay. The blue channel corresponds to the DAPI staining which stains the nuclei. Green light is emitted by the GFP which is expressed in the cell plasma. Black squres are the nanostructured patterns of the sample.

III. Results

The morphological parameters of the samples (pillar density, pillar height) were derived from scanning electron micrographs. The nanopillars are between 520-800 nm in height, and their density is 18-70/μm^2 depending on the fabrication parameters of the DRIE process [17]. Scanning electronmicrograph is shown on Figure 5.

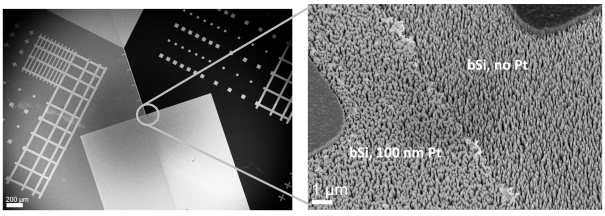

Fig. 5. Scannig electromicrogaphs of the prepared black Si samples. Based ont he SEM images the pillars' height and average density were calculated to characterise the differently etched nanosurfaces.

Based on the DAPI channel images adhered cells were qualitatively examined on diffent parts of the samples. The cells showed a remarkabe preference for the flat surface over the nanostructured one, as can be seen on a representative image of a sample on Figure 6. A method for nuclei counting is currently under development. Also a second measurement series with the same parameters is in progress to validate the results with statisticaly significat data.

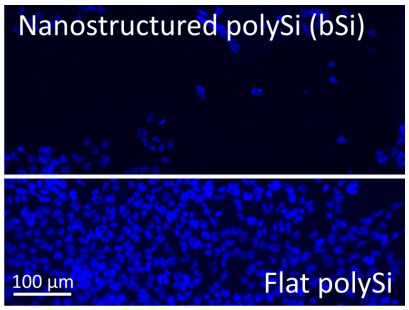

Fig. 6. DAPI channel fluorescent image of GFP NE-4C cells on flat vs. on nanostructured polySi surfaces. Significantly more cells were adhered on the flat surface.

IV. Conclusion and Future Plan

Based on our preliminary studies [17], the nanopattern morphology of our chips are tuneable. The surface area growth is significant compared to the Pt surface currently used as electrode contact site. As is was described before, the specific surface area growth can be measured by impedance reduction which is an additional advantage [17]. Cells seeded on the surfaces show a remarkable pereference to the flat surface over the nanostructured areas. The cells also show a notable preference for poly-Si surface over platinum. Our plan for the near future is to develop a quantitative method for the evaluation of the images. There is also significant information in the GFP channel images. Shape of the cells indicate their fate on the surface. Round like cells attaches to the surface less than flat cells which are likely to divide and form an aggregate which is the precondition for differentiating into neurons [18].

ACKNOWLEDGMENT

The authors are grateful to the supportive staff of the MEMS Lab in MFA, Centre for Energy Research, HAS and the work of Mr A. Straszner in deep reactive ion etching is also acknowledged. Thanks are also due to Zsófia Somogyi for her work with the cellular assays. The authors also would like to thank dr. Emília Madarász and Attila Jády from MTA KOKI for the opportunity of cooperation. Zs. Bérces is thankful for the KTIA_13_NAP-A-IV/6 and KAP-1.1-14-024 grants. A. Pongrácz is grateful for the Bolyai Grant of HAS. Z. Fekete is grateful for the KTIA-NAP-12-2-2015-0004 grant.

REFERENCES

[1] Dalby, M.J.; Pasqui, D.; Affrossman, S.: 'Cell response to nano-islands produced by polymer demixing: a brief review', IEE Proceedings - Nanobiotechnology, Volume 151, Issue 2, Pages 53-61, 2004.

[2] Turner, S. and Kam, L. and Isaacson, M. and Craighead, H. G. and Shain, W. and Turner, J.,'Cell attachment on silicon nanostructures' Journal of Vacuum Science and Technology B., 15, Pages 2848-2854, 1997.

[3] Moxon, K.A.; Kalkhoran, Nader M.; Markert, M.; Sambito, M.A.; McKenzie, J.L.; Webster, J.T., 'Nanostructured surface modification of ceramic-based microelectrodes to enhance biocompatibility for a direct brain-machine interface', Biomedical Engineering, IEEE Transactions on , Volume 51, Issue 6, Pages 881-889, 2004.

[4] Fredrik Johansson, Martin Kanje, Cecilia Eriksson andLars Wallman,'Guidance of neurons on porous patterned silicon: is pore size important? ', physica status solidi (c) Volume 2, Issue 9, Pages 3258–3262, 2005.

[5] Andrei V. Sapelkin, Susan C. Bayliss, Bayram Unal, Amanda Charalambou, 'Interaction of B50 rat hippocampal cells with stain-etched porous silicon', Biomaterials, Volume 27, Issue 6, Pages 842-846, 2006.

[6] J. Ma, F. Z. Cui, B. F. Liu, Q. Y. Xu, 'Atomic force and confocal microscopy for the study of cortical cells cultured on silicon wafers', Journal of Materials Science: Materials in Medicine, Volume 18, Issue 5, Pages 851-856, 2007.

[7] Saida P. Khan, Gregory G. Auner, Golam M. Newaz, Influence of nanoscale surface roughness on neural cell attachment on silicon, Nanomedicine: Nanotechnology, Biology and Medicine, Volume 1, Issue 2, Pages 125-129, 2005.

[8] N M Dowell-Mesfin, M-A Abdul-Karim, A M P Turner, S Schanz, H G Craighead, B Roysam, J N Turner and W Shain, Topographically modified surfaces affect orientation and growth of hippocampal neurons, J Neural Eng.; Volume 1 Issue 2, Pages 78-90., 2004.

[9] Y.W. Fan, F.Z. Cui, S.P. Hou, Q.Y. Xu, L.N. Chen, I.-S. Lee, Culture of neural cells on silicon wafers with nano-scale surface topography, Journal of Neuroscience Methods, Volume 120, Issue 1, Pages 17-23, 2002.

[10] A. M. P. Turner, N. Dowell, S. W. P. Turner, L. Kam, M. Isaacson, J. N. Turner, H. G. Craighead and W. Shain, 'Attachment of astroglial cells to microfabricated pillar arrays of different geometries', Journal of Biomedical Materials Research Volume 51, Issue 3, Pages 430–441, 2000.

[11] Gaëlle Piret, Maria-Thereza Perez, Christelle N. Prinz, 'Neurite outgrowth and synaptophysin expression of postnatal CNS neurons on GaP nanowire arrays in long-term retinal cell culture', Biomaterials, Volume 34, Issue 4, Pages 875-887,2013.

[12] Samuel Bechara, Lucas Wadman, Ketul C. Popat, 'Electroconductive polymeric nanowire templates facilitates in vitro C17.2 neural stem cell line adhesion, proliferation and differentiation', *Acta Biomaterialia*, Volume 7, Issue 7, Pages 2892-2901, 2011.

[13] YW Fan, FZ Cui, LN Chen, Y Zhai, QY Xu, IS Lee, Adhesion of neural cells on silicon wafer with nano-topographic surface, Applied surface science Volume 187 Issue 3, Pages 313-318, 2002.

[14] Alexei Verkhratsky (Editor), Arthur Morgan Butt (Editor), Glial Physiology and Pathophysiology, Wiley-Blackwell, ISBN: 978-0-470-97853-5, 2013.

[15] Annalisa Buffo, Inmaculada Rite, Pratibha Tripathi, Alexandra Lepier, Dilek Colak, Ana-Paula Horn, Tetsuji Mori, Magdalena Götz, 'Origin and progeny of reactive gliosis: A source of multipotent cells in the injured brain', PNAS, Volume 105 No. 9, Pages 3581–3586, 2008.

[16] Stefanie Robel, Benedikt Berninger, Magdalena Götz, 'The stem cell potential of glia: lessons from reactive gliosis', Nature Reviews Neuroscience Volume 12, Pages 88-104, 2011.

[17] Z Fekete, Á Horváth, Zs Bérces, A Pongrácz 'Black poly-silicon: a nanostructured seed layer for sensor applications' SENSORS AND ACTUATORS A-PHYSICAL Issue 216, Pages 277-286., 2014.

[18] Katalin Schlett, Emília Madarász, 'Retinoic acid induced neural differentiation in a neuroectodermal cell line immortalized by p53 deficiency', Journal of Neuroscience Research Volume 47 Issue 4, Pages: 405-415, 1997.

Morphological investigation of endocannabinoid signalling between GnRH neurons and its virus labelled kisspeptin afferents

Tamás WILHEIM
(Supervisor: Imre KALLÓ)
Pázmány Péter Catholic University, Faculty of Information Technology and Bionics
50/a Práter street, 1083 Budapest, Hungary
wilheim.tamas@itk.ppke.hu

***Abstract*—The kisspeptin neurons give important excitatory input to GnRH neurons. Previous studies showed, that the GnRH neurons mediate their synaptic input from glutamate- and GABAergic cells expressing cannabinoid type 1 receptors (CB1). Immunohistochemical triple labelling and 3D reconstruction were employed to identify CB1-positive neuronal connections of GnRH neurons in mice expressing CRE-GFP under the control of Kiss1 promoter. The whole cellular compartement of KP neurons were visualised by a CRE-dependent activation of a viral construction encoding channel rhodopsin and YFP. CB1 immunoreactivity was found in KP fibers, which were in close apposition to GnRH perikarya and/or processes. This result suggest that GnRH neurons are capable of influencing their input from kisspeptin neurons via the endocannabinoid - CB1 retrograde signalling.**

***Keywords*-GnRH; kisspeptin; retrograde signalling; afferents; 3D reconstruction;**

I. Introduction

Kisspeptin neurons provide an important excitatory input for the GnRH network in the hypothalamus [7-12]. The GnRH network gives the main output of the hypothalamic reproductive regulation circuitry by producing the GnRH hormone, secreted into the portal vessels of the hypophysis. Without kisspeptin, e.g. in kisspeptin knock out animals, GnRH release is absent, causing underdeveloped gonads, and infertility [14]. In rodents, two distinct kisspeptin populations exist: one, in the rostral periventricular area of the third ventricle (RP3V), and one in the arcuate nucleus (ARC) [1,13]. It was previously described, that GnRH neurons are capable to modulate their synaptic input from presynaptic GABA and glutamate terminals expressing cannabinoid type 1 receptor (CB1). This is an important regulation mechanism, because due to the elevated chloride levels in the adult GnRH cells, the GABA transmission causes depolarization in GnRH neurons, resulting that GABA, the classical inhibitory neurotransmitter is excitatory on GnRH neurons [2,3]. It was also shown, that kisspeptin is released only when the kisspeptin neuron is stimulated with a higher frequency (5-10Hz). Low frequency ($<$1Hz) resulted in classic neurotransmitter release. [19] Due to these properties of the GnRH cells, it is important that some inhibitory regulation is employed in the network. To investigate the possibility of endocannabinoid CB1 related retrograde signalling is present in the kisspeptin neurons, triple labelling immunohistochemistry was used in brain sections of mice expressing cre enzyme and GFP in kisspeptin neurons [15-18]. To visualize the kisspeptin cell membrane, an adeno-associated virus construct AAV-EF1a-DIO-hChR2(H134R)-EYFP was injected either into the preoptic area, or into the arcuate nucleus carrying channel rhodopsin and YFP. With this construct, the YFP migrates into the cell membrane, making it possible to visualize the whole cell compartment, compared to the direct kisspeptin immunolabelling, where only the kisspeptin containing compartments are visible.

II. Materials and methods

A. Animals

Adult, female Kiss1-CreGFP mice (n=2 b.w. 25-30g) were used. The Kiss1-CreGFP mouse expresses Cre recombinase and GFP under the endogenous Kiss1 promoter, making it possible to see GFP only when Kiss1 is expressed. These animals received a viral construct AAV-EF1a-DIO-hChR2(H134R)-EYFP injection into the POA and ARC to label the KP neurons. The animals were housed under controlled lighting(12:12h light-dark cycle; lights on at 07:00h, and temperature (22$\pm$2 °C), with access to food and water ad libitum. All studies were carried out with permission from the Animal Welfare Committee of the Institute of Experimental Medicine (No. 2285/003) and in accordance with legal requirements of the European Community (Decree 86/609/EEC). Surgery was performed on animals under deep anaesthesia induced by an intraperitoneally injected cocktail of ketamine (25mg/kg b.w.), xylavet (5mg/kg b.w.) and pipolphen (2.5mg/kg b.w.) in saline.

B. Tissue Preparation for Confocal Microscopy

The animals were injected with adeno-associated virus carrying cre-dependent channel rhodopsin, and YFP in the rostral periventricular area of the third ventricle (1 animal), and one in the arcuate nucleus (1 animal). The animals were perfused transcardially with phosphate-buffered saline (PBS; 0.1M) containing 4% paraformaldehyde (PFA). The brain was removed, postfixed for 24 hours, and transferred into 30% sucrose for cryoprotection, then 30m thick coronal sections were

T. WILHEIM, "Morphological investigation of endocannabinoid signalling between GnRH neurons and its virus labelled kisspeptin afferents" in *PhD Proceedings Annual Issues of the Doctoral School, Faculty of Information Technology and Bionics, Pázmány Péter Catholic University – 2015.* G. Prószéky, P. Szolgay Eds. Budapest: Pázmány University ePress, 2015, pp 97– 100.

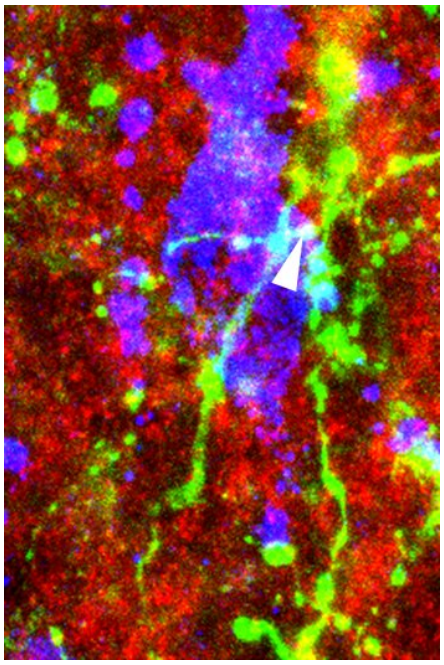

Fig. 1: 2D confocal maximum intensity image of CB1- and GFP-IR fibers on a GnRH neuron. Green channel: kisspeptin cell visualized with the YFP immunoreactivity in the cell membrane, red channel: CB1-IR, blue channel: GnRH-IR. The white arrow shows the kisspeptin varicosity apposed to a GnRH cell that was 3D reconstructed as shown in Fig.2 The virus was injected into the preoptic area.

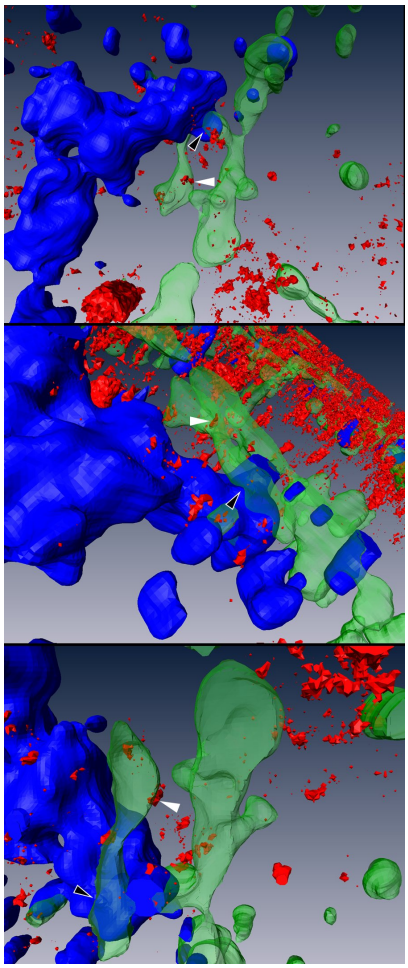

Fig. 2: 3D reconstruction of the confocal image shown in Fig. 1. Green channel: kisspeptin varicosity showing the YFP immunoreactivity in the cell membrane, red channel: CB1-IR, blue channel: GnRH-IR. The green kisspeptin varicosity is transparent, and it is in close apposition to the blue GnRH cell without a visible gap (marked with black arrow), the red CB1-IR is visible on the varicosity surface (marked with white arrow), and inside the varicosity. The 3 images show the same structure from different angles. As the connection of neurons cannot be evaluated easily in a projected image (2D), 3D reconstruction was employed. With rotating the 3D model interactively, it is easy to decide if there is a gap between structures that would rule out a synapse.

cut on a freezing microtome. After the endogenous peroxidase activity had been quenched with 0.5% hydrogen peroxide (20 min), sections were permeabilised with 0.5% Triton X-100 (23,472-9, Sigma, 20min). Finally, 2% normal horse serum was applied (20min) to reduce non-specific antibody binding. Subsequent treatments and interim rinses in PBS (3×5min) were carried out at room temperature, except for incubation in the primary antibody or fluorochrome.

C. Triple Immunofluorescence for GnRH, CB1 and YFP Immunoreactivity

Sections from the RP3V and pre-optic region of the virus injected kisspeptin-cre animals were incubated (72h) in a cocktail of the guinea pig anti-GnRH (#1018, Hrabovszky, 1: 50,000)[6] and rabbit anti-GFP (1: 2,000, AB10145 Millipore), goat anti CB1([5], 1:600) primary antibodies for the kisspeptin afferents, GnRH immunoreactivity was visualised with CY5-conjugated donkey anti-guinea pig IgG (#706-175-148, Jackson ImmunoResearch Laboratories, 1: 2,000, 2h). To visualise the KP-IR structures, the sections were incubated in FITC-conjugated donkey anti-rabbit (#711-095-152, Jackson ImmunoResearch Laboratories, 1: 1,000, 2 h). To visualise the CB1-IR structures, the sections were incubated in CY3-conjugated donkey anti-goat (#706-165-147, Jackson ImmunoResearch Laboratories, 1: 2,000, 2 h).

D. Confocal Laser Analysis and 3-D Reconstruction of GnRH-IR Afferents

The triple-labelled sections were analysed using a Nikon A1R confocal microscope (Nikon, Japan). Multiple stacks of optical slices (1024×1024 pixels, z-steps 0.15 μm) were obtained by scanning all of the KP-IR neurons unilaterally

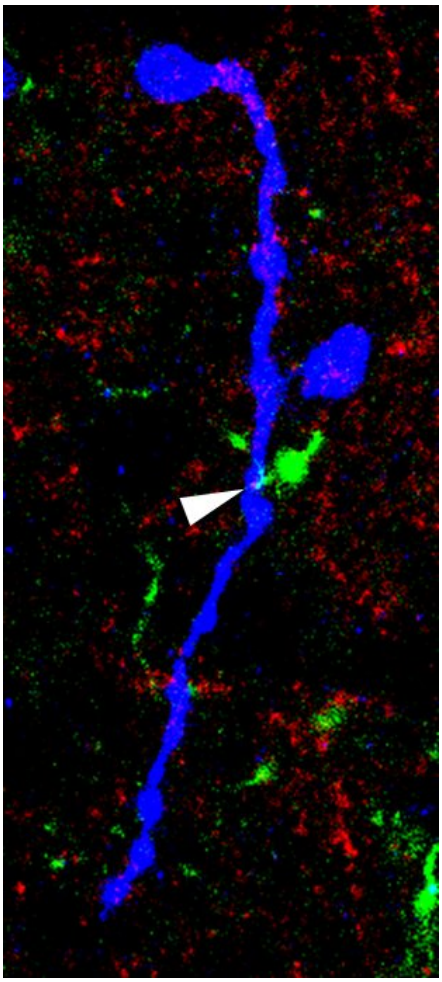

Fig. 3: 2D confocal image of CB1- and GFP-IR fibers on a GnRH neuron. Green channel: kisspeptin cell showing the YFP immunoreactivity in the cell membrane, red channel: CB1-IR, blue channel: GnRH-IR. The white arrow shows the kisspeptin varicosity on the GnRH cell that was 3D reconstructed as shown in Fig.4 The virus was injected into the arcuate nucleus.

in each of the selected coronal sections using a 60× oil immersion objective. The FITC, CY3, and CY5 fluorochromes were detected with laser lines 488nm, 561 nm, and 641nm laser excitation. The separately recorded green, red and the artificially blue coloured far red channels were merged and displayed with the ImageJ software [4] running on an IBM-compatible personal computer. The images acquired with the confocal laser microscope were further investigated using three dimensional (3D) analyses. The stack of optical slices were loaded into the visualisation software Amira (evaluation version, Visual Imaging Group) and the three channels containing images of consecutive optical slices were deconvolved with the built in deconvolution module, then rendered in three dimensions with surfaces generated from above threshold immunoreacitvity. The threshold was set individually for each image and colour channel to minimise any noise, while maintaining the proper cellular boundaries. The surfaces generated from the three channels in the same optical volume were visualised to check for cell-to-cell contacts, and the presence of CB1 receptor immunoreactivity. This enabled verification of the findings from the two dimensional confocal image analyses.

III. Results

The presence of cannabinoid receptor in the afferent terminal is necessary for the retrograde signalling pathway that inhibits synaptic input via releasing endocannabinoids that are detected by the CB1 receptors on the afferent terminal membrane. [2,3] First, I have tried triple labelling immunohistochemistry to visualize CB1 in the kisspeptin afferents of GnRH cells with labelling the kisspeptin directly, and I was able to show kisspeptin immunoreactive terminals in close apposition to GnRH that showed CB1 labelling. However, this approach is not optimal, since the kisspeptin in the process or terminal is packed into dense core vesicles trafficking, or waiting to be released in the terminal, but it does not fill the whole anatomical structure. The CB1 is a membrane receptor, it is expected mainly in the membrane, but with the direct kisspeptin labelling, only the kisspeptin containing parts of the cell can be visulalised. To overcome this problem, I used the virus construct to enable labelling the plasma membrane. The channel rhodopsin encoded by this virus is also a membrane protein, and it directs the YFP to the membrane, thus making the whole cell visible. With this method, it can be decided if the visible CB1 signal is part of the kisspeptin varicosity or not. Next step will be to design a control experiment. A CB1 knockout mouse line will be used to repeat the staining with a similar virus labelling. To quantitatively describe the CB1 immunoreactive signal in the membrane, we plan to make measurements on the 3D model. Euclidean distance can be measured between the CB1 signal, and the kisspeptin cell membrane, and based on the distance, it can be decided, whether the CB1 signal is inside the cell, meaning it is trafficking inside vesicles, or it is in the membrane, or outside in an other cell. The antibody we used recognises the C terminal end of CB1, which is the intracellular end, but counting the length of the 2 IgG molecules used for labelling, and the diffraction of the microscope, it is possible that the signal is detected both inside and outside the cell membrane as visible in figures 2 and 4.

Acknowledgment

The project was founded by OTKA K101326 grant.

References

[1] A. S. Kauffman, J. T. Smith: *Kisspeptin Signaling in Reproductive Biology* Springer Science+Business Media, ISBN 978-1-4614-6198-2

[2] Farkas I., Kalló I., Deli L., Vida B., Hrabovszky E., Fekete C., Moenter S. M., Watanabe M., Liposits Zs.: *Retrograde endocannabinoid signaling reduces GABAergic synaptic transmission to gonadotropin-releasing hormone neurons* Endocrinology. 151(12):5818-5829.

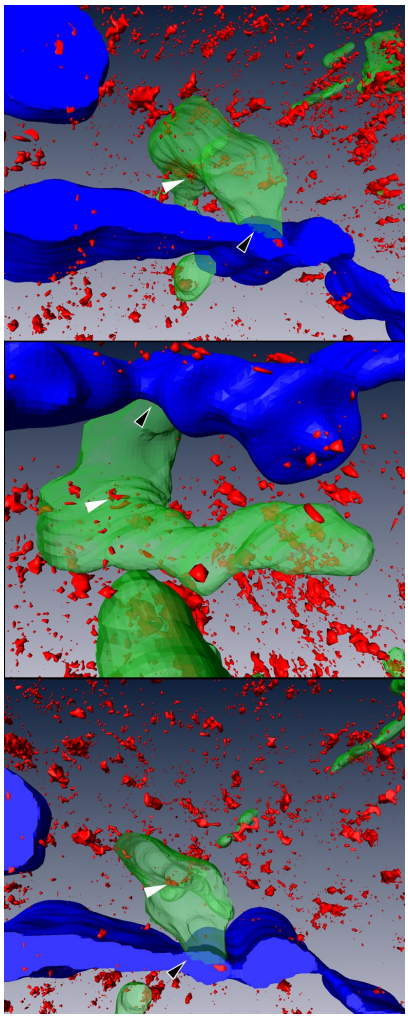

Fig. 4: 3D reconstruction of the confocal image shown in Fig. 3. Green channel: kisspeptin varicosity showing the YFP immunoreactivity in the cell membrane, red channel: CB1-IR, blue channel: GnRH-IR. The green kisspeptin varicosity is transparent, and it is in close apposition to the blue GnRH process without a visible gap (marked with black arrow) the red CB1-IR is visible on the varicosity surface (marked with white arrow), and inside the varicosity. The 3 images show the same structure from different angles. As the connection of neurons cannot be evaluated easily in a projected image (2D), 3D reconstruction was employed. With rotating the 3D model interactively, it is easy to decide if there is a gap between structures that would rule out a synapse.

[3] Glanowska K. M., Moenter S. M.: *Endocannabinoids and prostaglandins both contribute to GnRH neuron-GABAergic afferent local feedback circuits* J Neurophysiol. 106(6):3073-81.

[4] Rasband, W.S., *ImageJ*, U. S. National Institutes of Health, Bethesda, Maryland, USA, http://imagej.nih.gov/ij/, 1997-2014.

[5] Makara J, Katona I, Nyíri G, Nemeth B, Ledent C, Watanabe M,de Vente J, Freund T, Hájos N: *Involvement of nitric oxide in depolarization-induced suppression of inhibition in hippocampal pyramidal cells during activation of cholinergic receptors.*, 2007 J Neurosci 27:1021110222

[6] Hrabovszky E, Molnár CS, Sipos MT, Vida B,Ciofi P, Borsay BA, Sarkadi L, Herczeg L,Bloom SR, Ghatei MA, Dhillo WS, Kalló I, Liposits Z: *Sexual dimorphism of kisspeptin and neurokinin B immunoreactive neurons in the infundibular nucleus of aged men and women.*, Front Endocrinol (Lausanne) 2011;2:80

[7] Li XF, Kinsey-Jones JS, Cheng Y, Knox AM, Lin Y, Petrou NA, Roseweir A, Lightman SL, Milligan SR, Millar RP, OByrne KT: *Kisspeptin signalling in the hypothalamic arcuate nucleus regulates GnRH pulse generator frequency in the rat.*, PLoS One 2009; 4:e8334.

[8] Kinoshita M, Tsukamura H, Adachi S, Matsui H, Uenoyama Y, Iwata K, Yamada S, Inoue K, Ohtaki T, Matsumoto H, Maeda K: *Involvement of central metastin in the regulation of preovulatory luteinizing hormone surge and estrous cyclicity in female rats.*, Endocrinology 2005; 146: 44314436.

[9] Adachi S, Yamada S, Takatsu Y, Matsui H, Kinoshita M, Takase K, Sugiura H, Ohtaki T, Matsumoto H, Uenoyama Y, Tsukamura H, Inoue K, Maeda K: *Involvement of anteroventral periventricular metastin/kisspeptin neurons in estrogen positive feedback action on luteinizing hormone release in female rats.* J Reprod Dev 2007; 53: 367378.

[10] Clarkson J, dAnglemont de Tassigny X, Moreno AS, Colledge WH, Herbison AE: *Kisspeptin-GPR54 signaling is essential for preovulatory gonadotropin-releasing hormone neuron activation and the luteinizing hormone surge.* J Neurosci 2008; 28: 86918697.

[11] Roseweir AK, Kauffman AS, Smith JT, Guerriero KA, Morgan K, Pielecka-Fortuna J, Pineda R, Gottsch ML, Tena-Sempere M, Moenter SM, Terasawa E, Clarke IJ, Steiner RA, Millar RP: *Discovery of potent kisspeptin antagonists delineate physiological mechanisms of gonadotropin regulation.* J Neurosci 2009; 29: 39203929.

[12] Pineda R, Garcia-Galiano D, Roseweir A, Romero M, Sanchez-Garrido MA, Ruiz-Pino F, Morgan K, Pinilla L, Millar RP, Tena-Sempere M: *Critical roles of kisspeptins in female puberty and preovulatory gonadotropin surges as revealed by a novel antagonist.* Endocrinology 2010; 151: 722730.

[13] Kalló I, Vida B, Bardóczi Z, Szilvásy-Szabó A, Rabi F, Molnár T, Farkas I, Caraty A, Mikkelsen J, Coen CW, Hrabovszky E, Liposits Z.: *Gonadotropin-Releasing Hormone Neurones Innervate Kisspeptin Neurones in the Female Mouse Brain*, Neuroendocrinology 2013;98:281-289

[14] Uenoyama Y, Nakamura S, Hayakawa Y, Ikegami K, Watanabe Y, Deura C, Minabe S, Tomikawa J, Goto T, Ieda N, Inoue N, Sanbo M, Tamura C, Hirabayashi M, Maeda KI, Tsukamura H.: *Lack of pulse and surge modes and glutamatergic stimulation of luteinising hormone release in Kiss1 knockout rats.*, Neuroendocrinology 2015;98:187-197

[15] Gottsch ML, Popa SM, Lawhorn JK, Qiu J, Tonsfeldt KJ, Bosch MA, Kelly MJ, Ronnekleiv OK, Sanz E, McKnight GS, Clifton DK, Palmiter RD, Steiner RA.: *Molecular properties of Kiss1 neurons in the arcuate nucleus of the mouse.*, Endocrinology 2011;152:42984309

[16] Navarro VM, Gottsch ML, Wu M, García-Galiano D, Hobbs SJ, Bosch MA, Pinilla L, Clifton DK, Dearth A, Ronnekleiv OK, Braun RE, Palmiter RD, Tena-Sempere M, Alreja M, Steiner RA.: *Regulation of NKB pathways and their roles in the control of Kiss1 neurons in the arcuate nucleus of the male mouse.*, Endocrinology 2011;152:42654275

[17] Popa SM, Moriyama RM, Caligioni CS, Yang JJ, Cho CM, Concepcion TL, Oakley AE, Lee IH, Sanz E, Amieux PS, Caraty A, Palmiter RD, Navarro VM, Chan YM, Seminara SB, Clifton DK, Steiner RA.: *Redundancy in Kiss1 Expression Safeguards Reproduction in the Mouse.*, Endocrinology 2013;154:27842794

[18] Piet R, de Croft S, Liu X, Herbison AE.: *Electrical properties of kisspeptin neurons and their regulation of GnRH neurons.*, Frontiers in Neuroendocrinology 2015;36:15-27

[19] Liu X, Porteous R, d'Anglemont de Tassigny X, Colledge WH, Millar R, Petersen SL, Herbison AE.: *Frequency-dependent recruitment of fast amino acid and slow neuropeptide neurotransmitter release controls gonadotropin-releasing hormone neuron excitability.*, J Neurosci 2011;31:2421-2430

Program 2

COMPUTER TECHNOLOGY BASED ON MANY-CORE PROCESSOR CHIPS, VIRTUAL CELLULAR COMPUTERS, SENSORY AND MOTORIC ANALOG COMPUTERS

Head: Péter SZOLGAY

Real-time content adaptive depth retargeting for light field displays

Vamsi KIRAN ADHIKARLA
(Supervisor: Péter SZOLGAY)
Pázmány Péter Catholic University, Faculty of Information Technology and Bionics
50/a Práter street, 1083 Budapest, Hungary
adhikarla.vamsi.kiran@itk.ppke.hu

***Abstract*—Light field display systems present visual scenes using a set of directional light beams emitted from multiple light sources as if they are emitted from points in a physical scene. These displays offer better angular resolution and therefore provide more depth of field than other automultiscopic displays. However in some cases the size of a scene may still exceed the available depth range of a light field display. Thus, rendering on these displays requires suitable adaptation of 3D content for providing comfortable viewing experience. We propose a content adaptive depth retargeting method to automatically modify the scene depth to suit to the needs of a light field display. By analyzing the scene and using display specific parameters, we formulate and solve an optimization problem to non-linearly adapt the scene depth to display depth. Our method synthesizes the depth retargeted light field content in real-time for supporting interactive visualization and also preserves the 3D appearance of the displayed objects as much as possible. The proposed algorithm is embedded in an end-to-end real-time system capable of capturing and reconstructing light field from multiple calibrated cameras on a full horizontal parallax light field display. We *evaluate* the effectiveness of our approach on synthetic and real world scenes.**

***Keywords*-on-the-fly depth retargeting; multiprojector light field display; GPU; visually enhanced live 3D Video; multi-view capture and display**

I. Introduction

The main principle behind any glasses-free 3D display technology is direction-dependent light transmission. Ideally, to completely describe a scene in 3D, a display should reproduce light rays from all the points in all the directions within a given viewing zone. In practice, however, this is not possible due to the finite size of display hardware. Recent advances in computational displays showed several improvements in various dimensions such as color, luminance & contrast, spatial and angular resolution (see [1] for a detailed survey of these displays). Projection-based light-field displays, are among the most advanced solutions.

Taking inspiration from the real-world, a light field display emits light rays from multiple perspectives using a set of optical modules. The various emitted light rays hit a holographic screen which performs the necessary optical modulation for reconstructing a 3D scene. Even though these displays provide continuous views and improve over traditional automultiscopic solutions, the extent of practically displayable depth with reasonable 3D quality is still limited due to finite number of light generating optical modules. Scene points rendered outside this range are subjected to poor sampling and suffer from aliasing, which typically lead to excessive blurring in regions. This blurring makes it difficult to perceive details of very far objects from the screen, and leads to visual discomfort.

By matching the depth extent of scene to that of display by applying a process of *depth retargeting*, it is possible to greatly reduce the blurring artifacts, achieving all-in-focus rendering. In the current work, we address this problem by proposing a low-complexity real-time solution to adaptively map the scene depth to display depth by taking into account the perspective effects of a light field display and the saliency of the scene contents. The proposed retargeting module is integrated into a real-time light field rendering pipeline that can be fed with a live multi-view video stream captured from multiple cameras. Our improvements with respect to the state-of-the-art are the following:

- A perspective depth contraction method for live light field video stream that preserves the 3D appearance of salient regions of a scene. The deformation is globally monotonic in depth, and avoids depth inversion problems.
- A real-time plane sweeping algorithm which concurrently estimates and retargets scene depth. The method can be used for all-in-focus rendering of light field displays.
- An end-to-end system capable of real-time capturing and displaying with full horizontal parallax high-quality 3D video contents on a cluster-driven multiprojector light field display with full horizontal parallax.
- An evaluation of the objective quality of the proposed depth retargeting method.

II. Related work

Our end-to-end system enhances and integrates several state-of-the-art solutions for 3D video capture and rendering in wide technical areas. For comprehensive understanding, we refer the reader to established surveys (e.g., [2], [3]). In the subsequent paragraphs, we present some of the more relevant works. Content remapping is a well established approach for adapting image characteristics to limited displays, and is routinely used for adapting spatial and temporal resolution, contrast, colors, and aspect ratios of images. For the particular case of depth retargeting, Lang et al. [4] proposed

V. KIRAN ADHIKARLA, "Real-time content adaptive depth retargeting for light field displays" in *PhD Proceedings Annual Issues of the Doctoral School, Faculty of Information Technology and Bionics, Pázmány Péter Catholic University – 2015.* G. Prószéky, P. Szolgay Eds. Budapest: Pázmány University ePress, 2015, pp 103– 106.

a method for remapping stereoscopic 3D disparities using a non linear operator. The non-linear mapping is generated by sparse disparity estimation and combining the local edge and global texture saliency. The method is based on warping the stereo images independently to achieve depth retargeting. As the method relies on sparse disparities, warping can lead to noticeable artifacts especially near the depth discontinuities and may also distort any straight lines in the scene. Extending this method to remap full-parallax light field content would introduce artifacts because of the increased number of views. Kim et al. [5] extend the approach by proposing a framework for the generation of stereoscopic image pairs with per-pixel control over disparity, based on multi-perspective imaging from light fields. While their method might be extended to multiview images, the associated optimization problem is too costly to be solved in a run-time setting. Masia et al. [6] deal specifically with multiview displays by proposing a method for display-adaptive depth retargeting. They exploit the central view of a light field display to generate a mapping function and use warping to synthesize the rest of the light field. Their work strives to minimize perceived distortion using a model of human perception, but does not achieve real-time performance and does not include depth estimation. Piotr Didyk et al. [7] proposed a model for measuring perceived disparity and a way to automatically detecting the threshold for comfortable viewing. Their method can be used as a component to operate depth retargeting. We concentrate instead on overcoming device limitations. Birkbauer et al. [8] handle the more general problem of light field retargeting, using a seam-carving approach. The method supports visualizing on displays with aspect ratios that differ from those of the recording cameras, but does not achieve real-time performance. Content-aware remapping has also been proposed to achieve non-linear rescaling of complex 3D models, e.g. to place them in new scenes. The grid-based approach of Kraevoy et al. [9] has also been employed for image retargeting. Graf et al. [10] proposed an interesting approach for axis-aligned content aware 2D image retargeting, optimized for mobile devices. They rely on the image saliency information to derive an operator that non-linearly scales and crops insignificant regions of the image using a 2D mesh. Our method also takes the approach of using a discretized grid to quickly solve an optimization problem. In our case, we use a one-dimensional discretization of depth, which permits us to avoid depth inversion problems of solutions based on spatial grids.

III. Retargeting Model

If a 3D scene and display have the same depth extent no retargeting is required, but in a more general case, a depth remapping step is needed. Our aim is to generate an adaptive non-linear transform from scene to display that minimizes the compression of salient regions. To extract the scene saliency, we compute depth and color from perspectives of multiple display projection modules and combine this information. To make the process faster, we compute the saliency from central and two lateral perspectives and use this information to retarget the light field from all the viewing angles. Depth saliency is estimated using a histogram of the pre-computed depth map (depths are computed following all-in-focus rendering approach). To estimate color saliency, we compute a gradient map of the color image associated to the depth map of the current view and dilate it to fill holes. The gradient norm of a pixel represents color saliency. To avoid any abrupt depth changes we quantize the scene depth range into different depth clusters and accumulate the depth and color saliency inside each cluster. Using the length of a cluster and it's saliency, we solve a convex optimization to derive the retargeting function. our aim is to minimize:

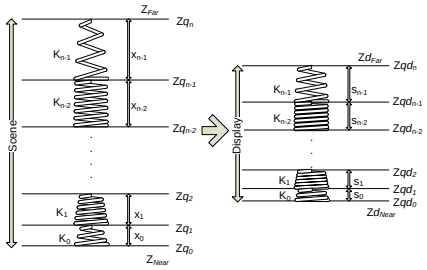

Fig. 1. Computation of content aware depth retargeting function.

$$\sum_{i=0}^{qn-1} \frac{1}{2} K_i \left(S_i - X_i\right)^2 \tag{1}$$

subject to: $\sum_{i=0}^{qn-1} S_i = D_d$; ${S_i > D_{cs}}^{min}, i = 0, 1, ..., n-1$, Where, X_i and K_i are the length and stiffness of i^{th} cluster spring, D_d is the total depth of field of the display and ${D_{cs}}^{min}$ are the minimum and allowable sizes of the resulting display space clusters. For each point in the scene, we compute a new point in the display $z_{display} = f(z_{scene})$ using piecewise linear interpolation. Any user looking from the central viewing position perceives no change in the apparent size of the objects as the scene points are adjusted in the direction of viewing rays.

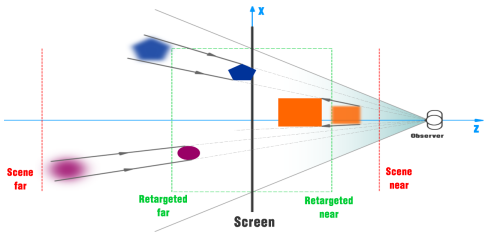

Fig. 2. Perspective Content adaptive retargeting.

IV. Results

On-the-fly light field retargeting and rendering is implemented on GPU using CUDA. We tested the results of our content aware retargeting on a Holografika 72in light field display that supports 50° horizontal Field Of View (FOV)

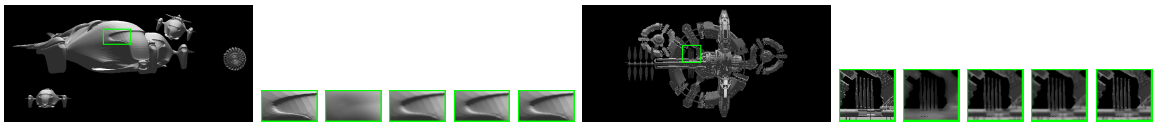

Fig. 3. Left: Sungliders scene. Right: Zenith scene. Left to right: ground truth central view and close-ups: ground truth, without retargeting, with linear, logarithmic and adaptive retargeting. Note that, as we present the content from display center viewing position, viewport content is not distorted in X-Y.

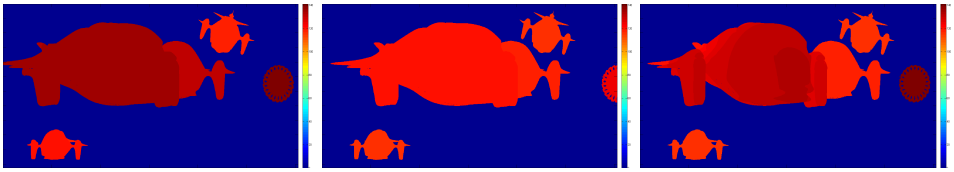

Fig. 4. Left: linear retargeting, middle: logarithmic retargeting and right: adaptive retargeting. The depth variations are better preserved for adaptive retargeting, thus producing increased parallax effect on light field display.

with an angular resolution of $0.8°$. The aspect ratio of the display is 16:9 with single view 2D-equivalent resolution of 1066×600 pixels. The display has 72 SVGA 800x600 LED projection modules which are pre-calibrated using an automatic multiprojector calibration procedure [11]. The front end is an Intel Corei7 PC with an Nvidia GTX680 4GB, which captures multiview images at 15 fps in VGA resolution using 18 calibrated Logitech Portable Web cameras. The camera rig covers a base-line of about 1.5m and is sufficient to cover the FOV of light field display. In the back end, we have 18 AMD Dual Core Athlon 64 X2 5000+ PCs running Linux and each equipped with two Nvidia GTX560 1 GB graphics boards. Each node renders images for four optical modules. Front-end and back-end communicate over a Gigabit Ethernet connection.

A. Retargeting synthetic light field content

As we aim to retarget the light field content in real-time, we limit objective quality evaluation of our method with ground truth and other real-time methods (in particualr, linear and logarithmic remapping [4]). The two synthetic scenes are Sungliders and Zenith. The ground truth central view and close-ups from the central views generated without retargeting, with linear, logarithmic and content adaptive retageting are shown in Fig. 3. The original depths of the scenes are 10.2m and 7.7m, that we remapped to a depth of 1m to match the depth range of our display. Similarly to Masia et al. [6], we generate the images by simulating the display behavior and our display parameters. Figure 3 shows the simulation results: ground truth central view and close-ups from the central views generated without retargeting, with linear, logarithmic and content adaptive retageting. To generate the results for logarithmic retargeting, we use a function of the form $y = a + b * log(c + x)$, where y and x are the output and input depths. The parameters a, b & c are chosen to map the near and far clipping planes of the scene to the comfortable viewing limits of the display. When the original scene is presented on the display, voxels that are very close to the user appear more blurry. Note that in all the three retargeting methods, after retargeting, the rendered scene is less blurry. The adaptive approach better preserves the object dephts, avoiding to flatten them. This is more evident for frontal objects between the screen and display near plane, which are almost flattened by the linear and logarithmic approaches and the blurry effect is still perceivable. We can see it from insets of Fig. 3, where near objects drawn with linear and logarithmic retargeting are less sharper than corresponding adaptive retargeted objects. Table I shows SSIM and RMSE values of various renderings from the two experimental sequences when compared to ground truth. The metrics show that our content adaptive retargeting performs better than linear, logarithmic and no retargeting.

TABLE I
CENTRAL VIEW SSIM AND RMSE VALUES OBTAINED BY COMPARISON WITH GROUND TRUTH IMAGE FOR SUNGLIDERS (S) AND ZENITH (Z) DATA SETS. SSIM=1 MEANS NO DIFFERENCE TO THE ORIGINAL, RMSE=0 MEANS NO DIFFERENCE TO THE ORIGINAL

	Without	Linear	Logarithmic	Adaptive
SSIM-S	0.9362	0.9733	0.9739	0.9778
SSIM-Z	0.8920	0.9245	0.9186	0.9290
RMSE-S	3.6118	2.0814	2.0964	1.9723
RMSE-Z	3.6700	2.8132	2.8910	2.7882

The flattening of objects in case of linear and logarithmic retargeting is clearly perceivable as we move away from central viewing position and manifests in the form of reduced motion parallax. Fig. 4 presents the color coded side view depth maps from the scene Sungliders for the three test cases. The global compression in linear retargeting results in the loss of depth resolution in the retargeted space. The non-linear logarithmic mapping leads large depth errors unless the objects are located very close to the display near plane. Adaptive retargeting approach produces continuous and better depth variations and thus preserves the 3D shape of objects. The performance of our method can be better explained from the original and retargeted depth histograms (see Fig. 6). Linear retargeting compresses the depth space occupied by scene objects and the empty spaces in the same way, logarithmic retargeting is highly dependent on object positions and results in large depth errors after retargeting. In contrast, our approach

Fig. 5. Real-time light-field capture and retargeting results.

best preserves the depth space occupied by objects and instead, compresses the less significant regions, thus maintains the 3D appearance of objects in the scene.

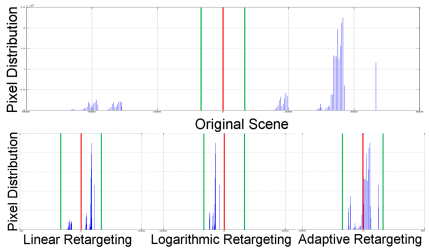

Fig. 6. Top row: Original scene, bottom row : left to right - retargeted scene using linear, logarithmic and adaptive retargeting.

B. Retargeting live multiview feeds

It should be noted that the 3D impression of our results on the light field display can not be fully captured by a physical camera. In Fig. 5, we present the screen shots of the light field display with various renderings at a single time instance of a multiview footage. For fair comparison, images are captured from the same point of view to show the perceivable differences between plain rendering, linear retargeting and adaptive retargeting. Our experiments show that the results from the real-world scenes conform with our simulation results on the synthetic scenes. The front end frame rate is limited at of $15fps$ by the camera acquisition speed. The back end hardware used in the current work supports an average frame rate of $11fps$. However, our experiments showed that Nvidia GTX680 GPU is able to support $40fps$.

V. Conclusions and Future Work

We presented a working method to perceptually enhance the quality of rendering on a projection-based light field display in a real-time capture and rendering framework. In particular, we addressed the problem of rendering scenes with greater depth than the tolerable depth of a light field display. To the best of our knowledge, we propose the first real-time setup that reconstructs an adaptively retargeted light field on a light field display from a live multiview feed. The method is very general and is applicable to 3D graphics rendering on light field display as well as to real-time capture-and-display applications. We showed that adaptive retargeting preserves the 3D aspects of salient objects in the scenes and achieves better results from all the viewing positions than linear and logarithmic approaches. One of the limitations of our end-to-end system is the inaccuracy of estimated depth values while retargeting and rendering. In future work, we plan to employ additional active sensors to get an initial depth structure of the scene, use human visual system aware saliency estimation, and conduct user studies to subjectively evaluate the performance of the method.

Acknowledgments

This research has received funding from the DIVA Marie Curie Action of the People programme of the EU FP7/2007-2013/ Program under REA grant agreement 290227. The support of the TAMOP-4.2.1.B-11/2/KMR-2011-0002 is kindly acknowledged.

References

[1] Belen Masia, Gordon Wetzstein, Piotr Didyk, and Diego Gutierrez, "A survey on computational displays: Pushing the boundaries of optics, computation, and perception," *Computers & Graphics*, vol. 37, no. 8, pp. 1012 – 1038, 2013.

[2] A. Kubota, A. Smolic, M. Magnor, M. Tanimoto, T. Chen, and C. Zhang, "Multiview imaging and 3DTV," *IEEE Signal Processing Magazine*, vol. 24, no. 6, pp. 10, 2007.

[3] A Smolic, "3D video and free viewpoint video – from capture to display," *Pattern Recognition*, 2010.

[4] Manuel Lang, Alexander Hornung, Oliver Wang, Steven Poulakos, Aljoscha Smolic, and Markus Gross, "Nonlinear disparity mapping for stereoscopic 3d," *ACM Trans. Graph.*, vol. 29, no. 4, pp. 75:1–75:10, 2010.

[5] Changil Kim, Alexander Hornung, Simon Heinzle, Wojciech Matusik, and Markus Gross, "Multi-perspective stereoscopy from light fields," *ACM Trans. Graph.*, vol. 30, no. 6, pp. 190:1–190:10, December 2011.

[6] Belen Masia, Gordon Wetzstein, Carlos Aliaga, Ramesh Raskar, and Diego Gutierrez, "Display adaptive 3d content remapping," *Comput. Graph.*, vol. 37, no. 8, pp. 983–996, Dec. 2013.

[7] Piotr Didyk, Tobias Ritschel, Elmar Eisemann, Karol Myszkowski, and Hans-Peter Seidel, "A perceptual model for disparity," *ACM Trans. Graph.*, vol. 30, no. 4, 2011.

[8] C. Birklbauer and O. Bimber, "Light-field retargeting," *Computer Graphics Forum*, vol. 31, no. 2pt1, pp. 295–303, 2012.

[9] Vladislav Kraevoy, Alla Sheffer, Ariel Shamir, and Daniel Cohen-Or, "Non-homogeneous resizing of complex models," vol. 27, no. 5, pp. 111, 2008.

[10] Daniel Graf, Daniele Panozzo, and Olga Sorkine-Hornung, "Mobile image retargeting," in *Proc. VMV*, 2013.

[11] Marco Agus, Enrico Gobbetti, Alberto Jaspe Villanueva, Giovanni Pintore, and Ruggero Pintus, "Automatic geometric calibration of projector-based light-field displays," in *Proc. Eurovis Short Papers*, June 2013, pp. 1–5.

Computational analysis of kinetic systems

Bernadett ÁCS
(Supervisor: Gábor SZEDERKÉNYI)
Pázmány Péter Catholic University, Faculty of Information Technology and Bionics
50/a Práter street, 1083 Budapest, Hungary
acs.bernadett@itk.ppke.hu

***Abstract*—In this paper we describe algorithmic methods for the computational analysis of kinetic systems. The proposed computational methods can be applied to compute a special linearly conjugate realization of a kinetic system, or to determine all possible graph structures describing realizations of a kinetic system. It is proven that these algorithms can effectively determine all the realizations meeting the descriptions.**

***Index Terms*—chemical reaction network, directed graph representation, optimization, weak reversibility, dynamically equivalent realization, linearly conjugate realization**

I. Introduction and basic notions

Chemical reaction networks (CRNs) obeying the mass action law can be originated from the dynamical modelling of chemical and biochemical processes. Reaction networks can describe all kinds of non-linear qualitative dynamical phenomena using a simple algebraic structure, which makes it appealing to develop computational model analysis methods for these kinds of for dynamical models.

A. Algebraic characterization

Definition 1. *Chemical reaction networks can be determined by three sets* (see, e.g. [2], [3]).

- *A set of **species**:* $\mathcal{S} = \{X_i \mid i \in \{1,\dots,n\}\}$
- *A set of **complexes**:* $\mathcal{C} = \{C_j \mid j \in \{1,\dots,m\}\}$*, where*
  $C_j = \sum_{i=1}^{n} \alpha_{ji} X_i \qquad \forall j \in \{1,\dots,m\}$
  $\alpha_{ji} \in \mathbb{N} \qquad \forall j \in \{1,\dots,m\},\ \forall i \in \{1,\dots,n\}$
  *The complexes are defined as formal linear combinations of the species with coefficients, called the **stoichiometric coefficients**.*
- *A set of **reactions**:* $\mathcal{R} \subseteq \{(C_i, C_j) \mid C_i, C_j \in \mathcal{C}\}$
  The reaction $C_i \to C_j$ *is represented by the ordered pair* (C_i, C_j).

The reaction speeds are determined by non-negative real numbers k_{ij} called the **reaction rate coefficient**. The reaction (C_i, C_j) takes place if and only if the coefficient k_{ij} belonging to it is positive.

Special matrices are applied to describe the properties of the reaction network.

Definition 2. *The **complex composition matrix** $Y \in \mathbb{N}^{n\times m}$ of the CRN is determined by the stoichiometric coefficients as follows:*

$$[Y]_{ij} = \alpha_{ji} \qquad \forall i \in \{1,\dots,n\},\ \forall j \in \{1,\dots,m\} \tag{1}$$

Definition 3. *The **Kirchhoff matrix** $A_k \in \mathbb{R}^{m\times m}$ of the CRN encodes the reaction rate coefficients by its off-diagonal entries. The diagonal entries are defined so that the sums of entries in each column are zero, therefore matrix A_k is also called a **column conservation matrix***

$$[A_k]_{ij} = \begin{cases} k_{ji} & \text{if } i \neq j \\ -\sum\limits_{l=1, l\neq i}^{m} k_{il} & \text{if } i = j \end{cases} \tag{2}$$

In this paper we are examining reaction networks where the dynamics of the concentrations are governed by the mass-action law. If the function $x : \mathbb{R} \to \mathbb{R}^n_+$ defines the **concentrations of the species** depending on time, then the dynamics can be described by the dynamical equation

$$\dot{x} = Y \cdot A_k \cdot \psi(x), \tag{3}$$

where $\psi : \mathbb{R}^n_+ \to \mathbb{R}^m_+$ is a monomial function

$$\psi_j(x) = \prod_{i=1}^{n} x_i^{\alpha_{ji}} \quad j \in \{1,\dots,m\} \tag{4}$$

As we have seen, the dynamics of a reaction network can be described by a polynomial system, however not every polynomial system describes a CRN.

Definition 4. *Let $x : \mathbb{R} \to \mathbb{R}^n_+$ be a function, $M \in \mathbb{R}^{n\times p}$ a matrix and $\varphi : \mathbb{R}^n_+ \to \mathbb{R}^p_+$ a monomial function. The polynomial system*

$$\dot{x} = M \cdot \varphi(x), \tag{5}$$

*is called **kinetic** if there exist a matrix $Y \in \mathbb{N}^{n\times m}$, and a Kirchhoff matrix $A_k \in \mathbb{R}^{m\times m}$, so that*

$$M \cdot \varphi(x) = Y \cdot A_k \cdot \psi(x) \tag{6}$$

where $\psi : \mathbb{R}^n_+ \to \mathbb{R}^m_+$ is a monomial function determined by the matrix Y, $\psi_j(x) = \prod_{i=1}^{n} x_i^{Y_{ij}}$ for $j \in \{1,\dots,m\}$.

If the matrices Y and A_k of a reaction network fulfil Equation (6), then the CRN is called a **dynamically equivalent realization** of the kinetic system (3), and it is denoted by the matrix pair (Y, A_k). However, reaction networks with different sets of complexes and reactions can be governed by the same dynamics. see e.g. [5].

For the kinetic property of the polynomial system a necessary and sufficient condition can be given by determining the

B. ÁCS, "Computational analysis of kinetic systems" in *PhD Proceedings Annual Issues of the Doctoral School, Faculty of Information Technology and Bionics, Pázmány Péter Catholic University – 2015.* G. Prószéky, P. Szolgay Eds. Budapest: Pázmány University ePress, 2015, pp 107–110.

sign-pattern of matrix M, and a dynamically equivalent realization called the **canonical structure** can be algorithmically determined, see [4].

The property of dynamical equivalence can be extended to the case when the polynomial system is subjected to a positive linear diagonal state transformation. Such transformations are known to preserve the kinetic property of the system.

The state transformation is performed by a positive definite diagonal matrix $T \in \mathbb{R}^{n\times n}$ as follows:

$$\bar{x} = T^{-1} \cdot x, \quad x = T \cdot \bar{x}. \tag{7}$$

Applying it to the polynomial system (5) we get

$$\begin{aligned} \dot{\bar{x}} &= T^{-1} \cdot \dot{x} = T^{-1} \cdot M \cdot \varphi(x) = T^{-1} \cdot M \cdot \varphi(T \cdot \bar{x}) \\ &= T^{-1} \cdot M \cdot \Phi_T \cdot \varphi(\bar{x}), \end{aligned} \tag{8}$$

where $\Phi_T \in \mathbb{R}^{n\times n}$ is a positive definite diagonal matrix so that $[\Phi_T]_{ii} = \varphi_i(T \cdot \mathbf{1}) \quad \forall i \in \{1, \dots n\}$, φ_i is the ith coordinate function of φ and $\mathbf{1} \in \mathbb{R}^n$ is a column vector with all coordinates equal to 1.

Definition 5. *A reaction network (Y, A'_k) is a **linearly conjugate realization** of the kinetic system (5) if there exists a positive definite diagonal matrix $T \in \mathbb{R}^{n\times n}$ such that*

$$Y \cdot A'_k \cdot \psi(x) = T^{-1} \cdot M \cdot \Phi_T \cdot \varphi(x), \tag{9}$$

where $Y \in \mathbb{N}^{n\times m}$, $\psi : \mathbb{R}^n_+ \to \mathbb{R}^m_+$ so that $\psi_j(x) = \prod_{i=1}^n x_i^{Y_{ij}}$ for $j \in \{1, \dots, m\}$, and $A'_k \in \mathbb{R}^{m\times m}$ is a Kirchhoff matrix.

Dynamical equivalence is a special case of linear conjugacy, when the matrix T, and therefore the matrices T^{-1} and Φ_T as well are identity matrices.

The monomial functions φ and ψ in equations (6) and (9) might be different, therefore in both cases the set of complexes is not fixed. By applying the method presented in [4] a suitable set can be determined, and also the matrices M and Φ_T have to be modified accordingly. By using the notation $A_k = A'_k \cdot {\Phi'_T}^{-1}$ we get the following equation:

$$Y \cdot A_k \cdot \psi(x) = T^{-1} \cdot M \cdot \psi(x) \tag{10}$$

From now on we will consider only linearly conjugate realizations on a fixed set of complexes. With this assumption a linearly conjugate realization can be determined only by the matrices T and A_k.

II. Graph representation

A reaction network can be represented by a weighted directed graph.

Definition 6. *The graph $G(V, E)$ representing the CRN is called **Feinberg-Horn-Jackson graph**, or **reaction graph** for short, if it is defined as follows:*

- *the **vertices** correspond to the complexes, $V(G) = \mathcal{C}$*
- *the **directed edges** describe the reactions, $E(G) = \mathcal{R}$, the directed edge from vertex C_i to C_j represents the reaction $C_i \to C_j$*
- *the **weights** of the edges are the reaction rate coefficients, $w((C_i, C_j)) = k_{ij} \quad \forall (C_i, C_j) \in \mathcal{R}$.*

Loops and multiple edges are not allowed in a reaction graph.

In this paper we do not consider the actual reaction rates, only the graph structure.

Definition 7. *A realization of a CRN is called a **dense realization** if the maximum number of reactions take place.*

The applicability of our algorithms highly depends on the property of dense realizations worded in Proposition 1, which was proven in [1].

Proposition 1. *Among all the realizations linearly conjugate to a given kinetic system and fulfilling a finite set of additional linear constraints there is a realization determining a super-structure.*

The super-structure is the reaction graph describing the dense linearly conjugate realization, which contains the reaction graph of every realization as subgraph. It is easy to see that that the super-structure is unique.

III. Optimization model

Linearly conjugate realizations can be computed by using linear optimization. It was described earlier that in case of a linearly conjugate realization Equation (10) must be fulfilled. Since the function ψ can be omitted on both sides of the equation, it can be written as follows:

$$T^{-1} \cdot M - Y \cdot A_k = \mathbf{0} \tag{11}$$

where $\mathbf{0} \in \mathbb{R}^{n\times m}$ denotes the zero matrix. The matrices Y and M are fixed, and the **variables** are represented by the diagonal entries of T^{-1} and the offdiagonal entries of A_k.

Equation (11) guarantees the linear conjugacy of the system, and equations (12), (13) and (14) ensure that the matrices T^{-1} and A_k meet their definitions.

$$[A_k]_{ij} \geq 0 \qquad \forall i, j \in \{1, 2, \dots m\},\ i \neq j \tag{12}$$

$$[A_k]_{ii} = -\sum_{\substack{j=1 \\ j\neq i}}^{m} [A_k]_{ji} \qquad \forall i \in \{1, 2, \dots m\} \tag{13}$$

$$[T^{-1}]_{ii} > 0 \qquad \forall i \in \{1, 2, \dots n\} \tag{14}$$

IV. Results

We are developing linear programming based algorithms for computing linearly conjugate realizations with special properties in regard to the graph structures. Since the actual values of the variables are not important in our work, and several computational solvers require bounded variables, the following property is essential. For linearly conjugate realizations we have shown in [1] that in case of any kind of upper bounds (all variables are non-negative by definition) it holds, that for all

possible graph structures there is a realization with variables between the given upper and lower bounds.

A. Computing dense realizations

Several algorithms include the computation of dense realizations as a subroutine. There are different methods for determining such a realization, but these usually use auxiliary variables and often integer variables. In this latter case the problem turns out to be a mixed integer linear programming (MILP) problem, which are known to be NP-complete. Furthermore, the strictly positive property of variables can not be described by non-strict inequalities, but in linear programming models only these kinds of constraints can be applied.

We have developed an iterative algorithm to compute dense realizations, which is based on a geometric approach. It requires only the (real-valued) variables necessary to describe the realizations and use only linear programming methods and only non-strict inequalities.

It has been submitted for publishing along with our algorithm for developing weakly reversible linearly conjugate realizations as [1].

B. Computing all graph structures - Version 1

It is known that a kinetic system can have several different linearly conjugate realizations, but this rises the questions: How many are there? What kind of graph structures are possible?

To answer these questions we developed an algorithm to compute all the reaction graphs describing linearly conjugate realizations of a given kinetic system. Since the number of the possible reaction graphs is exponential (2^m), we can not expect polynomial running time. The exact running time depends on the kinetic system, but we have proven that the proposed algorithm determines every reaction graph describing linearly conjugate realizations, and between the computation of two realizations only polynomial time passes.

C. Computing all graph structures - Version 2

Though the first algorithm seems to be effective, since each step takes only polynomial time, but it computes several realizations more than once. To avoid repeated computation we developed another algorithm to solve this problem, which computes each realization only once, though there might be steps requiring exponential running time. We can prove that this algorithm as well can compute every reaction graph structure describing linearly conjugate realizations.

The articles for publish our algorithms computing all reaction graph structures are under preparation.

D. Example

In this section we demonstrate all the linearly conjugate realizations of the kinetic system (15),

$$\begin{aligned} \dot{x}_1 &= 3k_1 \cdot x_2^3 - k_2 \cdot x_1^3 \\ \dot{x}_2 &= -3k_1 \cdot x_2^3 + k_2 \cdot x_1^3 \end{aligned} \tag{15}$$

where the set of complexes is fixed to be $\{C_1 = 3X_2,\ C_2 = 3X_1,\ C_3 = 2X_1 + X_2\}$. According to the definitions the matrices Y and M are as follows:

$$Y = \begin{bmatrix} 0 & 3 & 2 \\ 3 & 0 & 1 \end{bmatrix} \qquad M = \begin{bmatrix} 3k_1 & -k_2 & 0 \\ -3k_1 & k_2 & 0 \end{bmatrix}$$

As the result of the first algorithm we get 18 different reaction graphs denoted by $G_1, \ldots, G_{18}$. The reaction graph G_1 (the complete directed graph) describes the dense realization, and consequently all other reaction graphs are subgraphs of it.

This small example is special in the sense, that all the obtained reaction graphs describe not just linearly conjugate but at the same time dynamically equivalent realizations. In general there are many more linearly conjugate realizations than dynamically equivalent ones. An other interesting observation is that there are two reactions (C_3, C_1) and (C_3, C_2) which are either both present or both missing from the reaction graph. If in a realization these two reactions take place, then there is another realization, where all the reactions of the first realization take place, except (C_3, C_1) and (C_3, C_2). Consequently, the reaction graphs G_i with the special reactions, shown in Figure 1 determine the reaction graphs G_{i+9} without these edges for $i \in \{1, \ldots, 9\}$, shown in Figure 2.

V. Conclusion

We have designed a linear programming based iterative algorithm using the minimum number of variables to compute dense linearly conjugate realizations of a kinetic system (and fulfilling a finite set of linear constraints) in polynomial time.

We have developed two algorithms to determine all the possible reaction graphs describing linearly conjugate realizations of a kinetic system. Both algorithms have an advantage considering the running time, although the whole computation in both cases might require exponential time.

We have proven that all three algorithms work properly, determining all the required answers within the time bounds.

Acknowledgement

This project was developed within the PhD program of the Multidisciplinary Doctoral School, Faculty of Information Technology and Bionics, Pázmány Péter Catholic University, Budapest.

I am grateful to my academic advisor, Gábor Szederkényi for the interesting topic and all his help and support.

References

[1] B. Ács, G. Szederkényi, Z. A. Tuza, Z. Tuza, Computing Linearly Conjugate Weakly Reversible Kinetic Structures Using Optimization and Graph Theory, submitted to *MATCH Commun. Math. Comput. Chem.*, Accepted with minor revision.

[2] M. Feinberg, Lectures on chemical reaction networks, *Notes of lectures given at the Mathematics Research Center, University of Wisconsin* (1979).

[3] M. Feinberg, Chemical reaction network structure and the stability of complex isothermal reactors – I. The deficiency zero and deficiency one theorems, *Chem. Eng. Sci.*, **42** 10 (1987) 2229–2268.

[4] V. Hárs, J. Tóth, On the inverse problem of reaction kinetics, *Coll. Math. Soc. J. B.* **30** (1981) 363–379.

[5] F. Horn, R. Jackson, General mass action kinetics, *Arch. Ration. Mech. An.* **47** (1972) 81–116.

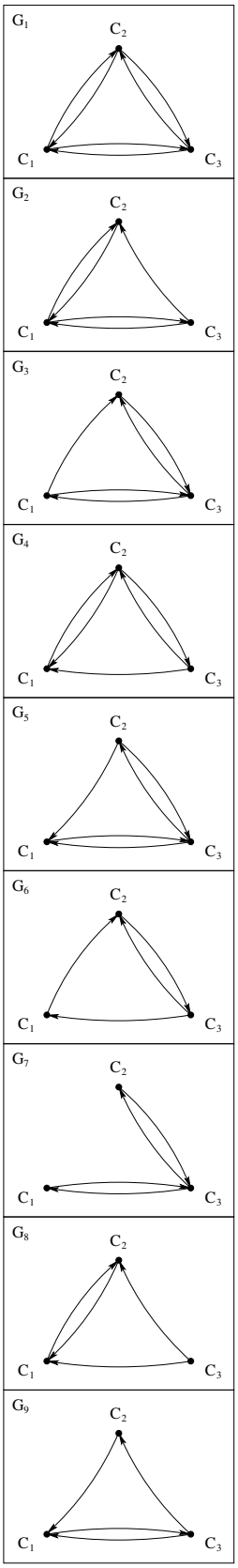

Figure 1. Reaction graphs with reactions (C_3, C_1) and (C_3, C_2) describing linearly conjugate realizations of the kinetic system (15)

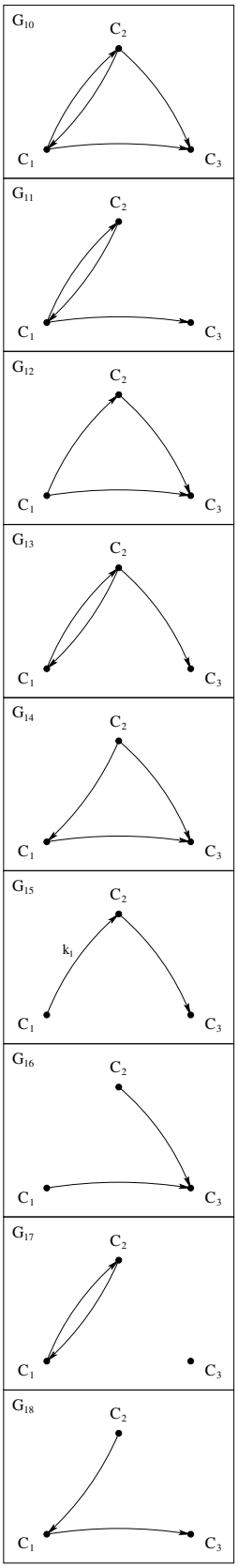

Figure 2. Reaction graphs without reactions (C_3, C_1) and (C_3, C_2) describing linearly conjugate realizations of the kinetic system (15)

Measuring wrist movements with inertial sensors

Bence József BORBÉLY
(Supervisor: Péter SZOLGAY)
Pázmány Péter Catholic University, Faculty of Information Technology and Bionics
50/a Práter street, 1083 Budapest, Hungary
borbely.bence@itk.ppke.hu

***Abstract*—In this study the design aspects and a proof of concept implementation of an inertial sensor based measurement setup is presented for kinematic analysis of wrist movements. Commercially available inertial sensor systems and packages are reviewed and compared to establish the design requirements for a custom-designed, task oriented measurement device. In addition to hardware considerations, current sensor fusion algorithms are discussed and compared on the basis of implementation complexity, hardware requirements and effectiveness to support the design decisions shown in the proof of concept implementation. Measurement data is also presented to validate system usability in a wrist movement task designed for device testing.**

I. Introduction

In the last decade, the field of inertial sensor based movement tracking has gained popularity and evolved from concept to commercially available, complex motion capture systems that provide accurate and reliable measurement of human body movements. This process was mainly driven by the developments in Micro-Electro-Mechanical-System (MEMS) sensor technology that eased system design and development via device miniaturization and integration, making wearable measurement system technology a reachable alternative to the classic line-of-sight measurement methods. These include optical (e.g. Vicon or OptiTrack) and ultrasound-based systems (Zebris), both providing good to excellent tracking accuracy in most cases, but having the sometimes restricting need for a controlled laboratory environment for proper operation (even when outdoor measurement is possible).

This restriction comes from the marker-based operation of these systems, where passive (mainly optical usage) or active (mainly ultrasound usage) markers are placed on anatomically relevant bony areas of body segments (near the joints in the case of extremities) and their spacial position is recorded in a device-specific measurement frame. This system architecture induces additional computational steps to determine the kinematics of the measured movement because the recorded marker coordinates have to be transformed into a protocol-specific external reference frame that is independent from the measurement system itself. Following this transformation step, anatomical joint angles have to be determined from the spacial position of the markers which may involve the development of custom algorithms or using readily available software tools such as OpenSim [1], an open source simulation software for human movements developed at Stanford University.

As a main difference to the above concept, inertial sensors give orientation information more accurately than position compared to marker-based methods, providing the possibility to calculate inter-segmental angles of measured body parts at a lower computational cost [2]–[4].

In the present work currently available inertial sensor packages are introduced focusing mainly on single-chip solutions and their application possibilities in custom wearable measurement system designs.

II. Technology overview

A. Inertial sensor based motion capture

There are commercial motion capture systems using inertial sensors focusing mainly on media content production like the 3DSuit from InertialLabs[1], different suits and gloves from Synertial[2] and the MVN system from Xsens[3] [5], which even provides a biomechanical option called MVN Biomech and was evaluated for academic use, too [6], [7]. While these systems are valuable motion capture options, the current study seeks the possibilities of self-developed inertial measurement to achieve the highest possible flexibility in system design and integration, especially considering the measurement of other modalities in the future like electrical muscle activities.

B. Inertial sensors (based on manufacturer descriptions)

Regarding the in house development of an inertial sensor based measurement system the used sensor package has to be carefully chosen based on available measurement modalities (e.g. 3-, 6-, or 9-axis measurement), resolution, package size and data fusion possibilities. In the following subsections the currently available single chip sensor packages are shortly presented.

1) ***MPU-9150 / MPU-9250****:* Manufactured by InvenSense[4], the MPU-9150 was the world's first integrated 9-axis device that combines a 3-axis MEMS gyroscope, a 3-axis MEMS accelerometer, a 3-axis MEMS magnetometer and a Digital Motion Processor (DMP) hardware accelerator engine. The sensor features three 16-bit analog-to-digital converters (ADCs) for digitizing the gyroscope outputs, three 16-bit ADCs for digitizing the accelerometer outputs and three 13-bit ADCs for digitizing the magnetometer outputs. For precision tracking of both fast and slow motions, the parts feature a user-programmable gyroscope full-scale range of $\pm$250, $\pm$500, $\pm$1000, and $\pm$2000 °/sec, a user- programmable accelerometer full-scale range of $\pm$2g, $\pm$4g, $\pm$8g, and $\pm$16g, and a magnetometer full-scale range of $\pm 1200\mu$T. The MPU-9150 is a multi-chip module (MCM) consisting of two dies

[1] http://inertiallabs.com/3dsuit.html
[2] http://synertial.com/brochure-suits/
[3] https://www.xsens.com/products/xsens-mvn/
[4] http://www.invensense.com/

B. BORBÉLY, "Measuring wrist movements with inertial sensors" in *PhD Proceedings Annual Issues of the Doctoral School, Faculty of Information Technology and Bionics, Pázmány Péter Catholic University – 2015.* G. Prószéky, P. Szolgay Eds. Budapest: Pázmány University ePress, 2015, pp 111– 114.

integrated into a single LGA package. One die houses the 3-axis gyroscope and the 3-axis accelerometer. The other die houses the AK8975 3-axis magnetometer from Asahi Kasei Microdevices Corporation. Communication with the sensor package can be performed using I^2C protocol.

The MPU-9250 is the successor of the first generation device with differences in the integrated magnetometer (the AK8963 is used here) resulting in a wider magnetic full-scale range ($\pm 4800 \mu T$), an additional communication interface (SPI) and smaller overall noise than its predecessor.

*2) **LSM9DS0 / LSM9DS1**:* The LSM9DS0 and LSM9DS1 are system-in-package devices from STMicroelectronics[5] featuring a 3D digital linear acceleration sensor, and a 3D digital angular rate sensor, a 3D digital magnetic sensor. Both devices include an I^2C and an SPI serial bus interface for communication. The LSM9DS0 has a linear acceleration full-scale range of $\pm$2g, $\pm$4g, $\pm$6g, $\pm$8g and $\pm$16g, an angular rate full-scale range of $\pm$245, $\pm$500 and $\pm$2000 °/sec and a magnetic field full-scale range of $\pm$2, $\pm$4, $\pm$8 and $\pm$12 gauss, while the LSM9DS1 shifts the magnetic full-scale range one level upwards as follows: $\pm$4, $\pm$8, $\pm$12 and $\pm$16 gauss. Both sensor packages are available in small size LGA packages.

*3) **MAX21100**:* Developed by Maxim Integrated[6], the MAX21100 is a special device in the field because however the chip itself features only a 6-axes sensing solution with a 3D accelerometer and 3D gyroscope having full-scale ranges of $\pm$2g, $\pm$4g, $\pm$6g, $\pm$8g, $\pm$16g, and $\pm$250, $\pm$500, $\pm$1000, $\pm$2000 °/sec, it contains a master I^2C interface for external magnetometer handling and an integrated Motion Merging Engine (MME) to perform a complete 9-axis sensor fusion process inside the IC. This technological improvement brings easier implementation of orientation tracking systems because it frees system developers from the implementation of sensor fusion algorithms on control hardware. The device is available in a tiny LGA package, but if 9-axis fusion is needed in the application the extra magnetometer IC have to be considered during the design phase.

*4) **BMX055 / BNO055**:* The BMX055 is a fully integrated device manufactured by Bosch Sensortec[7]. In contrast with the other packages, all sensors in the device are designed and manufactured inside the same company which promises the least technical difficulties during application development. The package features a 3D linear accelerometer with programmable full-scale range of $\pm$2g, $\pm$4g, $\pm$6g, $\pm$8g or $\pm$16g, a gyroscope programmable full-scale range of $\pm$125, $\pm$250, $\pm$500, $\pm$1000, $\pm$2000 °/sec and a magnetometer with full-scale ranges of $\pm$1200 (x, y direction) and $\pm$2500 μT (z direction). Like the other devices, the BMX055 is available in a small size LGA package.

As the evolution of the BMX055, to further improve usability and ease development, Bosch Sensortec developed the BNO055 which is a System in Package (SiP), integrating a triaxial 14-bit accelerometer, a triaxial 16-bit gyroscope with a range of ±2000 degrees per second, a triaxial geomagnetic sensor and a 32-bit microcontroller running the company's proprietary Kalman filter based sensor fusion algorithm. At just 5.2 x 3.8 x 1.1mm^3, it is significantly smaller than comparable discrete or system-on-board solutions while providing stable and ready to use device orientation data.

[5]http://www.st.com/web/en/home.html
[6]http://www.maximintegrated.com/
[7]https://www.bosch-sensortec.com/

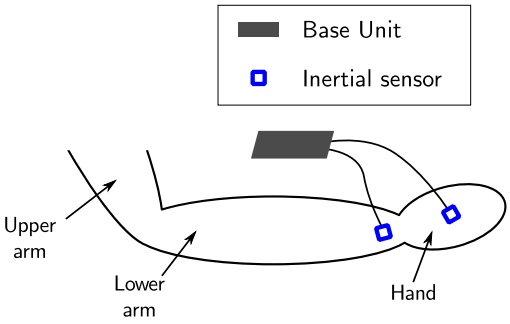

Fig. 1. Concept drawing of the measurement system. The Base Unit is separated in the current phase for evaluation purposes. Inertial sensors are placed at the distal end of the lower arm right before the wrist joint and on the back of the hand, allowing the measurement of the hand's relative orientation with respect to the lower arm's orientation.

C. Sensor fusion algorithms

1) Kalman filter: A widely used sensor fusion method is based on the Kalman filter [8] which operates recursively on streams of noisy input data to provide statistically optimal estimates of the underlying system states that are more precise than the ones based on measurements only. While the Kalman filter can be considered very popular among inertial sensor fusion tasks even in movement analysis [9], [10], there are other approaches to the problem that does not need preliminary system or noise models for acceptable operation.

2) Madgwick AHRS filter: One of these methods is a computationally efficient open source orientation filter [11] that is able to provide 9-axis fusion sensor fusion using a gradient descent algorithm. The filter has the benefits of being computationally inexpensive and effective at sampling rates as low as 10 Hz, making it an ideal looking choice for low power embedded application.

III. Proof of concept implementation

The concept of the system is depicted in Figure 1. The core of the design is a Base Unit responsible for controlling the measurements, collecting sensor data, performing pre-processing tasks and sending and/or storing the output data. There are two inertial sensors in the design which are placed at the distal end of the lower arm right before the wrist joint and on the back of the hand, respectively. This arrangement allows the measurement of the hand's relative orientation with respect to the lower arm's orientation, resulting in anatomically relevant joint angles of the wrist.

A. Base Unit

The block diagram of the Base Unit is depicted in Figure 2. It is designed with an STM32F407VG microcontroller unit (MCU) as its central element which is a high performance ARM Cortex-M4 core running at up to 168 MHz. The MCU has 1 MB flash and 192 kB SRAM, built-in 12-bit 2.4 MSPS ADCs, various serial peripherals (including I^2C, SPI and

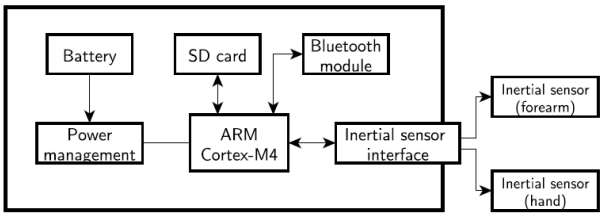

Fig. 2. Block diagram of the Base Unit. All measurement and processing is performed by an ARM Cortex-M4 core running at 168 MHz. The Base Unit contains a Power Management Unit to provide the digital supplies, data streaming (Bluetooth) and data storage (SD card) modules. Inertial sensors through a corresponding hardware interface.

UART), a dedicated SDIO interface for high speed SD card control and a 16-stream DMA controller. These properties make this device a good choice for device prototyping because it provides enough headroom for different development options. In the initial phase of development an STM32F4 Discovery board was used as the central hardware element of the system which provides access to almost all pins of this MCU and a debugger unit in the same package.

Device firmware was implemented in C using the *Eclipse* IDE (version Kepler) and the *GNU Tools for ARM Embedded Processors* package on an Ubuntu 12.04 LTS system. Device programming and debugging was performed with *OpenOCD* (versoin 0.8.0). The Base Unit's firmware was designed and implemented using *FreeRTOS*^{TM} [8], a free and industry standard real-time operating system for embedded applications. The MCU's DMA controller was utilized in each scenario where it was applicable to further improve execution parallelism.

B. Inertial sensors

To perform measurements of joint kinematics, MPU-9250 single chip 9 degrees-of-freedom MEMS inertial sensors were used. Considering sensor properties shown in Section II-B, this sensor was used based on the good balance of measurement properties and handling. It should be noted however, that in the final design the BNO055 package would worth trying because the integrated sensor fusion algorithm can offload the main processor by a great amount.

A custom device driver was developed for the inertial sensors to utilize control, calibration and measurement processes over the I^2C bus. Zero motion calibration of the accelerometer and the gyroscope was implemented as part of the sensor initialization process, while hard and soft iron calibration of the magnetometer was performed only once for each sensor and hard-coded into the sensor driver. However, there is a proprietary on-chip Digital Motion Processor (DMP) in each sensor package, it was not used during development because it is only capable of performing 6-axis (accelerometer + gyroscope) sensor fusion, and and there is no publicly available documentation for this unit. Instead, a computationally efficient open source orientation filter [11] was used to provide sensor orientations in software using a gradient descent based 9-axis fusion algorithm. The applied method provides direct quaternion output (avoiding the phenomenon of gimbal lock)

[8]http://www.freertos.org/

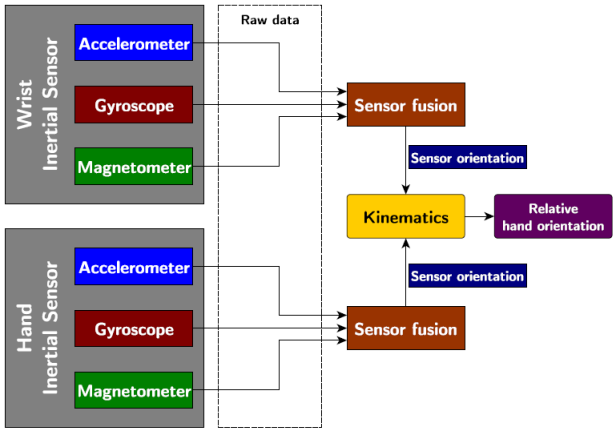

Fig. 3. Block diagram of the sensor fusion algorithm implemented on the proof of concept device.

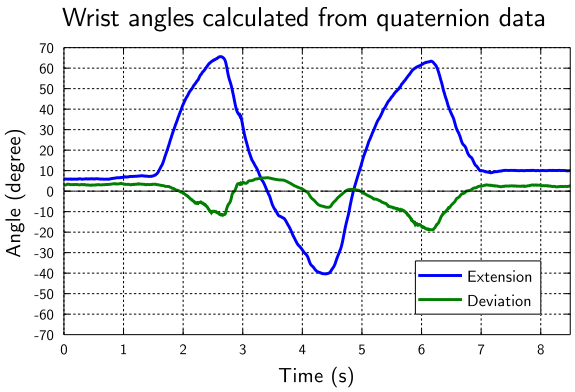

Fig. 4. Experimental measurement data from a wrist movement task while the subject performed a *rest-extension-flexion-extension-rest* sequence. Flexion and deviation angles were calculated from the combined quaternion data coming from the inertial sensors placed at the distal end of the forearm and at the back of the hand as shown in Figure 1.

and is easily capable to provide stable 200 Hz output rate enabling the system to meet and exceed the requirements for orientation data measurement.

C. Control and evaluation software

To control the test device and evaluate usability of the measurement setup, task specific MATLAB programs were designed and developed. The control part contained wireless command and data exchange, incoming data visualization and storage. In the evaluation part anatomical wrist angle calculation from separate quaternion inputs was implemented.

IV. Results

Anatomical wrist angles were calculated from differential quaternion data calculated from the wrist and hand sensors as shown in Figure 3. A simple algorithm was applied to get the extension and deviation angles by calculating the orthogonal projections of the hand vector determined by the differential quaternions on the sagittal and transversal planes

attached to the lover arm vector. Experimental measurement data from a wrist movement task is shown in Figure 4. while the subject performed a *rest-extension-flexion-extension-rest* movement sequence.

V. Conclusion and future work

In this study the design and proof of concept implementation of a biomedical measurement device with preliminary measurement data is presented showing its capability for kinematic measurements of the wrist. In the current state the design shows promising characteristics, however further testing and fine tuning is necessary to finalize the design. Further work includes finalization and integration of the whole design, PCB design and manufacturing of the device and data validity testing with reference measurements.

References

[1] S. Delp, F. Anderson, A. Arnold, P. Loan, A. Habib, C. John, E. Guendelman, and D. Thelen, "Opensim: Open-source software to create and analyze dynamic simulations of movement," *Biomedical Engineering, IEEE Transactions on*, vol. 54, no. 11, pp. 1940–1950, Nov 2007.

[2] H. Zhou, H. Hu, and Y. Tao, "Inertial measurements of upper limb motion." *Medical & biological engineering & computing*, vol. 44, no. 6, pp. 479–87, Jul. 2006.

[3] H. Kortier, V. Sluiter, D. Roetenberg, and P. Veltink, "Assessment of hand kinematics using inertial and magnetic sensors," *Journal of NeuroEngineering and Rehabilitation*, vol. 11, no. 1, p. 70, 2014.

[4] X. Chen, J. Zhang, W. Hamel, and J. Tan, "An inertial-based human motion tracking system with twists and exponential maps," in *Robotics and Automation (ICRA), 2014 IEEE International Conference on*, May 2014, pp. 5665–5670.

[5] D. Roetenberg, H. Luinge, and P. Slycke, "Xsens mvn: Full 6dof human motion tracking using miniature inertial sensors," Xsens Technologies, Tech. Rep., 2013.

[6] J.-T. Zhang, A. C. Novak, B. Brouwer, and Q. Li, "Concurrent validation of xsens mvn measurement of lower limb joint angular kinematics," *Physiological Measurement*, vol. 34, no. 8, p. N63, 2013.

[7] S. Thies, P. Tresadern, L. Kenney, D. Howard, J. Goulermas, C. Smith, and J. Rigby, "Comparison of linear accelerations from three measurement systems during reach and grasp," *Medical Engineering and Physics*, vol. 29, no. 9, pp. 967 – 972, 2007.

[8] R. E. Kalman, "A new approach to linear filtering and prediction problems," *Transactions of the ASME–Journal of Basic Engineering*, vol. 82, no. Series D, pp. 35–45, 1960.

[9] Y. Tian, X. Meng, D. Tao, D. Liu, and C. Feng, "Upper limb motion tracking with the integration of {IMU} and kinect," *Neurocomputing*, vol. 159, no. 0, pp. 207 – 218, 2015.

[10] G. Ligorio and A. Sabatini, "A novel kalman filter for human motion tracking with an inertial-based dynamic inclinometer," *Biomedical Engineering, IEEE Transactions on*, vol. PP, no. 99, pp. 1–1, 2015.

[11] S. Madgwick, A. Harrison, and R. Vaidyanathan, "Estimation of imu and marg orientation using a gradient descent algorithm," in *Rehabilitation Robotics (ICORR), 2011 IEEE International Conference on*, June 2011, pp. 1–7.

Validation of a non-invasive arterial pressure waveform measuring system

Sándor FÖLDI
(Supervisors: György CSEREY, Péter SÓTONYI)
Pázmány Péter Catholic University, Faculty of Information Technology and Bionics
50/a Práter street, 1083 Budapest, Hungary
folsa@digitus.itk.ppke.hu

***Abstract*—Measuring the continuous arterial blood pressure is very important in clinics: during surgery, monitoring intra- and postoperative patients, in intensive care and during patient transport in ambulance, because for immediate intervention the changes must be followed moment by moment. The most accurate solution for that is an invasive method realised with arterial catheterization. As an invasive method it has more risks and involves a greater strain thus it requires a good reason to be applied. It is also uncomfortable for either the practitioners and the patients. So a continuous non-invasive blood pressure monitoring device would be important, but it is still a great challenge to measure the blood pressure waveform non-invasively. There are several devices commercially available, but each has disadvantages and none of them has been used widespread yet. Beside the blood pressure values, the continuous arterial pulse waveform is also important. It can be used for pulse diagnosis and combined with the pressure values, it gives important information on other haemodynamic values.**

***Index Terms*—arterial blood pressure, non-invasive method, pulse diagnosis, arterial pulse waveform**

I. Introduction

Most people's first thought about blood pressure monitoring is the classical cuff-based blood pressure monitor. It can be enough for a routine check at home, but for hospitals and clinics in many cases it can not give enough information about the patients. Cuff-based blood pressure monitors can only measure a systolic and a diastolic blood pressure value at a given moment and can only make several measurements per minute. This information is not enough for monitoring the patients in intensive care or during surgery, where the continuous blood pressure waveform is required to monitor the sudden changes in blood pressure. The inflation of the cuff can be uncomfortable for the patient, the grip can be painful and in worst case it can cause microtrauma like haemorrhages. Nowadays the general standard in continuous blood pressure monitoring is arterial catheterization [1]. It is an invasive method, the arterial cannula is inserted into an artery, usually into the radial or the femoral artery. As an invasive method it has many disadvantages, for example the cannula can only be inserted and applied by a trained person, requires very strict hygiene conditions, could not be applied during non-invasive experiments without a clinical license and it is also very uncomfortable for patients. It has many risks, like injury of the artery, bleeding, hematoma formation, infection at the cannula site and embolism. These are several reasons why a non-invasive continuous blood pressure monitor is required. This continuous waveform can be useful in some examinations too.

One of the first continuous non-invasive blood pressure monitor was developed by Etienne Jules Marey in 1860 [2]. It was based on applanation tonometry, which is a non-invasive, reproducible and reliable technique that is able to estimate the central arterial blood pressure. One of its modern versions is the PulsePen device [3], which is also based on applanation tonometry. It is composed of one tonometer and an integrated electrocardiogram. It is very compact, the size of the PulsePen sensor is like a ball point pen. It is also easy to use. It can measure pulse wave velocity and estimate the wave reflections, which can give information about the arterial wall. Another tonometric device is the Tensys T-Line-device [4]-[8], which can be applied on the radial artery. It is one of the most accurate continuous non-invasive blood pressure monitors in the market. It has a very high accuracy in beat-to-beat blood pressure values, but also capable of waveform recording. First, the appropriate pulse taking position must be found, which is done by palpation. After the device is attached to the wrist at that position it automatically adjusts the position according to the biggest amplitude signal. Then it must be calibrated that is done by a classical cuff-based blood pressure monitor (it gives the baseline value) and a parameter calculation from data like the patient's gender, age, height and weight. This whole procedure could take 3-5 minutes. One of its disadvantages is that it must be recalibrated in case of every little movement, thus it can only be used effectively in general anesthesya.

Beside devices based on applanation tonometry there is another big group of continuous non-invasive blood pressure monitoring devices, which are based on the Peñaz principle [1], [9]. The Peñaz principle is based on the volume clamp method. The basic measuring device consists of a finger cuff, which contains a photoplethysmograph. It can estimate the blood volume of the finger by infrared light absorbance. This estimation is used in a feedback loop for the finger cuff to keep the blood volume constant. This basic idea is further developed by Nexfin [10], [11]. According to the feedback loop, a signal similar to the invasive continuous blood pressure waveform could be acquired. This method is realised in the Nexfin Finapres device. Another variation using this method is the CNAP CNSystem that has an integrated calibration by

S. FÖLDI, "Validation of a non-invasive arterial pressure waveform measuring system" in *PhD Proceedings Annual Issues of the Doctoral School, Faculty of Information Technology and Bionics, Pázmány Péter Catholic University – 2015.* G. Prószéky, P. Szolgay Eds. Budapest: Pázmány University ePress, 2015, pp 115– 118.

upper arm cuff-based blood pressure measurement [12], [13]. These devices have many disadvantages, they are affected by factors like skin colour, light conditions in the room, cold extremities, etc. They are also expensive.

Non-invasive continuous blood pressure waveform is also important in diagnostics. From this, many haemodynamic parameters can be estimated, like cardiac index that relates to cardiac output [14]. Good quality waveforms can be used for pulse diagnosis. It is a diagnostic method that can diagnose cardiovascular and inner-organ diseases according to the shape of the pulse wave measured on the radial artery at the wrist [15].

All the above mentioned devices can estimate the beat-to-beat blood pressure value with a relatively high accuracy, but the waveform is still a problem in most of the cases. Due to that fact, these devices have not been used for pulse diagnosis purposes except the PulsePen device. Another issue is the individual's movements. The validation of these devices is usually made in general anesthesya, which means the subject does not move during the measurement. This is a big limitation, because this way they can only be applied during surgery. These devices are expensive as well.

In the following sections our non-invasive continuous blood pressure waveform monitoring device is introduced with its current capabilities.

II. Method

A. Non-invasive pulse waveform measuring system

The measurements were made with an Optoforce OMD-20-SA-60N 3D force sensor [16]. This is an optical based sensor that can measure not only the magnitude of the force, but also the direction of it. It has high resolution, high sensitivity and a robust design. The sensor has a semispherical shape with 20 mm diameter. The sensing surface is silicone rubber, which is comfortable contacting with the wrist. It has also a low chemical reactivity that is an advantage in healthcare, because it can be disinfected easier. The sensor was attached to a wrist band specially design for pressure waveform measuring at the wrist. It consist of three elements: a band, a buckle and a sensor holding "slider". The sensor holding element was designed in Autodesk Inventor Professional 2015 software and printed with a 3D printer. It is easy to put the sensor into it and it holds the sensor steady. The most important function of this slider is that after the wrist band was put on the wrist, the sensor position can be adjusted to acquire the best quality pulse signal which basically means the highest amplitude. The signal of the sensor is visualized and recorded by the Optoforce Data Visualization software. Fig. 1. shows the non-invasive pulse waveform measuring environment.

B. Signal processing

For arterial blood pressure waveform signal processing, a wavelet based cascaded adaptive filter was used. This filter consists of two main parts: a discrete Meyer wavelet decomposition-based filter and a spline estimation filter [17]. By the wavelet decomposition filter the signal and the noise is

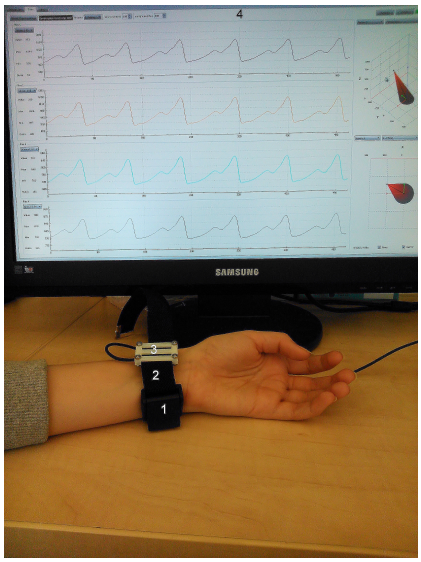

Fig. 1. Continuous non-invasive arterial blood pressure waveform measuring system. 1 - buckle, 2 - band, 3 - sensor holding "slider" with the Optoforce 3D force sensor, 4 - data visualization and recording software.

approximated on different decomposition levels. By subtracting the noise and recomposing the signal, most of the hand movement and breathing caused noises could be filtered. The next step before the spline estimation filter is detecting the onset points. The onset point indicates the start of the systole, so it is a local minimum point. Onset point detection is based on a slope sum function [18]. This converts the pulse signal into a simpler one whose extremes corresponds to the onset points. The extremes of this slope sum function could be found easily by a simple derivative method. After the onset points are detected, the spline estimation filter is applied that removes the baseline wander from the signal by approximating it with a spline function. The last step is signal segmentation according to the onset points. Fig. 2. summarizes the signal processing algorithm. The presented signal processing method could be used as a filter for signal waveform comparison. For blood pressure value comparison, the spline estimation filter must be omitted to reserve the diastolic blood pressure values.

C. Data collection

The measurements were made at the Semmelweis University Department of Vascular Surgery under clinical TUKEB license no. 186/2013. The individuals received written and oral information about the experiment and after their approval, a written informed consent was obtained. All individuals participated in Carotid surgery, thus the invasive blood pressure monitoring was necessary. Our measurements were made after the successful surgery and the patients were awake and monitored by trained nurses. The signal of the invasive catheter was read out by GE Dashboard 4000 patient monitor device and recorded on a PC by Datex-Ohmeda S/5 Collect software. The non-invasive signal was measured on the opposite arm with the presented measuring device. Invasive and non-invasive signals

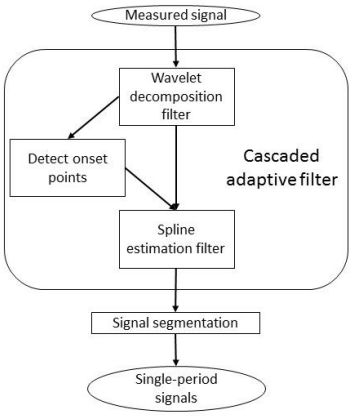

Fig. 2. Diagram of signal processing algorithm

TABLE I
CHARACTERISTICS OF PARTICIPANTS

	Range	Mean±sd
Age	57-77	65.2±7.7
Height (cm)	148-173	161.2±8.6
Weight (kg)	50-82	69.1±9.9
Heart rate (bpm)	57-90	72.4±10.1
Systolic BP (mmHg)	106-178	132.7±20.3
Diastolic BP (mmHg)	51-78	58.7±8.1

were recorded simultaneously for 20-30 minutes with 100 Hz sampling frequency. In this study 13 patients participated (7 men, 6 women), but 4 had to be excluded (3 men, 1 woman) because there were too many movements during the measurement. The characteristics of the participants (without the excluded) is represented in Table I.

D. Data comparison

This study focuses on the validation of the waveform. The invasive and non-invasive signals are both filtered by the signal processing method introduced above. After that each single-period pulse signal is normalized to 1 and the invasive and non-invasive signals are cross-correlated. Those single period signals that were corrupted by movement are excluded form the comparison, if the movement could not be filtered via signal processing. It is decided by the length of the processed single-period signals. If this length differs more than 20% of the length of the corresponding invasive single-period signal than the signal is excluded with the overlapped invasive signals. The rate of the excluded single-period signals is always less than 10% for the examined pulse signals.

III. RESULTS

For each individual the mean, the standard deviation, the minimum and maximum value and the median of correlation between the corresponding single period signals are presented in Table II. The highest average correlation value was 0.986±0.024 and most of the results are above 0.9, which means great similarity between the invasive and non-invasive measurements. Fig. 3. shows a short example of a highly correlated single-period site from a whole pulse waveform. For each individual there were some less correlated signals that can occur as a part of a movement. During the experiment the reproducibility was also tested. For 4 individuals two measurements were made consecutively by replacing the non-invasive sensor on the wrist. For each measurement pairs the mean correlation value of the corresponding invasive and non-invasive single-period pulse waveforms were: (0.939±0.142, 0.971±0.096); (0.968±0.055, 0.977±0.022); (0.986±0.024, 0.969±0.076); (0.935±0.073, 0.954±0.032) respectively.

TABLE II
CORRELATION OF SINGLE-PERIOD SIGNALS

Individual	Mean correlation±std.	Min.	Max.	Median
#1	0.939±0.142	-0.479	0.998	0.981
#2	0.968±0.055	0.240	0.992	0.980
#3	0.986±0.024	0.617	0.997	0.990
#4	0.960±0.090	0.176	0.999	0.991
#5	0.893±0.187	-0.590	0.990	0.945
#6	0.949±0.079	0.100	0.993	0.969
#7	0.960±0.111	-0.397	0.998	0.987
#8	0.935±0.073	-0.073	0.993	0.951
#9	0.984±0.064	0.112	0.999	0.992

IV. CONCLUSION

As Table II. shows for each individual the mean correlation value between corresponding invasive and non-invasive single-period signals were high. Considering the minimum correlation values for individuals there were some low values. According to the mean, standard deviation and median values these small correlations were rare. It could be occurred due to several reasons. One is that the participants were awake and sometimes made movements. As mentioned certain single-period signals were excluded from the examination but there are several that could be processed, but the waveform significantly differs due the the effect of movement. There are some other factors that should be considered for signal comparison. The non-invasive measurements were made on the opposite wrist than the position of the invasive catheter. This can mean a small shift between the two signals. It is also important in waveform similarity, because the two waveform can be different due to disease or differences between the conditions of the arterial wall in the two sides. For example in two cases the difference between blood pressure in the two arms was more than 20 mmHg that can mean a significant difference in waveform either.

Examining the reproducibility of non-invasive measurements high correlation values were obtained for the consecutive measurements. It means that the non-invasive pressure waveform measuring sensor can be applied reproducibly. It is important in its application as a monitoring device and as a diagnostic device either.

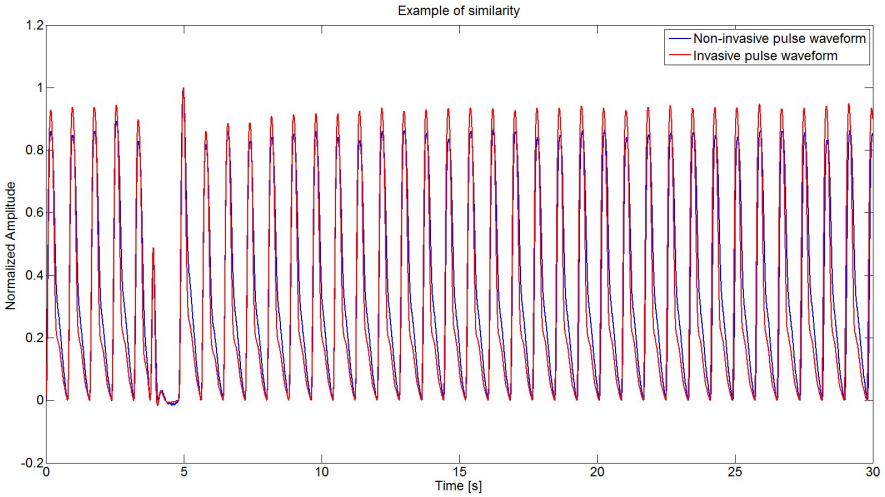

Fig. 3. An example of a highly correlated pulse waveform segment

This paper introduced a non-invasive pressure waveform measuring system and proved its usability by validating by an invasive arterial catheter. The next step will be the comparison of the blood pressure values and the output of the non-invasive sensor. We hope that in the future this system can be used for both diagnostic and monitoring tasks.

ACKNOWLEDGMENT

The author would like to thank Dr. György Cserey and Dr. Péter Sótonyi for their help and guidance. The support of the Multidisciplinary Doctoral School at the Faculty of Information Technology and Bionics (ITK - Research Faculty) at the Pázmány Péter Catholic University (PPCU - University of National Excellence) and the Semmelweis University Department of Vascular Surgery is also gratefully acknowledged. The author would also like to thank the nurses at the clinic for their help in the measurements. The technical background is acknowledged to Optoforce Ltd. The author would like to thank Flóra Zieger for the support and help in the project.

REFERENCES

[1] Chung, Elena, et al. *Non-invasive continuous blood pressure monitoring: a review of current applications.* Frontiers of medicine 7.1 (2013): 91-101.

[2] da Fonseca, Lucas José Sá, Marco Antônio Mota-Gomes, and Luíza A. Rabelo. *Radial Applanation Tonometry as an Adjuvant Tool in the Noninvasive Arterial Stiffness and Blood Pressure Assessment.* World Journal of Cardiovascular Diseases 2014 (2014).

[3] Salvi, Paolo, et al. *Validation of a new non-invasive portable tonometer for determining arterial pressure wave and pulse wave velocity: the PulsePen device.* Journal of hypertension 22.12 (2004): 2285-2293.

[4] Janelle, Gregory M., and Nikolaus Gravenstein. *An accuracy evaluation of the T-Line Tensymeter (continuous noninvasive blood pressure management device) versus conventional invasive radial artery monitoring in surgical patients.* Anesthesia & Analgesia 102.2 (2006): 484-490.

[5] Szmuk, P., et al. *An evaluation of the TLine Tensymeter continuous non-invasive blood pressure device during induced hypotension.* Anaesthesia 63.3 (2008): 307-312.

[6] Meidert, Agnes S., et al. *Evaluation of the radial artery applanation tonometry technology for continuous noninvasive blood pressure monitoring compared with central aortic blood pressure measurements in patients with multiple organ dysfunction syndrome.* Journal of critical care 28.6 (2013): 908-912.

[7] Saugel, B., et al. *Non-invasive continuous arterial pressure measurement based on radial artery tonometry in the intensive care unit: a method comparison study using the T-Line TL-200pro device.* British journal of anaesthesia (2013): aet025.

[8] Dueck, Ron, Oliver Goedje, and Paul Clopton. *Noninvasive continuous beat-to-beat radial artery pressure via TL-200 applanation tonometry.* Journal of clinical monitoring and computing 26.2 (2012): 75-83.

[9] Fortin, J., et al. *Continuous non-invasive blood pressure monitoring using concentrically interlocking control loops.* Computers in biology and medicine 36.9 (2006): 941-957.

[10] Martina, Jerson R., et al. *Noninvasive continuous arterial blood pressure monitoring with Nexfin.* Anesthesiology 116.5 (2012): 1092-1103.

[11] Schattenkerk, Daan W. Eeftinck, et al. *Nexfin noninvasive continuous blood pressure validated against Riva-Rocci/Korotkoff.* American journal of hypertension 22.4 (2009): 378-383.

[12] Hahn, R., et al. *Clinical validation of a continuous non-invasive haemodynamic monitor (CNAP 500) during general anaesthesia.* British journal of anaesthesia (2012): aer499.

[13] Ilies, C., et al. *Investigation of the agreement of a continuous non-invasive arterial pressure device in comparison with invasive radial artery measurement.* British journal of anaesthesia 108.2 (2012): 202-210.

[14] Fischer, M. O., et al. *Non-invasive continuous arterial pressure and cardiac index monitoring with Nexfin after cardiac surgery.* British journal of anaesthesia 109.4 (2012): 514-521.

[15] Bilton, Karen, Leon Hammer, and Chris Zaslawski, *Contemporary Chinese Pulse Diagnosis: A Modern Interpretation of an Ancient and Traditional Method*, Journal of Acupuncture and Meridian Studies, 2013.

[16] Optoforce Ltd., *Optoforce web page, http://optoforce.com/index.php*, 2015.

[17] Xu, Lisheng, *Baseline wander correction in pulse waveforms using wavelet-based cascaded adaptive filter*, Computers in Biology and Medicine 37.5 (2007): 716-731.

[18] Zong, W., et al. *An open-source algorithm to detect onset of arterial blood pressure pulses.* Computers in Cardiology, 2003. IEEE, 2003.

Solving tridiagonal system of equations and the Black-Scholes PDE on parallel processor architectures

Endre LÁSZLÓ
(Supervisor: Péter SZOLGAY)
Pázmány Péter Catholic University, Faculty of Information Technology and Bionics
50/a Práter street, 1083 Budapest, Hungary
laszlo.endre@itk.ppke.hu

***Abstract*—The most widely used parallel architectures in today's High Performance Computing systems utilize multi-core CPUs, many-core GPUs or Intel's MIC (Many Integrated Core) architectures. FPGAs (Field Programmable Gate Array) were also considered in some HPC applications recently. The effort of new algorithm and implementation development greatly influences the performance on these architectures, and the differences between their underlying ILP (Instruction Level Parallelism) parallelism - namely SIMT (Single Instruction Multiple Thread) and SIMD (Single Instruction Multiple Data) - and the gate level design of FPGAs require different approaches. In this annual report high performance solutions and results are presented for solving multiple scalar tridiagonal system of equations and solving the Black Scholes PDE. The scalar Thomas algorithm is implemented on all four hardware platforms, namely CPU, MIC, GPU and FPGA. For the GPU a hybrid algorithm based on Parallel Cyclic Reduction and Thomas algorithm is presented.**

I. Introduction

The numerical approximation of multi-dimensional PDE problems on regular grids often requires the solution of multiple tridiagonal systems of equations in each coordinate direction, like in the case of ADI (Alternating Direction Implicit) time discretization [1]. If we take the specific example of a regular 3D grid of size N^3, then an ADI time-marching algorithm will require the solution of N^2 separate tridiagonal system of equations along each line in the first coordinate direction, then along each line in the second direction, and then along each line in the third direction. Data layout which may be optimal for the solution in one particular direction, may be far from optimal for another direction.

The architectural, programmability and development issues regarding novel CPU, GPU and FPGA architectures are examined in the case of one dimensional finite difference problem like the one-factor Black-Scholes (BS) PDE. The BS PDE is a parabolic type defined with Dirichlet boundary conditions. Therefore the solution of this problem is similar to the solution of the heat equation in one dimension. The problem can be solved using explicit and implicit time marching. Although the explicit solution is programmatically much simpler, it requires significantly more time step computations than the implicit method, due to stability limit of the explicit method. Besides, the implicit method doesn't pose such restrictions on the grid resolution which is defined by the convergence criteria of the explicit method.

The balance of computational speed, programming effort and power efficiency are the key factors that decide where a certain architecture will be used in the engineering and research practice. Therefore, for solving the Black-Scholes PDE the following architecture-parallelisation tool combinations were chosen:

- Intel Xeon 2 socket server CPU with Sandy Bridge architecture: algorithms implemented using AVX ISA (Instruction Set Architecture) intrinsics in C/C++.
- NVIDIA Tesla K40 GPU with Kepler architecture: algorithms implemented with CUDA C programming language
- Xilinx Virtex7 FPGA: algorithms implemented with Vivado HLS (High Level Synthesis) C/C++ language.

The literature on the finite difference solution of the Black Scholes PDE is abundant, but only a few papers provide a thorough comparison of solvers on novel CPU, GPU and FPGA architectures. See [2] for efficient algorithms on CPUs and GPUs, [3] for comparison between GPU and FPGA implementations. FPGA implementations of the explicit solver are studied in [4] and [5], while implicit solution is considered in [6].

The structure of the report is the following. Algorithms for the solution of scalar tridiagonal system of equations is discussed in Section II. Then the Black-Scholes PDE and its numerical solution is discussed in Section III and the parallelized Black-Scholes PDE solvers are discussed in Section IV. Performance of standalone scalar tridiagonal solvers along with the specialized Black-Scholes PDE solvers are summarized in Section V and conclusion for the scalar tridiagonal solvers along with the parallel Black-Scholes PDE solvers are given in Section VI.

II. Solution of scalar tridiagonal systems

First, we briefly review the Thomas, PCR/CR and a hybrid algorithm. The tridiagonal system to be solved is represented

E. LÁSZLÓ, "Solving tridiagonal system of equations and the Black-Scholes PDE on parallel processor architectures" in *PhD Proceedings Annual Issues of the Doctoral School, Faculty of Information Technology and Bionics, Pázmány Péter Catholic University – 2015.* G. Prószéky, P. Szolgay Eds. Budapest: Pázmány University ePress, 2015, pp 119– 122.

as

$$a_i u_{i-1} + b_i u_i + c_i u_{i+1} = d_i, \quad i = 0, 1, \ldots, N-1$$

with $a_0 = c_{N-1} = 0$.

a) Thomas algorithm: The Thomas algorithm [7] is the single-thread sequential algorithm. It is simply a customization of Gaussian elimination to the case in which the matrix is tridiagonal. The algorithm requires at the minimum the loading of a_i, b_i, c_i, d_i, and the storing of the final answer d_i - this shows that the implementation of the algorithm is likely to be memory-bandwidth limited.

b) Parallel Cyclic Reduction: PCR [8] is an inherently parallel algorithm which is ideal when using multiple execution threads to solve each tridiagonal system. If the computations within each step are performed simultaneously for all i, then it is possible to reuse certain coefficients in the scratch memory.

c) Thomas-PCR hybrid algorithm: Hybrid algorithms have been studied in [9] [10] [11]. The proposed hybrid algorithm is a combination of the Thomas and PCR algorithms. Suppose the tridiagonal system is broken into a number of sections of size M, each of which will be handled by a separate thread. Within each of these pieces, using local indices ranging from 0 to $M-1$, a slight modification to the Thomas algorithm operating on rows 1 to $M-2$ enables one to obtain the solution of a smaller equation with respect to the neighboring values - this produces a reduced system. This reduced tridiagonal system can be solved using PCR, and the interior values can be computed as a function of the PCR solution.

A. SIMT and SIMD implementations

Hardware devices used in the research are a high-end, 2 socket Intel Xeon E5-2680 CPU, Intel Xeon Phi 5110P coprocessor and NVIDIA K40m GPU. In general, the largest difference between the vector level parallelism of the CPU and GPU are in the difference where the actual parallelism happens. In CPU code the compiler decides how a code segment can be parallelized with the available instruction set. Therefore, to exploit the power of a multicore CPU, the SIMD (Single Instruction Multiple Data) vector instruction set together with the multi-threaded execution needs to be exploited.

GPUs on the other hand leave the vector level parallelization for the hardware. This is called SIMT (Single Instruction Multiple Threads). It is decided in run-time by the scheduling and instruction dispatch unit whether an instruction can be accomplished in parallel or not. Global memory load on the GPU pose strict constraints on the access patterns used to solve systems of equations on a multidimensional domain. In order to utilize the whole, 32 byte cache line threads need to use all the data available in that line. When solving tridiagonal problems along the X dimension, the following algorithms are proposed: 1) Thomas algorithm with local data transpose in shared memory; 2) Thomas algorithm with local data transpose using register shuffle and 3) Thomas-PCR hybrid algorithm.

III. Black-Scholes equation and its numerical solution

The Black-Scholes (BS) PDE for derivative security pricing is a celebrated tool of the Black-Scholes theory [12]. The one-factor BS in the case of European call options is shown on Eq. (1).

$$\frac{\partial V}{\partial t} + rS\frac{\partial V}{\partial S} + \frac{1}{2}\sigma^2 S^2 \frac{\partial^2 V}{\partial S^2} - rV = 0 \tag{1}$$

The BS equation is a second order, parabolic, convection-diffusion type PDE sharing common numerical features with the heat equation. Both explicit and implicit solutions iterate in time backwards, since the problem is a final value problem rather than an initial value problem. After explicit (backward time differentiation) discretization of Eq. (1) the BS PDE boils down to the algebraic expression shown in Eq. (2). Evaluating this expression gives the price curve in the next time-step.

$$V_k^{(n+1)} = a_k V_{k-1}^{(n)} + b_k V_k^{(n)} + c_k V_{k+1}^{(n)} \tag{2}$$

with some a_k, b_k and c_k coefficients. $(n) = 0, ..., N-1$ superscript is the time coordinate with Δt time step, $k = 0, ..., K-1$ subscript is the price coordinate with ΔS price step (price step is factorized out).
Eq. (3) shows the implicit form of the solution of BS PDE, which requires the solution of a tridiagonal system of equations.

$$a_k V_{k-1}^{(n+1)} + b_k V_k^{(n+1)} + c_k V_{k+1}^{(n+1)} = V_k^{(n)} \tag{3}$$

with some a_k, b_k and c_k coefficients.

Since many options need to be calculated in a real-world scenario, a natural parallelism arises in computing these options in parallel.

IV. CPU, GPU and FPGA solutions for the Black-Scholes PDE

The problem of solving the explicit and implicit time-marching is done using stencil operations in the explicit case and using the Thomas algorithm for solving the tridiagonal system of equations arising in the implicit case. In depth details and comparison of the CPU and GPU implementations can be found in [2].

A. Stencil operations for explicit time-marching

The one dimensional, stencil-based computations required for the one-factor application can be efficiently implemented on both CPUs and GPUs.

d) CPU implementation: Stencil based computations can be efficiently implemented on CPUs equipped with vector instructions sets such as AVX or AVX2. Due to the efficient and large L1 cache (32KB) these problems on CPUs tend to be compute limited rather than bandwidth limited. On a typical CPU implementation the computations are parallelized over the set of options. Smaller subsets of options are solved using multithreading with OpenMP and options within a subset are solved within the lanes of CPU vectors.

e) GPU implementation: GPUs, due to the implemented thread level parallelism and compile-time register allocation give more freedom for better vectorization and optimization and therefore the achievable computational efficiency is very high. Among the many possible efficient algorithms discussed in [2] the best performing utilizes the new register shuffle instructions to share the work-load of computing a single timestep. The shuffle instruction (introduced in the Kepler architecture) makes communication possible between the threads inside a warp, ie. shuffle allows data to be passed between lanes (threads) in a vector (warp).

B. Thomas algorithm for implicit time-marching

The solution of the implicit form of the discretized BS equation requires the solution of a tridiagonal system of equations. The solution of the system is essentially the Gauss-Jordan elimination process of the matrix equation Eq. (4).

$$\begin{pmatrix} b_0 & c_0 & 0 & 0 & \cdots & 0 \\ a_1 & b_1 & c_1 & 0 & \cdots & 0 \\ 0 & a_2 & b_2 & c_2 & \cdots & 0 \\ \vdots & \vdots & \vdots & \vdots & \ddots & \vdots \\ 0 & 0 & 0 & \cdots & a_{K-1} & b_{K-1} \end{pmatrix} \begin{pmatrix} u_0 \\ u_1 \\ u_2 \\ \vdots \\ u_{K-1} \end{pmatrix} = \begin{pmatrix} d_0 \\ d_1 \\ d_2 \\ \vdots \\ d_{K-1} \end{pmatrix} \tag{4}$$

a) CPU solution: The CPU implementation relies on L1 cache performance and vectorization over options with either auto vectorization or explicit vectorization with instrinsic functions. Due to vectorization, 4 options with double precision or 8 options with single precision are solved in parallel with AVX or AVX2 instructions. The workload of the complete set of options is then parallelised using multithreading with OpenMP.

b) GPU solution: Just as in the case of the explicit solver, the GPU solver allows for more optimization. The discussion of these novel, optimized algorithms can be found in [2]. Beside the Thomas and the PCR (Parallel Cyclic Reduction) algorithms, a new hybrid Thomas/PCR algorithm is also introduced in [2]. The efficiency of the latter algorithm relies on the aforementioned register shuffle instruction and compile-time register allocation. The algorithm works on a work-sharing basis in three steps: 1) the system of size N is split into 32 pieces which are partially solved and results in a reduced system of size 64; 2) threads cooperate to solve the 64 size system with PCR; 3) the solution of the reduced system is used to solve the partially computed systems in step 1).

C. FPGA solution with Vivado HLS

Xilinx in its Vivado HLS (High Level Synthesis) suite started a new software-based syntheser for the C,C++ and System C languages. The Vivado HLS support for C with its customized support for the Xilinx FPGA is a potentially efficient solution.

1) Stencil operations for explicit time-marching: One of the key optimizations in FPGA circuit design is the maximization of the utilization of processing elements. This involves careful implementation that allow for pipelining computations to keep the largest possible hardware area busy. In HPC terminology this optimization is similar to cache-blocking, although the problem is not the data movement but rather keeping the system busy.

One way to create such a (systolic) circuitry is to create multiple interleaved processing elements with simple structure to allow low latency and high throughput. Each processing element is capable of handling the computation associated with three neighboring elements $f(u_{k-1}^{(n)}, u_k^{(n)}, u_{k+1}^{(n)})$ within a single timestep n, where f is the stencil operation. One may stack a number of such processing elements to perform consecutive timestep computations by feeding the result of processor $p = 1$ to $p = 2$ as shown on Figure 1.

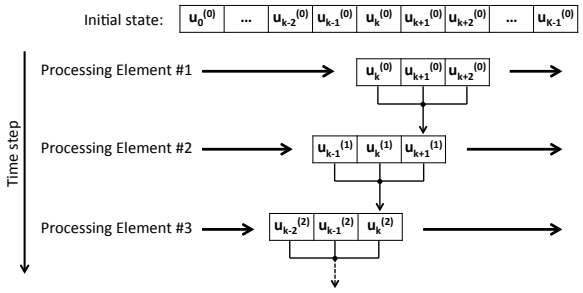

Fig. 1. Stacked FPGA processing elements to pipeline stencil operations in a systolic fashion. The initial system variables $u_0^{(0)}, ..., u_{K-1}^{(0)}$ are swept by the first processing element. The result $u_{k+1}^{(1)}$ is fed into the second processing element.

2) Thomas algorithm for implicit time-marching: The optimization of the implicit solver relies on the principle of creating independent processors to perform the calculation of independent options. Each of these processors is capable of pipelining the computation of more options into the same processor with the associated cost of storing the temporary (c^*, d^*) arrays of each option. The number of options that can be pipelined is defined by the depth of the forward sweep of the Thomas algorithm, which is 67 clock cycles in the present case. The temporary storage is implemented in the available Block RAM memories, but due to the deep pipeline the BRAM memory requirement limits the number of deployable processors.

V. Performance comparison

Execution performance of the scalar tridiagonal solvers is measured on a 256^3 cube domain. Results are presented on Figure 2. One can see, that the Thomas-PCR hybrid algorithm on the GPU is the most efficient in the X dimension.

The performance of the Black-Scholes PDE solvers are compared on Table I and II. FPGA performance is compared to highly optimized CPU and GPU code. Estimations based on the Xilinx Vivado toolset are made to predict the achievable clock frequency on a Xilinx Virtex 7 VX690T. Based on the figures it can be stated that the proposed FPGA implementation is slower than the highly optimized CPU implementation,

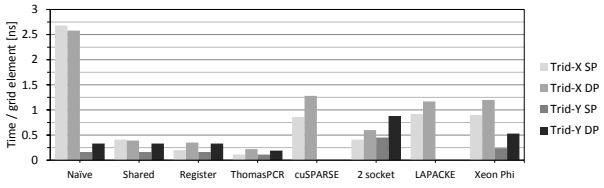

Fig. 2. Kernel execution times for solution of scalar problems.

TABLE I
PERFORMANCE - SINGLE PRECISION

	ps/element			GFLOPS			GFLOPS/W		
	C	G	F	C	G	F	C	G	F
Explicit	15.2	2	17.4	394	3029	344	1.46	12.9	8.6
Implicit	142.7	14.5	766	139	1849	26	0.51	7.9	0.65

Note: C - 2 Xeon CPUs, G - Tesla K40 GPU, F - Virtex 7 FPGA

TABLE II
PERFORMANCE - DOUBLE PRECISION

	ps/element			GFLOPS			GFLOPS/W		
	C	G	F	C	G	F	C	G	F
Explicit	29.8	4.1	48.2	201	1463	124	0.74	6.2	3.1
Implicit	358.8	43.5	1748	48	892	9.8	0.18	3.8	0.24

Note: C - 2 Xeon CPUs, G - Tesla K40 GPU, F - Virtex 7 FPGA

but it is significantly more power efficient. Compared to the GPU version the FPGA is significantly slower and even if the power dissipation of the GPU is higher than the FPGA the overall power efficiency is higher for the sake of the GPU.

VI. CONCLUSION

A number of algorithms for the solution of scalar tridiagonal problem have been shown. The performance of a new hybrid algorithm on GPU is presented. Performance is compared against other, highly optimized solvers on the most prominent HPC architectures today.

A well studied finite difference problem – the solution of the Black-Scholes PDE – was chosen to compare novel CPU, GPU and FPGA architectures. Efficient FPGA based implementation of the explicit and implicit Black-Scholes solvers have been created using Vivado HLS. The relatively low programming effort and the achieved efficiency of the resulting circuitry shows a promising step towards the applicability of FPGAs in an HPC environment and more specifically in finite difference calculations. The results clearly show the superior performance of GPUs both in terms of computational efficiency and power efficiency.

REFERENCES

[1] D. W. Peaceman and J. Rachford, H. H., "The numerical solution of parabolic and elliptic differential equations," *Journal of the Society for Industrial and Applied Mathematics*, vol. 3, no. 1, pp. pp. 28–41, 1955. [Online]. Available: http://www.jstor.org/stable/2098834

[2] M. Giles, E. László, I. Reguly, J. Appleyard, and J. Demouth, "GPU Implementation of Finite Difference Solvers," in *Proceedings of the 7th Workshop on High Performance Computational Finance*, ser. WHPCF '14. Piscataway, NJ, USA: IEEE Press, 2014, pp. 1–8. [Online]. Available: http://dx.doi.org/10.1109/WHPCF.2014.10

[3] Q. Jin, D. Thomas, and W. Luk, "Exploring reconfigurable architectures for explicit finite difference option pricing models," in *Field Programmable Logic and Applications, 2009. FPL 2009. International Conference on*, Aug 2009, pp. 73–78.

[4] G. Chatziparaskevas, A. Brokalakis, and I. Papaefstathiou, "An FPGA-based parallel processor for Black-Scholes option pricing using finite differences schemes," in *Design, Automation Test in Europe Conference Exhibition (DATE), 2012*, March 2012, pp. 709–714.

[5] T. Becker, Q. Jin, W. Luk, and S. Weston, "Dynamic constant reconfiguration for explicit finite difference option pricing," in *Reconfigurable Computing and FPGAs (ReConFig), 2011 International Conference on*, Nov 2011, pp. 176–181.

[6] S. Palmer and D. Thomas, "Accelerating implicit finite difference schemes using a hardware optimised implementation of the thomas algorithm for fpgas," *arXiv preprint arXiv:1402.5094*, 2014.

[7] L. H. Thomas, "Elliptic Problems in Linear Differential Equations over a Network," Columbia University, Tech. Rep., 1949.

[8] R. Sweet, "A parallel and vector variant of the cyclic reduction algorithm," *SIAM Journal on Scientific and Statistical Computing*, vol. 9, no. 4, pp. 761–765, 1988. [Online]. Available: http://epubs.siam.org/doi/abs/10.1137/0909050

[9] H. A. van der Vorst, "Large tridiagonal and block tridiagonal linear systems on vector and parallel computers," *Parallel Computing*, vol. 5, no. 12, pp. 45 – 54, 1987, proceedings of the International Conference on Vector and Parallel Computing-Issues in Applied Research and Development. [Online]. Available: http://www.sciencedirect.com/science/article/pii/0167819187900056

[10] S. Bondeli, "Divide and conquer: a parallel algorithm for the solution of a tridiagonal linear system of equations," *Parallel Computing*, vol. 17, no. 45, pp. 419 – 434, 1991. [Online]. Available: http://www.sciencedirect.com/science/article/pii/S0167819105801450

[11] N. Mattor, T. J. Williams, and D. W. Hewett, "Algorithm for solving tridiagonal matrix problems in parallel," *Parallel Computing*, vol. 21, no. 11, pp. 1769 – 1782, 1995. [Online]. Available: http://www.sciencedirect.com/science/article/pii/0167819195000330

[12] F. Black and M. S. Scholes, "The Pricing of Options and Corporate Liabilities," *Journal of Political Economy*, vol. 81, no. 3, pp. 637–54, May-June 1973. [Online]. Available: http://ideas.repec.org/a/ucp/jpolec/v81y1973i3p637-54.html

New sensor concept for intra-frame scene and speed capturing

Máté NÉMETH
(Supervisor: Ákos ZARÁNDY)
Pázmány Péter Catholic University, Faculty of Information Technology and Bionics
50/a Práter street, 1083 Budapest, Hungary
nemeth.mate@itk.ppke.hu

***Abstract*— Deployment of automated traffic surveillance systems play an important role in traffic law enforcement. Existing devices use RADAR or LIDAR technologies for speed measurement, as well as cameras for license plate recognition. It would be profitable to replace those relatively expensive active systems with a single camera for both tasks. An optical based vehicle speed measurement method is presented in this paper. The proposed method calculates speed estimates based on a single, superimposed frame, which contains information of the movement of certain objects during exposure, and can be obtained through modified shutter control. An applicable sensor structure and exposure-control are also shown, as well as some experimental results.**

Keywords—CMOS Sensor; Global Shutter Efficiency; Exposure Control; Speed Estimation; Motion Blur; Intra-Frame Speed Measurement

I. INTRODUCTION

Authorities use several devices for speed limit enforcement, to detect traffic violations. Conventional speed measurement systems are usually based on either RADAR or LIDAR speed guns [1]. Both techniques use active sensing technologies, which are more complicated and expensive than passive camera systems. On the other hand, there are methods in the literature aiming at producing reliable speed estimates, based on optical information only [2, 3, 4, 5]. Scientific studies in this field can be divided into two major research directions: optical flow (inter-frame), and motion-blur (intra-frame) based displacement calculation methods. Besides speed measurement, it is required for law enforcement authorities to be capable of identifying cars by number plate recognition. Hence it must be an essential feature of the system, to provide adequate image quality. The most important drawback of the motion blur based methods is that the measurement concept itself is based on the degradation of the image, which is controversial with precise number plate identification. Hence it is a difficult engineering task to apply one device for both measurement and identification. In this paper we propose a new method for intra-frame speed measurement, which meets the mentioned requirements, and present a suitable sensor structure and hardware-level control for such a system. The paper is composed in the following way. In the second section, the fundamental concept is described, and the speed estimation based on displacement is formulated. The third section presents a suitable pixel-level control method for the measurements, while in the last two sections, measurement results, proof-of-concept experiments and conclusions are presented.

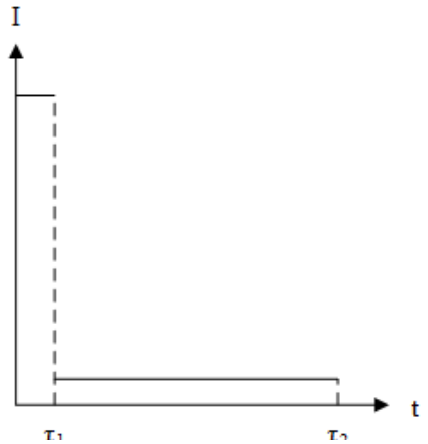

Figure 1. Exposure control scheme of the proposed method, with the primary $[0, \tau_1]$ and secondary $[\tau_1, \tau_2]$ exposure intervals

II. CONCEPT

The amount of incident light reaching the image sensor is determined by the camera's shutter speed (t), the lens's relative aperture (N) and the luminance of the scene (L_v). Considering a measurement situation with N, L_v given, the behavior of fast moving objects on the image plane can be controlled through shutter speed. The appearing motion blur on an image is proportional with the speed of the object and the shutter speed.

A. Measurement concept

M. NÉMETH, "New sensor concept for intra-frame scene and speed capturing" in *PhD Proceedings Annual Issues of the Doctoral School, Faculty of Information Technology and Bionics, Pázmány Péter Catholic University – 2015.* G. Prószéky, P. Szolgay Eds. Budapest: Pázmány University ePress, 2015, pp 123– 126.

Fig. 2. Expected superimposed image with the applied exposure control scheme

The measurement concept is based on a special control method of the sensor shutter. The proposed method ensures adequate image quality, while still holding information describing intra-frame motion of certain objects. The classical shutter cycle (open, close) is expanded with an intermediate, „semi-open" state. We defined two phases of the exposure (Fig. 1.). The first (open) phase is denoted with τ_1, in which ψ% of the dynamics is exposed with fast shutter speed, to minimize the impact of motion blur on the image. Then in the semi-open phase [τ_1, τ_2], the process continues with significantly longer exposure ($\tau_1 \ll \tau_2$), and lower intensity. Thus it is feasible with this control method to have a superimposed image, consisting of a sharp image, and a blurred image, where only the high intensity regions of the scene appear. In the case of a fast moving object with a light source (e.g. car on a highway with headlights on), this implies that a light beam appears on the image plane (Fig. 2.) according to the path of the movement of the light source. Considering a fixed [τ_1, τ_2] interval, the length of the beam is proportional with the speed of the object.

B. Calculation of speed estimates

The measurement geometry is presented in Fig. 3. Considering γ, e, c is known, as spatial geometry is known prior to the measurement, one can derive (1) and (2) from the given geometry

$$\frac{e}{c} = \mathrm{tg}\,\delta \tag{1}$$

$$\frac{e+d}{c} = \mathrm{tg}(\beta+\delta) \tag{2}$$

and

$$\delta = \gamma - \alpha - \beta \tag{3}$$

where γ is the angle between the image plane and the movement direction of the measured object, d is the displacement, and α, β can be derived from the image, assuming that the calibration parameters of the camera are known. After substitution of (1) and (3) into (2) and removing e and δ, we have

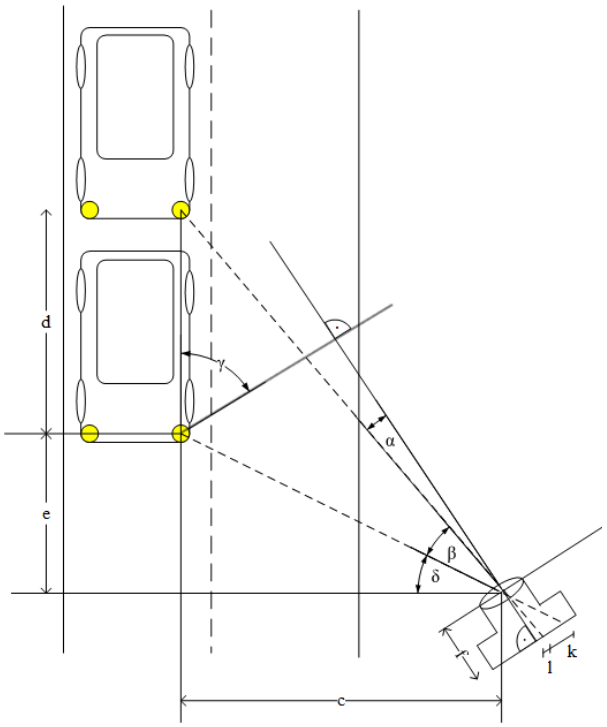

Figure 3. Geometry of the measurement setup

$$d = c(\mathrm{tg}(\gamma-\alpha) - \mathrm{tg}(\gamma-\alpha-\beta)) \tag{4}$$

If the interval of the secondary exposure is denoted with [τ_1, τ_2], movement speed of the measured object can be obtained as follows in (5)

$$v = \frac{d}{\tau_2 - \tau_1} \tag{5}$$

As a result, the expected accuracy of the speed measurement is proportional with the measurement accuracy of the light beam on the image plane (again, if we consider spatial geometry and camera parameters are known). Hence it would be an ideal situation if the exposure scheme could be defined in a way which could ensure the light beam to be at least 100 pixel long on the captured image, even in sufficiently low speed ranges of the measured vehicles. In this case the expected accuracy would be below 1%, without using subpixelization techniques. The lateral movement of the measured vehicle inside the lane was not taken into account and will appear as perturbation during the calculation.

Detection of the light beam superimposed on the initial image, and the related image processing methods along with the camera system and the embedded control, data acquisition and image processing circuitry, implemented on FPGA, will be presented in another paper.

III. Implementation

CMOS sensor technology enables pixel-level control features, therefore electrical shutters can be implemented with

pixel-level exposure control switch. This paper presents a special exposure-control concept for CMOS sensors, to implement the described measurement method. Most CMOS imagers apply rolling shutter readout method [6], where the exposure starts in a slightly delayed manner for every row of the sensor. This causes geometrically incoherent images when capturing objects moving at high speed. Hence in many machine vision applications, rolling shutter cameras are not applicable. This fact calls for the other type of CMOS sensors featuring global shutter pixels (Fig. 4.). In this case, every pixel is equipped with a pixel-level memory element, which allows simultaneous integration of the pixel array.

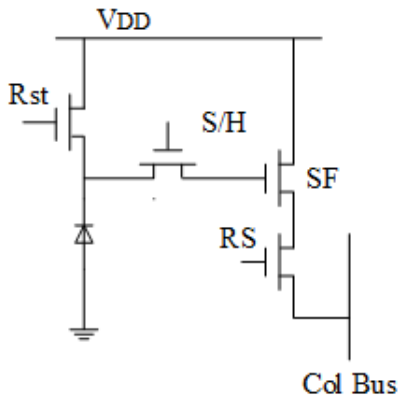

Figure 4. Transistor scheme of a common global shutter pixel

A. *Description of a global shutter pixel[6]*

A fundamental component of a global shutter (or snapshot) pixel is a sample-and-hold (S/H) switch with analog storage (parasitic capacitance in the amplifier input), and a source follower amplifier, which performs the in-pixel amplification. The schematic figure of a global shutter pixel is shown in Fig. 4. The incident light generated charge is stored in the in-pixel capacitance after the integration.

B. *Pixel control*

To ensure the sensor operates in accordance with the previously mentioned schedule, the S/H stage could be replaced with a suitable control circuitry, which implements analogous functionality of the "semi-open" state of the electrical shutter.

One important issue related with charge storage is the GSE (Global Shutter Efficiency). According to [7, 8, 9] an increasing tendency of CMOS image sensor manufacturers can be noticed to achieve better GSE values, which is defined as a ratio of photodiode sensitivity to pixel storage parasitic sensitivity. The GSE of specific CMOS sensor [7] (Aptina™ MT9M021) used in this study is shown in Fig. 5. Maintaining sensor performance, while reducing the pixel size requires higher quantum efficiency and lower noise floor. Electrical and optical isolation of the in-pixel storage nodes is also becoming more and more difficult with the shrinking pixel size. Aptina™'s recent 3,75 and 2,8µm (3rd and 4th generation) global shutter pixel arrays implement [7] some extra features like Correlated Double Sampling (CDS) to reduce the impact of dark current (thermal generation of electron-hole pairs in the depleted region) and readout noise and to improve GSE. On the other hand increasing pixel level functionality along with transistor number, is controversial with sensitivity, since the fill factor is decreasing.

In our experiments, we exploit the relatively low GSE of the Aptina™ MT9M021 sensor. The leakage of the S/H stage "simulates" the control method proposed in Section 2, assuming that τ_1, τ_2 represents exposure time and read-out time,

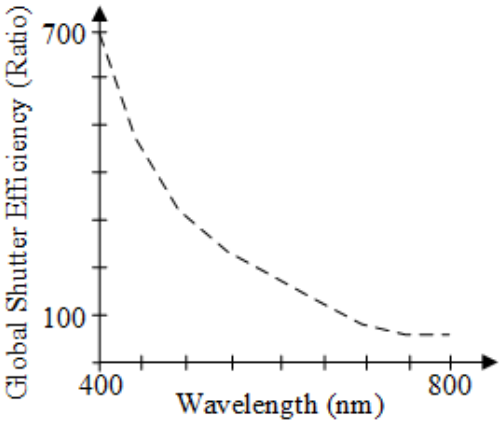

Figure 5. Global shutter efficiency for an Aptina™ 3rd generation 3.75µm pixel [7]

respectively. As a result, the qualitative characteristics of the secondary blurred image which will be superimposed on the initial sharp image, depends on the read-out time ($T_{readout}$). Read-out time can be calculated as follows in (7)

$$T_{readout} = \frac{1}{f_{pixclk}} N_{row} Row\_size \quad (7)$$

where f_{pixclk} denotes the readout frequency. Equation (7) implies that the readout time of a detected object depends on its vertical position on the image plane. As a result, (6) can be rewritten into the following form

$$v = \frac{d}{T_{readout}} \quad (8)$$

IV. Experimental results

This section presents some proof-of-concept measurement results, based on the proposed method. To verify the results, the knowledge of the "ground truth" is essential, therefore we applied an inertial measurement unit to gather GPS and

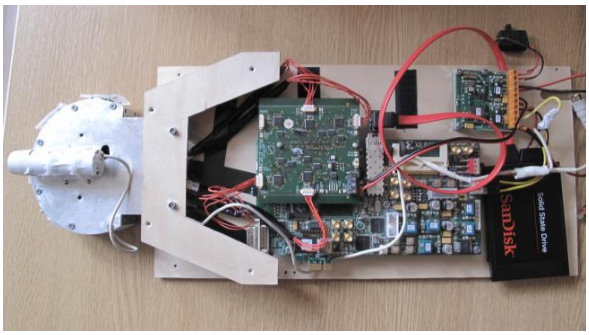

Figure 6. Image capturing system: four cameras are placed inside an aluminum holder frame. The camera on top of the frame belongs to the FPV (First Person View) system

acceleration data for the verification.

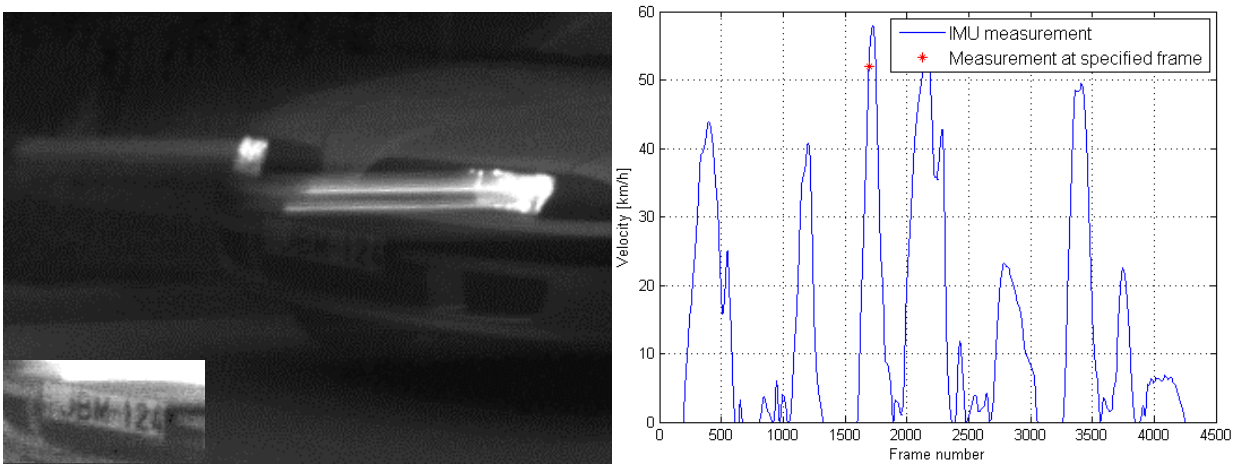

Figure 7. Relevant part of the image taken with the applied camera, and the associated IMU measurement graph

The used camera and image acquisition system was designed for a UAV's onboard collision warning system (Fig. 6.), as described in [10, 11], which seemed to be an appropriate choice for this application. The device applies a 1.2 Megapixel camera with Aptina MT9M021 sensor chip.

The measurement of the geometry (c, γ in Fig. 3.) of the selected experiment location was done. Fig. 7 shows the result of a specific measurement situation, with a selected frame and the appropriate IMU measurement highlighted (approx. 52km/h). After applying the image processing method and the speed calculation formula, the speed estimation is 51.3km/h, which means 1.36% error compared to the IMU measurement, which is comparable with the IMU measurement error.

Another uncertainty of the proposed method is in connection with the image processing component. Detection of both ends of the light beam is required for the method. The endpoint causes no difficulties, but the identification of the light source has some pixel uncertainty. To overcome this problem, a slightly improved exposure control scheme is proposed. With the modification of the shutter cycle, inserting one extra (short) close state after the primary exposure: [open, *short-close*, semi-open, close], one can achieve an image, where the light beam stripe is separated from the saturated areas of the light source, which simplifies the measurement of its length. On the other hand this method would require a sensor architecture with a true controllable shutter.

V. Conclusions

A new optical based speed estimation method was developed, capable of measuring speed of specified objects. The measurement results are encouraging, because the published intra-frame speed measurement solution [3] reached 2% accuracy and generated blurred image of the moving object (license plate unreadable in that case), while our first experiment generated higher accuracy and better image quality (license plate is clearly readable).

Acknowledgment

The support of the KAP-1.5-14/006 grant and the advices of László Orzó are greatly acknowledged.

References

[1] D. Sawicki, Traffic Radar Handbook: A Comprehensive Guide to Speed Measuring Systems, Author House, 2002

[2] F.W. Cathey, D.J. Dailey, "A Novel Technique to Dynamically Measure Vehicle Speed using Uncalibrated Roadway Cameras", www.its.washington.edu/pubs/AutoCamCal-IV05-2.pdf, accessed at 20.03.2015

[3] Huei-Yung Lin, Kun-Jhih Li, Chia-Hong Chang, "Vehicle speed detection from a single motion blurred image", Image and Vision Computing vol. 26, Issue 10, 1 October 2008, pp. 1327–1337

[4] Huei-Yung Lin, Chia-Hong Chang, "Automatic Speed Measurements of Spherical Objects Using an Off-the-Shelf Digital Camera", Proc. 2005 IEEE International Conference on Mechatronics July 10-12, 2005, Taipei, Taiwan

[5] Macelo Celestino, Oswaldo Horikawa, "Velocity measuerment based on image blur", ABCM Symposium Series in Mechatronics, Vol. 3, pp.633-642, 2008

[6] Orly Yadid-Pecht, Ralph Etienne-Cummings, CMOS Imagers From Phototransduction to Image Processing, Kluwer Academic Publishers, 2004

[7] Sergey Velichko et al., "Low Noise High Efficiency 3.75 µm and 2.8 µm Global Shutter CMOS Pixel Arrays", IISW 2013, Snowbird Resort, Utah, USA, June 12-16, 2013

[8] Stefan Lauxtermann, Adam Lee, John Stevens, Atul Joshi, "Comparison of Global Shutter Pixels for CMOS Image Sensors", IISW 2007, Cliffhouse Resort Ogunquit, Maine, USA, June 7-10, 2007

[9] Sergey Velichko et al., "A 1.2MP 1/3" Global Shutter CMOS Image Sensor with Pixel-Wise Automatic Gain Selection", IISW 2011, Ōnuma Quasi-National Park Hokkaido, Japan, June 8-11, 2011

[10] Akos Zarandy, Mate Nemeth, Zoltan Nagy, Andras Kiss, Levente Santha, Tams Zsedrovits, "A Real-Time Multi-Camera Vision System for UAV Collision Warning and Navigation", JRTIP, accepted, online published, DOI 10.1007/s11554-014-0449-3

[11] Akos Zarandy, Zoltan Nagy, Balint Vanek, Tamas Zsedrovits, Andras Kiss, Mate Nemeth, "A Five-Camera Vision System for UAV Visual Attitude Calculation and Collision Warning", ICVS 2013, St. Petersburg, Russia, July 16-18, 2013. Proc.

A Biomimetic hand test bed control design

Norbert SÁRKÁNY
(Supervisor: Péter SZOLGAY)
Pázmány Péter Catholic University, Faculty of Information Technology and Bionics
50/a Práter street, 1083 Budapest, Hungary
sarkany.norbert@itk.ppke.hu

***Abstract*—This paper presents the design concept and method of a biomotivated control design for a novel biomimetic hand test bed. The article focuses on the under standing of how is the interconnection and coupling in the forearm in a static state and during a dynamic actuation both as mechanically and electrically. A brief description of the system model and the control model is included and the target hard wear where the model will be used.**

I. Introduction

The main objective of our study was to get to understand the nature of movement, the kinematic analysis and muscle-skeletal model of the fingers and thei additional systems. At the moment we have designed a finger test bed[1] which has all the required parts to implement an accurate actuation which is derived from the human motor control systems. This article discuss the low level representation of movement control based on the coupling between the muscles both mechanically and electrically.

In the II. section the Biological motivation is presented based on the anatomy, in the III. section the dynamic model of the index finger is showen, the IV. section discuss and explains the coupled closed control-loop of the test bed, in the V. section the test bed prototype is shown and in the VI. section the conclusions and future works are described.

II. Biological motivation

Motivated by the human anatomy the control design is based on the physical structure of the forearm. The longitudinal view and cross-section of the muscles and force-delivering tendons of the forarm are shown in Fig. 1

The coupling between the muscles of the forearm is in two ways a simpler mechanical and an bioelectric way. We can see that the muscles are tightly placed and adhered to each other. During muscle contraction the main actuated muscle pulls the neighboring tissue with it and this realizes contraction in them too.

The bioelectric connection is the crosstalk between the muscles, cosed by the action potential during the stimulation. At the moment we do not deal with the electric coupling, but we focus on the mechanical.

III. System model

The first and intuitive way is to mechanically achieve the connection in the test bed but the main problem is that with mechanical coupling the system would increase its uncontrolled degree of freedoms (DOF) or make it more complex

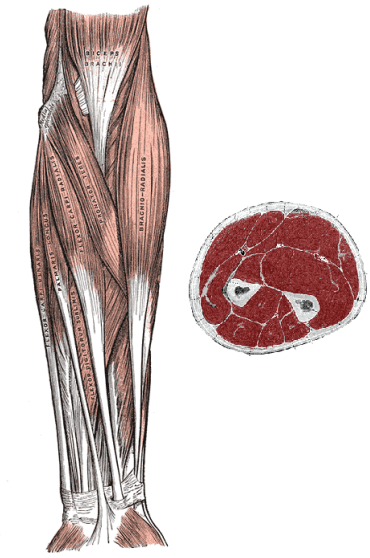

(a) Longitudinal (b) Cross section

Fig. 1: The human forearm and its muscles.[2]

just like we experienced in our previous study [1] . If the coupling is implemented with metal strand it is required firming them but when they are connected on the same pulley it is hard to achieve that.

The algorithmic implementation of the coupling could be realized in the high or the low level control. The high level representation in our research is an abstraction of the actuation.Thus the coupling can not prevail so accurate at this level. Unless separate actuation of the fingers is the task but these could also been represented as an abstraction.

The low level control without the coupling would be limited only on one joint representation, so this kind of implementation can achieve an affined behavior to reflexes. The coupling is present between the actuators (muscles) of the same finger and in a weaker level between the muscles of neighboring fingers.

The kinematic representation of the index finger is shown in Fig. 2 where φ_i is the actual motor angle , φ_i' is the calculated joint angle , τ_i is the measured motor torque, τ_i' is the joint torque calculated on the CoM of the phalanges and β is the angle range of the figer joints which is $130°$.

N. SÁRKÁNY, "A Biomimetic hand test bed control design" in *PhD Proceedings Annual Issues of the Doctoral School, Faculty of Information Technology and Bionics, Pázmány Péter Catholic University – 2015.* G. Prószéky, P. Szolgay Eds. Budapest: Pázmány University ePress, 2015, pp 127– 129.

The Numbering used for all variables associated with the joint and their actuator is as follow for every finger: 1 is for **MCP**(*metacarpophalangeal joint*), 2 **PIP**(*proximal interphalangeal joints*), 3 **DIP**(*distal interphalangeal joints*).

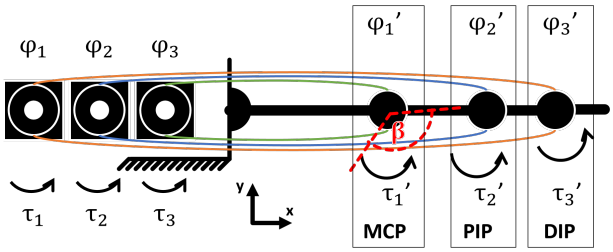

Fig. 2: The Kinematic model of a three-link open-chain finger and the base layout of the test bed.

For the torque driven motion of a three-link open-chain model the equations (1) were derived using a standard Lagrangian formulation [3], [4].

$$\tau(t) = M(\varphi(t))\ddot{\varphi}(t) + C(\varphi(t), \dot{\varphi}(t))\ddot{\varphi}(t) + N(\varphi(t)) + \tau_d = K_\tau I(t) \quad (1)$$

In the equation (1) $M(\varphi(t))$ is the given phalanges $3X3$ inertia matrix such that the total rotational kinetic energy of the system can be calculated as shown in equtaion (2) where ω is the angular velocity and M is moment of inertia by extension to a 3D coordinate system the equatiuon change as follows (3) .

$$E_r = \frac{1}{2} M\omega^2 \quad (2)$$

$$E_r = \frac{1}{2}\dot{\varphi}^T M(\varphi)\dot{\varphi} \quad (3)$$

$C(\varphi(t), \dot{\varphi}(t))$ is a $3X3$ matrix that contains centrifugal and Coriolis contributions to joint torques that can be calculated shown in equation (4).

$$C_{ij}(\varphi, \dot{\varphi}) = \frac{1}{2}\sum_{k=1}^{3}\left(\frac{\partial M_{ij}}{\partial \varphi_k} + \frac{\partial M_{ki}}{\partial \varphi_j} - \frac{\partial M_{jk}}{\partial \varphi_i}\right)\dot{\varphi}_k \quad (4)$$

$N(\varphi(t))$ is a $3X1$ vector of joint torque generated by gravity and τ_d is the disturbance. We represented the mathematical terms that describes the physical effects that occurs at the finger phalanges.

Based on the explained equations above we put together a Matlab Simulink model shown in Fig. 3 using the Simscap library. This way, in Matlab we could build the whole model of the system using physical connections. Thus the structure of the model is similar to the system we are developing as well.

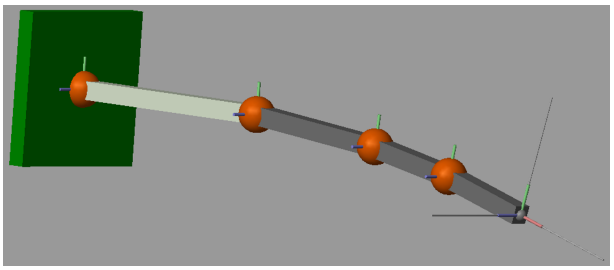

Fig. 3: Matlab Simulink simulation.

IV. Control Model

The concept mentioned in section II is the bases for the control model which is implemented.

Fig. 4 shows the basic control design for our system which is a slightly modified direct torque based *PID* control. The coupling appears at the out put of the *PID* which is the current input of our motor. At the moment the coupling is represented with a scalar taken from our previous study [1] showen in equation (5) and (6).

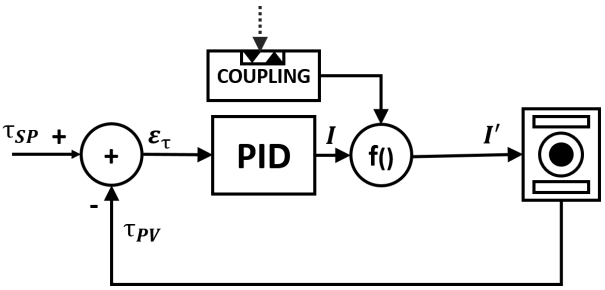

Fig. 4: The basic closed-loop control model for one joint actuation.

$$\varphi_{i,DIP} = \frac{2}{3}\varphi_{i,PIP} \quad (5)$$

$$\varphi_{i,MCP} = \frac{4}{3}\varphi_{i,PIP} \quad (6)$$

In Fig. 5 we can see the main concept of the coupling between the fingers and their phalanges. In our actuation model the grasping is a fully controlled process where the **DIP** joint starts the actuation and it has the maximum rate of applied force. In principle we think that if we only direct control the corresponding motor for the **DIP** it would pull all the others too.

V. Hardware Prototype

The finger test bed is designed by reproducing, as close as possible to the size and kinematics of the human finger. Fig. 6 shows the prototype of the biomimetic finger.

In our first prototype to achieve human-like motion we had implemented mechanical constraints but it showed that

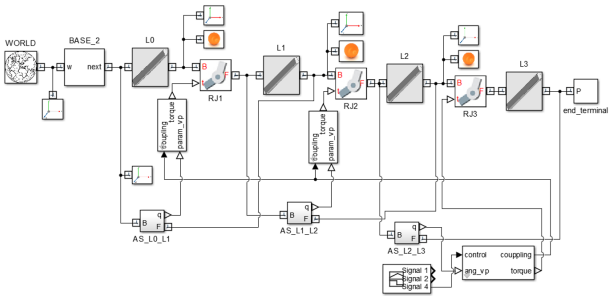

Fig. 5: The representation of the coupling between the fingers and their phalanges.

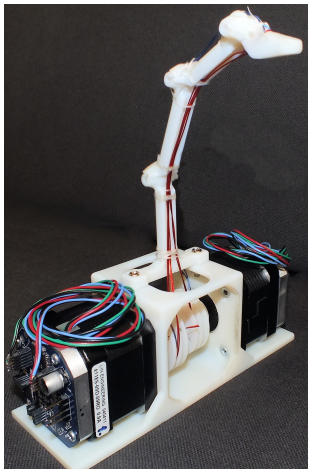

Fig. 6: The biomimetic finger testbed prototype.

this kind of coupling between the finger joints achieve not so human-like motion thats why we decided to implement a different kind of coupling which is able to provide a more dynamic motion and response to the environment.

VI. Conclusion & Future work

We have shown a control design for a biomimetic test bed that could achieve a human-like motion. Now that we have an initial model the next step is to bring the test bed and the model together on the same platform. There are other really important aspects that we have to examine at the moment one of them is the above mentioned high level abstract control based on the functional, biological structure of the cerebellum.

Acknowledgment

This research project was supported by the University of National Excellence Program and the Research Faculty grant awarded to the Pázmány Péter Catholic University, Faculty of Information Technology and Bionics.

References

[1] N. Sarkany, G. Cserey, and P. Szolgay, "An introduction of the biomimetic hand testbed: Skeletal structure and actuation," in *Robotic and Sensors Environments (ROSE), 2013 IEEE International Symposium on*. IEEE, 2013, pp. 43–48.

[2] R. Drake, W. Vogl, and A. Mitchell, *Gray's anatomy for students*. Elsevier/Churchill Livingstone Philadelphia, 2005.

[3] F. L. Lewis, D. M. Dawson, and C. T. Abdallah, *Robot manipulator control: theory and practice*. CRC Press, 2003.

[4] J. Craig, "Introduction to robotics: mechanics and control," 2005.

Analysis of femoral sEMG, kinematics and time synchronization during cycling

Ádám VÁLY
(Supervisor: József LACZKÓ, Péter SZOLGAY)
Pázmány Péter Catholic University, Faculty of Information Technology and Bionics
50/a Práter street, 1083 Budapest, Hungary
valy.adam@itk.ppke.hu

***Abstract* – During lower limb rehabilitation, it is often necessary to perform exercises at a constant speed on an ergometer for predefined periods of time. Due to the geometry of the limb and neural properties, the ability to perform these tasks at a constant speed varies with each subject. In this report, a research about the relations of femoral sEMG and kinematics with respect to two speed and three resistance conditions is presented with a statistical perspective. 15 able bodied subjects (age 24 ± 4 years) participated in this research. The sEMG of vastus lateralis, rectus femoris, vastus medialis and biceps femoris on the left leg was measured along with kinematics for each subject. For each measurement, it was possible to extract kinematic and sEMG data for consecutive complete revolutions of the ergometer crank. These results indicate that there is no significant correlation between different properties of the sEMG associated with each complete revolution, however if resistance or speed is increased, sEMG amplitude averages increase and flexor-extensor muscle co-contraction ranges decrease.**

***Keywords* – surface EMG, kinematics, biomechanics**

I. INTRODUCTION

Rehabilitation of the lower limb after spinal cord injury or stroke is critical if one wishes to avoid deterioration of the limb and keep their quality of life. A common method for achieving this is performing cycling tasks on an ergometer with variable power output.

These types of exercises are commonly used to study relationships between sEMG, kinematics and muscle forces [1-5] which reflected on many details of human motion during cycling.

However, when a subject is asked to pedal at a constant speed, it is very difficult to keep that speed even if feedback is available (e.g. via ergometer display). Therefore, the time needed to complete each 360 degree revolution, temporal stability varies. At present, the author has no information on any study related to the temporal stability of cycling on an ergometer.

II. METHODS

15 able bodied subjects (age 24 ± 4 years) voluntarily participated in the research. They were asked to do 20 second cycling exercises at two speeds (45 and 60 rpm) and three resistance levels (designated levels 1, 5 and 9) on a SciFit ISO7000R ergometer, resulting in 6 RCs which were performed in a random order for each subject. The corresponding torques were 2,55 Nm, 9,55 Nm and 22,30 Nm at 45 rpm and 2,55 Nm, 15,92 Nm, 34,24 Nm at 60 rpm. Therefore total of 90 measurements were made.

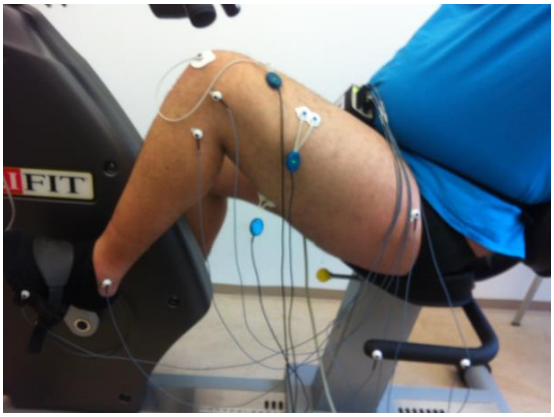

Fig. 1. The complete experimental setup on a subject

A. sEMG measurements

Surface EMG electrodes were placed on the left leg, on vastus lateralis (VL), rectus femoris (RF), vastus medialis (VM) and biceps femoris (BF). The four channels were recorded simultaneously by a Zebris CMS-HS system (Isny, Germany) and processed on a PC by NI LabVIEW (Austin, Texas) software.

The overall measurement bandwith of the Zebris CMS-HS is 1 kHz of which 900 Hz was allocated to sEMG measurement. Because sEMG signals, as described in [6] are exposed to a number of different artifacts during measurement (such as cortical, cardiovascular effects and 50 Hz power supply), raw signals were filtered with a fourth-order Butterworth filter, between 4-48 Hz and 52-250 Hz to obtain relevant amplitudes. A 40 sample window RMS filter was then applied to extract the envelope of the sEMG signal of each channel.

For the previously mentioned 90 measurements, there were 7 kinematic and 4 sEMG signals, totalling 990 data sets containing approximately 20.000 data points each.

Á. VÁLY, "Analysis of femoral sEMG, kinematics and time synchronization during cycling" in *PhD Proceedings Annual Issues of the Doctoral School, Faculty of Information Technology and Bionics, Pázmány Péter Catholic University – 2015.* G. Prószéky, P. Szolgay Eds. Budapest: Pázmány University ePress, 2015, pp 131– 134.

B. Kinematic data measurement and processing

Zebris ultrasonic kinematic markers were placed on 7 positions on the subjects and the ergometer. The first marker was specially fitted to the pedal axle of the ergometer crank so that it would provide crank angle measurements.

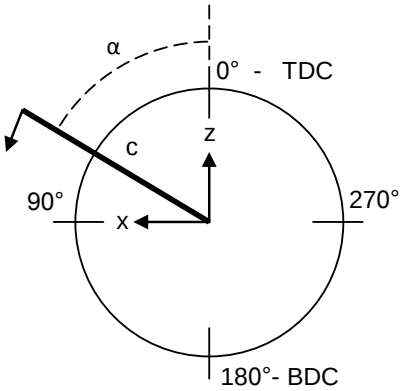

Fig. 2. Coordinate system for the ergometer crank (c), positions of top dead (TDC) and bottom dead centers (BDC) and crank angle (α).

Marker 2 was positioned on the ankle, marker 3 on the fibula head, marker 4 on the epicondilus, marker 5 on the tuberculum maior and markers 6 and 7 were placed on the ergometer as a horizontal reference. The 7 markers each transmitted their (x, y, z) coordinates at 100 Hz.

The measured kinematic data initially contained measurement errors and missing data represented by NaN data. These were filtered out using linear interpolation. Afterwards, since kinematics were measured at 100 Hz and sEMG at 900 Hz, there was no way to assign one kinematic measurement to each sEMG data point. Therefore a linear interpolation was applied on all kinematic data which resulted in the same number of kinematic measurement points as sEMG measurements.

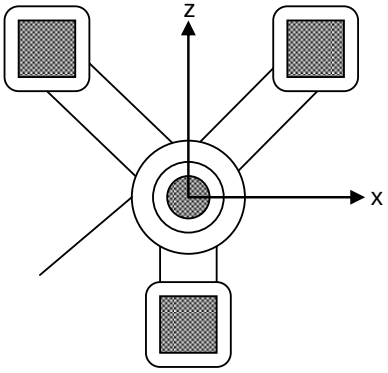

Fig. 3. Axes for kinematic measurements with the Zebris CMS-HS system.

C. Complete revolutions of the crank

Using data from marker 1 it is possbile to extract the exact crank angles compared to the top dead center using the law of cosines.

$$\alpha = \begin{cases} \arccos\left(\dfrac{a \cdot b}{|a||b|}\right), P_c(x) \geq P(x) \\ 360 - \arccos\left(\dfrac{a \cdot b}{|a||b|}\right), P_c(x) < P(x) \end{cases}$$

where α is the crank angle, a is the crank vector from the center of rotation to the top dead center, b is the vector from the center of rotation to the current crank position, $P_c(x)$ is the x coordinate of the center of rotation and $P(x)$ is the x coordinate of the current crank position.

The resulting crank angle-time diagram allows for the calculation of start and end time instances for each complete revolution of the crank. Since the number of crank angle calculations match sEMG measurements, sEMG activity for every complete revolution or cycle for any subject can be extracted and 20 second measurements can be partitioned to yield individual cycles. These crank angle-sEMG graphs correspond to those found in [5].

The length of each cycling period was also extracted using crank angles.

D. Coactivation of muscles

A muscle is considered active if it's momentary amplitude is above the threshold function

$$K = \overline{EMG} \cdot s$$

where s is 0,35 if the muscle is VF, RF and VM, and 0,45 if the muscle BF. $\overline{EMG}$ is the sEMG signal averaged over 10 cycles. sEMG amplitude is a function of crank angle, therefore muscle activation ranges - size of the set of crank angle values at which the muscle is active - can be acquired. If two muscles are considered active at the same crank position, they are coactive.

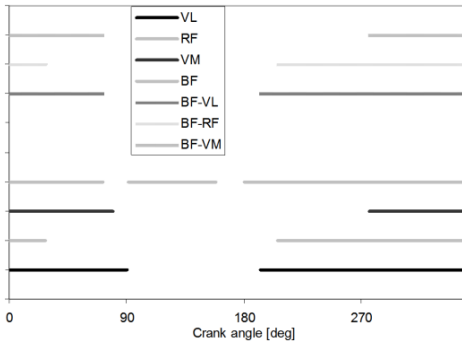

Fig. 4. Coactivation ranges of muscles of a subject with respect to crank angle at high speed, high resistance

E. Statistical analysis of sEMG data

Change in the sEMG amplitude levels when cycling against a greater resistance was calculated for each muscle at all six RCs. For each muscle of each participant, the average sEMG activity over 10 cycles was extracted.

To determine coactivation ranges for each RC, the average activity of all muscles averaged over all subjects was calculated. Afterwards, the previously described activation treshold was applied to the averaged sEMG-s and coactivation ranges found.

Correlation with cycle period length was examined for sEMG amplitude average (V_1), maximum (V_2) and minimum (V_3) amplitude values, and the integral of sEMG considered from 0 mV (V_4) and from minimum sEMG amplitude (V_5).

$$V_{1,i,j,k} = \overline{EMG}_{i,j,k}$$
$$V_{2,i,j,k} = \max(EMG_{i,j,k})$$
$$V_{3,i,j,k} = \min(EMG_{i,j,k})$$
$$V_{4,i,j} = \sum EMG_{i,j,k}$$
$$V_{5,i,j} = \sum \left[EMG_{i,j,k} - \min(EMG_{i,j,k})\right]$$

where *EMG* is the surface EMG signal for one muscle with respect to time, i is the subject, j is the RC and k is the muscle identifier, $i \in [1,15]$, $j \in [1,6]$, $k \in [1,4]$.

F. Timing error of subjects

As mentioned in the introduction, it is very difficult for subjects to perform cycling tasks at a constant speed. The timing error of a cycling exercise is the difference (in milliseconds) between the time instant at which the crank should have returned to the TDC (if the subjects were capable of cycling at exactly 45 and 60 rpm, respectively) and the actual time instant at which the crank did return to the TDC.

III. RESULTS

There is a significant increase of sEMG amplitude levels at both speed conditions when going from medium to high resistance level. It is also important that the increase of sEMG amplitudes is non-linear with respect to speed, that is if the resistance is increased by the same level, sEMG amplitudes increase at a higher rate if speed is higher as well.

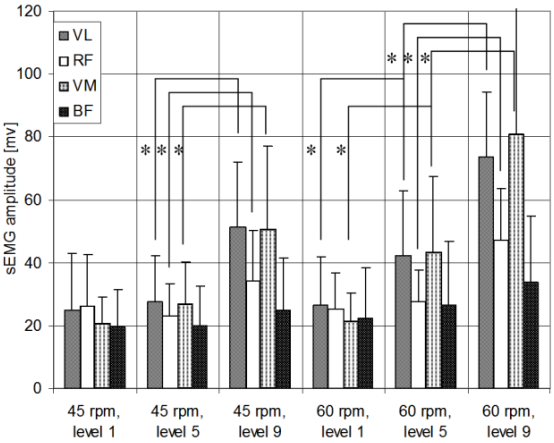

Fig. 5. Average sEMG amplitude of 10 cycles averaged over all participants. A * marks a significant difference.

The coactivation range for flexor-extensor muscle pairs (BF-VM, BF-VL, BF-RF, BF-VM-VL) decreases when increasing resistance from low to medium level. This decrease is lower however, when further increasing resistance from medium to high level.

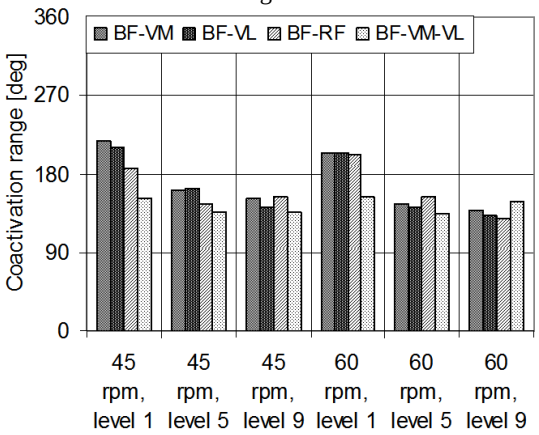

Fig. 6. Coactivation range sizes (in degrees) of flexor-extensor muscle pairs. The ranges decrease when going from low to medium resistance but the decrease is less when going from medium to high resistance.

Points of coactivation with respect to crank angle was also measured for all conditions. While most flexor-extensor muscle pairs are active around the TDC, there is BF-RF coactivity after the crank passed the BDC.

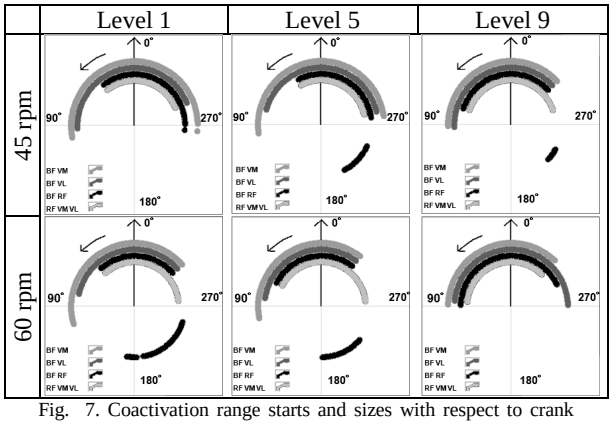

Fig. 7. Coactivation range starts and sizes with respect to crank angle. Most coactivation is around the TDC.

The timing error of every subject through a 10 second period was calculated for each RC. From these, the difference between the lowest and the highest timing error for each consecutive cycling period was also computed. This timing error difference monotonically increases throughout the 10 second period.

At low resistance, subjects cycled faster as well as slower than the desired speed producing a timing error difference at 10 seconds of 1240 ms at 45 rpm and 810 ms at 60 rpm, however when resistance was increased from low to medium, all subjects cycled faster, producing timing errors up to 580 ms at 45 rpm and 690 ms at 60 rpm.

Timing error difference further decreased when going from medium to high resistance but at a much lower rate, 460 ms at 45 rpm and 640 ms at 60 rpm. The high decrease between low and medium resistance and the low decrease between medium and high resistance is similar to the decrease of coactivation ranges.

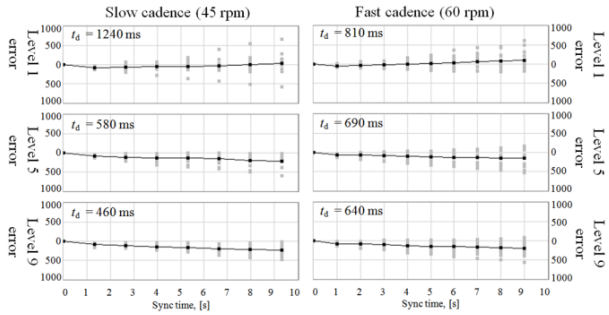

Fig. 8. Individual (gray) and average (black) timing errors of subjects at different RCs. Note that when resistance is not low, almost all subjects cycle faster than the desired speed.

Correlation between different qualities of the sEMG signals (V_1-V_5) and the time required to perform one cycle was insufficient. The highest degree of correlation, 0.5655 was calculated for V_5 biceps femoris averaged over all subjects and all 6 conditions. All other degrees of correlation for all muscles at all conditions were less than 0.5, meaning there is no considerable correlation between the sEMG signals per cycle and the actual time needed to finish the corresponding cycle.

IV. DISCUSSION

Results of this report suggest that when resistance at a constant speed is increased, power output of the lower limb is increased by reducing the coactivation range of flexor-extensor muscle pairs. A change in speed results only in the increase of sEMG amplitudes.

Improvement of these strategies of neural adaptation may be important in rehabilitating subjects with stroke or spinal cord injury. Step 1 of the therapy should involve increasing resistance at a lower speed to re-establish control of coactivation of flexor-extensor muscle pairs. Afterwards, increase in speed may help in producing higher EMG values.

When someone needs to be trained with an exercise that needs constant cycling speed, it is helpful if there is a small resistance to work against. A further increase in resistance will not improve timing considerably but will cause an earlier fatigue.

In the case of constant speed cycling exercises, small increases or decreases of consecutive cycles (and therefore, timing errors) appear to have no effect on the characteristics of the sEMG signals of the measuresd muscles.

V. ACKNOWLEDGMENTS

The author wishes to acknowledge the guidance of József Laczkó and Péter Szolgay. The time and effort of the 15 volunteers is also greatly appreciated. This work is supported by the Pázmány Péter Catholic University - University of National Excellence, the Faculty of Information Technology - Research Faculty, grants TÁMOP-4.2.1./B-11/2-KMR-2011-0002 and TÁMOP-4.2.2./B-10/1-2011-0014 by the European Union, and KAP 15-1/21 by the Pázmány Péter Catholic University.

VI. REFERENCES

[1] Baum BS and Li Li, "Lower extremity muscle activities during cycling are influenced by load and frequency", *J. Electromyogr. Kines.* 13, 181-190 (2003)

[2] W.D. McLeod and T.A. Blackburn, "Biomechanics of Knee Rehabilitation with Cycling", *Am J Sports Med* June 1980 vol. 8 no. 3 175-180

[3] P.Katona, T.Pilissy, A.Tihanyi and J.Laczko, "The combined effect of cycling cadence and crank resistance on hamstrings and quadriceps muscle activities during cycling", *Acta Physiologica Hungarica* 101: (4) pp. 505-516.

[4] B. I. Prilutsky and R. J. Gregor, "Analysis of Muscle Coordination Strategies in Cycling", *IEEE Trans. Rehabil. Eng.*, Vol 8. No. 3. September 2000

[5] M. O. Ericson, R. Nisell, U. P. Arborelius, and J. Ekholm, "Muscular activity during ergometer cycling," *Scand. J. Rehab. Med.*, vol. 17, pp. 53–61, 1985.

[6] G. Kamen, D. A. Gabriel:
„Essentials of Electromyography,"
Human Kinetics, 2010, ISBN(10): 0-7360-6712-4

Program 3

FEASIBILITY OF ELECTRONIC AND OPTICAL DEVICES, MOLECULAR AND NANOTECHNOLOGIES, NANO-ARCHITECTURES, NANOBIONIC DIAGNOSTIC AND THERAPEUTIC TOOLS

Head: Árpád CSURGAY

GPU-based live fusion of multi-view microscopy data

Bálint BALÁZS
(Supervisor: Lars HUFNAGEL, Balázs RÓZSA)
Pázmány Péter Catholic University, Faculty of Information Technology and Bionics
50/a Práter street, 1083 Budapest, Hungary
balba@digitus.itk.ppke.hu

***Abstract*—Multi-view light-sheet microscopy is one of the best tools to investigate early embryonic development due to its inherent optical sectioning, fast imaging speed and low phototoxicity. Evaluating the data however is an extremely challenging step, although just as crucial as the imaging itself. During each experiment multiple 3D datasets are generated which have to be further processed (fused) before any evaluation step. This can severely affect the effectiveness of the workflow.**

Here we present a fast, GPU based image fusion method for opposing camera views which can be performed live, directly on the microscope. Instead of the previously described 3D registration methods, this implementation directly fuses the camera images before saving it in the 3D stack. Although this gives a strict constraint for the precision of the microscope alignment, the benefits are well worth it.

This kind of direct fusion gives several benefits. First, the time consuming 3D fusion can be omitted, and the data can be directly used for manual or automatic evaluation without any further preprocessing steps. Second, since the original views are not needed, necessary storage space is also reduced by half.

We implemented the direct fusion method in a massively parallel way in the CUDA environment, along with further image preprocessing steps. These were then integrated in our existing LabVIEW-based microscope software, and successfully used to image fluorescent beads and fluorescently labeled *Drosophila melanogaster* embryos.

Keywords*—light-sheet microscopy; image preprocessing; GPU computing; affine transformation; *Drosophila melanogaster

I. Introduction

Imaging embryonic development over large spatial and temporal scales have always been a great desire for developmental biologists, and a great challenge for optics developers. Single-Plane Illumination Microscopy [1] provides a convenient and effective way to image such processes [2], utilizing dedicated optics for illumination which generates a light-sheet in the focal plane of the detection objective, thus providing true optical sectioning. This illumination scheme allows for fast imaging times while keeping laser exposure and thus phototoxicity to the smallest possible level [3].

Depending on the optical realization, single plane illumination microscopy is well suited for a variety of samples spanning a large scale from micrometers to even centimeters. It has been applied to image the neuronal network in whole mouse brain [4], to reconstruct the early devlopment in zebrafish embryos [5], and *Drosophila melanogaster* embryos [6], [7]

Because light-sheet microscopy uses a simple wide-field detection scheme, it is also possible to combine it with other imaging techniques that further improve image quality, such as structured illumination [8], Bessel beams [9], 2-photon excitation [10], and the combination of these [11].

In 2014 light-sheet microscopy was selected as Method of the Year by Nature Methods [12] which shows its enormous influence on developmental biology and also on microscope development.

Despite the advantages, imaging optically opaque samples, such as the *Drosophila m.* embryo can be still challenging due to scattering effect inside the tissue, and refractive index mismatches from the mounting medium. A straightforward way to improve image quality for such samples is to record multiple views from different directions, and later stitch these views to create a single, high quality stack. This can be easily achieved by rotating the sample, however this can be already to slow for certain processes.

The recently introduced Multi-View Single-Plane Illumination Microscope [6], which was developed in our lab, together with the Simultaneous Multiview Light-sheet Microscopy [7] provide an elegant solution for multi-view imaging. These setups utilize two illumination and two detection objectives, to give altogether four different combinations of illumination and detection, *i.e.* four different views. Although this is enough to fully visualize an opaque sample, several image preprocessing steps are necessary before any evaluation can be performed to combine the four stacks to a single, high quality 3D image.

By combining scanned light-sheet [5] witch confocal slit detection on the camera chip [13], it is possible to exclude out of focus, scattered illumination light. This way it's already possible to illuminate simultaneously, which leaves us with only two views, the views of the two opposing cameras.

II. Multi-view image fusion

To perform image fusion of opposing cameras, first image registration is necessary: the coordinate systems of both views have to be properly overlapped. Ideally a single mirroring transformation would be enough to superpose the two camera images, however in practice the microscope can never be aligned with such precision. Other types of transformations are also necessary: translation to account for offsets in the field of view; scaling in case of slightly different magnifications;

B. BALÁZS, "GPU-based live fusion of multi-view microscopy data" in *PhD Proceedings Annual Issues of the Doctoral School, Faculty of Information Technology and Bionics, Pázmány Péter Catholic University – 2015.* G. Prószéky, P. Szolgay Eds. Budapest: Pázmány University ePress, 2015, pp 137– 140.

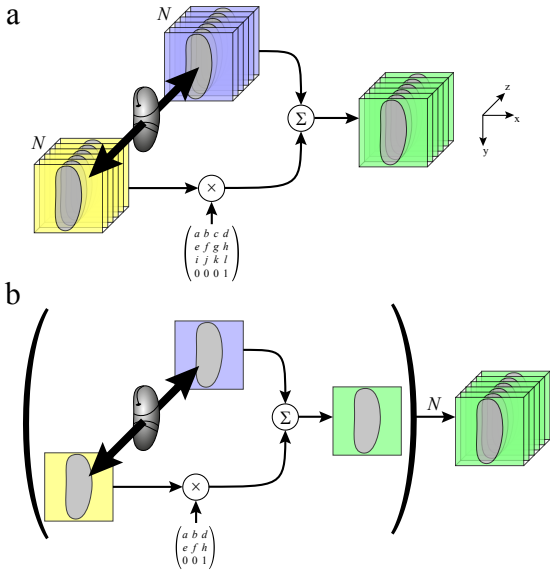

Fig. 1. Multi-view fusion methods for light-sheet microscopy. a) Full 3D stacks are acquired from the opposing views (yellow and blue), which are then registered in 3D space using previously acquired affine transformation parameters. Registered stacks are then weighted averaged to create the final fused stack (green). b) Images from opposing views are directly fused plane by plane. Registration takes place in 2D space thus reducing computational effort and memory requirements. The registered planes are then weighted averaged to create the final fused image.

and also shearing if the detection plane is not perfectly perpendicular to the sample movement direction. To combine all of these effects, a full 3D affine transformation is necessary to properly align the two camera images (Fig. 1 a). This transformation can be represented by a matrix multiplication with 12 different parameters:

$$\begin{pmatrix} a & b & c & d \\ e & f & g & h \\ i & j & k & l \\ 0 & 0 & 0 & 1 \end{pmatrix} \times \begin{pmatrix} x \\ y \\ z \\ 1 \end{pmatrix} = \begin{pmatrix} ax+by+cz+d \\ ex+fy+gz+g \\ ix+jy+kz+l \\ 1 \end{pmatrix}$$

where x, y, z are the coordinates of the original 3D image, and $a, b, c, d, e, f, g, h, i, j, k, l$ are the affine transformation parameters.

These parameters are traditionally acquired by imaging fluorescent beads suspended in a gel cylinder. The bead recordings are segmented, matching beads are automatically detected in each camera view, and using the RANSAC method the affine transformation parameters are determined. For two opposing views these parameters are only dependent on the optical setup itself, and not the sample or the experiment. Because of this, it is sufficient to determine the transformation parameters only after modifying/realigning the microscope.

This method of fusion however is quite cumbersome for the average user. The raw data is made up of two stacks, each of which only has one half with high contrast To evaluate the experiment, the user either has to look at both recordings, or wait for the offline fusion to complete, and examine the result.

It would be much more practical to already fuse the opposing views before displaying or saving the image. Since the two cameras ideally image the same z plane, it should be possible to reduce the alignment problem to a 2D affine transformation:

$$\begin{pmatrix} a & b & d \\ e & f & h \\ 0 & 0 & 1 \end{pmatrix} \times \begin{pmatrix} x \\ y \\ 1 \end{pmatrix} = \begin{pmatrix} ax+by+d \\ ex+fy+g \\ 1 \end{pmatrix}$$

If this is possible, then fusion can be carried out separately for each image plane (Fig. 1 b), which would greatly facilitate live image fusion. The requirements for this are the following:

$$|cz| < \sigma_{xy} \qquad \forall z \qquad (1)$$

$$|gz| < \sigma_{xy} \qquad \forall z \qquad (2)$$

$$|ix+jy+(k-1)z+l| < \sigma_z \qquad \forall x, y, z \qquad (3)$$

where σ_{xy} is the lateral resolution, and σ_z is the axial resolution of the microscope:

$$\sigma_{xy} = \frac{0.61 \cdot \lambda}{NA} = \frac{0.61 \cdot 500 \text{ nm}}{1.1} = 277 \text{ nm}$$

$$\sigma_z = \frac{2 \cdot n \cdot \lambda}{NA^2} = \frac{2 \cdot 1.33 \cdot 500 \text{ nm}}{1.1^2} = 1099 \text{ nm}$$

If these conditions hold (*i.e.* the microscope is properly aligned), then direct plane by plane fusion will not result in any loss of information compared to the full 3D image fusion.

III. Image Preprocessing Pipeline

To perform the image fusion step as fast as possible, thus enabling it's use for live imaging, we used CUDA (Compute Unified Device Architecture) [14] to implement the algorithm on a graphics card (NVIDIA, GTX 750). This architecture offers a convenient way to harness the massively parallel computing capabilities of the many streaming multiprocessors residing on a GPU (graphics processing unit). Since each processing step we require is pixel based, they can be inherently parallelized to gain tremendous advantage in computing time.

To utilize the GPU for the image processing step, the images first have to be transferred from the computer main memory to the graphics card memory. Because of the limited bandwidth of the PCIe 2.0 16x bus, this step is actually the bottleneck, and not the computation itself. To optimize data transfer speed, several techniques can be used.

First, one has to make sure that the space for the original image data is allocated as paged-lock memory. This is possible with `cudaMallocHost`. This function will make sure that the memory space allocated on the host will be page-locked *i.e.* it's contents cannot be temporarily swapped to the pagefile on the hard disk, and it is actually mapped to the physical memory. Otherwise, with normal allocation functions this is not guaranteed by the operating system, and the memory is only mapped to the physical memory when it's contents are accessed, which heavily influence read/write speed.

Second, if the same operation is carried out for many images (as in the case of our live fusion method), the data transfer for the next image can already be carried out while the previous image is being processed, thus masking at least one of the data transfers between the main memory and the graphics card.

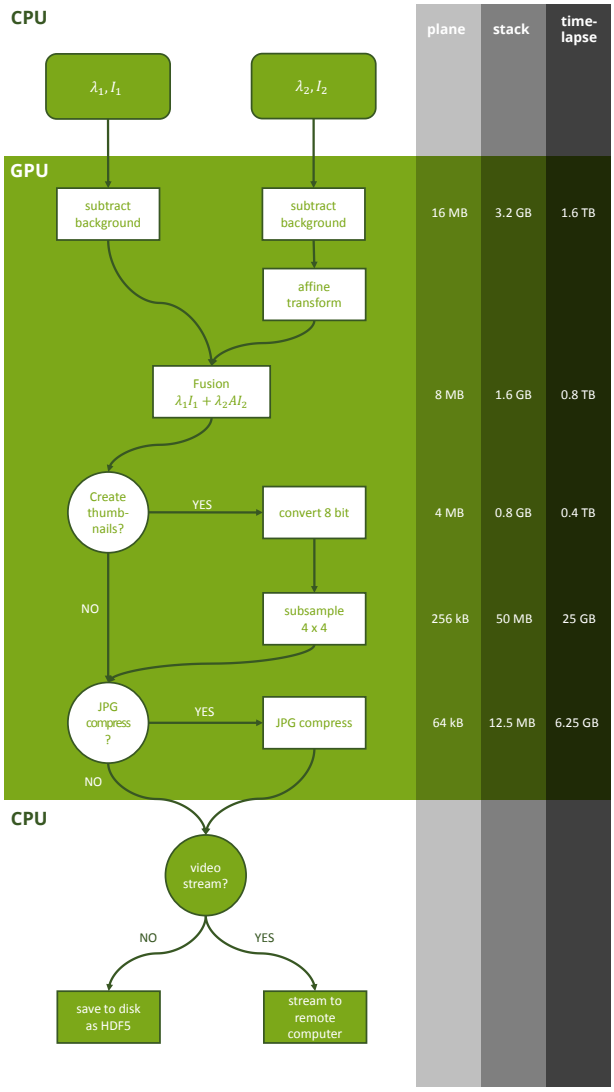

Fig. 2. Image preprocessing pipeline. The pipeline comprises of two parts: processing on CPU (white background) and processing on GPU (green background). Images are first transferred from the CPU to the GPU, where the preprocessing steps take place. These include background subtraction, affine transformation, weighted averaging and optionally thumbnail generation and image compression. After the preprocessing steps the image is transferred back to the CPU, and saved on the hard drive, or streamed to a remote computer. Data sizes after each preprocessing step are shown in the gray bands for planes, stacks and time-lapses.

To maximize GPU utilization, and ultimately justify the long data transfer times, in addition to the plane by plane fusion (which is actually an affine transformation followed by weighted average), we also implemented background subtraction, subsampling, LUT conversion from 16 bits to 8 bits, and JPEG compression in our pipeline (Fig 2). All of these steps either enhance image quality (such as background subtraction), reduce data size (LUT conversion, subsampling, JPEG), or both (fusion).

Since our microscope control software is implemented in LabVIEW, all the functions in our pipeline were incorporated in a dynamic linked library (DLL) which can be loaded by LabVIEW to use the CUDA functions. Furthermore, to facilitate the integration to existing software, we created a LabVIEW library based on these CUDA functions, to provide a consistent and easy to use interface for further development.

IV. Results

The image preprocessing pipeline was tested our previously described Multi-View Single Plane Illumination Microscope (MuVi-SPIM)[6]. For the background subtraction we recorded 1500 dark images with each camera and averaged them, to obtain the camera specific background images. Before image acquisition these were uploaded to the GPU memory, and were readily available for the pipeline.

After careful alignment of the microscope to meet the previously discussed requirements (Eqs. (1) – (3)), we imaged fluorescent beads in a gel suspension to obtain the affine transformation parameters. After making sure that these parameters indeed fulfill the previously set requirements, these were also uploaded to the GPU memory for further use in our pipeline.

To validate our hypotheses, that 2D direct image fusion is sufficient instead of the full 3D fusion, we image several samples. First, we imaged the flourescent beads again, now with the live fusion enabled, to make sure our registration parameters are correct. Manual evaluation of the data revealed that the fusion indeed worked, without any artifacts, for example double beads which would indicate an imprecision in alignment or in the transformation parameters.

We also applied the live fusion fo a real biological specimen, namely *Drosophila melanogaster* embryos expressing H2Av-mCherry histone marker. The embryos were imaged first without direct fusion enabled, and immediately afterwards with direct fusion enabled (Fig. 3). Image quality dependency on the depth of the imaging plane is especially apparent in single-view stacks. Planes closer to the camera give a sharp, high contrast image, while planes further then the middle of the embryo are severely degraded due to scattering.

Stacks obtained with the live fusion enabled show a consistently high image quality throughout the entire stack, independent of the depth. This allows us to keep only the already fused data, thus effectively reducing the storage requirement by half, and facilitating further data processing steps.

V. Conclusions

In this paper we showed the importance of multi-view imaging in light-sheet microscopy, and the necessary steps to perform the fusion of opposing camera views. We developed a direct plane by plane fusion method which was implemented in CUDA, and can be performed live, directly on the microscope. This results in a single, high quality recording, which can be directly used later for further processing or data evaluation. We showed the viability of the method by imaging fluorescent beads, and fluorescently labeled *Drosophila m.* embryos, which showed superior image quality to both of the original views. As a further consequence, data handling

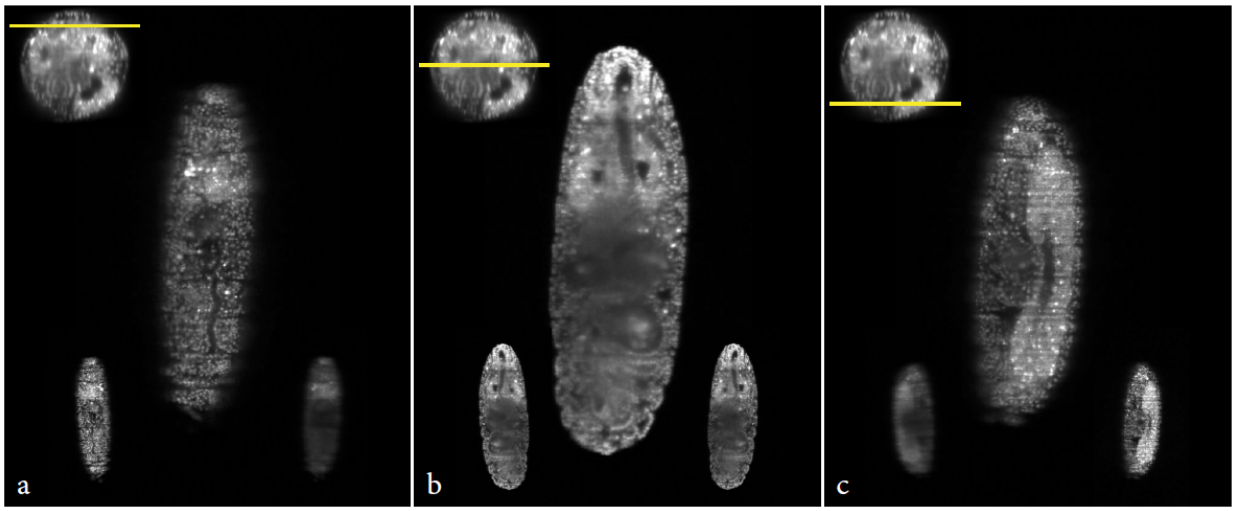

Fig. 3. GPU fused images of a *Drosophila melanogaster* embryo. Two stacks were taken in quick succession first without fusion, then with fusion enabled. Fused images are shown in the middle of each subfigure, while the individual camera images are in the bottom insets. The top-left inset depicts the z-position of the shown images. a) Image from closer to the left camera. b) Image from the center of the embryo. c) Image from closer to the right camera.

became easier, less storage is needed for further experiments, and considerable time is spared by eliminating the need for the 3D fusion step.

Despite the many advantages, further development is still necessary. For several samples orthogonal views are desired, or in some cases the optical setup is already designed with orthogonal detection[15]. In these cases to properly fuse the different directions, multi-view deconvolution is necessary [16], [17] to gain maximum information from both views.

Acknowledgments

This research was supported by the EMBL International PhD Programme. Special thanks to Gustavo Quintas Glasner de Medeiros, Nils Norlin, Marvin Albert, Dimitri Kromm and Lars Hufnagel.

References

[1] J. Huisken, J. Swoger, F. Del Bene, J. Wittbrodt, and E. H. K. Stelzer, "Optical Sectioning Deep Inside Live Embryos by Selective Plane Illumination Microscopy," *Science*, vol. 305, no. 5686, pp. 1007–1009, 2004.

[2] M. Weber and J. Huisken, "Light sheet microscopy for real-time developmental biology," *Current Opinion in Genetics & Development*, vol. 21, no. 5, pp. 566–572, 2011.

[3] E. G. Reynaud, U. Kržič, K. Greger, and E. H. Stelzer, "Light sheet-based fluorescence microscopy: more dimensions, more photons, and less photodamage," *HFSP J*, vol. 2, no. 5, pp. 266–275, Oct. 2008.

[4] H.-U. Dodt, U. Leischner, A. Schierloh, N. Jährling, C. P. Mauch, K. Deininger, J. M. Deussing, M. Eder, W. Zieglgänsberger, and K. Becker, "Ultramicroscopy: three-dimensional visualization of neuronal networks in the whole mouse brain," *Nature Methods*, vol. 4, no. 4, pp. 331–336, Mar. 2007.

[5] P. J. Keller, A. D. Schmidt, J. Wittbrodt, and E. H. K. Stelzer, "Reconstruction of Zebrafish Early Embryonic Development by Scanned Light Sheet Microscopy," *Science*, vol. 322, no. 5904, pp. 1065–1069, Nov. 2008.

[6] U. Krzic, S. Gunther, T. E. Saunders, S. J. Streichan, and L. Hufnagel, "Multiview light-sheet microscope for rapid in toto imaging," *Nat Meth*, vol. 9, no. 7, pp. 730–733, Jul. 2012.

[7] R. Tomer, K. Khairy, F. Amat, and P. J. Keller, "Quantitative high-speed imaging of entire developing embryos with simultaneous multiview light-sheet microscopy," *Nat Meth*, vol. 9, no. 7, pp. 755–763, Jul. 2012.

[8] P. J. Keller, A. D. Schmidt, A. Santella, K. Khairy, Z. Bao, J. Wittbrodt, and E. H. K. Stelzer, "Fast, high-contrast imaging of animal development with scanned light sheet-based structured-illumination microscopy," *Nat Meth*, vol. 7, no. 8, pp. 637–642, Aug. 2010, light-sheet structured illumination.

[9] T. A. Planchon, L. Gao, D. E. Milkie, M. W. Davidson, J. A. Galbraith, C. G. Galbraith, and E. Betzig, "Rapid three-dimensional isotropic imaging of living cells using Bessel beam plane illumination," *Nat Meth*, vol. 8, no. 5, pp. 417–423, May 2011.

[10] T. V. Truong, W. Supatto, D. S. Koos, J. M. Choi, and S. E. Fraser, "Deep and fast live imaging with two-photon scanned light-sheet microscopy," *Nat Meth*, vol. 8, no. 9, pp. 757–760, Sep. 2011.

[11] B.-C. Chen, W. R. Legant, K. Wang, L. Shao, D. E. Milkie, M. W. Davidson, C. Janetopoulos, X. S. Wu, J. A. Hammer, Z. Liu, B. P. English, Y. Mimori-Kiyosue, D. P. Romero, A. T. Ritter, J. Lippincott-Schwartz, L. Fritz-Laylin, R. D. Mullins, D. M. Mitchell, J. N. Bembenek, A.-C. Reymann, R. Böhme, S. W. Grill, J. T. Wang, G. Seydoux, U. S. Tulu, D. P. Kiehart, and E. Betzig, "Lattice light-sheet microscopy: Imaging molecules to embryos at high spatiotemporal resolution," *Science*, vol. 346, no. 6208, p. 1257998, Oct. 2014.

[12] "Method of the Year 2014," *Nat Meth*, vol. 12, no. 1, pp. 1–1, Jan. 2015.

[13] E. Baumgart and U. Kubitscheck, "Scanned light sheet microscopy with confocal slit detection," *Opt. Express*, vol. 20, no. 19, pp. 21 805–21 814, 2012.

[14] "CUDA Parallel Computing Platform." [Online]. Available: http://nvidia.com/object/cuda_home_new.html

[15] Y. Wu, P. Wawrzusin, J. Senseney, R. S. Fischer, R. Christensen, A. Santella, A. G. York, P. W. Winter, C. M. Waterman, Z. Bao, D. A. Colón-Ramos, M. McAuliffe, and H. Shroff, "Spatially isotropic four-dimensional imaging with dual-view plane illumination microscopy," *Nat Biotech*, vol. 31, no. 11, pp. 1032–1038, Nov. 2013.

[16] U. Kržič, "Multiple-view microscopy with light-sheet based fluorescence microscope," Ph.D. dissertation, Ruperto-Carola University of Heidelberg, Germany, 2009.

[17] M. Temerinac-Ott, O. Ronneberger, P. Ochs, W. Driever, T. Brox, and H. Burkhardt, "Multiview Deblurring for 3-D Images from Light-Sheet-Based Fluorescence Microscopy," *Image Processing, IEEE Transactions on*, vol. 21, no. 4, pp. 1863 –1873, Apr. 2012.

Decorrelation ultrasound as a tool for investigating post-mortem tissue effects

Gergely CSÁNY
(Supervisor: Miklós GYÖNGY)
Pázmány Péter Catholic University, Faculty of Information Technology and Bionics
50/a Práter street, 1083 Budapest, Hungary
csany.gergely@itk.ppke.hu

A revised form of this manuscript is due to appear as a proceedings paper for *2015 ICU (International Congress on Ultrasonics)*.

***Abstract*—Decorrelation ultrasound is being increasingly used to investigate long-term biological phenomena. In the current work, ultrasound image sequences of mice who did not survive anesthesia (in a separate investigation) were analyzed and post-mortem tissue effects were observed via decorrelation calculation. A method was developed to obtain a quantitative parameter characterizing the rate of decorrelation. The results show that ultrasound decorrelation imaging is an effective and promising method of observing post-mortem tissue effects and point to further studies elucidating the mechanism behind these effects.**

***Keywords*-decorrelation; correlation; autocorrelation; post-mortem; exponential curve fit; time constant; long-term; tissue effects; decomposition**

I. Introduction

Decorrelation ultrasound (here after DECUS) is being increasingly used to investigate long-term biological phenomena such as response to therapy or slow blood perfusion in the capillaries [1–3]. DECUS is useful for obtaining information from dynamic changes (eg. characterizing changes in a time-domain sequence of some data). For a temporal sequence of ultrasound signals, it can provide important and quantitative information about scatterer dynamics. As shown by Abbey et al. [1], static, dynamic scatterers as well as noise can be quantitatively separated via decorrelation.

A potential application of DECUS is the investigation of postmortem effects in tissue. To our knowledge, the results of such experiments have not yet been published in the literature. Post-mortem tissue effects – such as post-mortem blood movements, rigor mortis, or decomposition) occur over the time-course of several minutes to hours (or even days), thereby making conventional ultrasound Doppler techniques unusable. The investigation of these effects is of potential interest in forensics, such as in understanding the post-mortem redistribution of various drugs [4].

II. Background

As described by Abbey et al. [1], comparing images generated in the same spatial frame – but at different moments in time – makes it possible to differentiate between components of the imaged object, based on signal statistics.

Three basic components can be identified in the cumulative signal correlation data (Figure 1). The correlation contribution of static scatterers is constant. However, contribution of dynamic scatterers to the overall signal correlation is decaying in time: it is assumed to show an exponential decay. The third component is noise (arising from the way of data acquisition), which is assumed to be totally uncorrelated in time, so that its decorrelation component has the form of a Dirac delta function.

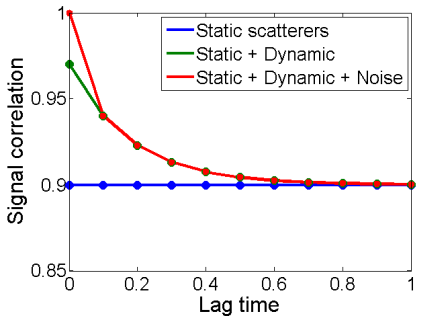

Fig. 1. Components of the cumulative correlation signal. Modified from [1: 2254].

Measuring and examining the overall correlation signal of images in time gives important information about the components of the signal. The drop in the beginning of the cumulative correlation function (the drop between the auto-correlation value (1.0) of the first image and the correlation value measured for – the first – two different images) accounts mostly for the effect of noise. The limiting value of the decaying function (ideally) represents the total contribution of static scatterers to the overall (cumulative) signal (image) correlation. The interval between the correlation contribution level of static scatterers and the highest value of the cumulative correlation signal, right after the drop referring to noise, shows the contribution of dynamic scatterers. This interval makes it possible to calculate the proportion of dynamic scatterers versus static scatterers in the imaged region. By examining the decaying function, temporal changes in the imaged object can be characterized and quantitatively described by calculating a time constant for the decay.

G. CSÁNY, "Decorrelation ultrasound as a tool for investigating post-mortem tissue effects" in *PhD Proceedings Annual Issues of the Doctoral School, Faculty of Information Technology and Bionics, Pázmány Péter Catholic University – 2015.* G. Prószéky, P. Szolgay Eds. Budapest: Pázmány University ePress, 2015, pp 141– 144.

As has been shown above, using statistical signal analysis, dynamic processes can be analyzed quantitatively and important information can be collected about static, dynamic and noise components of the measurement signals.

III. Materials and methods

A. Data acquisition

Ultrasound (US) images of nude mice were collected under anesthesia as part of a separate investigation into cancer growth of xenografts implanted into their hind legs. Two of the mice did not survive the anesthesia procedure and ultrasound images were obtained post-mortem. To investigate post-mortem changes to tissue, a sequence of ultrasound images were collected at regular time intervals. The linear array transducer was kept in a fixed location observing the hind legs of the animal. An Analogic US research system (BK Medical, Denmark) was connected to 5–12 MHz linear array.

In the current work, results are presented using two separate sequences of ultrasound images, one from each of the mice. One was a 53 minutes long sequence with 10.6 s time intervals. The other sequence of images was collected in 36 hours using a time interval of 5 minutes. Based on these two image sequences, long-term tissue effects could be observed as well as short-term changes – the latter with a higher temporal resolution.

B. Decorrelation analysis

In order to get an insight into the dynamics of the imaged tissues, decorrelation analysis was done separately for each spatial location – for every image pixel in the ultrasound image frame (see Fig. 2.a.). For each pixel, the autocorrelation function of the temporal RF (radiofrequency) signal amplitude changes was calculated for positive time lags (see Fig. 2.b.). The initial parts of the autocorrelation functions fitted well to an exponential decay. Therefore, to estimate the rate of decorrelation, a time constant was calculated for each pixel via exponential curve fitting (see Fig. 2.c.).

The method used for exponential curve fitting was based on the mathematics of the gradient of exponential functions. Namely, for an exponentially decaying function f (with amplitude A and time constant τ):

$$f(t) = Ae^{-t/\tau}$$

the gradient of the function is:

$$f'(t) = -\tfrac{1}{\tau}Ae^{-t/\tau} = -\tfrac{1}{\tau}f(t)$$

Thus, the time constant of the function can be determined using the following equation:

$$\tau = -\tfrac{f(t)}{f'(t)}$$

Given the estimated time constants τ for each spatial location in the image frame, dynamic behavior of scatterers in different spatial locations was visualized by creating a map of τ (using the same image frame as for the acquisition of data – see Fig. 2.c.).

IV. Results

A. Tissue changes on small time-scale (seconds – 1 hour)

In the case of the 53-minute-long acquisition (10.6 s temporal resolution), relatively short-term post-mortem tissue effects were observed. One of these effects is post-mortem blood movement which phenomenon is discussed in [4].

The map of time constants – calculated via exponential curve fitting to the pixelwise temporal autocorrelation functions (see Fig. 2.) – is shown in Fig. 3. The regions with smaller time constants correspond to the more dynamically changing regions observed in the original B-mode US image flow (see Fig. 4. as an illustration and reference for Fig. 3.).

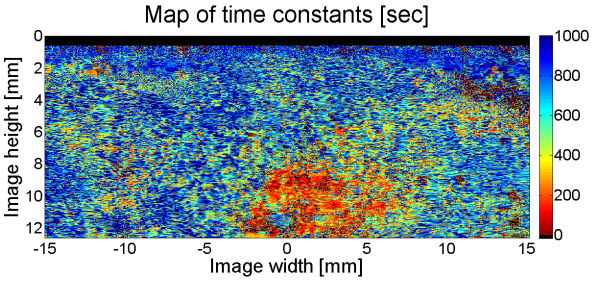

Fig. 3. Spatial map of time constants calculated from fitted exponential curves. Warmer colors indicate smaller time constants – thus, a faster decay in correlation. On the other hand, colder colors refer to slower decay (with larger time constants) and indicate the places of (more) static scatterers. In order to achieve a better resolution for smaller time constant values, a limit of 1000 s is set for visualizable differences.

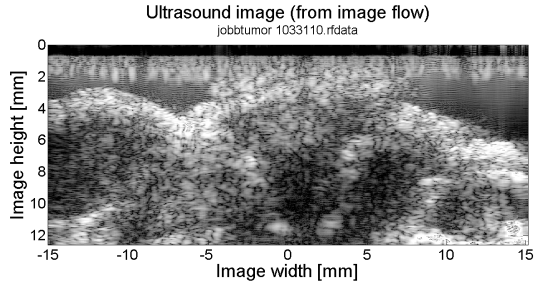

Fig. 4. A (typical) B-mode (brightness-mode) US image from the image sequence (for reference).

In some well-defined regions – like the central ventral region of the animal (region between -1–4 mm axially, 8–12 mm laterally) – periodic changes were observed qualitatively in the B-mode image sequence. Autocorrelation sequences showed a relatively fast decay rate for these regions (characterized by time constant values around 100 seconds) and also showed an oscillatory component with a periodicity in the range of 10–15 minutes (see Fig. 5.). Since the abdominal aorta of the mouse was located in the area mentioned above, the occurrence of this oscillatory behavior (in the scale of $\sim$10 minutes) is presumed to be related with post-mortem blood movements.

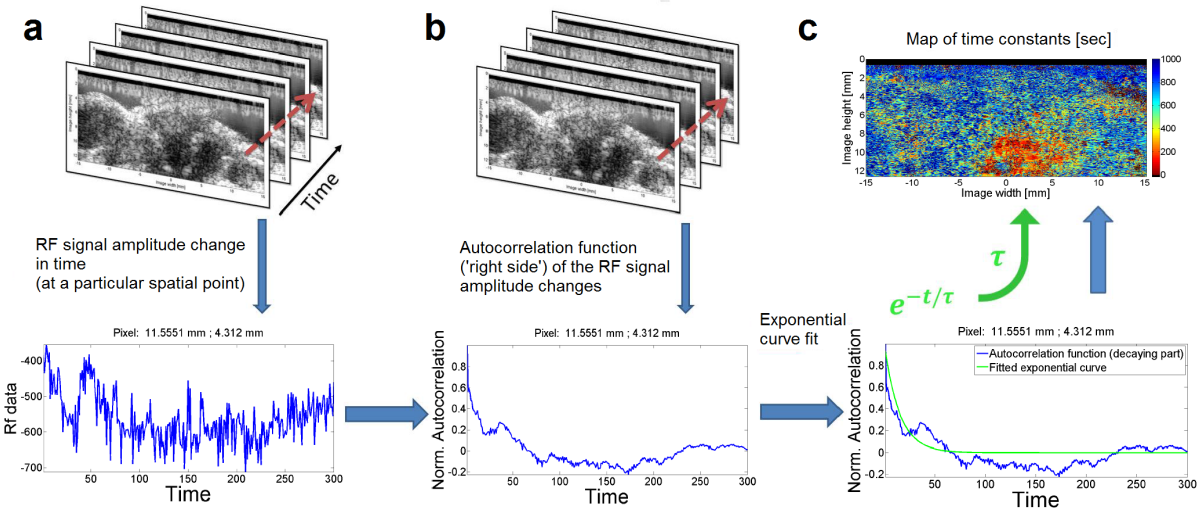

Fig. 2. Method for calculating the map of time constants via exponential curve fitting to autocorrelation functions of pixelwise temporal RF signal changes. (a) Observing RF signal amplitude change in time (for a given pixel); (b) Calculation of autocorrelation functions (for positive time lags); (c) Spatial map of time constants calculated from fitted exponential curves.

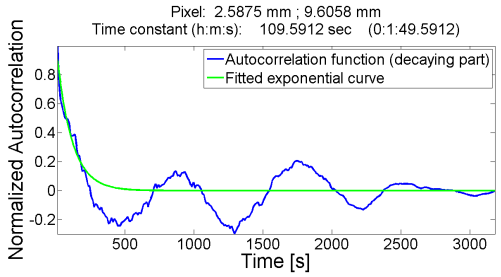

Fig. 5. Example of the results of decorrelation analysis for pixels region of imaged in the central ventral the mouse. Initially, a nearly exponential decay with a time constant of ∼100 seconds can be observed, followed by oscillatory behavior with a periodicity in the range of 10–15 minutes.

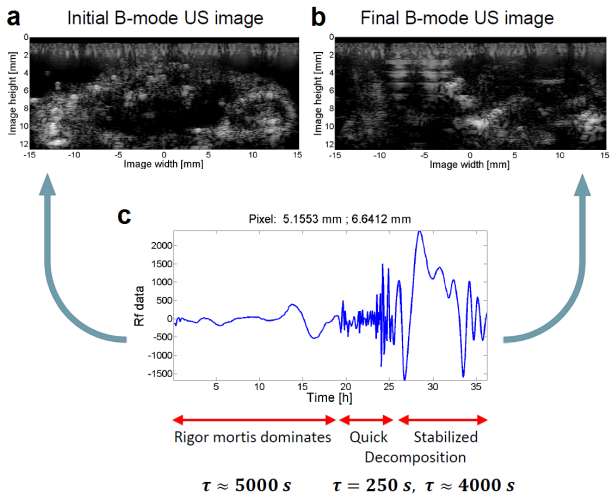

Fig. 6. Long-term tissue effects.
(a) First B-mode image from the image sequence (made at the time of death); (b) Final B-mode image from the image sequence (made 36 hours after death); (c) A sequence of temporal RF signal amplitude changes showing typical phases observed, together with calculated time constants for each phase, separately.

B. Tissue changes on long time-scale (hours – days)

To investigate relatively long-term tissue effects, a 36-hours-long post-mortem ultrasound image sequence was analyzed with a temporal resolution of 5 minutes. Different phases of post-mortem effects were observed in the temporal evolution of raw ultrasound signals and time constants were calculated for each (see Fig. 6.).

The ultrasound images did not show significant variation for the first 13–19 hours following death. This predominantly static period is in accordance with rigor mortis (being an important post-mortem effect describing long-term, static muscle contraction following death, in absence of ATP molecules which would allow actin–myosin complexes to disintegrate [5]).

The generally static phase was followed by a period of dynamical changes hypothesized to be related to decomposition. Here, two phases could be clearly separated. Firstly, relaxation of the corpse (after rigor mortis was ended) resulted in relatively quick changes in RF signal amplitudes coming from a given spatial point. A time constant of approximately 250 seconds was calculated for this phase, observed between 19 and 26 hours following death. From observation of the B-mode image sequence, the rapid oscillatory changes in the RF signal in this phase are assumed to arise from large-scale

global movement of the mouse as it relaxes following rigor mortis, rather than any real oscillatory motion.

In the third phase, slower changes with a time constant of $\sim$4000 seconds were observed. These changes are hypothesized to be due to advanced decomposition.

V. Conclusion

The results show that dynamic behavior of temporal changes in tissue can be quantitatively characterized by decorrelation analysis on US image sequence. Post-mortem image sequences (exempt from artifacts caused by voluntary motion of the animal) were used to show that DECUS can serve as an effective method of observing post-mortem tissue effects. Decorrelation analysis method was developed providing a quantitative parameter (time constant of the exponential curve fitted to the initial decaying part of the autocorrelation sequence) for a given spatial location (image pixel). Based on this method, creating a map of these quantitative parameters has been showed as a useful tool of visualizing relative dynamicity of spatial locations in the frame of a temporal image sequence.

Short-term and long-term tissue effects were observed post-mortem (using the above mentioned methods). However, further studies are needed elucidating the mechanism behind these effects as well as further improvements of the methodology (curve fitting algorithm, pixel-wise or global analysis, possibilities for scatterer-tracking).

Moving towards applications, a method may be developed in the future for classifying tissue changes based on decorrelation analysis of an ultrasonic image sequence.

Acknowledgement

The author would like to thank his supervisor, Miklós Gyöngy (PhD) for the helpful and professional guidance and also thank both his supervisor and Lajos Balogh (PhD) for providing data of mice (examined in this paper).

References

[1] Craig K. Abbey, Min Woo Kim and Michael F. Insana, *Perfusion Signal Processing for Optimal Detection Performance*, 2014 IEEE International Ultrasonics Symposium Proceedings, pp. 2253-6, 2014.

[2] T. R. Fosnight, F. M. Hooi, R. D. Keil, S. Subramanian, P. G. Barthe, Y. Wang, X. Ren, S. Ahmad, M. B. Rao and T. D. Mast, *Motion-Corrected Echo Decorrelation Imaging of In Vivo Focused and Bulk Ultrasound Ablation in a Rabbit Liver Cancer Model*, 2014 IEEE International Ultrasonics Symposium Proceedings, pp. 2161-4, 2014.

[3] S. Subramanian, S. M. Rudich, A. Alqadah, C. P. Karunakaran, M. B. Rao and T. D. Mast, *In Vivo Thermal Ablation Monitoring Using Ultrasound Echo Decorrelation Imaging*, Ultrasound in Med. & Biol., Vol. 40, No. 1, pp. 102114, 2014.

[4] Anne-Laure Pélissier-Alicot, Jean-Michel Gaulier, Pierre Champsaur and Pierre Marquet, *Mechanisms Underlying Postmortem Redistribution of Drugs: A Review*, Journal of Analytical Toxicology, Vol. 27, pp. 533544, 2003.

[5] J. E. Hall and A. C. Guyton, *Guyton and Hall Textbook of Medical Physiology*, Philadelphia, PA: Saunders/Elsevier, 2011.

Simulation of energy transfer between coupled two-state atoms

Imre Benedek JUHÁSZ
(supervisor: Árpád CSURGAY)
Pázmány Péter Catholic University, Faculty of Information Technology and Bionics
50/a Práter street, 1083 Budapest, Hungary
juhim@digitus.itk.ppke.hu

***Abstract*—Experiments performed in recent years suggest that quantum effects might play a crucial role in biological processes such as in energy transfer taking place in photosynthetic complexes. To study the latter phenomenon, I developed a quantum mechanical model and implemented a simulator program using *Quantum Toolbox in Python* (*QuTiP*). The simulator solves the Lindblad master equation of a system consisting of *N* coupled two-state atoms, defined by energy, coupling and dissipation parameters, thereby it enables the investigation of excitation-propagation between the atoms. This preliminary study presents the constructed model and a simulation example illustrating the capabilities of the simulator.**

I. Introduction

Photosynthetic complexes are important examples of biological systems in which quantum processes are assumed to be essential. [1], [2], [3] Compared to other phenomena explained by quantum models, energy transfer in photosynthetic complexes can be examined experimentally in a relatively direct manner using laser-based techniques, [4] such as two-dimensional electronic spectroscopy. [5] These experiments aim to scan the excitedness of the molecules to reveal how the energy harvested by the antenna protein is delivered by the photosynthetic complex to the reaction center with almost 100% efficiency. [2] However, the interpretation of the measurement data is usually not trivial.

In this paper, I present a simple quantum mechanical model consisting of coupled two-state atoms, based on which I implemented a simulator program using *Quantum Toolbox in Python* (*QuTiP*) [6] enabling the investigation of the energy transfer between the atoms with variable energy, coupling, and dissipation parameters. The temporal dynamics of the system is obtained by the numerical solution of the Lindblad equation. The effect of the environment is taken into account as an exponential decay from the excited to the ground state.

The construction of this article is the following: In Section II, I shortly present the theoretical background. Sections III and IV delineate the simulation model and a simulation example, respectively. Finally, the paper closes with conclusions in Section V.

II. Concepts and theoretical background

One can describe the state of a pure, closed (i.e. non-dissipative) quantum system with a state function ψ which can be represented by a ket vector $|\psi\rangle$. The time-evolution of the system is formulated by the time-dependent Schrödinger equation:

$$\mathrm{i}\hbar\frac{\mathrm{d}}{\mathrm{d}t}\left|\psi(t)\right\rangle = \hat{H}(t)\left|\psi(t)\right\rangle \tag{1}$$

with the initial condition $|\psi(t_0)\rangle = |\psi_0\rangle$ defining the initial state. $\hat{H}(t)$ denotes the Hamiltonian, i.e. the total energy operator of the system. The state of open (i.e. dissipative) systems, however, is described by the density operator

$$\hat{\rho} = \sum_n p_i \left|\psi_i\right\rangle\left\langle\psi_i\right|, \tag{2}$$

where p_n denotes the classical probability that the system is in state $|\psi_i\rangle$. The time-evolution of the density operator is given by the Liouville–von Neumann equation [6]:

$$\frac{\mathrm{d}\hat{\rho}_{tot}(t)}{\mathrm{d}t} = -\frac{\mathrm{i}}{\hbar}\left[\hat{H}_{tot}(t), \hat{\rho}_{tot}(t)\right] \tag{3}$$

with the initial condition $\hat{\varrho}_{tot}(t_0) = \hat{\varrho}_{tot,0}$. In Eq. (3), the total Hamiltonian $\hat{H}_{tot}$ is the sum of the Hamiltonian of the system, the environment and the interaction:

$$\hat{H}_{tot} = \hat{H}_{sys} + \hat{H}_{env} + \hat{H}_{int}. \tag{4}$$

In general, we are interested in the evolution of the system only, but not that of the environment; thus, it is reasonable to introduce the reduced density operator [7]:

$$\hat{\varrho} = \mathrm{Tr}_{env}\left[\hat{\varrho}_{tot}\right]. \tag{5}$$

Tr_{env} denotes the trace with respect to the environment. The time-evolution of the reduced density operator is formulated by the Lindblad master equation [6], [7]:

$$\begin{aligned}\frac{\mathrm{d}\hat{\rho}(t)}{\mathrm{d}t} = -\frac{\mathrm{i}}{\hbar}\left[\hat{H}(t), \hat{\rho}(t)\right] + \sum_n \Bigg[\hat{C}_n\hat{\rho}(t)\hat{C}_n^\dagger \\ -\frac{1}{2}\hat{\rho}(t)\hat{C}_n^\dagger\hat{C}_n - \frac{1}{2}\hat{C}_n^\dagger\hat{C}_n\hat{\rho}(t)\Bigg],\end{aligned} \tag{6}$$

where $\hat{C}_n$ are the so called collapse operators expressing the effect of the environment on the system.

The state vectors and the operators can be represented by vectors and matrices, respectively, as I will present it in the following section.

I. JUHÁSZ, "Simulation of energy transfer between coupled two-state atoms" in *PhD Proceedings Annual Issues of the Doctoral School, Faculty of Information Technology and Bionics, Pázmány Péter Catholic University – 2015.* G. Prószéky, P. Szolgay Eds. Budapest: Pázmány University ePress, 2015, pp 145– 148.

III. Simulation model

The goal of this study is to investigate how the energy is transferred in a system composed of *N* coupled two-state atoms. To do so, we have to give the description of (1) one atom, (2) the coupling between the atoms, and (3) the effect of the environment on the system.

The state of a two-state atom can be formulated as

$$|\varphi\rangle = c_1 |0\rangle + c_2 |1\rangle , \tag{7}$$

where c_1 and c_2 are complex amplitudes for which

$$|c_1|^2 + |c_2|^2 = 1, \tag{8}$$

furthermore

$$|0\rangle = \begin{bmatrix} 1 \\ 0 \end{bmatrix} \text{ and } |1\rangle = \begin{bmatrix} 0 \\ 1 \end{bmatrix} \tag{9}$$

are the ground and excited state of the atom, respectively, forming a basis for the two-dimensional Hilbert space $\mathcal{H}$, whose elements describe the state of the atom. The Hamiltonian of the atom is

$$\hat{H} = \begin{bmatrix} 0 & 0 \\ 0 & E \end{bmatrix} \tag{10}$$

with E denoting the energy difference between the two states.

The state of the composite system built up from *N* two-state atoms with state functions $|\varphi_i\rangle$ is

$$|\psi\rangle = |\varphi_1\rangle \otimes |\varphi_2\rangle \otimes \ldots \otimes |\varphi_N\rangle , \tag{11}$$

which is an element of the 2^N dimensional Hilbert space $\mathcal{H}_{comp} = \mathcal{H}_1 \otimes \mathcal{H}_2 \otimes \ldots \otimes \mathcal{H}_N$. We use the Lindblad equation to determine the evolution of the system; thus, $\hat{H}_{env}$ is neglected. The $2^N \times 2^N$ dimensional Hamiltonian of the composite system can be constructed as follows:

$$\hat{H}_{comp} = \sum_{i=1}^{N} E_i \hat{A}_i^\dagger \hat{A}_i + \sum_{i=1}^{N-1} \sum_{j=i+1}^{N} G_{ij} (\hat{A}_i + \hat{A}_i^\dagger)(\hat{A}_j + \hat{A}_j^\dagger), \tag{12}$$

where the first sum contains the energies E_i of the atoms, while the terms added up in the double sum express the energies of the interaction of the *i*-th and *j*-th atoms [6], G_{ij} denoting the strength of the coupling. The collapse operator $\hat{A}_i$ of the *i*-th atom is

$$\hat{A}_i = \hat{X}_1 \otimes \hat{X}_2 \otimes \ldots \otimes \hat{X}_N, \tag{13}$$

where

$$\hat{X}_j = \begin{cases} \begin{bmatrix} 0 & 1 \\ 0 & 0 \end{bmatrix} & \text{if } j = i, \\ \begin{bmatrix} 1 & 0 \\ 0 & 1 \end{bmatrix} & \text{if } j \neq i, \end{cases} \tag{14}$$

i.e. $\hat{X}_j$ is either the 2×2 unitary or the 2×2 annihilation operator. The effect of the environment on the *i*-th atom is expressed by the collapse operator

$$\hat{C}_i = \sqrt{\kappa_i} \hat{A}_i \tag{15}$$

describing the exponential decay of the *i*-th atom from the excited state to the ground state [6].

After defining the parameters describing the energies, couplings and relaxations of the atoms, furthermore the initial density operator and the collapse operators of the system, we construct the Lindblad equation (Eq. 6) according to the above formulae. To obtain the temporal dynamics of the system, the Lindblad equation is solved numerically for time instants t_0, t_1, …, t_M being distributed equidistantly between $t = 0$ and $t = T$ with timestep Δt. (Note that the numerical solver uses $\hbar = 1$.) Having in our possession the density matrices $\hat{\rho}(t_i)$, we can determine the occupation probability of the excited state of the *j*-th atom at time instant t_i as

$$P_{j,e}(t_i) = \mathrm{Tr}\left(\hat{\rho}(t_i) \hat{A}_j^\dagger \hat{A}_j\right) \tag{16}$$

[7], where $\hat{A}_j^\dagger \hat{A}_j$ is the number operator of the given state.

The most elusive component of this model is the characterization of the efficiency of the energy transfer. To keep the computational complexity low, let us assume that the *N*-th atom irreversibly transmits the energy being present in its excited state as a quantum (or in other words, in one step) to some target atom out of the modeled system. Since the total initial energy of the system suffices only one such quantum, the energy transmission can happen only once during the simulation. The probability that the energy transmission takes place during a timestep is the product of the probability that the transmission has not happened yet, the probability that the *N*-th atom is in the excited state at the moment, and a coefficient k which characterizes the speed of the transmission. We assume that the energy transmission is an exponential process with time constant τ; therefore, its probability can be formulated as

$$f(t) = 1 - \exp(t/\tau); \tag{17}$$

thus, $k = f(\Delta t)$. According to the above, the probability that by the *i*-th time instant t_i, the energy has arrived to the *N*-th atom and has been transmitted to the outer target atom can be formulated by the following, monotonically increasing function:

$$\Theta(t_i) = \begin{cases} 0 & \text{if } i = 0, \\ \Theta(t_{i-1}) + & \\ \quad + (1 - \Theta(t_{i-1}))\, P_{N,e}(t_i) k & \text{if } i > 0. \end{cases} \tag{18}$$

IV. Simulation example

Based on the model presented above, I implemented a simulator using *Quantum Toolbox in Python* (QuTiP), a Python-based, open-source framework, which provides vector- and matrix-based representation for states and operators, furthermore a numerical solver for the Lindblad master equation.

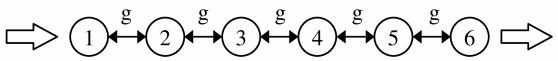

Figure 1. The topography of atoms used in the presented simulations. Couplings G_{ij} are set to g if there is an arrow between the i-th and j-th, and to 0 otherwise.

In this preliminary study, the parameters describing the couplings and the relaxation processes were chosen arbitrarily, therefore I pass over the units of the quantities. For the simulations presented in this paper, I set the simulation length T to 400, the timestep Δt to 1, and the time constant τ of the energy transmission by the N-th atom to 40. The modeled system consisting of $N = 6$ atoms receives energy in the form of excitation of the first atom. The first atom is, therefore, initially in the excited state, while the others are in the ground state, that is

$$|\psi(t=0)\rangle = \begin{bmatrix}0\\1\end{bmatrix} \otimes \begin{bmatrix}1\\0\end{bmatrix} \otimes \ldots \otimes \begin{bmatrix}1\\0\end{bmatrix}. \tag{19}$$

The atoms are chosen to be identical and thus resonant: they have the same energy gap $E_i = 1$ between the ground and excited states and the same dissipation rate $\kappa_i = 0.01$ for $i = 1, 2, \ldots, 6$. They are coupled to each other forming a chain (Fig. 1):

$$G_{ij} = \begin{cases} g & \text{if } |i-j| = 1, \\ 0 & \text{otherwise.} \end{cases} \tag{20}$$

Figures 2(a), (b), and (c) show the temporal dynamics of the systems with $g = 0.02, 0.04, 0.08$, respectively. As the simulation starts, the excitation energy of the 1st atom propagates towards the 2nd, then the 3rd atom, and so forth (solid line curves). When the excitation reaches the 6th atom, the expectation value of the energy transmitted to the outer target atom (denoted by Θ, dashed line) rises steeply. However, the energy begins soon to propagate back towards the 1st atom, stopping the increase of Θ. In the meantime, the system dissipates energy continuously, resulting in the exponential decrease of the total energy (dotted line). Increasing the coupling strength g, the excitation propagates faster along the chain of atoms, therefore it outruns the dissipation. As a consequence, more energy is transmitted towards the target.

V. Conclusion

I constructed a quantum mechanical model based on which I implemented a simulation program in Python that enables the investigation of energy transfer between coupled two-state atoms. To illustrate the capabilities of the simulator, I showed a simulation example.

In the following, I plan to set the model parameters to physically relevant values in order to model real systems or published experiments. In addition, the model can be developed using time-dependent operators and more sophisticated approaches of the system–environment interaction.

Acknowledgment

The author would like to thank Professor Árpád Csurgay for his guidance. Grant from KAP-3.3-14/003 is gratefully acknowledged.

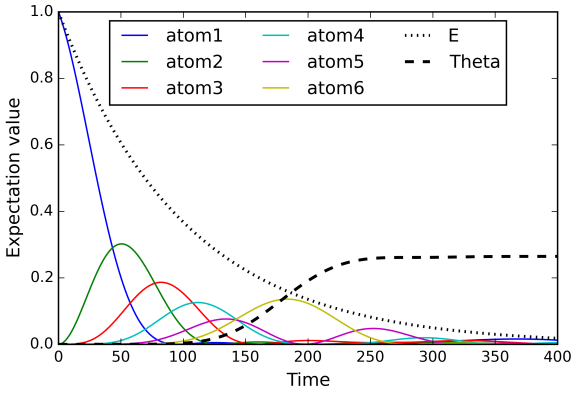

(a)

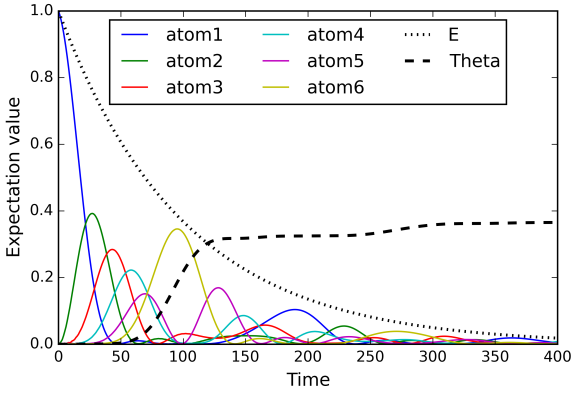

(b)

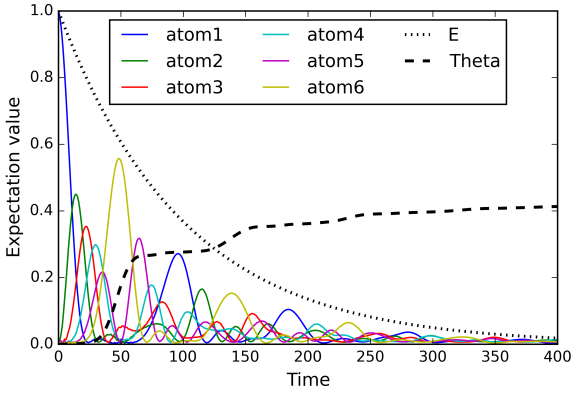

(c)

Figure 2. Time-evolution of the system. The curves with solid line delineate the probabilities that the atoms are in the excited state. The dotted and the dashed lines depict the total energy of the system and the energy transmitted by the 6th atom towards the outer target atom, respectively.

REFERENCES

[1] M. Sarovar, A. Ishizaki, G. R. Fleming, and K. B. Whaley, "Quantum entanglement in photosynthetic light-harvesting complexes," *Nature Physics*, vol. 6, no. 6, pp. 462–467, Jun. 2010.

[2] G. R. Fleming, G. D. Scholes, and Y.-C. Cheng, "Quantum effects in biology," *Procedia Chemistry*, vol. 3, no. 1, pp. 38–57, Jan. 2011.

[3] F. Fassioli, R. Dinshaw, P. C. Arpin, and G. D. Scholes, "Photosynthetic light harvesting: excitons and coherence," *Journal of The Royal Society Interface*, vol. 11, no. 92, pp. 20 130 901–20 130 901, Dec. 2013.

[4] S. Lloyd, "Quantum coherence in biological systems," *Journal of Physics: Conference Series*, vol. 302, p. 012037, Jul. 2011.

[5] M. Cho, T. Brixner, I. Stiopkin, H. Vaswani, and G. R. Fleming, "Two dimensional electronic spectroscopy of molecular complexes," *Journal of the Chinese Chemical Society*, vol. 53, no. 1, pp. 15–24, 2006.

[6] J. R. Johansson, P. D. Nation, and F. Nori, "QuTiP: An open-source Python framework for the dynamics of open quantum systems," *Computer Physics Communications*, vol. 183, no. 8, pp. 1760–1772, 2012.

[7] Pier Paolo Civalleri, "Two-state quantum systems," Pázmány Péter Catholic University, Budapest, May 2014.

Hybrid YIG-ferromagnet structures for spin-wave devices

Ádám PAPP
(Supervisor: Árpád CSURGAY, György CSABA (Notre Dame), Wolfgang POROD (Notre Dame))
Pázmány Péter Catholic University, Faculty of Information Technology and Bionics
50/a Práter street, 1083 Budapest, Hungary
papad@digitus.itk.ppke.hu

***Abstract*—We study coupled ferromagnetic layers, which could facilitate low loss, sub 100 nm wavelength spin-wave propagation and manipulation. One of the layers is a low-loss garnet film (such as yttrium iron garnet (YIG)) that enables long-distance, coherent spin-wave propagation. The other layer is made of metal-based (Permalloy, Co, CoFe) magnetoelectronic structures that can be used to generate, manipulate and detect the spin waves. Using micromagnetic simulations we analyze the interactions between the spin waves in the YIG and the metallic nanomagnet structures and demonstrate the components of a scalable spin-wave based signal processing device. We argue that such hybrid-metallic ferromagnet structures can be the basis of potentially high-performance, ultra low-power computing devices.**

This paper is substantively identical to [1].

***Keywords*-spin wave; YIG; dispersion relation**

I. Introduction

A holy grail of nanoelectronic research is to develop devices and circuit technologies that could surpass CMOS technology at least in certain figures of merit. Magnetoelectronic devices are top contenders for the title of such 'beyond Moore' technologies. Spin can enrich the functionality of electrical circuits [2], but magnetization state [3], [4], or the spin-wave amplitude and phase [5], [6], [7], [8] may entirely substitute electrical charge as information carrier.

A unique strength of spin-wave based computing paradigms is that they allow the realization of wave-based, non-Boolean computing algorithms. For example, by using wave interference as the elementary operation one can design massively parallel signal processing algorithms and essentially re-invent optical computing [9] on the nanoscale [10] [11] [12]. Spin-waves can be used for on-chip communication [5], and if needed, Boolean logic operations can be performed as well [13]. The small wavelength of spin-waves (potentially $\lambda < 10$ nm) and their high frequency (potentially in the several 100 GHz range) enables fast, high-integration devices and also CMOS-compatibility.

Spintronic devices (such as spin-torque oscillators (STOs), magnetoresistive structures) are made from amorphous, metallic ferromagnets (Permalloy, CoFe, etc.) that are conductors and can be deposited and patterned with straightforward technologies. It is also experimentally demonstrated that short-wavelength spin waves can be generated in such ferromagnetic thin films [14], which opens the way for spin-wave based computing devices. Due to the large damping constant of metallic ferromagnets, the typical spin wave decay length is on the order of 2 μm [14], so only very small-scale spin-wave devices could be built [15]. Strong damping also comes with high thermal noise, which degrades signal integrity. Spin-wave based computing blocks must be scalable beyond a few micrometer size, since magneto-electrical interfaces and / or spin-wave amplifiers come with a large energy and area footprint.

Unlike metallic ferromagnets, Yttrium Iron Garnet (YIG) is an excellent medium for spin-wave propagation, having one to three orders of magnitude smaller magnetic damping than Permalloy [16]. But YIG is an insulator, it is challenging to deposit high-quality YIG thin films and also challenging to pattern YIG on the nanoscale. Spin-waves in YIG are usually excited by RF antennas and it is very difficult to excite short-wavelength, exchange-dominated waves this way [17]. Magnetostatic waves can be straightforwardly excited but they typically have several micrometers or longer wavelength [18], making them impractical for microelectronics applications. In fact, most experimental studies on YIG-based devices deal with long-wavelength magnetostatic waves in YIG, and it is often taken for granted that the devices will be scalable all the way down to the regime of exchange waves [8].

It remains a fundamental challenge for spin wave based devices that no material is known that would simultaneously allow low-damping propagation of short-wavelength spin waves and electrical generation/manipulation/detection of spin waves in nanoscale magnetic structures. Our paper addresses this problem by a magnetic bi-layer, which is built from Permalloy nanostructures grown on top of a low-damping YIG film.

The operation of the proposed structure relies on exchange and dipolar interactions between a continuous YIG film and patterned Permalloy-based devices and layers on top of this film. Spin waves created in the Permalloy layer can be injected in the YIG film and the local stray field from nanomagnets on top of the YIG film can alter the propagation of the spin waves inside the YIG film. The YIG layer need not to be patterned and is expected to remain a low damping propagation medium.

Similar bi-layers were studied for applications in bubble memories [19] and very recently, spin-wave propagation in these bilayers were characterized as well [20], [21]. To our knowledge, no application areas for such bi-layers (apart from the now obsolete bubble memories) were proposed.

Á. PAPP, "Hybrid YIG-ferromagnet structures for spin-wave devices" in *PhD Proceedings Annual Issues of the Doctoral School, Faculty of Information Technology and Bionics, Pázmány Péter Catholic University – 2015.* G. Prószéky, P. Szolgay Eds. Budapest: Pázmány University ePress, 2015, pp 149– 152.

II. Micromagnetic model of the Permalloy-YIG system

We used the established OOMMF [22] code and determined the behavior of spin waves by postprocessing time-domain results.

For Permalloy we used values for saturation magnetization $M_s^{Py} = 8.6 \cdot 10^5$ A/m, exchange stiffness $A_{exch}^{Py} = 1.3 \cdot 10^{-11}$ J/m and damping constant $\alpha^{Py} = 0.008$. For YIG we used saturation magnetization $M_s^{YIG} = 1.6 \cdot 10^5$ A/m, exchange constant $A_{exch}^{YIG} = 4 \cdot 10^{-12}$ J/m and approximated the damping constant $\alpha^{YIG} = 0.001$ [23]. We assumed K = 0 crystalline anisotropy for both materials [23].

One of the most important parameters of our simulations is the exchange parameter between the YIG and the permalloy layer, which characterized the strength of the ferromagnetic interaction between the metal layers. Neglecting higher-order interaction terms, the ferromagnetic interaction can be described either by a J bilinear exchange constant or an $A_{\text{interface}}$ interface exchange stiffness. There are surprisingly few experimental works characterizing this interaction. Chun et. al. [24] studied an Fe/YIG system, finding a high $A_{\text{interface}}$, typical of coupled metallic ferromagnetic layers. Youssef et. al. [20] measured a similar system using FMR techniques [25] [26], but the resulting exchange constant is much lower and more similar to values found in exchange-coupled layers.

In our simulations we used the $J = 1.8 \cdot 10^{-4}$ J/m^2 value [20] as the lower bound for the interaction and we studied spin-wave behavior for higher interaction strengths as well.

In order to study wave propagation (for the simulations of Section III and VI) we created spin waves in the YIG film by a high-frequency spin torque current. This is an artificial way and serves only the purpose to study wave propagation; we study realizable scenarios in Section IV. We also used a relatively coarse numerical grid ($\Delta x = \Delta y = \Delta z = 5$ nm), to avoid exceedingly long simulation times.

To set the magnetization direction in the film and keep it from breaking to domains we applied a B_{ext} = 0.9 T external magnetic field in 87° out of plane. For the simulation we define a linearly increasing damping coefficient in a 25 nm region around the edges in order to realize absorbing boundary conditions.

III. Exchange-wave propagation in a coupled YIG-Permalloy bilayer

The dispersion relation for exchange-dominated waves is textbook material and for simplified geometries, analytical solutions are available [18]. We numerically determined the $f(k)$ and $H(k)$ functions for our geometry and the results are shown in Figure 1. Note that the frequency ranges (few tens GHz) and the wavelengths ($\lambda < 100$ nm) are both highly compatible with potential micro and nanoelectronic applications.

If a 5 nm thick Permalloy layer is placed on top of a 5 nm YIG film, then the two layers interact via dipole and exchange interactions. For the studied geometry, assuming the lowest estimate for $A_{\text{interface}}$, exchange interaction is dominant. Fig 2

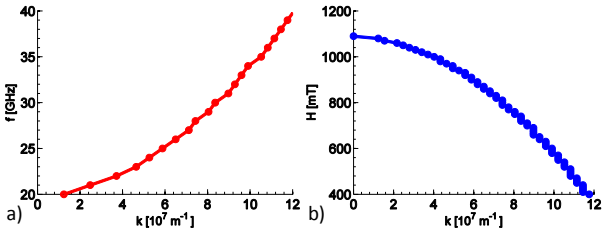

Fig. 1. Dispersion relation in a 5 nm thick YIG film. a) the frequency - wavenumber relation. b) The external field - wavenumber relation. Wavelengths ($\lambda = 2\pi/k$) and frequencies are ideal for many nano/microelectronic applications.

shows a pseudocolor plot of the dispersion relation for various $A_{\text{interface}}$ values. The plot was generated by taking the spatial Fourier transformation of the spin-wave amplitude in YIG, so if multiple modes are present, their relative intensity is shown as well.

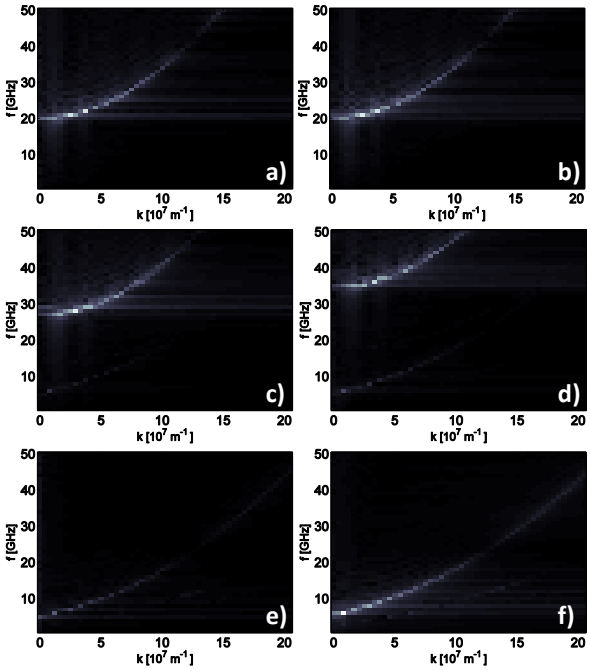

Fig. 2. Numerically calculated dispersion plots for a YIG-Py bilayer. a) Stand-alone YIG film. b) $A_{\text{interface}} = 0$ J/m c) $A_{\text{interface}} = 0.5 \cdot 10^{-12}$ J/m d) $A_{\text{interface}} = 1 \cdot 10^{-12}$ J/m e) $A_{\text{interface}} = 6 \cdot 10^{-12}$ J/m f) Single Permalloy film. The YIG mode shifts due to the interaction and an additional Permalloy mode appears for stronger couplings.

For small interaction strengths, the dispersion curve shifts to higher frequencies – qualitatively, this is a consequence of the higher effective exchange stiffness that the YIG layer experiences. A low-frequency node appears for higher coupling strengths, which is a propagating exchange wave in Permalloy – we verified this by running simulations for a stand-alone Permalloy layer under the same conditions as Figs. 2a-e was made and the $f(k)$ curve is almost identical to the low-

frequency mode of Figs. 2c-e. The Permalloy mode remains weak even for stronger coupling strengths and it appears that the damping of the YIG film is not significantly increased by the Permalloy film on top.

At a given excitation frequency, the wavelength shift caused by the Permalloy overlayer can be interpreted in such a way that the Permalloy overlay changes the effective index of refraction of the YIG film. In analogy to optical devices one may potentially design lenses [12], phase shifters and holograms for on-chip 'YIG optical devices'.

IV. Spin-wave injection structures

Exchange waves in YIG could be created by very small-size antennas [8] or nanoscale inhomogenities of a YIG film [27]. This is very challenging – and probably a primary reason behind the lack of studies concerning exchange waves in YIG. In ferromagnetic conductors, propagating exchange waves can be straightforwardly created by spin-torue oscillators [14]. It may be possible to use the exchange coupling mechanism between the YIG layer and the Permalloy to inject short-wavelength spin-waves into YIG. In order to study the feasibility of such a device, we performed simulations on a spin-torque structure, which is exchange-coupled to a YIG layer. A sketch of a highly idealized arrangement is shown in Fig. 3.

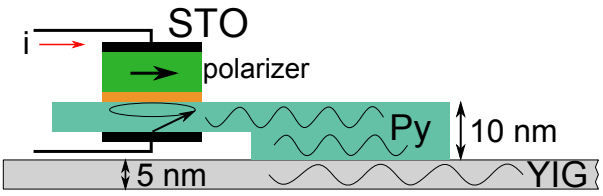

Fig. 3. Sketch of the proposed structure for spin wave injection to YIG. The spin waves generated in the Py layer couple into and propagate in the underlaying YIG film.

Magnetization oscillations are generated in the free layer of the STO and via a short protrusion, they arrive to the underlying YIG film. The simulations (in Fig 4) show that the spin waves couple into the YIG and propagate there.

We used an AC current to drive the STO, so the free layer frequency is injection locked to this frequency – this way one can arbitrarily define the phase, frequency and driving current of the STO. We neglected the Oersted field coming from the leads of the STO.

The above-shown models are based on an idealized geometry – but they show that it is in principle possible to inject spin waves from STO-based sources to YIG via coupling between the two films. The size of the spin-wave generating structure ($d < 100$ nm) matches the wavelength of exchange waves, which may allow high-efficiency spin-wave injection into a single propagating mode.

V. Magnonic crystals from bilayers

As an example for 'spin-wave optics' devices, we show how a magnonic crystal-like structure can be constructed from the proposed bilayers. Magnonic crystals are mostly made from

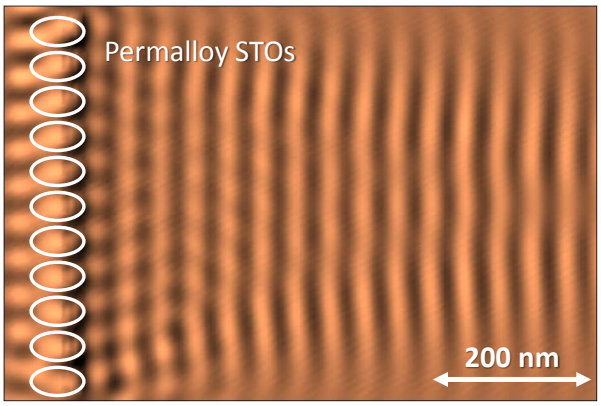

Fig. 4. Waves injected in a YIG film by a line of matching phase STOs. The STOs are phase-locked and generate a coherent waveform, which is coupled into the YIG layer.

metallic ferromagnets and are widely studied [28], but their usefulness is severely limited by the high damping of the metallic ferromagnet. Permalloy-YIG bilayer based devices may solve this problem.

The simulation example of Fig. 5 shows spin-wave propagation in a YIG film, with Permalloy stripes on top of it. The Permalloy stripes periodically modulate the index of refraction and act akin to a one-dimensional magnonic crystal. Depending on the spacing of the stripes and the wavelength, this periodic potential may reflect or transmit incoming spin waves. The magnonic crystal is defined without patterning the YIG film, circumventing technological challenges and increased damping from rough edges.

VI. Conclusion

We have shown proof of principle simulations for Permalloy-YIG bilayer devices. We argued that this device unites the benefits of metal-based magnetoelectronic components and low-damping YIG films and can have potential for spin-wave based signal processing devices.

There are a number of ongoing efforts aiming to incorporate YIG (or similar low damping materials) into spintronic devices – spin Hall effect (SHE) is one promising way to do that [23]. Our work shows a complementary approach, which does not require the use of new physics phenomena, rather, it relies on the integration of known spintronic devices with YIG.

Acknowledgment

The authors are grateful to George Bourianoff (Intel Corp, Austin, TX) and for Giovanni Carlotti (University of Perugia) for motivating discussions. This work was partially supported by the NSF/SRC grant 'Nanoelectronics Beyond 2020' and by a grant from Intel corporation.

References

[1] A. Papp, W. Porod, and G. Csaba, "Hybrid yttrium iron garnet-ferromagnet structures for spin-wave devices," *Journal of Applied Physics*, vol. 117, no. 17, p. 17E101, May 2015.

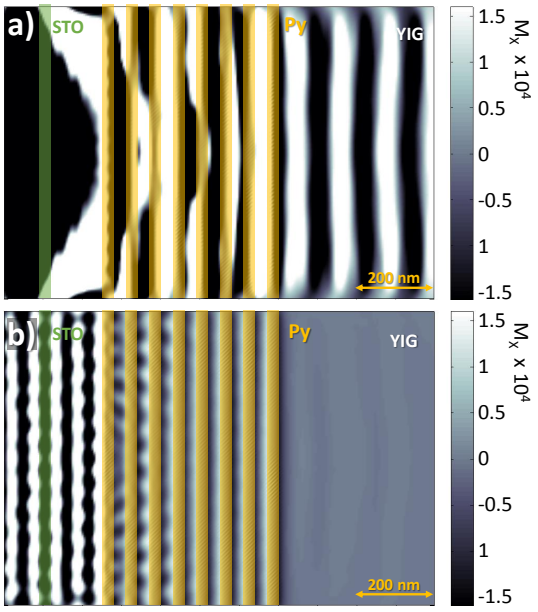

Fig. 5. One dimension crystal made out of Py on top of YIG film. a) f = 24 GHz b) f = 38 GHz. The position of the 30 nm spaced Permalloy stripes is denoted by the yellow lines. Different frequencies/wavelength may be completely transmitted or reflected by the crystal.

[2] S. Bader and S. Parkin, "Spintronics," *Annual Review of Condensed Matter Physics*, vol. 1, no. 1, pp. 71–88, Aug. 2010.

[3] A. Imre, "Majority Logic Gate for Magnetic Quantum-Dot Cellular Automata," *Science*, vol. 311, no. 5758, pp. 205–208, Jan. 2006.

[4] I. Eichwald, S. Breitkreutz, G. Ziemys, G. Csaba, W. Porod, and M. Becherer, "Majority logic gate for 3d magnetic computing," *Nanotechnology*, vol. 25, no. 33, p. 335202, Aug. 2014.

[5] A. Khitun and K. L. Wang, "Nano scale computational architectures with Spin Wave Bus," *Superlattices and Microstructures*, vol. 38, no. 3, pp. 184–200, Sep. 2005.

[6] G. Csaba, M. Pufall, D. E. Nikonov, G. I. Bourianoff, A. Horvath, T. Roska, and W. Porod, "Spin torque oscillator models for applications in associative memories." IEEE, Aug. 2012, pp. 1–2.

[7] G. Csaba and W. Porod, "Computational Study of Spin-Torque Oscillator Interactions for Non-Boolean Computing Applications," *IEEE Transactions on Magnetics*, vol. 49, no. 7, pp. 4447–4451, Jul. 2013.

[8] A. V. Chumak, A. A. Serga, and B. Hillebrands, "Magnon transistor for all-magnon data processing," *Nature Communications*, vol. 5, p. 4700, Aug. 2014.

[9] D. G. Feitelson, *Optical computing: a survey for computer scientists*. MIT Press, 1988.

[10] A. Khitun, "Magnonic holographic devices for special type data processing," *Journal of Applied Physics*, vol. 113, no. 16, p. 164503, 2013.

[11] F. Gertz, A. Kozhevnikov, Y. Filimonov, and A. Khitun, "Magnonic Holographic Memory," *IEEE Transactions on Magnetics*, pp. 1–1, 2014.

[12] G. Csaba, A. Papp, and W. Porod, "Spin-wave based realization of optical computing primitives," *Journal of Applied Physics*, vol. 115, no. 17, p. 17C741, May 2014.

[13] T. Schneider, A. A. Serga, B. Leven, B. Hillebrands, R. L. Stamps, and M. P. Kostylev, "Realization of spin-wave logic gates," *Applied Physics Letters*, vol. 92, no. 2, p. 022505, 2008.

[14] M. Madami, S. Bonetti, G. Consolo, S. Tacchi, G. Carlotti, G. Gubbiotti, F. B. Mancoff, M. A. Yar, and J. kerman, "Direct observation of a propagating spin wave induced by spin-transfer torque," *Nature Nanotechnology*, vol. 6, no. 10, pp. 635–638, Aug. 2011.

[15] A. Khitun, D. E. Nikonov, M. Bao, K. Galatsis, and K. L. Wang, "Efficiency of Spin-Wave Bus for Information Transmission," *IEEE Transactions on Electron Devices*, vol. 54, no. 12, pp. 3418–3421, 2007.

[16] A. A. Serga, A. V. Chumak, and B. Hillebrands, "YIG magnonics," *Journal of Physics D: Applied Physics*, vol. 43, no. 26, p. 264002, Jul. 2010.

[17] P. E. Zil'berman, A. G. Temiryazev, and M. P. Tikhomirova, "Short spin waves of exchange nature in ferrite films: excitation, propagation, and potential applications," *Physics-Uspekhi*, vol. 38, no. 10, pp. 1173–1177, Oct. 1995.

[18] A. G. Gurevich and G. A. Melkov, *Magnetization oscillations and waves*. CRC press, 1996.

[19] R. Suzuki, M. Takahashi, T. Kobayashi, and Y. Sugita, "Planar domains and domain wall structures of bubbles in Permalloycoated garnet films," *Applied Physics Letters*, vol. 26, no. 6, p. 342, 1975.

[20] J. Ben Youssef, V. Castel, N. Vukadinovic, and M. Labrune, "Spin-wave resonances in exchange-coupled Permalloy/garnet bilayers," *Journal of Applied Physics*, vol. 108, no. 6, p. 063909, 2010.

[21] N. Vukadinovic, J. Ben Youssef, V. Castel, and M. Labrune, "Magnetization dynamics in interlayer exchange-coupled in-plane/out-of-plane anisotropy bilayers," *Physical Review B*, vol. 79, no. 18, May 2009.

[22] M. J. Donahue and D. G. Porter, *OOMMF User's Guide, Version 1.2a3*. National Institute of Standards and Technology, Gaithersburg, MD, 1999, interagency Report NISTIR 6376. [Online]. Available: http://math.nist.gov/oommf/

[23] O. d'Allivy Kelly, A. Anane, R. Bernard, J. Ben Youssef, C. Hahn, A. H. Molpeceres, C. Carretero, E. Jacquet, C. Deranlot, P. Bortolotti, R. Lebourgeois, J.-C. Mage, G. de Loubens, O. Klein, V. Cros, and A. Fert, "Inverse spin Hall effect in nanometer-thick yttrium iron garnet/Pt system," *Applied Physics Letters*, vol. 103, no. 8, p. 082408, 2013.

[24] Y. S. Chun, "Interlayer perpendicular domain coupling between thin Fe films and garnet single-crystal underlayers," *Journal of Applied Physics*, vol. 95, no. 11, p. 6858, 2004.

[25] J. F. Cochran, B. Heinrich, and A. S. Arrott, "Ferromagnetic resonance in a system composed of a ferromagnetic substrate and an exchange-coupled thin ferromagnetic overlayer," *Physical Review B*, vol. 34, no. 11, pp. 7788–7801, Dec. 1986.

[26] S. Klingler, A. V. Chumak, T. Mewes, B. Khodadadi, C. Mewes, C. Dubs, O. Surzhenko, B. Hillebrands, and A. Conca, "Measurements of the exchange stiffness of YIG films using broadband ferromagnetic resonance techniques," *Journal of Physics D: Applied Physics*, vol. 48, no. 1, p. 015001, Jan. 2015.

[27] A. G. Temiryazev, M. P. Tikhomirova, and P. E. Zilberman, "Exchange spin waves in nonuniform yttrium iron garnet films," *Journal of Applied Physics*, vol. 76, no. 9, p. 5586, 1994.

[28] G. Gubbiotti, S. Tacchi, M. Madami, G. Carlotti, A. O. Adeyeye, and M. Kostylev, "Brillouin light scattering studies of planar metallic magnonic crystals," *Journal of Physics D: Applied Physics*, vol. 43, no. 26, p. 264003, Jul. 2010.

High efficiency two-photon glutamate uncaging by correction of spontaneous hydrolysis

Dénes PÁLFI
(Supervisor: Balázs RÓZSA)
Pázmány Péter Catholic University, Faculty of Information Technology and Bionics
50/a Práter street, 1083 Budapest, Hungary
palfi.denes@itk.ppke.hu

***Abstract*— Two-photon uncaging has been widely used to mimic fast synaptic release of different neurotransmitters; to rapidly and focally release different inhibitors or analogues; or to reproduce complex spatial and temporal patterns of ongoing neuronal activity. However, the currently available caged materials are just at the limit of their usability and have several drawbacks. For example, caged neurotransmitters with an increased rate of photochemical release also suffer from high spontaneous hydrolysis rates. Here, using quantum chemical modeling we show the mechanisms of hydrolysis and two-photon activation, and synthesized more effective caged compounds. Moreover, using a multidisciplinary approach we have developed a new enzymatic elimination method with a broad application range in one- and two-photon uncaging experiments. This removes neurotransmitters escaping from the caged materials during experiments. Therefore, the method allows the use of caged compounds with an increased rate of photochemical release. We demonstrate the efficiency of the method on novel caged glutamate compounds in neurophysiological experiments. One of these materials has more than 7.2 times higher photochemical release rate upon two-photon activation and has a smaller GABA-receptor blocking effect.**

***Keywords*- two-photon, uncaging, caged neurotransmitters, glutamate dehydrogenase, enzymatic elimination**

I. INTRODUCTION

Two-photon photochemical uncaging has revolutionized many areas of cell- and neurobiology because it allows rapid photochemical release of neurotransmitters in small volumes, thus it is capable of mimicking fast synaptic quantal release[1]. Glutamate is one of the major transmitters in the nervous system, and therefore several caged glutamate compounds have been developed[2,3]. They are generally used in neurophysiology experiments for investigating postsynaptic mechanisms and dendritic signal integration[4-6]. However, only 2(S)-2-amino-5-(4-methoxy-7-nitro-2,3-dihydro-indol-1-yl)-5-oxo-pentanoic acid (MNI-Glu) has been used widely in two-photon experiments. This is due to the strict constraints for an appropriate caged compound, including efficient uncaging with high chemical yield, fast two-photon induced release, low spontaneous hydrolysis rate, and low side effects of the caged compound on different receptors[2].

It is possible to release glutamate from MNI-Glu in a few locations using two-photon laser scanning; however, high-speed photochemical release of glutamate in multiple 3D locations would be required to reproduce fast physiological release during different synchronized brain activities (such as during sharp-waves or gamma oscillations). Novel 3D scanning technologies can provide the required spatially and temporally complex fast activation patterns[5-10], but the rate of photochemical release, and the toxicity induced by the required high laser intensity, are both limiting factors. Fast photochemical release necessitates not only a highly efficient two-photon absorption cross-section (σ) but also high quantum yield (Φ) in the photochemical reaction of the caged compound. Unfortunately, the relationship between the chemical structure and quantum yield or absorption cross-section has not been investigated yet. Furthermore, the required high Φ in the case of the vast majority of these compounds is accompanied by a more unstable chemical structure, rendering them more sensitive to spontaneous hydrolysis. Indeed, different levels of hydrolysis can be shown for most of the caged compounds at physiological pH and temperature values[11]: this can result, for example, in intensive precipitation of the caging compound, dendritic swelling, robust changes in electrophysiological properties, or toxicity[12]. For some caged materials, the presence of spontaneous hydrolysis is not so evident, but still the persistent release of neurotransmitters from the caged compounds can induce several 'side effects' on different receptors as the escaped neurotransmitters accumulate during the long measurement times characteristic of most physiological experiments. Here, we have shown that DNI-Glu•TFA, in combination with enzymatic hydrolysis correction, is a faster and more effective caged compound than MNI-Glu•TFA. A further important criterion of a good caged glutamate candidate is the reduced GABA receptor effect[13].

II. SYNTESIS OF FOUR CHEMICAL COMPOUNDS

In order to compensate for the spontaneous hydrolysis of materials with fast photochemical reactions, we aimed to understand the relationship between spontaneous hydrolysis, two-photon photochemical cross-section, two-photon spectrum, and chemical structure. Therefore, we synthesized four

D. PÁLFI, "High efficiency two-photon glutamate uncaging by correction of spontaneous hydrolysis" in *PhD Proceedings Annual Issues of the Doctoral School, Faculty of Information Technology and Bionics, Pázmány Péter Catholic University – 2015.* G. Prószéky, P. Szolgay Eds. Budapest: Pázmány University ePress, 2015, pp 153– 155.

chemical analogues of MNI-Glu and compared measured data with the predictions from the quantum chemical model.

The first compound, MNI-Glu trifluoroacetate (MNI-Glu•TFA), was prepared by a well-known method, but we isolated the TFA salt without using chromatography and with a higher yield than previously reported. Previously reported methods for the production of 2(S)-2-amino-5-(4-methoxy-5,7-dinitro-2,3-dihydro-indol-1-yl)-5-oxo-pentanoic acid claimed that this material is impractical for the day-to-day use because it's synthesis is inefficient, the material precipitates rapidly, it's quantum yield is not high enough, and two-photon uncaging of the solution of this material does not evoke any current from hippocampal neurons[14-16]. Therefore, for the production of 2(S)-2-amino-5-(4-methoxy-5,7-dinitro-2,3-dihydro-indol-1-yl)-5-oxo-pentanoic acid trifluoroacetate (DNI-Glu•TFA) we have developed a more efficient synthesis than the previously reported methods. One-step dinitration of 1H-Indole-1-pentanoic acid, α-[[(1,1-dimethylethoxy)carbonyl]amino]-2,3-dihydro-4-methoxy-δ-oxo-, 1,1-dimethylethyl ester in acetonitrile with nitronium tetrafluoroborate is possible, providing DNI-Glu•TFA with a better yield and higher purity, making it possible to yield DNI-Glu•TFA before it spontaneously hydrolyzes. Synthesis was also successful when glutamate was bound reversely to 7-nitro-indolene (MNI-Ulg•TFA) or 5,7-nitro-indolene (DNI-Ulg•TFA). The reaction mechanism of the release of the glutamate from MNI-Glu•TFA and from DNI-Glu•TFA has been investigated by first principle molecular quantum mechanics using the DALTON 2.0 quantum chemistry program. From the theoretical results we can expect that the photochemical cleavage leads to a several times faster, therefore more efficient or more productive, uncaging reaction for DNI derivates, which – together with the larger absorbance – results in a significant overall increase in quantum yield of the photochemical process. The photochemical pathways of MNI-Ulg•TFA and DNI-Ulg•TFA are almost identical and their energy values are also very close to their corresponding isomer pairs MNI-Glu•TFA and DNI-Glu•TFA, respectively. The proximity of the triplet and singlet surfaces may suppose a faster de-excitation in molecules where the glutamate was bound reversely (MNI-Ulg•TFA, DNI-Ulg•TFA) as compared to MNI-Glu•TFA and DNI-Glu•TFA, decreasing significantly the Φ value. The only drawback of DNI-Glu•TFA vs. MNI-Glu•TFA indicated by the quantum theory is the augmented ground state (non-photochemical) hydrolysis, which could expose aqueous tissue to an increasing glutamate concentration everywhere in the bath and sample. Therefore, we also used a second method to estimate the hydrolytic rate of DNI-Glu•TFA more accurately. The ratio of the hydrolytic rates of DNI-Glu•TFA vs. MNI-Glu•TFA can be estimated from the amidicity values (analogues to carbonylicity values) of MNI-Glu•TFA and DNI-Glu•TFA for their respective ground state. The amidicity values are 65.3% and 54.5% respectively, and this 10.8% difference in amidicity (ΔAM) corresponds to about a 29-fold increase in the rate constant of spontaneous hydrolysis.

III. Enzymatic Correction of spontaneous Hydrolysis

In order to avoid the numerous negative effects of spontaneous hydrolysis, and therefore allow the use of caged compounds with high Φ value, it was necessary to develop a selective method for glutamate elimination, which does not change the concentration of the caged compound and has no side effects on the tissue. Enzymes, being selective for their substrates and working in very low concentrations, seem an obvious choice. Two key processes are responsible for glutamate degradation, transamination and deamination. We chose glutamate dehydrogenase because its coenzyme, nicotinamide adenine dinucleotide phosphate ($NADP^+$) is not metabolized by brain tissue[17]. In order to determinate the required enzyme and coenzyme levels, we first estimated the spontaneous hydrolysis rate of DNI-Glu•TFA by measuring the free glutamate concentration through the OPA/MPA (ortho-phthaldialdehyde/3-mercaptopropionic acid) converted product with high-pressure liquid chromatography. The required elimination speed was estimated to be about 0.2 μM/min from these measurements. Next we used Michaelis-Menten kinetics to calculate the required v_{max} in order to keep the ambient glutamate concentration below 1 μM. As one unit is defined as the amount of the enzyme that catalyzes the conversion of 1 μM substrate per minute (at 25°C and at saturated coenzyme concentration), we added, in the first step, 200-520 units/l of glutamate dehydrogenase (corresponding to a 200-520 μM/min vmax rate) to the bath perfusion and applied $NADP^+$ in a saturating concentration (200 μM as the Km for $[NADP^+]$ is in the range of <0.1 μM for different variants of the enzyme and reactions. The enzymatic reaction effectively decreased glutamate concentration and however, the efficiency of the method decreased with longer measurement times. Most of the laboratories where uncaging experiments are performed freeze and reuse solutions of caged materials and therefore need good glutamate elimination even in a longer time window. Moreover, the unit activity of glutamate dehydrogenase is defined for the reverse direction (for 2-oxoglutarate to glutamate conversion), and the speed of the forward reaction is estimated to be more than one order of magnitude smaller; therefore, we repeated our measurements using a 10-fold higher unit activity (2000-5200 units/l). The higher enzyme concentration improved the efficiency of glutamate elimination. It is important to note that the rate of added glutamate elimination is approximately 6 orders of magnitude smaller than the rate of glutamate uptake in acute slices[18]; therefore, the enzymatic method cannot interfere with the glutamate uptake system in the small tissue volumes. In contrast, it effectively eliminates increased glutamate levels in the whole perfusion volume. As expected from the well-known specificity of enzymes, the enzymatic reaction was sufficiently selective because the enzyme did not decrease the concentration of the much larger caged compound. The stability of DNI-Glu•TFA in the presence of the enzymatic reaction was further validated in physiological measurements, since the amplitude of the uncaging-evoked responses did not change significantly during the experiments (**Fig. 1**). The use

of the enzymatic elimination method allows a more precise comparison of the overall photochemical yield of MNI-Glu•TFA, DNI-Glu•TFA, MNI-Ulg•TFA, and DNI-Ulg•TFA, because the modulatory effect of the elevated ambient glutamate concentration is eliminated. During this comparison we activated the same temporally and spatially clustered patterns of inputs in CA1 neurons, and compared the somatic membrane potential and dendritic Ca^{2+} responses induced in the presence of DNI-Glu•TFA, MNI-Ulg•TFA, and DNI-Ulg•TFA to the ones induced in the presence of MNI-Glu•TFA, because MNI-Glu properties are well-documented in the literature[1, 14]. The same laser intensity which induced only small EPSPs and small dendritic Ca^{2+} responses (1.43 ± 0.15 mV and 1.22 ± 0.11 ΔF/F, respectively) in the presence of MNI-Glu•TFA, elicited approximately 10-fold higher responses in the presence of DNI-Glu•TFA (15.22 ± 0.28 mV and 7.95 ± 0.25 ΔF/F, respectively). However, the dendritic and somatic membrane compartments can nonlinearly amplify high-amplitude EPSPs, therefore the overall photochemical yield cannot be determined at a single laser intensity. Thus we performed a series of uncaging measurements at increasing laser intensities; plotted the responses as a function of the second order of the laser intensity; and measured the increased photochemical yield as a relative x-axis shift of the responses in the presence of DNI-Glu•TFA and MNI-Glu•TFA by calculating the distance between the two point sets using unconstrained nonlinear optimization. The average distance between the two point sets revealed that the release of glutamate with the same rate from MNI-Glu•TFA requires 7.17 ± 0.84-fold higher two-photon excitation as compared to DNI-Glu•TFA ($p < 0.00001$, n= 10), which corresponds to an 7.17 ± 0.84 increase in two-photon photochemical yield (**Fig. 2**). This agrees well with the value predicted by quantum chemical modeling (10-fold increase). Next, we repeated these experiments by comparing the efficiency of the photochemical release of the reversely coupled compounds (MNI-Ulg•TFA and DNI-Ulg•TFA) relative to the release of MNI-Glu•TFA. Again, this agreed well with the quantum chemical modeling: uncaging responses were reduced to 51.07 ± 6.76 % ($p < 0.001$, n = 4) in the presence of MNI-Ulg•TFA and increased to 125.3 ± 4.1 % ($p = 0.003$, n = 3) for DNI-Ulg•TFA as compared to MNI-Glu•TFA. Our data showed that the efficiency of photochemical release calculated from the quantum chemical model and from the uncaging measurements correlated well for all of the four uncaging materials (R = 0.9877).

IV. Discussion

In summary, the enzymatic glutamate elimination shown here is a major addition to the uncaging toolbox available for scientists: it allows the use of new, or previously neglected and excluded caged compounds with fast photochemical reactions and high spontaneous hydrolysis rates by eliminating the undesired side-effects of glutamate molecules escaping from caged compounds. In general, this method can be used for eliminating the auto-hydrolysis effect of caged molecules by applying such a reagent (preferably an enzyme) which eliminates the formed but undesired amount of the spontaneously released compound.

References

[1] Matsuzaki, M. et al. Dendritic spine geometry is critical for AMPA receptor expression in hippocampal CA1 pyramidal neurons. Nat Neurosci 4, 1086-1092 (2001).

[2] Warther, D. et al. Two-photon uncaging: New prospects in neuroscience and cellular biology. Bioorganic and Medicinal Chemistry 18, 7753-7758 (2010).

[3] Kantevari, S., Matsuzaki, M., Kanemoto, Y., Kasai, H. & Ellis-Davies, G.C. Two-color, two-photon uncaging of glutamate and GABA. Nat Methods 7, 123-125 (2010).

[4] Losonczy, A., Makara, J.K. & Magee, J.C. Compartmentalized dendritic plasticity and input feature storage in neurons. Nature 452, 436-441 (2008).

[5] Katona, G. et al. Roller coaster scanning reveals spontaneous triggering of dendritic spikes in CA1 interneurons. Proceedings of the National Academy of Sciences of the United States of America 108, 2148-2153 (2011).

[6] Chiovini, B. et al. Dendritic spikes induce ripples in parvalbumin interneurons during hippocampal sharp waves. Neuron 82, 908-924 (2014).

[7] Fernandez-Alfonso, T. et al. Monitoring synaptic and neuronal activity in 3D with synthetic and genetic indicators using a compact acousto-optic lens two-photon microscope. J Neurosci Methods 222, 69-81 (2014).

[8] Quirin, S., Jackson, J., Peterka, D.S. & Yuste, R. Simultaneous imaging of neural activity in three dimensions. Front Neural Circuits 8, 29 (2014).

[9] Cotton, R.J., Froudarakis, E., Storer, P., Saggau, P. & Tolias, A.S. Three-dimensional mapping of microcircuit correlation structure. Front Neural Circuits 7, 151 (2013).

[10] Go, M.A. et al. Four-dimensional multi-site photolysis of caged neurotransmitters. Frontiers in cellular neuroscience 7, 231 (2013).

[11] Hagen, V. et al. {7-[Bis(carboxymethyl)amino]coumarin-4-yl}methoxycarbonyl derivatives for photorelease of carboxylic acids, alcohols/phenols, thioalcohols/thiophenols, and amines. Chemistry (Weinheim an der Bergstrasse, Germany) 14, 1621-1627 (2008).

[12] Pettit, D.L., Wang, S.S.H., Gee, K.R. & Augustine, G.J. Chemical two-photon uncaging: A novel approach to mapping glutamate receptors. Neuron 19, 465-471 (1997).

[13] Fino, E.A., R.;Peterka, D. S.;Salierno, M.;Etchenique, R. & Yuste, R. RuBi-Glutamate: two-photon and visible-light photoactivation of neurons and dendritic spines Frontiers in Neural Circuits 3 (2009).

[14] Fedoryak, O.D., Sul, J.Y., Haydon, P.G. & Ellis-Davies, G.C. Synthesis of a caged glutamate for efficient one- and two-photon photorelease on living cells. Chem Commun (Camb), 3664-3666 (2005).

[15] Papageorgiou, G., Ogden, D., Kelly, G. & Corrie, J.E. Synthetic and photochemical studies of substituted 1-acyl-7-nitroindolines. Photochem Photobiol Sci 4, 887-896 (2005).

[16] Graham, E.-D., Vol. WO 2008/094922 A1 (2008).

[17] Dávid, C. et al. Glia, Edn. 1. . (Akadémia Kiadó Zrt, Budapest; 2008).

[18] Dzubay, J.A. & Jahr, C.E. The concentration of synaptically released glutamate outside of the climbing fiber-Purkinje cell synaptic cleft. Journal of Neuroscience 19, 5265-5274 (1999).

Program 4

HUMAN LANGUAGE TECHNOLOGIES, ARTIFICIAL UNDERSTANDING, TELEPRESENCE, COMMUNICATION

Head: Gábor PRÓSZÉKY

Towards recognizing thematic roles for verbal frames by linking two independent language resources for a parser based on the supply and demand paradigm

Balázs INDIG
(Supervisor: Gábor PRÓSZÉKY)
Pázmány Péter Catholic University, Faculty of Information Technology and Bionics
50/a Práter street, 1083 Budapest, Hungary
indig.balazs@itk.ppke.hu

***Abstract*—Amongst the objectives of the MTA-PPKE Hungarian Natural Language Research Group is to develop a psycholinguistically motivated language processing system, which can process raw text and can build rich syntactic and semantic representation [1]. One of the key steps is to recognize and classify the verb-argument relations which is found in natural language sentences such as grammar roles and thematic roles.**
In this paper we introduce the ongoing research aiming to extend the verbal construction frame database of the MTA-PPKE parser. In our work we try to use and reuse more previously developed language resources if possible.

***Keywords*-grammar; parser; thematic-roles; language-resources**

I. Introduction

The main principle of the parser is parallelism. Many different "resource-thread" works by overriding and correcting each other. The inner-workings of these resource-threads are similar to the Categorical grammars [2]. The relations between language units are characterised by correspondence between "supplies" and "demands" of the so-called "structural-threads". In this paradigm the potential arguments in the sentence such as noun phrases form "offers", which is consist of lexical, morphological, and semantic properties, that can connect with one of the compatible "expectations" or "structural prediction"[1] of the corresponding argument frames of the verbs in the sentence [3].
In the next sections we first introduce the mechanisms of our parser that handle verbal argument frames and then we outline the the possibility of extending the argument frame database used in our parser with thematic role descriptions with the help of the VerbNET English language resource.

II. Parsing verbal argument frames

To support the parsing of verbal argument frames, we use the noun phrase and verbal argument rule database *MetaMorpho* Hungarian-English (and English-Hungarian) rule-based translation system [4] which is consists of context-free, feature-structure-based rewrite rules.
One portion of the rules has one thing in common. Every right-hand-side symbol contain lexical bounding. These rules characterises the lexicon, namely semantic and other properties of the noun, adjective and adverbial phrases which may span one or multiple words [5]. Examples can be seen in table I.

Noun phrase	Features
"házörző kutya" (watchdog)	noun, countable, animate
"tegnapelőtt" (the day before yesterday)	adverb of time
"hindi" (hindi)	noun/adjective, language

TABLE I
Examples of noun phrases, that span multiple tokens and their features. (Extracted from MetaMorpho)

The other class of the interesting cases of the MetaMorpho rules contains a lexical constraint for at least one, but not all right-hand-side symbol. While for the other constituents is bound only by means of word class, morphology and semantic constraints. These rules include the ones which are lexically bound at least at the verbal position. The argument positions can be bound only by idiomatic means. For examples see table II.

Verb pattern	Description
<somebody> jövendöl (foretell) <something><to somebody>	Only the verb is bound lexically
szó esik (talk) <about something>	There are auxiliary elements in an idiomatic construction

TABLE II
Examples of verb argument frame patterns. (Extracted from MetaMorpho)

Our parser reads the input strictly left-to-right, one token in each step. The appearance of every newly read token updates the graph that representing the relations of the already appeared tokens by ammending it. Ideally, arriving at the end of the sentence means that the representation contains the

[1] which may form pairs with offers

B. INDIG, "Towards recognizing thematic roles for verbal frames by linking two independent language resources for a parser based on the supply and demand paradigm" in *PhD Proceedings Annual Issues of the Doctoral School, Faculty of Information Technology and Bionics, Pázmány Péter Catholic University – 2015.* G. Prószéky, P. Szolgay Eds. Budapest: Pázmány University ePress, 2015, pp 159– 161.

correct parse.
Using the *Humor* morphological analyser tool [6] the parser annotates the tokens with their corresponding candidate tags and subsequently a special Part-of-Speech tagger that is similar to PurePOS [7], but only uses left-context ranks the candidates, which produces a local decision problem with probability scores without the Viterbi beam search. The N best candidates then used in parallel by the parsers main component [3] to rule out the best parse.
The identifying of the verb-argument relations during the processing of the sentence is based on the principle of *supply and demand*. At the appearance of the tokens belonging to a noun phrase we try to match new lexical rules or continue the ongoing rules which span multiple tokens by using their word class and morphological properties. If we fully recognize a possible noun phrase that span one or multiple token, we try to feed them to the empty argument frames of the verbs occurred in the sentence before. The appearance of a verbal token entails the loading of all the possible argument frames, that belongs to the verb, and the parser immediately tries to fill argument positions with the already appeared and fully recognized noun phrases.

III. Identifying Thematic roles

Additionally, beyond the recognition of verb-argument relations, the argument frames are suitable for characterizing the verb-argument relations as well[2]. The thematic role descriptions, which needed for characterizing semantic representation are only available only in the 10% of the verbal argument frame database of MeatMorpho. These are made for an independent project that were using MetaMorpho to support inspection of narrative psychological structures in historical texts [8].
However, the verbal argument frame rules have an important feature: they have two sides, Hungarian and English, and they contain the English equivalent for the Hungarian side: For every source language side (Hungarian) parser rule exists a corresponding destination side (English) generator rule, which is the translation of the given verb argument construction.
So it is possible to use freely available English language resources to complete first the English side of the rules, then transform the changes back to the Hungarian side using their property that there are in pairs. Thus connecting the rule pairs of MetaMorpho with the external resource by the correct mapping of rules. Hence creating a linked resource.
A similar resource is for example is the *Unified VerbIndex (VerbNet)*, that is the product of the *SemLink project* [9]. The VerbNet is a verb dictionary that is linked with *ProbBank* a syntactically and semantically annotated corpus and with the FrameNet semantic frame database. In this resource the English verb argument frames and their syntactic and semantic informations are gathered in good quality.
Our goal is to link the rules of MetaMorpho to this unified resource and to automatically complete the English verb argument frames of MetaMorpho with thematic roles as much as possible. After this, we translate the gained information to the Hungarian side of the Verbal argument frame rules of MetaMorpho.
It is important for this task to be as precise as possible, to ease the later manual correction to not worsen the quality of MetaMorpho as it is made purely by humans without machine help.
In the next section we describe the initial practical problems of linking MeatMorpho and VerbNet together and transferring the thematic role descriptions of VerbNet into MeatMorpho by an automatic approach.

IV. Mapping the verbal argument frames of MeatMorpho with VerbNet

During the implementation it must be taken into account, that the resources differ in many way and we must *unify* these differences to harmonize the resources. Both resources might contain errors, that might have negative influence on finding of parallel frames.
The creators of MetaMorpho were only loosely restricted by rules or conventions. Partly they worked on their own way, therefore there are no written documentation on the principles of development. During our observations, in the rule database of MetaMorpho we have found numerous typographical mistake and other errors which are due to human mistakes. Some part of these errors of course can be corrected automatically by spell checker, but the initial tests shows that these errors are often from rare words, that is unknown to the spell checker.
An other significant problem, that makes difficult to harmonize the two resources is the question of American and British English spelling. While MetaMorpho was originally intently developed for the British orthography[3], on the contrary VerbNet was made for the American English spelling.
In VerbNet in contrary to the flat list structure of MetaMorpho the verbs are grouped in classes by the similarity of their frames and each class may contain multiple frame, that corresponds to all the verbs in the class. There are even a class hierarchy, so classes may have subclasses and subclasses inherits properties from the higher classes and may specify them further. See detailed statistics in table III.

Description	Number of verbs
Verbs in VerbNet	6343
Has no frames, only mentioned in other resources	2057
Has frames, possible to link	4286
Verbs occurs in only one class	2957

TABLE III
THE CLASSIFICATION OF VERBS THAT OCCUR IN VERBNET BY THEIR DISTRIBUTION

There are multi-part or phrasal verbs, which are handled differently in the aforementioned resources. In VerbNet

[2]This includes syntactic and semantic relations too, but in this paper we focus on thematic roles

[3]Even though there are some occurrence of both spelling of the same verb in different rules, due to inconsistency.

words are connected with underscore ("_") symbol, but in MetaMorpho words are connected with space and are between apostrophes. We wanted to check how many phrasal verb is in English, so we used one of the most throughout resources available, the Princeton WordNet [10]. Details can be found in table IV.

Description	No. of verbs
Number of verbs in WordNet	7440
Number of phrasal verbs in WordNet	1410
Number of phrasal verbs in VerbNet	404
Number of verb stems, from phrasal verbs in VerbNet	223

TABLE IV
THE CLASSIFICATION OF PHRASAL VERBS THAT OCCUR IN WORDNET AND VERBNET

There are about 1 to 10 ratio between the number of rules and unique verbs in MetaMorpho as seen in table V. This is due to the idiomatic or other restrictions, which each makes separate rules for the verbs. This phenomena affects little more than the third of the rules. On the other hand, during the development of MetaMorpho it was not a goal to achieve good recall on the English side of the verbs. It was enough to keep the recall high on the Hungarian side and optimize the rules for precision. We must note, that this phenomena may cause problems later.

Description	No. of verbs
Number of verb argument frame rules	30 292
Number of unique English verb stems	3505
Number of verb stems, that are not exist in VerbNet	920
Is treated misspelled or unknown by the spell checker	143
(English) Idiomatic or other restriction in rules	10694
(Hungarian) Idiomatic or other restriction in rules	8347

TABLE V
THE CLASSIFICATION OF VERBS IN METAMORPHO

According to our experiments, the 42% of the verbs of the rules of MetaMorpho is listed in multiple classes of VerbIndex, so not just the frames, but the classes is also must be disambiguated.

V. RESULTS

The most simple subset of MetaMorpho rules can be characterized by the SUBJ V [OBJ] pattern. This means about 20 000 rules. Even without using the ontologies, we could produce 1658 unambiguous and 2908 ambiguous linking, by only checking for the corresponding verbs.
However, we see great room for improvement as the ambiguous links, as far we can see, can be disambiguated using the ontologies.

VI. FUTURE WORK

We divided features from VerbNet into three groups, the prepositions, the syntactic and the semantic restraints. The latter two needed to be harmonized between the resources. In MetaMorpho, all the restraints are stored in a homogeneous flat list, that makes nearly impossible to disambiguate the different types of restraints. In VerbNet, the COMLEX [11] formalism is used[4] and the three types of constraints are stored separately, making it fairly easy to store them in different ontologies.
The harmonizing task required to set up two ontologies, that contain the logical relations between the two featureset. For example: *Human* is a subset of *Animate*.
The logic reasoning task was made by the Racer reasoner engine [12]. The ontologies will be built manually.

VII. CONCLUSION

In this paper, we introduced the verb argument handling module of our parser, that is based on the supply and demand paradigm and examined the possibility of automatic transferring of thematic roles from one language resource to another, namely from VerbNet to MetaMorpho by linking them. We described our initial steps to find links between the described verbs, and also outlined our vision of the further development to fulfill the task of automatic linking of these resources.

ACKNOWLEDGMENT

I would like to gratefully and sincerely thank to my supervisor for his guidance, understanding, patience, and my colleges for their valuable help.

REFERENCES

[1] B. Indig, "Towards a psycholinguistically motivated performance-based parsing model," in *Proceedings of PPKE-ITK Doctoral School 2014.*
[2] G. Morrill, *Categorial grammar: Logical syntax, semantics, and processing*. Oxford University Press, 2010.
[3] B. Sass, "Egy kereslet-kínálat elvű elemző működése és a koordináció kezelésének módszere." in *Tanács Attila, Vincze Veronika (szerk.) XI. Magyar Számítógépes Nyelvészeti Konferencia, Szeged, 2015.*
[4] G. Prószéky and L. Tihanyi, "Metamorpho: A pattern-based machine translation system," in *Proceedings of the 24th'Translating and the Computer'Conference*, 2002, pp. 19–24.
[5] K. Orosz, "Főnevek szemantikai jegyei s kódolásuk a metamorpho projektben." in *Tanács Attila, Vincze Veronika (szerk.) I. Magyar Számítógépes Nyelvészeti Konferencia, Szeged, 2006.*
[6] G. Prószéky and A. Novák, "Computational morphologies for small uralic languages," *Inquiries into Words, Constraints and Contexts Festschrift in the Honour of Kimmo Koskenniemi on his 60th Birthday*, pp. 116–125, 2005.
[7] G. Orosz and A. Novák, "Purepos 2.0: a hybrid tool for morphological disambiguation." in *Proceedings of Recent Advances in Natural Language Processing, Hissar, Bulgaria, 7-13 September 2013.*
[8] O. Vincze, K. Gábor, B. Ehmann, and J. László, "Technológiai fejlesztsek a nooj pszichológiai alkalmazásában," in *Tanács Attila, Vincze Veronika (szerk.) I. Magyar Számítógépes Nyelvészeti Konferencia, Szeged, 2006.*
[9] E. Loper, S.-T. Yi, and M. Palmer, "Combining lexical resources: mapping between propbank and verbnet," in *Proceedings of the 7th International Workshop on Computational Linguistics, Tilburg, the Netherlands*, 2007.
[10] C. Fellbaum, *WordNet*. Wiley Online Library, 1998.
[11] R. Grishman, C. Macleod, and A. Meyers, "Comlex syntax: Building a computational lexicon," in *Proceedings of the 15th conference on Computational linguistics-Volume 1*. Association for Computational Linguistics, 1994, pp. 268–272.
[12] V. Haarslev, K. Hidde, R. Möller, and M. Wessel, "The racerpro knowledge representation and reasoning system," *Semantic Web Journal*, vol. 3, no. 3, pp. 267–277, 2012.

[4] in conjunction with WordNet categories

Content independent playlist generation

Mátyás JANI
(Supervisor: György TAKÁCS, Gergely LUKÁCS)
Pázmány Péter Catholic University, Faculty of Information Technology and Bionics
50/a Práter street, 1083 Budapest, Hungary
jani.matyas@itk.ppke.hu

***Abstract*—Several playlist generation methods were proposed in the past decade. Most of these are based on features of the playlist elements, such as different kind of audio features and meta-data. These methods were developed primarily for the purpose of generating playlists containing exclusively music pieces. Our target goal – an on-line audio social media platform – requires playlists containing both speech programs and music pieces.**

Disregarding the content specific information it becomes possible to handle speech and music programs uniformly. The remaining data is the interaction between users (listeners or playlists) and items (tracks).

A novel graph based method relying only on the user-item interaction is proposed in the study. The preliminary results show that our method performs better than the other tested content independent methods, and that it performs only slightly worse than a baseline method incorporating artist meta-data information.

***Keywords*-playlist generation; recommender systems; collaborative filtering;**

I. Introduction

Music discovery shifted towards stream services as these platforms become popular, which brought the need for personalized music recommendation, and automatic playlist generation for large number of listeners and contents. The final goal of our project is a small community audio social media platform, similarly to a personalized radio, with speech programs (podcasts, news, interviews, etc.) and musical pieces. The literature concerning playlist generation deals almost exclusively with playlists of musical pieces. Only limited studies [1], [2] are available on mixed music and speech playlist generation.

Including different types of content makes the recommendation task more complicated. Content based recommender systems rely on features extracted from the content. In the case of homogeneous data, these features can be compared to each other directly, but different content types might require different features, and comparing them is not so straightforward. One solution is to use methods which does not rely on content based features, only on user-item interactions.

This study focuses on content independent approaches of playlist generation. These so-called collaborative filtering approaches can provide very good results, sometimes even better than pure content based methods [3]. The content independence has the benefit of handling mixed content types uniformly, but it is not clear if speech and music programs should be really treated uniformly. We believe that the best results can be achieved only with both content independent and content dependent information, mostly because of the cold-start problem and the sparsity of the user-item interaction data.

The user information is disregarded in our experiments, so each playlist is treated as coming from a different user, similarly to [4]. As there are no user generated mixed speech and music playlists available, playlists containing only music were involved in our tests.

II. Playlist Evaluation

Different playlist generating methods can be compared by A-B tests involving human listeners. While these tests provide valuable subjective results, they are time-consuming and costly.

Objective metrics based on music meta-data, including *tag-diversity*, *coherence* can be found in the dissertation of Ben Fields [5]. In [6] artist name, genre tags and album meta-data are used to evaluate the author's playlist generation method. The problem with these metrics are that they measure only a related attribute of the playlists, not their general fitness.

Existing playlists can be obtained from on-line services. The obtained playlists can be split into training and test set. If the playlist generator methods produce probability-like scores, it is possible to compare their *Average Log-likelihood* score on the test set, as in [3], [7], [8].

In this study the methods are compared to each other using the *Hit Rate* measure. Test playlists without the last track are fed to a playlist generator trained on the $Train$ set. The playlist generator has to return the recommendation list for the last track: a set of suspected relevant songs. The hit rate is the ratio of the test playlists where the real last song is on the recommendation list. The hit rate can be computed for different sizes of recommendation lists, it increases monotonically by the size of the list. This measure was introduced in [9]. The formula for calculating the hit rate as defined by [4]:

$$HitRate(Train, Test, n) = \frac{1}{\|Test\|} \sum_{(h,t)\in Test} \delta_{t,R_{Train}(h,n)} \tag{1}$$

where h is the test playlist without the last song ("history"), t is the real last track on the playlist, $\delta_{t,R_{Train}(h,n)} = 1$ if t is on the recommendation list $R_{Train}(h,n)$ with size n, otherwise it is 0.

M. JANI, "Content independent playlist generation" in *PhD Proceedings Annual Issues of the Doctoral School, Faculty of Information Technology and Bionics, Pázmány Péter Catholic University – 2015.* G. Prószéky, P. Szolgay Eds. Budapest: Pázmány University ePress, 2015, pp 163–166.

III. Playlist Generation Methods

A. Content Independent Methods

Popularity Ranking approach discards all information about the current playlist when recommending the next song. It calculates the probabilities of the songs for the next track from the global popularity of the songs. The popularity is estimated using the play count in the training set. When creating a playlist of size n the first n songs with the highest play counts are selected.

Latent Dirichlet Allocation (LDA) is a method for discovering hidden topics in documents [10]. In the context of playlist generation the model is applied on the tags of the songs by [5], [9]. In this study it is applied as a content independent method: the tracks are considered as words and the playlists as documents.

Taking the playlists as users and tracks as items any kind of collaborative filtering approach can be considered. The *nearest neighbour (kNN)* method in our context – as in [4] – searches for similar playlists, not similar songs. The playlist similarity is based on the binary cosine similarity of the playlists, considering the tracks on them. *Matrix factorization* based collaborative filtering approaches are not included in our tests, as several papers reported inferior performance of these methods for playlist generation and music recommendation [9], [11].

Frequent pattern based methods like association rules and sequential patterns were considered for generating playlists in [4], [8]. The results show that these methods preform well among the collaborative filtering approaches (regarding hit rate). They are not included in our tests, but due to their good performance these should be included in the future.

Similarly to LDA, language modelling approaches (e.g. *n-grams*) can be employed considering the playlists as sentences and the tracks as words. It must be noted that there are several differences between text corpora and playlists [7] which might affect the performance of these methods.

A related space-embedding *Markov-model* based approach for playlist generation is compared to smoothed *bi-gram* models in [7], and superior performance is reported. This space-embedding model is excluded from our tests due to the reported bad performance compared to other playlist generation methods and slow training time [4].

B. Methods Based on Artist Meta-data

Same Artist – Greatest Hits (SAGH) was proposed as a personalized music recommender in [11], and is also included in the tests of [4]. The method recommends the popular songs of artists that the given user listened to previously. In our experiments the user information is disregarded, only the artists in the playlist history h are considered.

A new baseline method, *Collocated Artist – Greatest Hits (CAGH)* was introduced in [4]. The similarity between a pair of artists is based on the frequencies of their co-occurances on playlists normalized by their individual frequencies. This similarity measure along with song popularity is used to recommend songs.

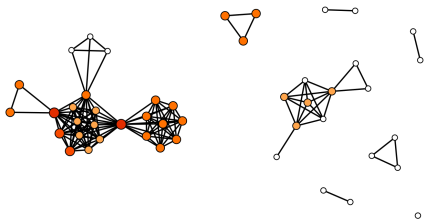

Fig. 1. Track co-occurance graph – the vertex sizes and colors change with play count, the playlists are cliques of the graph

There are methods using other types of meta-data and audio content, but those are not included in the experiments.

C. Proposed Method: Co-occurrence Graph (COG)

The idea is to build a weighted graph based on track co-occurrences on playlists. Each song in the $Train$ set is a vertex and songs on the same playlist in the $Train$ set are connected with edges (see Fig. 1). Similar songs can be defined as songs with small distance between their vertices in the graph. The weight of the edge between song a and b is expressed as:

$$\text{weight}(a,b) = 1 - \frac{\sum_p (\delta_{a,p} \cdot \delta_{b,p})}{\sqrt{\sum_p \delta_{a,p} \cdot \sum_p \delta_{b,p}}} \tag{2}$$

with $\delta_{a,p} = 1$ if song a is on playlist p, otherwise it is 0. The score function can be defined as:

$$\text{score}_{\text{COG}}(t,h) = \max_{\substack{x \in T \\ (a,b) \in P(h,x)}} \sum \text{weight}(a,b) - \sum_{(a,b) \in P(h,t)} \text{weight}(a,b) \tag{3}$$

where $P(h,x)$ is the shortest path (set of edges) between tracks on playlist history h and song x, T is the set of songs in the $Train$ set, t is the real last track on the playlist. The role of the distance of the longest path from h is to avoid negative scores. This score function was established only for ranking purposes, a different score function might be preferred for calculating probabilities.

Calculating the distance between h and t (and also between h and all the other x songs) is computationally intensive. However, for selecting a next song the recommendation list does not have to contain all of the songs. Usually it is enough to find the closest couple of hundred songs, and pick one randomly with probabilities obtained from the scores. If we bound the number of vertices to visit, this algorithm can be even more efficient than CAGH or kNN.

In our implementation the search is bounded by the number of discovered nodes. Dijkstra's search algorithm is used from multiple starting nodes (h), and when the number of discovered nodes is equal to the pre-defined threshold, the search is terminated. The first k discovered nodes are not necessarily the same as the closest k nodes.

TABLE I
PROPERTIES OF THE DATASETS

	Development	Test
Plays	364818	573017
Playlists	86850	128595
Tracks	37352	100928
Avg. tracks/playlist	4.20	4.46
Avg. track usage count	9.77	5.68
Artists	5142	13428
Avg. artists/playlist	2.10	2.07
Avg. artist usage count	70.95	42.67

IV. DATASET

Playlist data fetched from *last.fm*[1] by Òscar Celma [12] was used in the experiments. This dataset consists of the total listening history of approximately 1000 last.fm users up till May 5 2009. The dataset contain the track name, artist name, user id and the timestamp for each playback. For tracks and artists available in the *musicbrainz*[2] database their corresponding musicbrainz ids were also included in the dataset.

The following pre-processing steps were performed to prepare the dataset for playlist generation evaluation:

1) songs without musicbrainz id and artist ids were excluded, the durations of the remaining songs were retrieved from the musicbrainz database
2) if the timestamp + duration was within 1 minute of the next track's timestamp, the track and the next track were considered as being on the same playlist
3) the playlists received a unique identifier, playlists with only one track were removed
4) playlists with playlist id $<$ 250000 were added to the development set (containing playlists from users 1...31)
5) playlists with 250000 $\leq$ playlist id $<$ 500000 were added to the evaluation set (containing playlists from users 31...84, without overlapping with the development set)
6) the development set was further filtered by iteratively removing playlists containing songs which only appeared once in the set (three iterations were run, no such filtering step was performed on the test set)
7) the development and evaluation sets were divided to train/test subsets by 0.632 boosting

The properties of the final datasets are concluded in Table I.

V. PRELIMINARY RESULTS

The models were trained on the train parts of the given dataset, and the hit rate curves were calculated on the test parts. The limits for the size of the recommendation lists (the limits of the x axes) are set to contain approximately 1.5% of the tracks in the datasets, to get in line with other studies [9], [4].

[1]http://www.last.fm/
[2]https://musicbrainz.org/

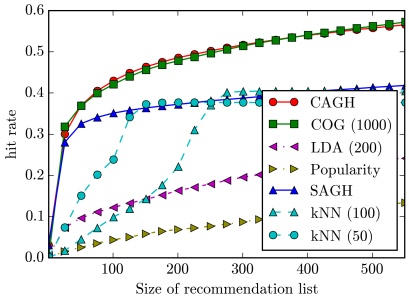

Fig. 2. Hit rate curve on the filtered development set

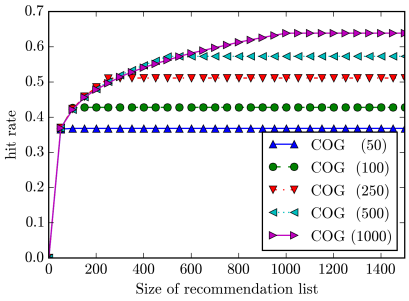

Fig. 3. Effect of the bound parameter

The algorithms were tested on the development set first. The results can be observed in Fig. 2. The worst performing methods, Popularity and LDA with 200 latent topics, are excluded from later tests. The kNN methods with k = 50 and 100 neighbours have different characteristics than the rest of the methods. The left sides of their curves are concave, and they reach their maximum hit rates at lower recommendation list sizes. COG with the bound threshold set to 1000 is clearly better than kNN and SAGH methods, and has a very close performance to CAGH.

The COG method's maximum hit rate is limited by the bound parameter. In our implementation the bound parameter had a direct impact on the size of the recommendation list, as it was equal to the number of tracks discovered during the graph search. The effect of this parameter can be observed in Figure 3.

The results on the test set are similar to the development set (Fig. 4.). The only exception is that CAGH clearly outperforms COG on this dataset.

VI. COMPUTATIONAL COMPLEXITY CONSIDERATIONS

The complexity is not a single property, as the time for fitting and updating the model, the time for making recommendations for a next track, and storage sizes are all different aspects. In this part we only investigate the recommendation

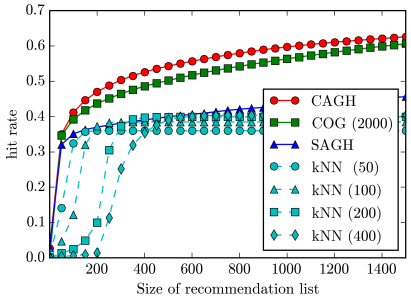

Fig. 4. Hit rate curve on the test set

and the model update times.

The time complexity of making a recommendation in the case of the nearest neighbour, SAGH and CAGH methods was investigated in the appendix of [8]. Their reported results are: $O(|P| \cdot (|h| + M) + k \cdot |T|)$ for kNN, $O(|h|)$ for SAGH (with only the greatest hits stored for each artist) and $O(|h| \cdot |A| \cdot |T|)$ for CAGH, where $|P|$ is the number of playlists in the training set, $|h|$ is the number of tracks on the playlist history for which a next track is recommended, M is the maximum size of the playlists, k is the number of neighbours considered for kNN, $|T|$ is the number of tracks in the training set and $|A|$ is the number of artists.

The recommendation time complexity of the COG method depends on the type of bound. In our implementation we limit the number of discovered tracks (vertices). This means that the complexity depends on the number of out edges from the vertices which are found before reaching the bound. The worst case scenario is a complete subgraph, with number of edges propotional to the square of the number of vertices. If we denote the bound threshold by B the overall complexity including the queue complexity of Dijkstra's search is $O(B^2 \cdot \log B)$, which is independent from the number of tracks. The average complexity will be lower because of the sparseness of the problem.

The model update complexity of kNN is constant, it is just adding the playlist to the set of training playlists. In the case of SAGH there is an extra cost of updating the play counts for the tracks of the artists, which is proportional to the number of tracks on the update playlist. The artist similarity has to be updated for CAGH. Only artists on the update playlist are affected, if the number of artists on the update playlist is $|A_{update}|$, then the complexity is $O(|A_{update}|^2)$. The update process for COG involves the creation of new edges or increasing the edge counts between tracks on the update playlist, if the weights are calculated at search time. If the number of tracks on the update playlist is $|T_{update}|$ then the complexity is $O(|T_{update}|^2)$. In the case of offline weight calculation, all the edges of the updated vertices have to be updated as well. In general $|A_{update}| \leq |T_{update}|$, so the update complexity of COG is the highest among these methods, but it is still in the magnitude of the update complexity of CAGH.

VII. Conclusion

The results show that the COG method introduced in this paper has very promising properties. It is a content independent method for playlist generation with comparable, but slightly lower performance than the best performing (content based) method, CAGH. COG's computational complexity is also comparable to CAGH, and it can be limited easily by a single parameter.

There are, however, some concerns with COG. If the graph is disconnected (has more than one components), then starting from one component songs from only that component will be returned. This problem can be solved by introducing a smoothing factor for randomly jumping to any song by a given low probability. The effect of the bound parameter on the quality of the resulting playlist is not clear. This should be investigated by using other evaluation methods (like avg. log-likelihood), and by involving other datasets. It might be interesting to try and compare different bound conditions and different edge weight functions.

References

[1] M. Jani, G. Lukács, and G. Takács, "Experimental Investigation of Transitions for Mixed Speech and Music Playlist Generation," in *Proceedings of ACM International Conference on Multimedia Retrieval*. Glasgow, United Kingdom: ACM, 2014, pp. 392–398.

[2] I. Benyeda, M. Jani, and G. Lukács, "Beszéd-zene lejátszási listák nyelvtechnológiai vonatkozása," in *Proc. of XI. Magyar Számítógépes Nyelvészeti Konferencia, MSZNY 2015*, Szeged, Hungary, 2015, pp. 257–268.

[3] B. Mcfee and G. Lanckriet, "The Natural Language of Playlists," in *Proceedings of the 12th International Society for Music Information Retrieval Conference*, Miami (Florida), USA, Oct. 2011, pp. 537–541, http://ismir2011.ismir.net/papers/PS4-11.pdf.

[4] G. Bonnin and D. Jannach, "A comparison of playlist generation strategies for music recommendation and a new baseline scheme," in *Workshops at the Twenty-Seventh AAAI Conference on Artificial Intelligence*, 2013.

[5] B. Fields, "Contextualize Your Listening: The Playlist as Recommendation Engine," Ph.D. dissertation, Goldsmiths University of London, London, 2011.

[6] B. Logan, "Content-Based Playlist Generation: Exploratory Experiments," in *ISMIR 2002, 3rd International Conference on Music Information Retrieval, Paris, France, October 13-17, 2002, Proceedings*, 2002, pp. 295–296.

[7] S. Chen, J. L. Moore, D. Turnbull, and T. Joachims, "Playlist Prediction via Metric Embedding," in *Proceedings of the 18th ACM SIGKDD International Conference on Knowledge Discovery and Data Mining*, ser. KDD '12. New York, NY, USA: ACM, 2012, pp. 714–722.

[8] G. Bonnin and D. Jannach, "Automated Generation of Music Playlists: Survey and Experiments," *ACM Comput. Surv.*, vol. 47, no. 2, pp. 26:1–26:35, Nov. 2014.

[9] N. Hariri, B. Mobasher, and R. Burke, "Context-aware Music Recommendation Based on Latent Topic Sequential Patterns," in *Proceedings of the Sixth ACM Conference on Recommender Systems*, ser. RecSys '12. New York, NY, USA: ACM, 2012, pp. 131–138.

[10] D. M. Blei, A. Y. Ng, and M. I. Jordan, "Latent dirichlet allocation," *the Journal of machine Learning research*, vol. 3, pp. 993–1022, 2003.

[11] B. McFee, T. Bertin-Mahieux, D. P. W. Ellis, and G. Lanckriet, "The million song dataset challenge," in *Proc. of the 4th International Workshop on Advances in Music Information Research*, ser. AdMIRe, Apr. 2012.

[12] O. Celma, "Music recommendation," in *Music Recommendation and Discovery*. Berlin, Heidelberg: Springer Berlin Heidelberg, 2010, pp. 43–86.

Defining the optimal feature set for quality estimation task for the output of English-Hungarian machine translation systems

Zijian Győző YANG
(Supervisor: Gábor PRÓSZÉKY)
Pázmány Péter Catholic University, Faculty of Information Technology and Bionics
50/a Práter street, 1083 Budapest, Hungary
yang.zijian.gyozo@itk.ppke.hu

***Abstract*—Nowadays, as machine translation systems has become popular, the quality estimation for machine translation systems has become an important task. The automatic evaluation methods for machine translation use reference translations. To create reference translations we need human translators, which are very expensive and time-consuming. These automatic evaluation methods are not real-time and for English-Hungarian the correlation between the results of these methods and that of human evaluation is very low. The other kind of evaluation approach is called quality estimation. These methods address the task by estimating the quality of translations as a prediction task. In this task different language specific and language independent features are extracted from the source and translated texts. Then, using these features the quality estimation model is built with machine learning algorithms. This approach has not been used for evaluating English to Hungarian translations before. Between English and Hungarian, there are significant differences in morphology, syntax and word order or number. Therefore we need to optimize the quality estimation tools and models to Hungarian. In this study, different quality estimation models are built. For building the models automatic metrics and human judgments are used. We performed the experiments on more corpora. We research the optimal feature-set of the model, which is trained on human scores, for English-Hungarian. We created a feature selection method, which achieved better results than using all features and using the baseline features.**

***Keywords*-quality estimation; machine translation; machine learning**

I. Introduction

In the machine translation task, the quality measurement of the translation output has become inevitable part of it. Knowing the quality scores of machine translated segments can solve a lot of problems. A quality indicator can help human annotators in their post-edit tasks, or help machine translation systems to find and combine the best translations. This indicators also can filter out and inform about unreliable translations. Thus, a reliable evaluation model can save a lot of time and money for people and companies. The automatic evaluation methods cannot perform this task well enough, because these need reference translations. It means that after the automatic translation, we also have to create a human translated sentence to compare it to the machine translated output. Creating human translations is very expensive and slow process, which means that the evaluation is not real-time.

The task of quality estimation (QE) tries to solve these problems. Using quality estimation we can save considerable time and money for human annotators, researchers and companies. This new approach does not use reference translations and it can evaluate in real-time. In this study, we train and apply QE models for Hungarian. We also developed a feature selection method, which gained better result than the all features we used for English-Hungarian and then the baseline feature-set.

Hungarian is an agglutinating and compounding language. Between English and Hungarian, there are significant differences in morphology, syntax and word order or number. Furthermore, the free order of grammatical constituents, and different word orders in NPs and PPs are also characteristics of Hungarian. Thus, features used in a QE task for English-Spanish or English-German, which produced good results, perform much worse for English-Hungarian.

The structure of this paper is as follows: First we will shortly introduce automatic machine translation evaluation methods and their problems. Then, we will present the quality estimation methods an our experiments in the task of QE. Thereafter we describe the optimalization of these QE models. Last, we will show our results and future work.

II. Related Work

There are two kinds of evaluation methods for machine translation. The first type uses reference translations, i.e. it compares machine translated sentences to human translated reference sentences, and measures the similarities or differences between them. Commonly used methods with reference translation include BLEU [1], and other methods based on BLEU or TER [2].

The BLEU method (BiLingual Evaluation Understudy) computes weighted n-gram matches for sentences. The advantages of BLEU are that it is fast and cheap, if we already have a set of reference translations. The TER (Translation Error Rate) method computes error rate between human translated sentences and machine translated sentences. This method counts the number of corrections that has to be done on the

Z. YANG, "Defining the optimal feature set for quality estimation task for the output of English-Hungarian machine translation systems" in *PhD Proceedings Annual Issues of the Doctoral School, Faculty of Information Technology and Bionics, Pázmány Péter Catholic University – 2015.* G. Prószéky, P. Szolgay Eds. Budapest: Pázmány University ePress, 2015, pp 167– 170.

machine translated sentences in order to get the reference sentences.

Other types of evaluation methods do not use reference translations. This unsupervised approach is called Quality Estimation of machine translation. This method addresses the problem by evaluating the quality of machine translated segments as a prediction task. For example, Gamon et al. [3] use linear and nonlinear combinations of a language model and an SVM classifier to find the erroneous translations. Albrecht and Hwa [4] present a method that uses regression learning and a set of indicators of adequacy and fluency as references to evaluate the translation at the sentence level.

In our research, we use the framework called QuEst [5], developed by Specia and Gimenez. They implemented features, which are extracted from the source or translated sentences. Then, using machine learning methods, they train the features on post-edit effort scores and build the quality estimation model to predict the quality of machine translated output. Then they optimized the feature set, and reduced it to 17 baseline feature set. They tried more than 160 features for English-Spanish to predict HTER (Human Translation Error Rate). Our aim to find the optimal feature set for Hungarian.

III. Quality Estimation

In the quality estimation task, we extract different kinds of feature indicators from the source and translated sentences, without using reference translations. From source sentences complexity features can be extracted (e.g. number of tokens in the source segment). From the translated sentences, QuEst extracts fluency features (e.g. percentage of verbs in the target sentences). From the comparison between the source and the translated sentences, adequacy features are extracted (e.g. ratio of percentage of nouns in the source and target). We can also extract features from the decoder of the machine translation system. These are the confidence features (e.g. features and global score of the SMT system), but we did not use these confidence features, because we in our experiments we have translations from different machine translation systems, we did not use these features. Numeric values as quality indicators can be extracted from the features. Using quality indicators, we can build quality estimation models with different machine learning methods. With these QE models we can predict the quality of machine translation output in real-time.

IV. Datasets

In our experiments, we used three corpora. The first corpus (C1) contains 1950 English sentences of mixed topics (subtitles, literature, Bible etc.) from the Hunglish corpus [6]. The translated segments are translated by the Google translate, the Bing translate, the MetaMorpho [7] rule based machine translation system and the MOSES [8] statistical machine translation toolkit. The reference sentences are human translated sentences from the Hunglish corpus. The training corpus contains perfect and completely wrong translations.

The second corpus (C2) is a subset of the first one, which contains 550 segments with human evaluated scores.

Adequacy	**Fluency**
1: none	1: incomprehensible
2: little meaning	2: disfluent Hungarian
3: much meaning	3: non-native Hungarian
4: most meaning	4: good Hungarian
5: all meaning	5: flawless Hungarian
0: I do not understand this English sentence	

TABLE I
Adequacy and fluency scales for human evaluation

For creating human scores, we developed a website[1] with a form for human annotators to evaluate the translations. In this website we can see an English source sentence, and a translated Hungarian sentence. People can give quality scores from 1 to 5, from two points of view: adequacy and fluency (see Table 1). 550 sentences were evaluated by at least 3 human translators. The translators were Hungarian people who have minimum B2 level English language skill. As we can see in the Table I, we added a ”0 (I do not understand the English sentence) score, to filter out the uncertain judgements.

The third corpus (C3) is domain (IT) specific, which contains 6283 segments. The source sentences are English, the translated segments are translated by MOSES, the reference translation texts are post-edited sentences corrected by human translators.

V. Methods

First, we created the quality indicators extracted from the features. Then, using human or automatic evaluation scores with a machine learning method are used to build the QE model (see Figure 1). To create the quality indicators from features, we used the QuEst framework. In this study, 77 features (77F) were extracted from the three corpora. The set of 77 features contains 74 features implemented by Lucia et al. and 3 additional features developed by us. In the 74 features, there are adequacy features (e.g. ratio of percentage of nouns in the source and target, ratio of number of tokens in source and target, etc.), fluency features (e.g. perplexity of the target, percentage of verbs in the target, etc.) and complexity features (e.g. average source token length, source sentence log probability, etc.). The 3 added features are: counting precision score, recall score and f1 score using a dictionary. Since Hungarian language tools are not implemented or do not exist, there are language specific features that could not be extracted. For the machine learning task, we used the Weka system [9] to create 6 classifiers with 10 fold cross-validation: Gausian Processes with RBF kernel (GP), Linear Regression (LinReg), Support vector machine for regression with NormalizedPolyKernel (SMOreg), Bagging with M5P classifier (Bag), M5Rules and M5P tree. Further on, we show only the results of the first four classifiers, because these methods gain the best scores. For evaluating the performance of our methods, we used the statistical correlation, the MAE (Mean absolute error) and the RMSE (Root mean-squared

[1] http://nlpg.itk.ppke.hu/node/65

error) evaluation metrics. The correlation ranges from -1 to +1, and the closer the correlation to -1 or +1 is, the better it is. In the case of MAE and RMSE the closer the value to 0, the better.

Fig. 1. QE algorithm

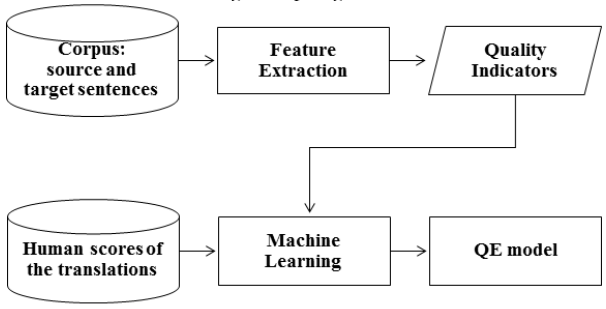

VI. Experiments and optimalization

First task (T1): C1 is evaluated with using automatic evaluation methods: TER, BLEU and NIST[10].

Second task (T2): C1 and C3 are evaluated and are compared using automatic metrics. Since the difference of size of the two corpora is big, We created and evaluated a subset of C3 (SC3), which contains 2000 sentences.

Third task (T3): using C2 and the 77F, we built and evaluated QE models, trained on adequacy scores, fluency scores and average score of adequacy and fluency scores (A+F).

Fourth task (T4): We optimized the 77F to English-Hungarian. For optimizing, we used two different methods: (1) we used the CfsSubsetEval (using BestFirst searching method and 10 fold cross-validation) attribute selection method in Weka, (2) we implemented our own algorithm. In our own method, first, the features are randomly mixed, then quality scores are extracted from the first feature, and MAE score is counted from it. Then, the quality scores extracted from the second feature are added and it was evaluated again, then the third feature was added and evaluated and so on, until all the 77 features scores were added. This sorting method was repeated 15 times. During this process, there were features which increased the MAE result, while others caused decreasement. The features, which increased the MAE scores at least 5 times and with a minimum of 0.005 MAE score, were kept, the others were sorted out. Then the whole process was repeated until all the irrelevant features were sorted out. At the end, 20 features remained, which achieved the best result for English-Hungarian.

VII. Results and Evaluation

The system-level result of the T1 evaluation: TER: 0.6107, BLEU: 0.3038, NIST: 5.1359. These results describe the quality of the T1 corpus. According to the TER and the BLEU scores, 30% of the T1 corpus are correct translations.

		GP	LinReg	SMOreg	Bag
TER	Corr	**0.4897**	0.4013	0.4369	0.4484
	MAE	0.2753	0.2905	**0.2716**	0.283
	RMSE	**0.3521**	0.3702	0.3664	0.3605
BLEU	Corr	**0.3914**	0.3723	0.3881	0.3571
	MAE	0.2741	0.2821	**0.2347**	0.2828
	RMSE	**0.3468**	0.3506	0.3753	0.3526
NIST	Corr	**0.3222**	0.2907	0.3176	0.2576
	MAE	2.9986	3.0102	**2.8112**	3.0597
	RMSE	**3.6379**	3.6877	3.7821	3.7178

TABLE II
Evaluation of T1

		GP	LinReg	SMOreg	Bag	M5R	M5P
Adequacy	Corr	0.4862	0.4556	0.485	**0.5006**	0.4172	0.4375
	MAE	1.0258	1.0232	**0.9936**	0.9987	1.0542	1.0263
	RMSE	1.2145	1.2559	1.2391	**1.2026**	1.2885	1.2685
Fluency	Corr	**0.6192**	0.5915	0.6112	0.6043	0.5624	0.5721
	MAE	0.9125	0.9222	**0.8889**	0.9043	0.9413	0.9267
	RMSE	1.1062	1.1432	**0.9043**	1.121	1.1796	1.1703
A+F	Corr	0.5763	0.5459	**0.5784**	0.5678	0.5054	0.4994
	MAE	0.9076	0.9199	0.9036	**0.9006**	0.9357	0.9316
	RMSE	**1.0925**	1.1291	1.1214	1.099	1.1722	1.175

TABLE IV
Evaluation of T3

To predict the automatic evaluation scores, as we can see in Table II, the GP method achieved the best results in Correlaion and in RMSE, in all cases. In MAE evaluation, the SMOreg method won in all the three cases, but in the Correlation and RMSE, the SMOreg method was the second best. Hence for automatic evaluation scores GP and SMOreg methods are the best.

As we can see in Table III, the GP, the Bag and the SMOreg methods produced the best results. The result of evaluation of the SC3 is the best in most cases. Furthermore, the SC3 apart from the MAE and RMSE in TER, always performed about double value of the result of C1. One reason of the better result is the SC3 is domain specific corpus, the other reason is that there are translations, which have the same source sentence.

In the T3 experiment, the GP, the Bag and the SMOreg methods gained the best results. As we can see in Table IV, the models trained on Fluency scores achieved the best results. It is interesting, that during SMOreg experiment, the features which have the highest weights, are mostly complexity features.

During T4, first, we used the 77F and A+F human scores to build and evaluate the quality estimation models. Then, using the CfsSubsetEval method, 23 features (23F) were selected, and using these 23F, we built the QE models and evaluated them. We also evaluated the C2 with the baseline 17 features (17F). As we can see in Table V, using our feature selection method, we could gain ˜8% better correlation than the 17 baseline feature set. Furthermore, our own selection method gained the best results, it was better than the CfsSubsetEval method, and it achieved better result than the model, which used 77 features.

		TER			BLEU			NIST		
		Corr	MAE	RMSE	Corr	MAE	RMSE	Corr	MAE	RMSE
1950	GP	**0.4897**	0.2753	**0.3521**	**0.3914**	**0.2741**	**0.3468**	**0.3222**	2.9986	**3.6379**
	LR	0.4013	0.2905	0.3702	0.3723	0.2821	0.3506	0.2907	3.0102	3.6877
	SMOreg	0.4369	**0.2716**	0.3664	0.3881	0.2347	0.3753	0.3176	2.8112	3.7821
	Bag	0.4484	0.283	0.3605	0.3571	0.2828	0.3526	0.2576	**3.0597**	3.7178
2000	GP	**0.7818**	0.2138	**0.3528**	0.8671	0.1285	0.1835	**0.7647**	1.893	**2.8944**
	LR	0.6558	0.265	0.4247	0.774	0.1747	0.2319	0.6851	2.2966	3.271
	SMOreg	0.7146	0.2151	0.3961	0.8291	0.1303	0.2081	0.709	1.9006	3.2173
	Bag	0.7514	**0.2048**	0.3713	**0.9105**	**0.0965**	**0.1517**	0.7081	**1.8624**	3.2025
6283	GP	**0.7572**	0.2154	**0.3655**	0.8725	0.1198	0.1786	**0.7574**	1.8914	**2.9181**
	LR	0.6495	0.2672	0.4255	0.7594	0.18	0.2375	0.6628	2.3696	3.3475
	SMOreg	0.717	0.215	0.392	0.8352	0.124	0.2051	0.7253	**1.8367**	3.1259
	Bag	0.7438	**0.2065**	0.3745	**0.9035**	0.0929	**0.1564**	0.5131	1.8731	4.6389

TABLE III
EVALUATION OF T2

		Corr	MAE	RMSE
77F	GP	0.5763	0.9076	**1.0925**
	LinReg	0.5459	0.9199	1.1291
	SMOreg	**0.5784**	0.9036	1.1214
	Bag	0.5678	**0.9006**	1.099
23F	GP	0.5297	0.9491	**1.1327**
	LinReg	0.5118	0.9507	1.1491
	SMOreg	**0.5351**	**0.9192**	1.1509
	Bag	0.4841	0.9705	1.1693
17F	GP	0.5069	0.9598	1.1513
	LinReg	0.4872	0.9635	1.1686
	SMOreg	**0.5184**	**0.9303**	**1.1505**
	Bag	0.4998	0.9491	1.157
20F	GP	**0.5875**	0.8823	**1.0805**
	LinReg	0.5467	0.9093	1.1194
	SMOreg	0.5773	**0.8729**	1.1055
	Bag	0.5562	0.9022	1.1098

TABLE V
EVALUATION OF T4

VIII. CONCLUSION

We built different quality estimation models for English-Hungarian translations. In our experiments, we used automatic metrics and human judgements as well. In the experiment with human judgements, we optimized the quality model to English-Hungarian. In this task, we created a sorting method to find the best features. With our sorting process, we could produce a sorted feature set which contains 20 features. These 20 features produced better results than the 17F baseline feature set, than the 23F and than the 77F. We propose that these 20 features can be the baseline set for English-Hungarian translations. In our experiment, we built different quality estimation models, which can be used for predicting machine translation outputs for English-Hungarian.

In the future, we plan to try more features implemented by Lucia at al. and also further investigate the addition of our own features. We also plan to increase the size of the C2 corpus. Our goal is to build a stable and reliable QE model for English-Hungarian.

REFERENCES

[1] K. Papineni, S. Roukos, T. Ward, and W.-J. Zhu, "Bleu: A method for automatic evaluation of machine translation," in *Proceedings of the 40th Annual Meeting on Association for Computational Linguistics*, ser. ACL '02. Stroudsburg, PA, USA: Association for Computational Linguistics, 2002, pp. 311–318. [Online]. Available: http://dx.doi.org/10.3115/1073083.1073135

[2] M. Snover, B. Dorr, R. Schwartz, L. Micciulla, and J. Makhoul, "A study of translation edit rate with targeted human annotation," in *In Proceedings of Association for Machine Translation in the Americas*, 2006, pp. 223–231.

[3] M. Gamon, A. Aue, and M. Smets, "Sentence-level mt evaluation without reference translations: Beyond language modeling," in *In European Association for Machine Translation (EAMT*, 2005.

[4] J. S. Albrecht and R. Hwa, "Regression for sentence-level mt evaluation with pseudo references," in *In Proceedings of the 45th Annual Meeting of the Association for Computational Linguistics (ACL*, 2007, pp. 296–303.

[5] L. Specia, K. Shah, J. G. de Souza, and T. Cohn, "Quest - a translation quality estimation framework," in *Proceedings of the 51st Annual Meeting of the Association for Computational Linguistics: System Demonstrations*. Sofia, Bulgaria: Association for Computational Linguistics, August 2013, pp. 79–84. [Online]. Available: http://www.aclweb.org/anthology/P13-4014

[6] P. Halácsy, A. Kornai, L. Németh, B. Sas, D. Varga, T. Váradi, and A. Vonyó, "A Hunglish korpusz és szótár." in *III. Magyar Számítógépes Nyelvészeti Konferencia*. Szegedi Egyetem, 2005.

[7] A. Novák, L. Tihanyi, and G. Prószéky, "The metamorpho translation system," in *Proceedings of the Third Workshop on Statistical Machine Translation*, ser. StatMT '08. Stroudsburg, PA, USA: Association for Computational Linguistics, 2008, pp. 111–114. [Online]. Available: http://dl.acm.org/citation.cfm?id=1626394.1626405

[8] P. Koehn, H. Hoang, A. Birch, C. Callison-Burch, M. Federico, N. Bertoldi, B. Cowan, W. Shen, C. Moran, R. Zens, C. Dyer, O. Bojar, A. Constantin, and E. Herbst, "Moses: Open source toolkit for statistical machine translation," in *Proceedings of the 45th Annual Meeting of the ACL on Interactive Poster and Demonstration Sessions*, ser. ACL '07. Stroudsburg, PA, USA: Association for Computational Linguistics, 2007, pp. 177–180. [Online]. Available: http://dl.acm.org/citation.cfm?id=1557769.1557821

[9] M. Hall, E. Frank, G. Holmes, B. Pfahringer, P. Reutemann, and I. H. Witten, "The weka data mining software: An update," *SIGKDD Explor. Newsl.*, vol. 11, no. 1, pp. 10–18, Nov. 2009. [Online]. Available: http://doi.acm.org/10.1145/1656274.1656278

[10] C.-Y. Lin and F. J. Och, "Automatic evaluation of machine translation quality using longest common subsequence and skip-bigram statistics," in *Proceedings of the 42Nd Annual Meeting on Association for Computational Linguistics*, ser. ACL '04. Stroudsburg, PA, USA: Association for Computational Linguistics, 2004. [Online]. Available: http://dx.doi.org/10.3115/1218955.1219032

APPENDIX

PROGRAM 1: Bionics, Bio-inspired Wave Computers, Neuromorphic Models	
Name	**Supervisor**
Flóra BÁLINT	Zsolt LIPOSITS MD DSc Imre FARKAS MD PhD
Virág BOKODI	István ULBERT MD DSc Dániel FABÓ MD PhD
Réka DÉNES	Zsolt RÓNAI MD PhD Zoltán GÁSPÁRI PhD
Dániel DUDOLA	Zoltán GÁSPÁRI PhD
Erzsébet FARKAS	Csaba FEKETE MD DSc
Bálint FILE	István ULBERT MD DSc Dániel FABÓ MD PhD
Edit GYŐRI	István ULBERT MD DSc Dániel FABÓ MD PhD
Márton HARTDÉGEN	Kristóf IVÁN PhD
Katharina HOFER	István ULBERT MD DSc
Attila JÁDY	György KARMOS MD PhD Emília MADARÁSZ DSc
János JUHÁSZ	Sándor PONGOR MHAS
Ágnes KANDRÁCS	István ULBERT MD DSc
Annamária KISS-TÓTH	Zoltán GÁSPÁRI PhD
Kinga KOCSIS	István ULBERT MD DSc
Bertalan KOVÁCS	Zoltán GÁSPÁRI PhD
Eszter LEELŐSSYNÉ TÓTH	Péter FÜRJES PhD Kristóf IVÁN PhD
Zselyke MAGYARI	István PETÁK MD PhD András HORVÁTH PhD
Domokos MESZÉNA	István ULBERT MD DSc
Vivien MICZÁN	István KATONA DSc András HORVÁTH PhD
Ágnes POLYÁK	Krisztina KOVÁCS DSc
Zsófia SZTYÉHLIKNÉ BÉRCES	Kristóf IVÁN PhD Anita PONGRÁCZ PhD
Tamás WILHEIM	Imre KALLÓ MD PhD

PROGRAM 2: Computer Technology Based on Many-core Processor Chips, Virtual Cellular Computers, Sensory and Motoric Analog Computers	
Name	**Supervisor**
Vamsi KIRAN ADHIKARLA	Péter SZOLGAY DSc
Bernadett ÁCS	Gábor SZEDERKÉNYI DSc
Bence József BORBÉLY	József LACZKÓ PhD Péter SZOLGAY DSc
Sándor FÖLDI	György CSEREY PhD Péter SÓTONYI MD PhD
Endre LÁSZLÓ	Péter SZOLGAY DSc
Máté NÉMETH	Ákos ZARÁNDY DSc
Norbert SÁRKÁNY	György CSEREY PhD Péter SZOLGAY DSc
Ádám VÁLY	Péter SZOLGAY DSc József LACZKÓ PhD

PROGRAM 3: Feasibility of Electronic and Optical Devices, Molecular and Nanotechnologies, Nano-architectures, Nanobionic Diagnostic and Therapeutic Tools	
Name	**Supervisor**
Bálint BALÁZS	Balázs RÓZSA PhD
Gergely CSÁNY	Miklós GYÖNGY PhD
Imre Benedek JUHÁSZ	Árpád CSURGAY MHAS
Ádám PAPP	Árpád CSURGAY MHAS
Dénes PÁLFI	Balázs RÓZSA PhD

PROGRAM 4: Human Language Technologies, Artificial Understanding, Telepresence, Communication	
Name	**Supervisor**
Balázs INDIG	Gábor PRÓSZÉKY DSc
Mátyás JANI	György TAKÁCS PhD
Győző YANG ZIJIAN	Gábor PRÓSZÉKY DSc